THERMO-MECHANICAL CHARACTERIZATION OF SILICON CARBIDE-SILICON CARBIDE COMPOSITES AT ELEVATED TEMPERATURES USING A UNIQUE COMBUSTION FACILITY

DISSERTATION

Ted T. Kim, Captain, USAF

AFIT/DS/ENY/09-S01

DEPARTMENT OF THE AIR FORCE

AIR UNIVERSITY

AIR FORCE INSTITUTE OF TECHNOLOGY

Wright-Patterson Air Force Base, Ohio

AFIT/DS/ENY/09-S01

THERMO-MECHANICAL CHARACTERIZATION OF SILICON CARBIDE-SILICON
CARBIDE COMPOSITES AT ELEVATED TEMPERATURES USING A UNIQUE
COMBUSTION FACILITY

DISSERTATION

Presented to the Faculty

Department of Aeronautics and Astronautics

Graduate School of Engineering and Management

Air Force Institute of Technology

Air University

Air Education and Training Command

In Partial Fulfillment of the Requirements for the

Degree of Doctor of Philosophy

Ted T. Kim, BS, MS

Captain, USAF

September 2009

AFIT/DS/ENY/09-S01

THERMO-MECHANICAL CHARACTERIZATION OF SILICON CARBIDE-SILICON
CARBIDE COMPOSITES AT ELEVATED TEMPERATURES USING A UNIQUE
COMBUSTION FACILITY

Ted T. Kim, BS, MS
Captain, USAF

Approved:

_____   _____
Shankar Mall (Chairman)   date

_____   _____
Richard D. Branam (Member)   date

_____   _____
Yung Kee Yeo (Member)   date

_____   _____
Ronald J. Kerans (Member)   date

_____   _____
Larry P. Zawada (Member)   date

Accepted:

_____ _____
Marlin U. Thomas   date
Dean, Graduate School of Engineering and Management

Abstract

Ceramic Matrix Composites (CMCs) comprising silicon carbide (SiC) fibers coated with boron nitride (BN) interphase in a silicon carbide matrix (SiC/BN/SiC) are primary candidates for advanced gas turbine engine applications that require exceptional strength retention at elevated temperature. However, the material is known to exhibit considerably reduced strength retention after oxidation of the boron nitride interphase in the harsh combustion environment of gas turbine engines. The oxidation-induced degradation of the CMCs is related to mechanical loading, such as fatigue of turbine components during engine operation. This research investigated four different types of CMCs under simultaneous application of a combustion environment and mechanical loading. Three of the materials were woven Melt-Infiltrated (MI) BN/SiC reinforced by Hi-Nicalon Type S (Hi-Nic-S), Sylramic (Syl) and Sylramic with insitu BN coating (Syl-*iBN*) fibers, respectively. They were made by the slurry cast method. The other CMC was MI Hi-Nic-S/BN/SiC made using the prepreg MI processing.

The representative environment in this study was a lean-burn combustion that was sufficient for a material surface temperature of $1235 \pm 50^{\circ}$C and flow velocity of *Mach* 0.5. Using a unique test facility as part of this study, the flame was applied on only one side of the specimens to maximize contribution of the thermal gradient and simulate a turbine airfoil heating. Simultaneously, the fatigue behavior of the four CMCs were characterized by applying a cyclic mechanical loading with peak stress ranging from 50% to 125 % of the stress at which the monotonic stress-strain curve deviates from linearity (called proportional limit) at the frequency

and stress ratio (*R*) of 1 Hz and 0.05, respectively. An accelerated durability testing method adopted for this work sets the fatigue runout life to 25 hours or 90,000 cycles in order to test as many specimens as possible and to access the durability potential of each material. The runout specimens were tested for residual strength under room temperature monotonic tension.

The test results showed an inversely related relationship between peak stress and fatigue life for each CMC. The extent of oxidation was greater for a specimen with longer fatigue life, which was attained by applying a lower stress. Substantial thermal gradient stress induced by the directional heating significantly lowered the apparent fatigue strength. This was suggested by considerably low applied fatigue stress that caused failure in all four CMCs, and was discussed in detail using finite element modeling (FEM) and micrographic analysis in Chapter VI. Of the three woven MI CMCs, the one reinforced by *Syl-iBN* fibers demonstrated the highest mechanically applied fatigue stress at runout of 110 MPa, or 66% of its *PL* and was followed by the one reinforced by *Syl* fibers, which showed the runout applied peak stress of 81 MPa or 53% of its *PL*. Next, prepreg MI Hi-Nic-S/BN/SiC with higher matrix density was shown to have an applied runout stress at runout of 105 MPa or 53% of its *PL*, which was considerably greater than 70 MPa or 58% of its *PL* at the runout for woven MI CMC reinforced by Hi-Nic-S fibers. Overall, woven MI Syl-*iBN*/BN/SiC performed the best of the four CMCs having demonstrated the highest apparent fatigue strength of 110 MPa and the highest residual strength of 279 MPa, followed by prepreg MI Hi-Nic-S/BN/SiC with the fatigue strength of 105 MPa at runout and the residual strength of 264 MPa. Woven MI Syl/BN/SiC and woven MI Hi-Nic-S/BN/SiC were third and fourth CMCs in the order of performance.

Acknowledgements

Table of Contents

List of Figures

List of Tables

THERMO-MECHANICAL CHARACTERIZATION OF SILICON CARBIDE-SILICON CARBIDE COMPOSITES AT ELEVATED TEMPERATURES USING A UNIQUE COMBUSTION FACILITY

I. Introduction

Demands for next generation turbine engines for advanced aircraft with increased thrust-to-weight ratio and reliability have propelled on-going research efforts to develop light-weight materials capable of high-performance at elevated temperatures. The efficiency of a gas turbine engine improves with increased turbine inlet temperature (TIT) [1-7]. The TIT is determined by the heat released by combustion and degree of its dilution by component cooling air. So a small efficient engine will require combustion gas with high temperature [8-10]. Figure 1 [11] is a schematic capturing a cross-sectional view of a gas turbine engine. In the downstream of the combustion chamber, the hot products pass at high velocity into the turbine before exit through the exhaust nozzle. The turbine vanes and blades shown in Figure 2 [12] are exposed to this gas path to varying degrees of severity in terms of temperature, stress and gas species contents. Turbine engine manufacturers have made tremendous advancements over the years to develop cooling technology that allows the operation of metal alloys at surface temperature higher than $1000^{o}C$ [9,13]. However, the cooling is provided at the expense of efficiency. Hence, some engineers and scientists have shifted their attention from conventional metal alloys to ceramic matrix composite material (CMC) with exceptional high-temperature strength retention capability. The CMC components in turbine engine applications require reduced cooling due to its high temperature capability and thus have the potential of offering the desired strength and durability at higher thrust-to-weight ratio [1,9,14-16].

1
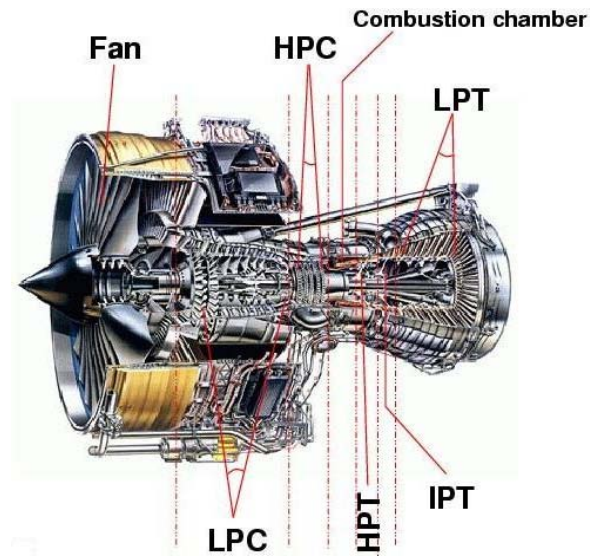
Figure 1: Cut-out View of a Jet Engine from T. Sourmail, 2003 (Trent 800: Courtesy Rolls-Royce Plc.) [11]
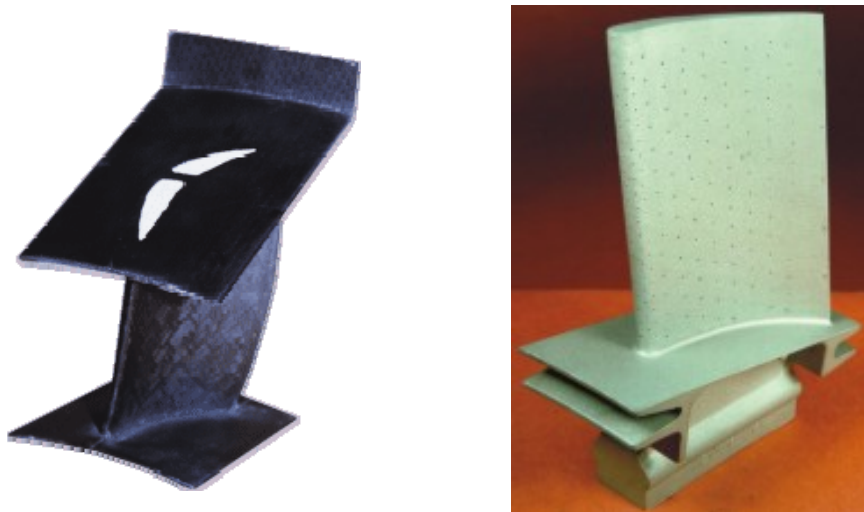
Figure 2: Turbine Vane and Turbine Blade [12]

Since the early 1980s, researchers have studied continuous fiber-reinforced CMCs [5,13,17-20] to gain an understanding on how they can be used in applications where the material requirements exceed what the current nickel base super-alloy can offer [13,21]. CMCs offer low

density, high strength and toughness, and higher temperature performance, and can handle harsh combustion environments encountered in gas turbine engines [7,9,14-1516,18,22-24]. Combustor liners, vanes and blades in application environments are subjected to the harsh combustion conditions. These applications are of great importance to the United States Air Force (USAF), NASA, and the civilian aircraft industry [13,18] and are the focus of this research. A number of USAF and NASA programs in past decade have shown that silicon carbide (SiC) fiber reinforced silicon carbide matrix composites (SiC/SiC CMCs) hold the most promise for high temperature, high oxidation applications [7,9,14-18,22,23,25-27], and therefore they have been explored under several demonstrator programs. There are several commercially available SiC fibers such as Hi-Nicalon Type S (Hi-Nic-S) and Sylramic (Syl). Carbon (C) and boron nitride (BN) have been choices as fiber-matrix interphase materials in the SiC/SiC CMCs.

Challenges imposed on turbine engine materials of hot section components include high temperature, thermal stress, centrifugal stress, contact stress, high frequency and low frequency cycle fatigue, fatigue, creep (stress rupture), oxidation, and corrosion [1]. These challenges are interlinked with one another, as turbine components are under simultaneous subjection to multiple of the above issues. For a realistic experimental validation of potential turbine engine material, a test setup that can facilitate simultaneous consideration of multiple of these interdependent parameters is essential to material development for high temperature, high velocity combustion environment such as in gas turbine engines.

1.1 CMCs of this research

A SiC/SiC CMC system consists of brittle ceramic components such as silicon carbide (SiC) fibers, interphase, and SiC matrix. Yet, the CMC can be engineered to demonstrate pseudo-

plasticity that allows a large strain to failure that any of the three constituents cannot individually attain. Both the fibers and matrix carry appreciable load, unlike composites where the fibers are essentially the sole carrier of the load [28]. Engineering the most appropriate interphase for a given material is a key to attaining an optimal combination of load carrying capability and fracture toughness in CMC that suits the application. The ability to share the applied load between the fibers and matrix is important to enhance the damage tolerant behavior of CMC. The interphase debonding behavior that plays a crucial role in the load sharing of continuous fiber reinforced CMCs is governed by a number of factors including coating thickness, residual stress, coefficient of friction, interfacial fracture topography, wear properties as well as compliance, fracture toughness and surface roughness of the interphase [29-37]. Many of these factors are interdependent with one another and vary with change in surrounding constituents. To make the matter more complicated, many of these determinants of the interphase behavior can undergo a progressive change with mechanical or thermal loadings. The interphase behavior can be altered also by environmental effects such as oxidation. As the service temperature exceeds 450°C [13], the interphase oxidizes upon exposure to the environment, and thus its ability to transfer load and deflect cracks starts deteriorating. The resulting reduction in strain tolerance causes the CMC to behave like a monolithic ceramic, failing catastrophically showing little damage tolerance. Therefore, the interphase is one of the more significant constituents of CMCs that affects the performance of the material under mechanical and thermal stress in the harsh environment of combustion at elevated temperature [37,38]. Several efforts have been underway to modify the interphase to achieve better oxidative durability of CMCs [22,26,39]. One such effort involves the pre-formation of an in-situ BN layer to the SiC fiber before chemically depositing the BN interphase and reinforcing SiC matrix. This NASA proprietary technology was implemented into

4

the Syl-*iBN*/BN/SiC, which consisted of Sylramic fibers with *iBN* layer, BN interphase, CVI SiC and MI SiC matrices [26]. The initial development of this material comprised woven cloth and matrix densified by a slurry cast melt infiltration (MI) process and is thus referred to as the "woven MI Syl-*iBN*/BN/SiC." A more prominent variation of this material comprising the same constituents, is currently under development. This new version is manufactured using the *prepreg* MI process, which refers to a CMC manufacturing process that involves individually coated fibers made into a unidirectional prepreg tape, before being laminated into a composite. The process usually results in denser SiC matrix with lower porosity than its woven cloth counterpart [40]. Presently, these two CMCs are considered the strongest and the most oxidation-resistant systems under the thermo-mechanical loading condition [22,26,39]. Both will be described in more details in Chapter II.

In addition, woven MI Hi-Nic-S/BN/SiC and prepreg MI Hi-Nic-S/BN/SiC are alternatives to Syl-*iBN*/BN/SiC systems for gas turbine engine applications. They are of high commercial interest with a lower cost and wider availability of the Hi-Nicalon fibers that possess high temperature stability and good tow characteristics. Very low matrix porosity for CMCs fabricated using the prepreg MI process was expected to provide the prepreg MI Hi-Nic-S/BN/SiC CMC with an improved resistance to oxidation in high temperature application. These two Hi-Nic-S fiber based CMCs and the woven MI Syl-*iBN*/BN/SiC, along with the woven Syl/BN/SiC with no *iBN* layer, were the materials of this study.

1.2 Interphase degradation by oxidation

Degradation occurs when the composite constituents are altered due to the exposure to harsh environments causing a reduction in the composite's material strength, toughness, and

damage tolerance. Degradation phenomena of SiC/BN/SiC CMCs have been documented in previous studies under laboratory and humid environment conditions [13,41-44]. Cracks caused by applied and thermally-induced stresses allow the environment into the interior of the CMC, resulting in the deterioration of the interphase and the load bearing capability of the fibers by oxidation [13]. One important mechanism can be described as the welding of closely located fibers, which occurs when the oxidative environment attacks the exposed fibers and interphase triggering chemical reactions that consume the functional interphase material to produce liquid borosilicate glass, which solidifies to remove the toughness mechanisms [13,17,27,45]. The term, *embrittlement* or *embrittled* is often used to describe the above described oxidative degradation. Although the embrittlement is somewhat of a misnomer due to the inherent brittle properties of the constituents that make up the CMC, the term is used to describe the degradation in the pseudo-plastic behavior of the CMC in the context of this study. These chemical reactions are enhanced by moisture, which accelerates the oxidation [13,47]. The moisture content is an important consideration as it is unavoidable by-product of combustion in gas turbine engine.

Many previous experimental efforts devoted to understand the durability of SiC/SiC CMCs in combustion environment have been carried out without any direct mechanical load [45-47,58,84,77]. These studies typically exposed SiC/SiC composites in a burner rig for certain duration, and then evaluated such parameters as the weight loss, residual strength and microstructures. Other studies [13,27,28,48,49] investigated the strength degradation phenomena under creep or fatigue loading without exposure to combustion environment. These studies would use a high temperature furnace to simulate the combustion temperature. Some of them incorporated limited environmental control by either adjusting moisture contents or purging the furnace using air, argon or nitrogen [13,48,50]. The detrimental effects of water vapor and other

oxidants in air on oxidation were documented. In all of the experimental efforts on the SiC/SiC CMCs in oxidizing environments, degradation was reported with the extensive oxidative degradation documented with microscopic characterization.

Though these previous studies were invaluable in increasing the fundamental understanding of the oxidative degradation, they were often limited to the one-on-one correlation between parameters. They lack the involvement of the realism and intricacies of the gas turbine engine environment needed for a good simulation that would provide engine designers with the realistic strength data and serve as the basis for their decision making in material selection. There are several experimental facilities that simulate the real gas turbine environment, but they are very expensive to operate and logistically difficult to sustain testing for the length of duration that qualifies for an assessment as to the environmental durability potential of CMCs. Hence, there was a need for a versatile test facility that combines realistic combustion environment with mechanical loading capabilities facilitating the simulation of creep and fatigue scenarios.

1.3 Problem Statement

This study is motivated by the overall goal of improved efficiency of turbine engines via successful insertion of SiC/BN/SiC CMCs. To approach the goal, it was necessary to increase the understanding of different variations of the SiC/BN/SiC CMCs in relation to applied mechanical loading and oxidizing combustion environment. The specific objectives of the current study were twofold. The first was to develop an experimental setup and protocols that facilitate the evaluation for the potentials of CMCs as structural components in gas turbine engine hot-section components. The second objective was to carry out tests on four different types of SiC/BN/SiC CMCs using the burner rig facility by incorporating mechanical fatigue loading in a prescribed combustion

environment representing a typical operating condition for an advanced gas turbine engine. This study developed a testing protocol tailored to evaluate and compare the degradation phenomena due to oxidation and fatigue loadings of the four SiC/BN/SiC CMCs in a combustion environment similar to gas turbine engines.

The four SiC/BN/SiC CMCs considered in this study were woven MI Syl-*iBN*/BN/SiC, the woven MI Syl/BN/SiC, woven Hi-Nic-S/BN/SiC and prepreg MI Hi-Nic-S/BN/SiC. The experiments and analyses performed under this study investigated the degradation induced by oxidation and mechanical loading in a given combustion environment for each of the four material systems, and further led to comparisons among the four systems. Specifically, the comparison of the mechanical and microscopic characteristics between woven MI Syl-*iBN*/BN/SiC and woven MI Syl/BN/SiC revealed the effectiveness of *iBN* fiber coating layer in the given combustion environment in terms of the increase in fatigue life and strength. Similar comparison between woven MI Syl/BN/SiC and woven MI Hi-Nic-S/BN/SiC allowed qualitative assessment on the effect of the fiber type in fatigue behavior in the given condition. In addition, the comparison between woven MI Hi-Nic-S/BN/SiC and prepreg MI Hi-Nic-S/BN/SiC facilitated a comparative discussion of the two CMCs manufactured by different processing methods.

1.4 Approach

To accomplish the objectives and to facilitate the comparisons stated above, the early part of this study was devoted to the development of the AFIT/AFRL Burner Rig equipped with the capability to simultaneously apply mechanical and combustion environment to a test specimen.

Using the completed test system, the four CMCs were evaluated for their fatigue behaviors in a combustion environment similar to gas turbine engines.

Fatigue was chosen to be the loading type applied on the CMCs, as previous studies [50,51] indicated that fatigue could cause severe reduction in life. Each CMC system is subjected to fatigue loading of constant frequency and stress ratio with peak stress varying from 50% to 125% of the monotonic, as-received proportional limit (*PL*), from one test to another, in a prescribed combustion condition uniformly applied to all CMCs tested. The *PL* refers to the highest stress which a CMC can sustain without deviating from proportionality of stress-strain curve. The 25-hour test duration was selected to simulate a typical length of total hot time in engine and to ensure that the environmental effects are soundly established as well as to conduct a reasonable number of experiments required to draw a valid statistical conclusion. From the test phase, the plot of the peak stress and its corresponding number of cycles-at-failure, or S-N curve, was recorded for each CMC.

Each test was configured such that the prescribed combustion impinged on one side of the specimen to induce thermal gradient stress across thickness. Hence, the asymmetric chemical and thermal field surrounding each test specimen was imposed simultaneously with a constant fatigue loading until the specimen failed or survived after the 25-hour test limit.

Using the specimen from each test, the analysis of oxidation was investigated on both fractured and sectioned surfaces using Scanning Electron Microscopy (SEM), Field Emission SEM (FESEM) and Energy Dispersive Spectroscopy (EDS). The extent of oxidation determined from each fractured surface was correlated to the corresponding experimental parameters such as the load applied and the duration of combustion exposure. Useful net stress was estimated based on the applied peak stress and the fraction of the intact fracture surface.

The microscopic analysis of the test specimens was incorporated with the finite element analysis (FEA), in pursuit of capturing the significance of thermal gradient effect on test specimen to analyze failure mechanisms. The chemistry of the gas surrounding a specimen was profiled as it pertains to the propensity for oxidation fractographically observed on fracture surfaces.

1.5 Chapter Summary

In this chapter, the SiC/BN/SiC CMCs were introduced as the material of the current study being projected for gas turbine engine applications. Oxidation was a degradation mechanism for the CMCs, which could potentially make CMCs unsuitable for stressed application such as turbine vanes and blades. The overall objectives of this study were to develop the AFIT/AFRL Burner Rig and to test and compare the degradations in the load carrying capabilities of four different SiC/BN/SiC CMCs with fatigue loading in a combustion environment representative of gas turbine engines. The approach taken to attain these objectives was also outlined.

1.6 Outline of this Thesis

The next chapter provides the background for the degradation by oxidation as well as the fatigue behavior of CMCs in general. The four CMCs selected for this study briefly introduced in Chapter I, are discussed in detail in the next chapter. Also, the combustion environment of a gas turbine engine is discussed and compared to the test conditions provided by other test facilities from previous studies. The discussion in Chapter II leads to the recognition of the need for a versatile burner rig facility in order to achieve the goals of this study. Chapter III presents the detailed discussion of the development of the AFIT/AFRL Burner Rig facility. Experiments conducted to validate parameters as well as to calibrate the instruments for real-time monitoring are described in detail. This chapter also discusses the experimental methodology and justifies the

approach taken to result in the pre-test and post-test procedures. Chapter IV provides an in-depth discussion of each of the four CMCs based on experimental data. The discussion of each CMC is developed in a pattern to facilitate comparisons among them in Chapter V in which they are compared on the basis of fiber coating, fiber type, and manufacturing method. Chapter VI analyzes the test results based on the fatigue strength and fractographic details observed from the four CMCs as well as the chemical and thermal environments surrounding the test specimen. Finite element analysis was carried out to substantiate the experimental observations by simulating the stress condition of test specimen with the observed thermal profile undergoing fatigue loading. Chapter VII summarizes the research presented in this dissertation and includes recommendations for future work.

II. Background

This chapter provides general background for the characterization of the degradation phenomenon of CMCs in simulated gas turbine engine environment. First, an overview of CMCs is provided. Then, the previous experimental efforts to simulate the combustion environments using burner rigs are reviewed. Next, the four SiC/BN/SiC CMC systems selected for this study are introduced with the focus on the characteristic details that make each system unique. This is followed by the background study for the interphase degradation in an oxidizing environment. Lastly, the failure mechanism of a continuous fiber reinforced CMC under fatigue loading is reviewed.

2.1 Background on CMCs

CMCs consist of ceramic fibers and interphase, which are chemically and physically distinct from each other, distributed within a continuous ceramic matrix [13] (Figure 3). Ceramic materials can withstand very high temperatures due to ionic bending [38], making them ideal for high temperature applications. Ceramic fibers provide CMCs with high strength and high elastic modulus. Compared with other CMCs reinforced with particulates or whiskers, the continuous ceramic fiber-reinforced ceramic matrix composites offer significantly higher fracture toughness, allowing the composites to fail non-catastrophically [20].
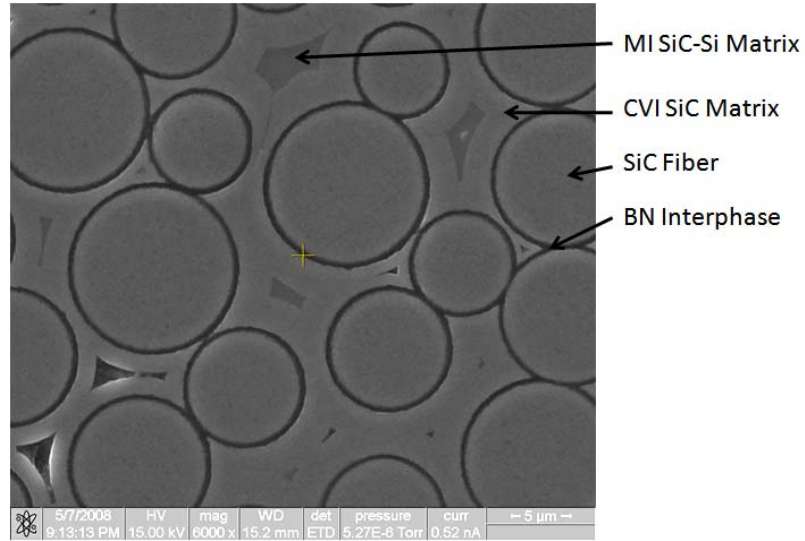
Figure 3: CMC Constituents – Surface Perpendicular to Fibers

The fiber architecture determines the CMC material properties [52]. For applications involving multi-axial loading, composites can be fabricated with two dimensional ply layup, two dimensional woven, or a three dimensional fiber configuration. Ceramic fibers give CMCs the toughness that monolithic ceramics lack as well as some load carrying capability. Pores formed in the matrix both during processing and in service are unavoidable at the current stage of processing technology. These pores are the most probable crack initiation sites. The interphase encircling each fiber, as shown in Figure 3, has low friction and forms a relatively weak chemical bond with the fiber and matrix surfaces in contact, thus readily allowing debonding and subsequent sliding to occur in such a way that the resulting frictional dissipation gives rise to inelastic strains [52,53-55]. This local stress redistribution mechanism alleviates the elastic stress concentration that causes catastrophic failure [52].

Carbon (C) and Boron Nitride (BN) are two widely used interphase materials. BN is the primary interphase material for this study, though there are some CMCs in this study with the fibers having residual carbon inherited from processing. At the service temperature exceeding

450°C, the BN interphase oxidizes upon the exposure to the ambient (e.g. Crack propagation provides an ingress route for O_2 to the interphase), and ultimately causes an accelerated failure of the composite [13]. This oxidation is especially detrimental in the presence of applied tensile load, which widens cracks allowing rapid degradation.

Typical service conditions of gas turbine hot-section components such as turbine vanes and blades include harsh combustion environments with high-speed stream of hot gas products containing oxidizers impinging on the turbine components under stress from various sources including thermal gradients, centrifugal force, high frequency and low frequency cyclic fatigue, and creep loading [1]. The CMC hot-section components under such severe condition must exhibit long term durability for a high payoff in the application to offset the relatively high cost of manufacturing. Four of the relatively state-of-the-art SiC/BN/SiC CMC systems are investigated for their potential as the gas turbine hot-section component material in the demanding service environment.

2.2 Combustion Environments

Previous studies involving the characterization of the SiC/SiC CMCs including the oxidative degradation, e.g. embrittlement, have been primarily concerned with the failure and damage mechanisms at elevated temperatures in the ambient laboratory and/or humid environment [13,42-44]. These studies offer baseline information in relation to one or two independent variables. However, they do not simulate the actual harsh environment conditions as well as the synergistic effects of all the primary variables of the realistic gas turbine engine conditions. Several primary variables are dynamically interrelated to one another; temperature change may vary the gas velocity and/or the composition of combustion byproducts. The change

in combustion byproducts alters the chemical environment surrounding test materials. Therefore, the tests done in environments where only one variable is controlled does not reflect realistic turbine engine operating conditions, and their results cannot be used with confidence in material selection for an advanced gas turbine engine.

Burner rig test facilities are sometimes used to simulate the gas turbine engines instead of full scale engine tests due to the economic and logistic issues. For example, the NASA facility burns jet or simulated jet fuels and air in controlled ratios to produce combustion gas chemistries and temperatures that are realistic to those in gas turbine engines [56,58]. In addition, the test section simulates the pressures and gas velocities representative of gas turbine engines [57-59]. There have been relatively few studies with CMC systems using burner rigs [39,46,60], and the majority of these tests involve the characterization of CMCs without any direct mechanical load on the test coupon in combustion environment, though there may have been indirect mechanical load from the gas flow, pressure and thermal gradient. In some of these previous efforts, the coupons would be subjected to a set of combustion environmental conditions for a prescribed duration in a burner rig, and the coupon would subsequently be evaluated at room temperature for residual mechanical properties such as residual strength, weight loss, oxidation of fiber/matrix interphase, damage mechanisms etc [39,46,59]. This sequential approach may benefit towards the understanding of the effect of a given combustion environment with the set time of exposure, but it does not represent a realistic condition subjected to a load-carrying structural component in a gas turbine engine.

The following section reviews these previous experimental efforts to simulate the hydrocarbon combustion environments for materials testing. Discussion identifying the driving force behind the research efforts in regard to simulating the combustion environment is followed

by the review of the burner rig test facilities that have previously been developed. The need for a new state-of-the-art burner rig facility is identified.

2.2.1 Motivation

Figure 4 [11] depicts a schematic cross-section of a turbofan engine along with the temperature and pressure profile along the engine. From left to right, air is drawn into the rotating compressor via the intake and is compressed to a higher pressure before entering the combustion chamber. Fuel is mixed with the compressed air and ignited by flame in the combustor. The exothermic combustion reaction produces gas with high temperature. Hot combustion products leaving the combustor expand through the turbine. Although this expansion process reduces the turbine exit gas temperature and pressure, both parameters are usually still well above ambient conditions. The gas stream exiting the turbine expands to ambient pressure via the propelling nozzle, producing a high velocity jet in the exhaust trail. If the jet velocity exceeds the aircraft flight velocity, there is a forward thrust upon the airframe.

For a given amount of fuel injected, increasing the overall pressure ratio of the compression system raises the combustor entry temperature and turbine inlet temperature (TIT) [1-7]. Thus, the operation of an efficient engine will produce combustion gas with high temperature. To this end, the TIT envelop is constantly being pushed higher in search of a more efficient engine. However, current nickel-base super-alloy turbine components soften and melt at temperatures between 1200 and 1400°C [61], and thus cannot maintain their structural integrity without appropriate thermal protection.
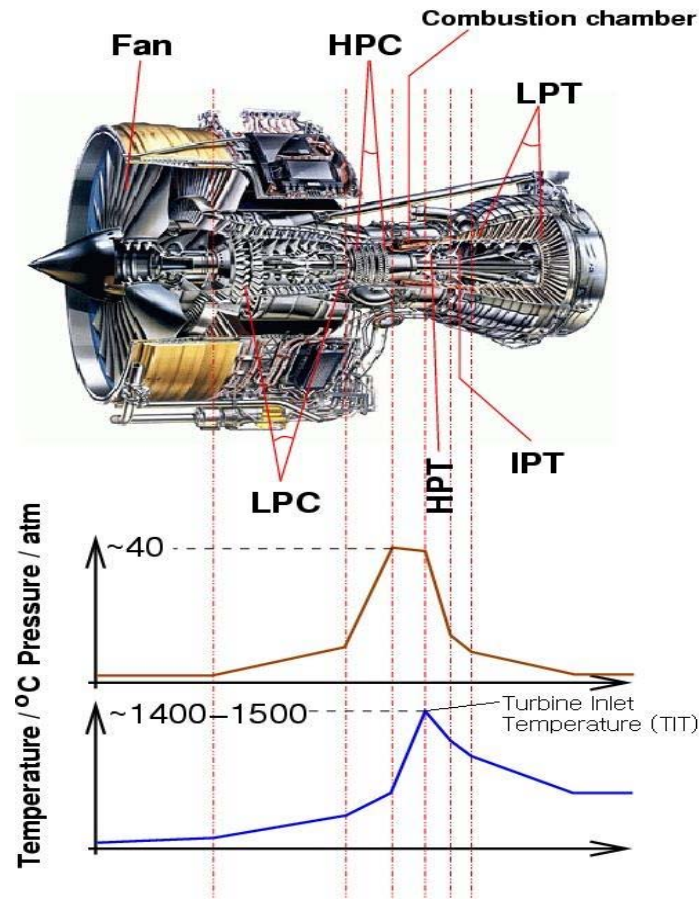
Figure 4: A jet engine with the pressure and temperature profiles from T. Sourmail, 2003

(Trent 800: Courtesy Rolls-Royce Plc.) [11]

The CMCs are attractive materials for current and future engine hot-section components to fill this need [1-7,14-16]. They are relatively high strength materials and can retain strength at high temperature. The ability to retain strength is important for hot section components of an engine due, not only to the functional mechanical loading on structural components, but also to the thermal gradient stresses, which arise from non-uniform temperature field surrounding the components, as many components are subjected to a directional heating that gives rise to the temperature gradients. The development of ceramic hot-section components must be validated through experimental validation in service environments. A full scale experiment using the

17

specimens shaped into similar scale and geometry as the real turbine components in a real service environment is extremely expensive and logistically difficult to accomplish. Alternatively, burner rig facilities are generally used to simulate the service environments.

Turbine Vanes and blades are located further downstream of the combustor, and are exposed to similar environments with higher temperature and high gas flow velocity. Unlike the combustor liner, turbine blades are rotating components subjected to high centrifugal load at the attachment with the rotor [70]. This imposes low cycle fatigue on the components. Table 1, reproduced from DiCarlo and Van Roode's work published in Ref 7, shows approximate maximum stress conditions for SiC/SiC hot-section components in advanced gas turbine engines Component stresses are indicated as in-plane tensile (σ_x) and thru-thickness tensile (σ_z). These stresses arise from a combination of aerodynamic forces, mechanical loads and thermal gradient stresses due to cooling on the backside of the component. Progressive development of better performing CMC systems would continually push the stress levels higher such that the component designer will have higher allowable design stresses to work with [7]. In order to aid in successful implementation of the ceramic vanes and blades, experimental efforts must be put forth that address the increased environmental harshness and increased loading, using the successful SiC/BN/SiC composites as baseline materials.

Table 1: Maximum Stress Conditions for SiC/SiC CMC Components [7].

Component	Max Stress (MPa)	Max Stress Locations	Primary Cooling
Combustor Liner	$\sigma_x \sim 100$	Attachments	Hot Surface
Turbine Shroud	$\sigma_x \sim 100$	Wall at gas inlet	Backside
Turbine Vane	$\sigma_x \sim 100$, $\sigma_z \sim 30$	Leading, trailing edges	Backside
Turbine Blade	$\sigma_x \sim 300$, $\sigma_z \sim 30$	Airfoil hot side at root	Backside

2.2.2 Simulation with Burner Rigs

It is generally accepted that an ideal combustion burner rig facility would have the following features [63]. First, the rig must be able to produce the combustion gas with the temperature that is high enough to meet a continually increasing TIT requirement. The TITs in the gas path of modern high-performance jet engines can exceed 1650°C [61].

Secondly, high temperature gradients in the materials generate stresses and results in thermo-mechanical fatigue (TMF) during service environment [62]. In addition, all engine components are subject to some type of mechanical loading. Therefore, the rig must also have the ability to apply the static and cyclic loadings both thermally and mechanically. This feature is essential to study the thermo-mechanical fatigue (*TMF*) with both in-phase (*IP*) and out-of-phase (*OP*) cyclic loading scenarios. The *IP* refers to the case where the maximum load in tension is reached at the maximum temperature, whereas the *OP* is the case where the maximum load in compression is reached at the maximum temperature. Both *IP*- and *OP-TMF* are of great concerns in designing of a gas turbine engine.

Third, the rig should produce a high velocity of gas flow approaching or exceeding *Mach 1*.0. The *Mach* number increases with increasing flow velocity, and decreasing temperature. It also depends on the gas composition, which determines the gas constant (*R*) and the ratio of specific heats (γ) for a given temperature.

The next feature of importance for an ideal burner rig involves the high pressure capability [63]. Today, advanced turbine engines have the chamber pressure of approximately 40 *atms* [11], and this envelope is pushed even higher as the needs for more efficient, next generation engines increase. In the combustor, pressure increase shifts the chemical equilibrium of the combustion reaction toward the side with fewer moles of gas [64]. This, assuming stoichiometry, increases the

rate of combustion reaction and promotes the formation of more combustion products for the same rate of fuel consumption. In addition, the formation of volatile species such as *Si(OH)$_4$ (g)* and *SiO (g)* occurs at much greater rates as the surrounding gas containing moisture becomes more pressurized. The loss of material due to this increased volatility at high pressure environment degrades the material integrity and causes an accelerated failure [47,83-86,91,92,56].

The fifth recommended feature for an ideal burner rig is that it must be able to simulate both fuel-lean and fuel-rich operations of the gas turbine engine. The ability to operate in fuel-lean condition is important in simulating a typical turbine engine operation. Conversely, the fuel-rich operation represents the condition in the immediate downstream of the fuel injection as well as the engine undergoing afterburning or hot streaking. The fuel-rich and fuel-lean operations involve different chemical species and flame radicals [63]. In the following section, several experimental facilities currently available for material testing are reviewed individually. The characteristics of each rig are compared against the ideal features discussed here.

2.2.3 Burner Rig Facilities

2.2.3.1 NASA 0.3 Mach Atmospheric Pressure Burner Rig (APBR)

The 0.3 *Mach* Atmospheric Pressure Burner Rig (APBR) was developed by the NASA Lewis Research Center for thermal and thermo-mechanical durability testing. Figure 5 [65] depicts the flame impingement onto a test specimen in the test cell. Preheated air at 260°C and JP-4 jet fuel with a fixed equivalence ratio of 0.5 is pumped into the combustion chamber to initiate the combustion process, ejecting into the atmosphere a jet flame with temperature and gas velocity up to 1370°C and 0.3 *Mach* , respectively [65]. Using this rig, Ertürk and St. Hilaire [66] investigated the thermal fatigue behavior of *Si$_3$N$_4$* ceramic composites of different fiber

architectures. Other researchers studied the heat transfer during the thermal fatigue of CMC using the rig [67]. Although the burner rig incorporates the constant loading capability up to 250 MPa, it falls short of meeting many of the prescribed requirements including the gas temperature and widely variable operating equivalence ratios among others. There are other APBRs with similar features and higher temperature capability (e.g. up to 1650°C) available elsewhere, one of which is shown in Figure 6 [68]. However, this APBR facility, unlike the NASA APBR, does not have the means provided to incorporate the mechanical loading.
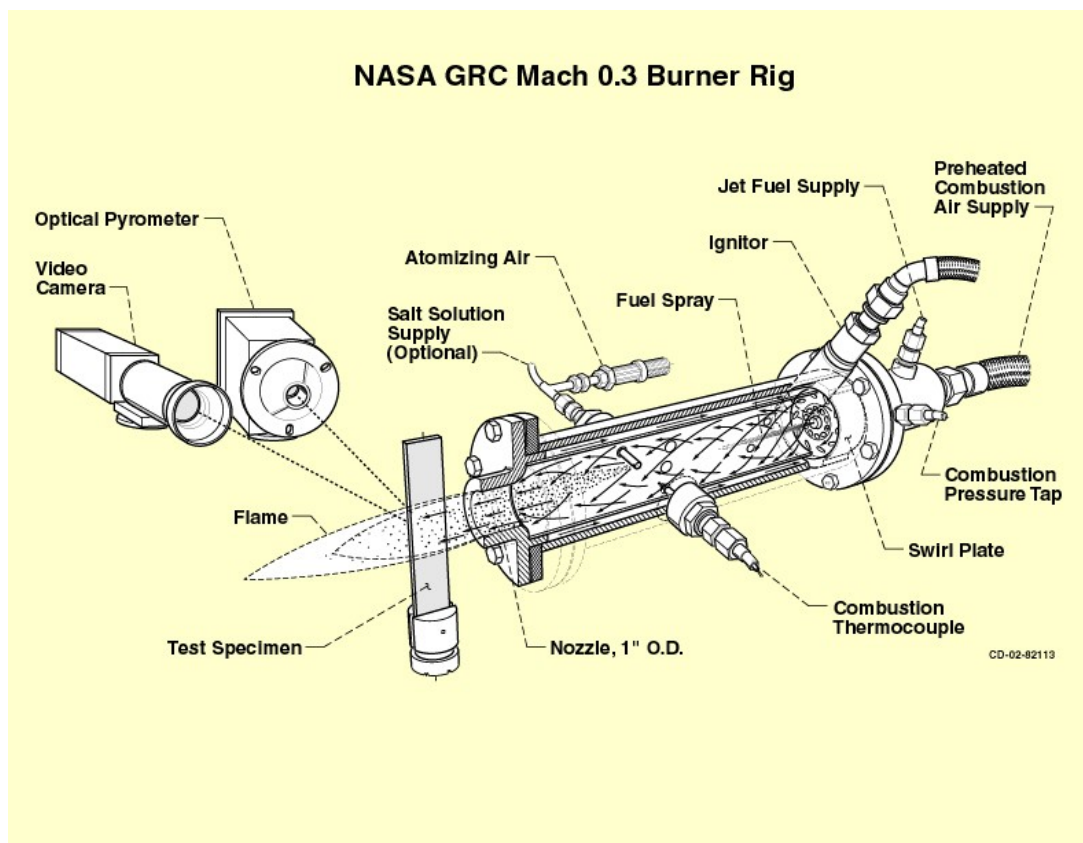
Figure 5 : Schematic of the 0.3 *Mach* APBR at NASA Lewis Research Center [65]
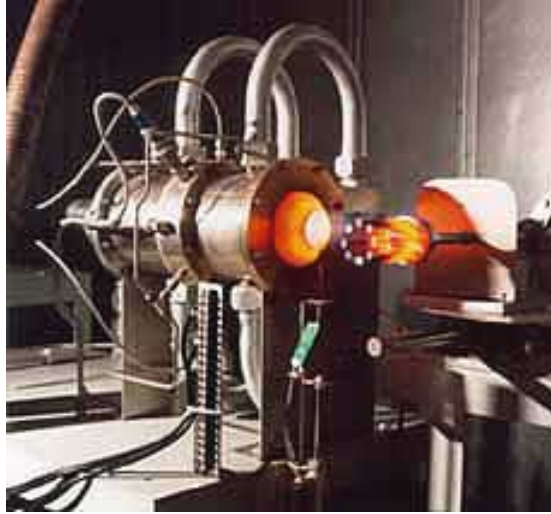
Figure 6: The APBR at National Aerospace Laboratory – The Netherlands [68]

2.2.3.2 NASA High Pressure Burner Rig (HPBR)

The High Pressure Burner Rig (HPBR) is another burner rig developed by the NASA Glenn Research Center in efforts to understand the high temperature degradation mechanisms in advanced materials of gas turbine engines [58]. From right to left in the schematic shown in Figure 7 [58], preheated air enters the pressurized chamber where it is directed through a swirler and mixed with jet fuel, causing ignition of the flame with temperature and velocity up to $1650^{\circ}C$ and 30 *m/s*. The combustion products flow downstream into the test section over the specimen held within a fixture. The uniqueness of this burner rig lies in its ability to simulate both lean and rich burn operating conditions and the ability to vary test pressures from 4 to 12 atm. Still, the maximum flow velocity of only 30 *m/s* is significantly below the required value, and more importantly, the rig does not provide a means to control mechanical load on the specimen.
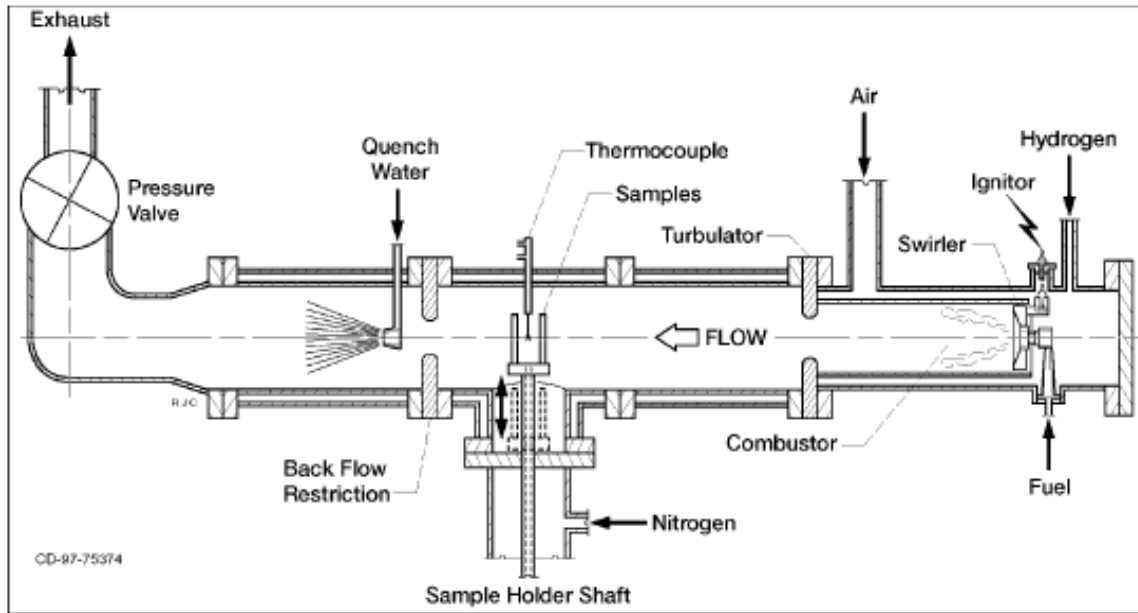
Figure 7: Schematic of the High Pressure Burner Rig (HPBR) [58]

2.2.3.3 Oak Ridge National Laboratory (ORNL) Furnace: "Keiser Rig"

The Keiser Rig is a high-temperature, high pressure tube furnace, which was originally constructed to conduct corrosion/leak tests on ceramic materials for a steam reformer application [69]. It primarily consists of a large box furnace containing several ceramic SiC pressure vessels and a multiple-flow gas-supply/manifold system as shown in Figure 8 [69]. This furnace permits simultaneous exposure of numerous specimens at temperatures up to 2800^oF and pressures as high as 34 *atms* [69]. The Keiser Rig was used to study the materials degradation observed in environmental durability testing [45,70]. The Keiser Rig is not equipped with the capability to apply load and is essentially a furnace wherein the gas flow velocity is negligible, and does not have the capability to impose a thermal gradient in controlled way. The rig is excellent for its designed purpose of researching long term environmental effect on materials, but may not

23

simulate the turbine components under load and the impingement of high velocity gas flow that accompanies thermal gradient. .
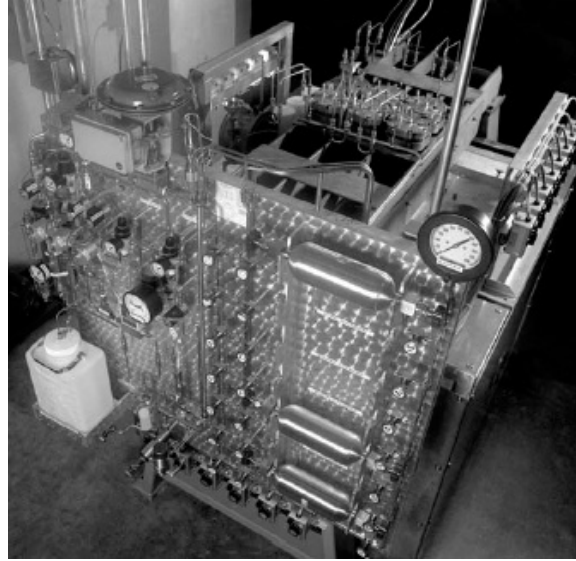
Figure 8: ORNL's Keiser Rig [69]

2.2.3.4 Wind Tunnel Experimental Simulation System (WS)

The *WS* system shown in Figure 9 [72], located at Laboratory of Thermal Structure Composites, Northwestern Polytechnical University in China, couples a combustion wind tunnel and a servo-hydraulic testing system (Instron™). The wind tunnel combustion gas with temperature up to 1600°F flows at the speed up to *Mach 1.0* downstream and impinges on a test specimen placed between the upper and lower grips of the Instron™ loading device. This atmospheric pressure system includes a combustion atmosphere adjustment device which allows the change in partial pressure of oxygen and water in the flame, facilitating the parametric studies of oxidation effect. However, the large scale wind tunnel system is extremely expensive to operate for the extended period of time necessary for durability testing [71,72]. This, coupled

with its difficulty in simulating thermal fatigue, renders the WS system falling short of the desired requirements for an ideal burner rig.

Figure 9: Wind tunnel experimental system at Northwestern Polytech University in China

2.2.3.5 NASA Rich-Quench-Lean (RQL) sector Rig

The *RQL* process refers to a fuel injection system for a gas turbine engine combustor, wherein multiple flow passages form [60]. The annular *RQL* rig is positioned in the downstream of the combustor test facility shown in Figure 10 [60]. Hot air produced by the facility enters the inlet of the *RQL* rig, wherein a fuel-rich mixture is ignited by the fuel/air nozzles and enters the rich zone liners. In passing each of the following zones, a controllable amount of air is mixed with the burning fuel, creating a more fuel-lean environment in the next zone. This stepwise decrease of equivalence ratios from upstream to downstream aids in creating the realistic combustion flow condition encountered inside the combustor of an aircraft gas turbine engine. It is in the piccolo probe where the first stage turbine vanes of an aircraft turbine engine can be simulated. Although

the rig was designed to test the annular combustor liners experiencing differential fuel/air ratios, the rig remains useful for the simulation of turbine vanes and blades. This is because the rig can simulate the lean-burn exposures of the gas products with high velocity, high pressure, and high temperature [60]. However, no loading capability and the prohibitive cost associated with this large scale experimentation make it difficult to argue against the need for a compact, less-expensive and more versatile rig.
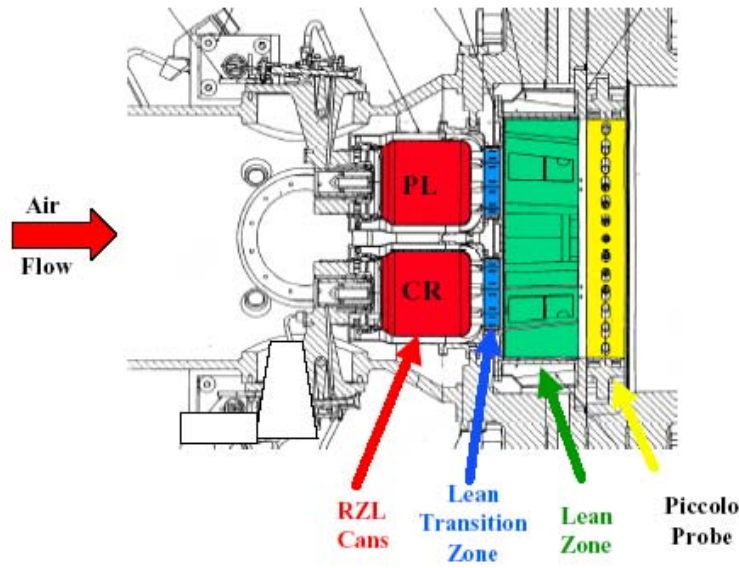
Figure 10: Top view of the RQL sector rig, showing the main components [60]

Table 2 summarizes the comparisons of the five combustion simulation facilities introduced in this section in relation to the ideal features suggested earlier. Each shaded block indicates that the pertinent feature is not satisfied by each facility. The details of the shortcomings are briefly described in the shaded blocks. It is readily apparent from the table that none of the five test facilities can satisfy all the ideal features. In terms of capabilities, the Wind Tunnel Experimental Simulation System (WS) in China comes closest to the ideal system except that it is atmospheric system with nominal deficiency in the temperature requirement and the inability to

simulate a quick thermal cycling. Aside from the uncertainty cast around this system due to the unavailability of its graphic representation, this full scale combustion wind tunnel system is understandably "very expensive" to operate for long term durability testing [71].

Table 2: Comparisons of combustion simulation facilities

Ideal Features	NASA 0.3 Mach APBR	NASA HPBR	ORNL "Keiser Rig"	Wind Tunnel System (WS)	RQL Sector Rig
Type	Burner Rig	Burner Rig	Furnace	Burner Rig	Burner Rig
Temperature exceeding 3000^oF	Up to 2500^oF		Up to 2800^oF	Up to 2900^oF	Up to 2000^oF
Gas Velocity approaching 1 Mach	0.3 Mach	Up to 30 m/s	"Very Slow"		Unknown
High Pressure (Pressure Varying Capability)	Atmospheric Pressure			Atmospheric Pressure	
Variable Fuel-Lean Operation	$\Phi = 0.5$ (Fixed)		N/A		
Variable Fuel-Rich Operation	No Fuel-Rich Capability		N/A		
Static Loading		No	No		No
Cyclic Loading	No	No	No		No
Thermal Cycling					
Cost	Low	Moderate	Low	Extremely Expensive	Extremely Expensive

Each of the aforementioned test facilities was built with a different set of motivation, objectives and conditions, and thus the evaluation based on the requirements identified for the purpose of this research may not be fair or warranted. However, it is clear from the comparisons that none comes close to meeting all the criteria to facilitate this research, and this raised the need for a more versatile test rig led to the development of the AFIT/AFRL Burner Rig. While the test facility we developed also falls short of addressing all the suggested features, such as high

pressure capability, it does meet majority of the criteria at relatively low cost of operation, making

it adequate for the proposed study. Details about this rig are provided in the next chapter.

2.3 Potential CMCs for hot-section application in gas turbine engines

2.3.1 Current Materials Limitation

Highest temperature components of modern gas turbines are constructed of nickel-base

super-alloys [9,13]. The vanes and turbine blades made of these super-alloys have difficulty in

sustaining in the high temperature environment, and require adequate cooling. Cooling is

achieved by taking air from the compressor and ducting it to the hot components. After serving as

coolant this air is returned to the turbine [1]. This process incurs a significant penalty in engine

efficiency. With the continuous push for the development of higher efficiency engines, CMCs

have been explored as potential replacement of the nickel super-alloys because of their

exceptional innate high-temperature capability, which reduces the need for the cooling.

2.3.2 SiC/BN/SiC Materials

SiC/SiC CMCs are currently the best choice for applications in high temperature and high

moisture environments [7,13-16]. C and BN interphase materials are typically used with SiC

fibers, such as Hi-Nicalon Type S (Hi-Nic-S), Sylramic, and Sylramic-*iBN (*Syl-*iBN)*. Nicalon

and Sylramic are two types of fibers that have relatively long pedigree of success in providing

fibers for the development of CMCs. Hi-Nic-S is an improved version of the earlier Nicalon fiber

that found its applications in turbine engine applications, and Syl-*iBN* is the NASA-proprietary

in-situ BN coated Sylramic fiber that demonstrated mechanical properties improved from the

Sylramic fiber including its resistance to environmental degradation. Details of each fiber and the

difference between fibers are discussed in details in the ensuing section. Regardless of the type of

fiber, increased fiber volume will result in higher strength, but also brings a number of negative ramifications such as decreased thermal conductivity and increased susceptibility to matrix cracking [18,22,23].

Between C and BN, BN is considered a better interphase material because it displays sufficient compliance for matrix cracking deflection around the fibers and it is less susceptible to oxidation than carbon-based coatings [13,22,25]. In addition, the in-situ BN layer (*iBN*), grown on Sylramic fibers by the NASA proprietary thermal treatment that involves diffusion of boron sintering aids out of the fibers in nitrogen environment [7,22,26]. The *iBN* serves as a buffer layer that inhibits detrimental chemical attack from inadvertent oxygen and also reduces detrimental mechanical interactions between contacting fibers [7,22,26]. The *iBN*-coated fibers, in the case of woven MI Syl-iBN/BN/SiC, are coated with SiC by Chemical Vapor Infiltration (CVI) and subsequently with a proprietary mixture of chemicals including SiC and Si by Melt-Infiltration (MI) [45, 73]. The combination of the fibers, the BN-interphase and the matrix provides the CMC materials properties needed for the high-temperature application in engine hot sections [22,26,39], where oxidative degradation by aggressive ambient gases makes the durability of components an important issue.

Several variations of SiC/BN/SiC materials have been investigated for combustor liner application. The Syl-*iBN*/BN/SiC system, when properly melt-infiltrated to minimize porosity, is one of the strongest and the most resistant systems in high temperature, oxidizing environments due to high fiber strength and the *iBN* layer [22,23,26,39]. There are other SiC/BN/SiC systems that have been demonstrated for successful combustor liner application using the *HPBR* [15] and *RQL* test rig [60].

In this study, four variations of SiC/BN/SiC composites are investigated in a high-temperature, oxidizing condition that also involves mechanical loading for simulation of a turbine blade; (1) woven MI Syl-*iBN*/BN/SiC, (2) woven Syl/BN/SiC, (3) woven MI Hi-Nic-S/BN/SiC, and (4) prepreg MI Hi-Nic/BN/SiC. The proprietary BN interphases in the CMC systems are typically doped with silicon and forms a combined B_2O_3-SiO_2 oxidation product, and the presence of the SiO_2 greatly slows oxide volatilization and thus reduces overall oxidation rates of the fiber coatings [13,144].

2.3.3 Specific Materials in This Study

2.3.3.1. Woven MI Syl-iBN/BN/SiC and Woven MI Syl/BN/SiC

Two of the CMCs chosen for this study use the Sylramic based fibers, namely Sylramic and Sylramic-iBN (Syl-*iBN*). For both CMCs, the fiber tows, each of which has approximately 800 of these fibers, are woven into a cloth in a five-harness satin (*5HS*) weave pattern [28,73], depicted in Figure 12 [18,28]. For woven MI Syl/BN/SiC, six of the woven cloths are stacked, warp-aligned and molded. Then, the silicon doped BN interphase is deposited on the fiber using the CVI process. The resulting woven perform is passed through in a slurry containing SiC and then melt-infiltrated by Si along with some other proprietary chemicals to produce a denser matrix containing predominantly SiC and Si [22, 74]. This process is depicted in Figure 13. In the case of woven MI Syl-iBN/BN/SiC, there is an extra heat treatment applied after the weaving process. The *iBN* of the Syl-*iBN* fiber is a product of the NASA proprietary thermal treatment applied on the woven cloth of the Sylramic fibers in a controlled nitrogen environment, which causes mobile boron sintering aids in the Sylramic fiber to diffuse out of the fiber bulk and to form a thin in-situ grown BN (*iBN*) layer on each fiber surface. The resulting *iBN* layer on the

Sylramic fiber adds to creep and oxidation resistance over as-produced Sylramic fiber, as the *iBN* serves as a buffer layer that reduces detrimental mechanical interactions between contacting fibers [22]. Figure 11A & B show the SEM of the pristine woven MI Syl-iBN/BN/SiC and woven MI Syl/BN/SiC taken in backscattered electron mode (BSE). Along with the CMC constituents, also depicted in the figure are the voids that have been sealed off during CVD processing surrounded by CVI SiC matrix on 90° tows as shown in Figure 11, defined here as trapped voids

A   B
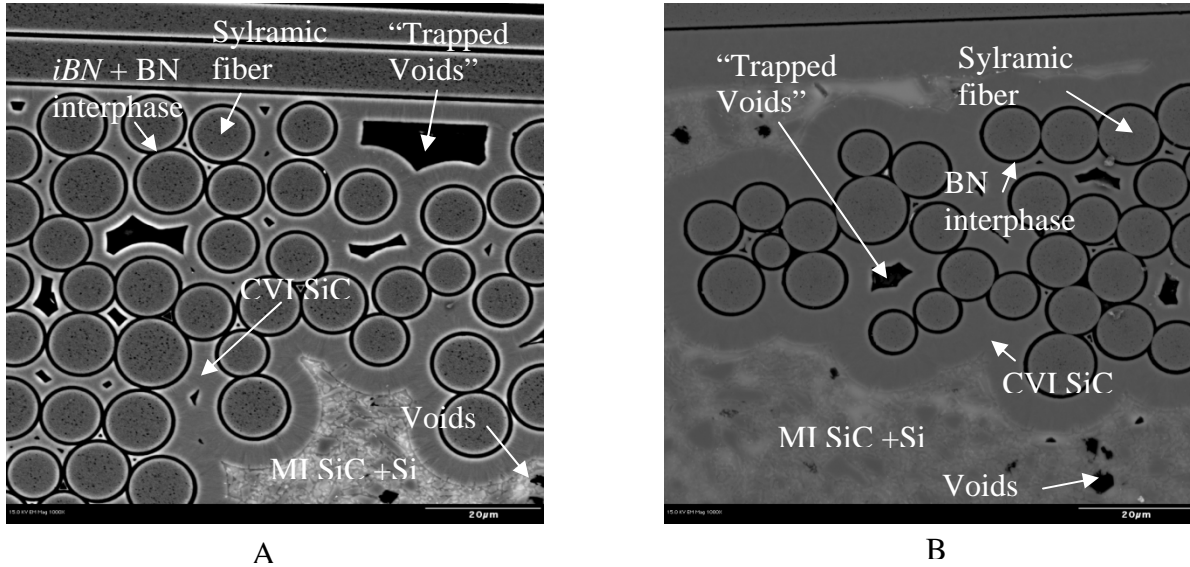
Figure 11: Microstructure of pristine samples; (A) woven MI Syl-iBN/BN/SiC and (B) woven MI Syl/BN/SiC

The rest of the processing steps for woven MI Syl-iBN/BN/SiC are similar to that described for the woven MI Syl/BN/SiC. Due to the similarities in the processing steps taken in manufacturing both the CMCs, with notable difference that one has the fiber with an in-situ BN layer, the difference in mechanical properties may be attributed to the presence of the *iBN*. It is understood that there are intricate details of the processing that relate to the size of SiC particles and the presence and contents of Si as well as other elements in the MI matrix, which affect the thermal residual stress that builds up during processing. Such details are unavailable due to the proprietary reason.

31
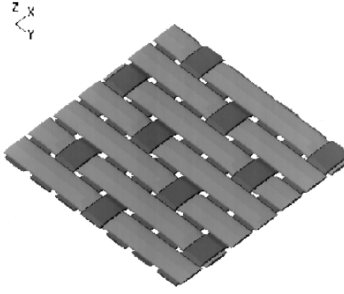
Figure 12: Five-harness Satin Weave [18,28]
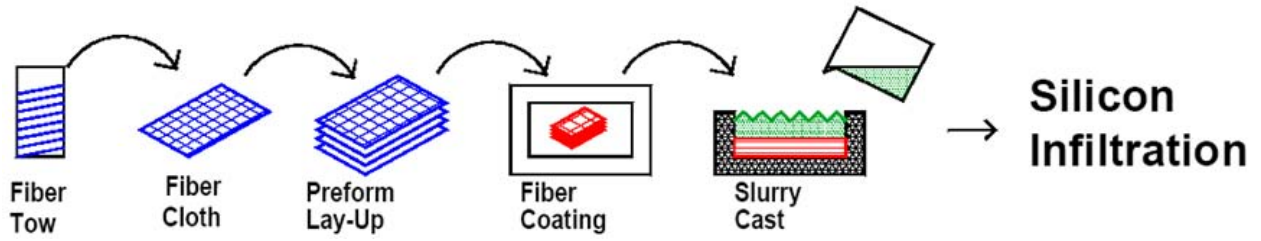
Figure 13: Manufacturing Steps of Woven Slurry Cast MI CMC [74]

2.3.3.2. Woven MI Hi-Nic-S/BN/SiC and Prepreg MI Hi-Nic/BN/SiC

The other two CMCs of this study use the Hi-Nicalon Type S fiber (Hi-Nic-S). The woven MI Hi-Nic-S/BN/SiC is manufactured using the casting process very similar to those used for the two Sylramic based CMCs, with architecture of fibers woven in 5*HS* stacked and warp aligned before slurry casted in SiC, followed by the melt-infiltration using Si for matrix densification. The woven MI Hi-Nic-S/BN/SiC consists of two more plies and has slightly less fiber volume and higher matrix porosity than the two Sylramic based CMCs. The volume fractions are supplied by GE, the manufacturer of the three CMCs, which are verified in house using microscopic images, and the porosity of the woven MI Hi-Nic-S/BN/SiC is estimated by comparing the area fractions of voids on micro level images based on the reported porosity level for the two Sylramic CMCs.

The fourth CMC of this study, Prepreg MI Hi-Nic-S/BN/SiC uses the same fiber as the woven MI Hi-Nic-S/BN/SiC, but is processed with significantly different fiber architecture and processing method. Using the prepreg MI processing developed by General Electric Global Research Center (GEGRC) [74], each Hi-Nic-S fiber is coated with a double-layer of BN and then with a thin Si_3N_4 layer by the CVI process. The thin Si_3N_4 layer is to protect the enclosing BN during processing. Each coated fiber is then impregnated by being run through matrix slurry. Using the subsequent wet drum winding process, unidirectional tapes are formed. Eight of the tapes are laid up and laminated in $[0/90/90/0]_s$ to shape into preforms before a subsequent molten Si MI processing is applied [73,74,76]. The prepreg MI process is illustrated in Figure 14.
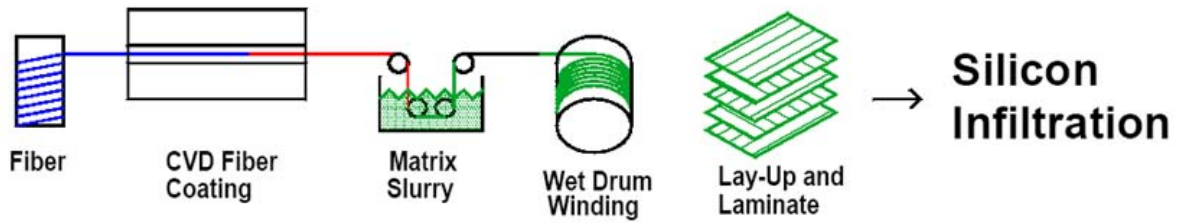
Figure 14: Manufacturing Steps of Prepreg MI CMC [74]

Figure 15A & B show SEM of pristine woven MI Hi-Nic-S/BN/SiC and prepreg MI Hi-Nic-S/BN/SiC taken in backscattered electron mode (BSE). Each prepreg tape embeds 20~25 *vol %* of the Hi-Nic-S fiber [76], i.e. considerably less than those of the woven MI CMCs. Unlike the slurry cast MI process, the fibers are coated and impregnated before preform shaping, and, therefore, the matrix slurry has the chance to better penetrate all inter-fiber voids [73,76]. Consequently, the prepreg MI Syl-*iBN*/BN/SiC has lower residual porosity than the slurry cast MI Syl-*iBN*/BN/SiC [7,22, 73,76]. Pores provide ingress routes for the oxidative environment, and severe degradation of the composite performance is experienced as the oxidants reach and react with the interphase and fibers. Thus, it might be expected that the prepreg MI Hi-Nic-S/BN/SiC

should outperform the slurry cast woven MI Hi-Nic-S/BN/SiC in an oxidizing environment. This is to be verified by the current study that subjects both CMCs in the same oxidizing combustion environment coupled with fatigue loading. [74]. Currently, there is no published report available on the high-temperature durability of the prepreg MI CMC system. Table 3 summarizes the compositions and architectural information of the aforementioned four CMCs in this study to facilitate comparisons.
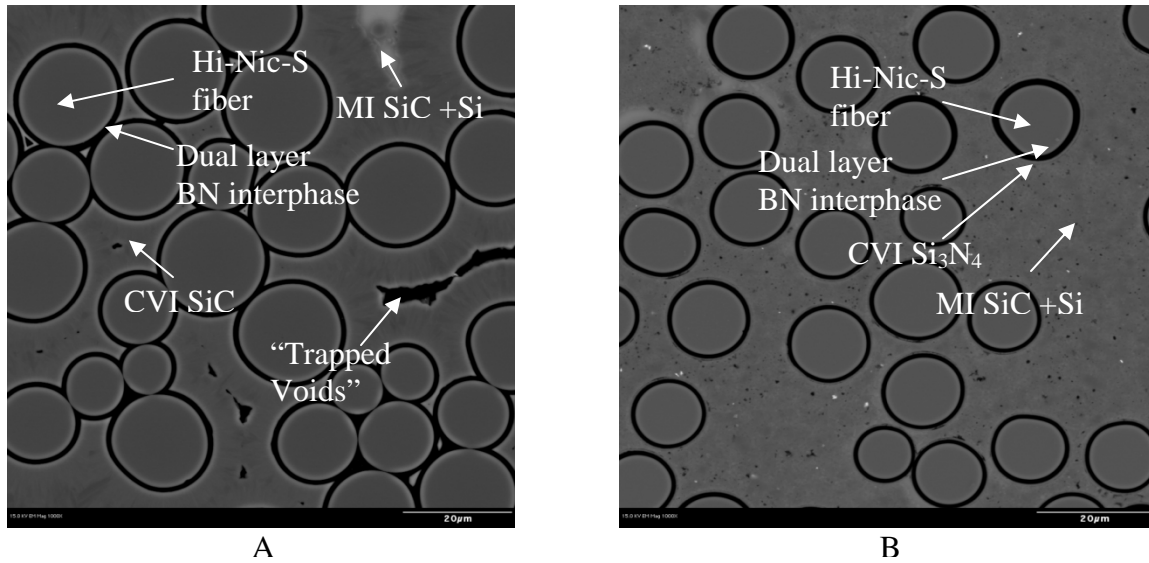
Figure 15: Microstructure of pristine materials; (A) woven MI Hi-Nic-S/BN/SiC and (B) Prepreg MI Hi-Nic-S/BN/SiC

Table 3: Compositions of CMCs [22,75, 76]

	Fiber vol %	Pattern	Layup	Plies	Ends per Inch (EPI)
Woven MI Syl-iBN/BN/SiC	38~40	5HS	Warp-aligned	6	20
Woven MI Syl/BN/SiC	38~40	5HS	Warp-aligned	6	20
Woven MI Hi-Nic-S/BN/SiC	35.7	5HS	Warp-aligned	8	18~20
Prepreg MI Hi-Nic-S/BN/SiC	20~25	Prepreg Tape	[0/90/90/0]$_s$	8	N/A

2.3.3 Comparisons

The four CMC systems can be grouped in terms of the fiber type and the processing methodology used. Within each group, however, each system has its unique distinction. For

example, two slurry-casted woven MI CMC systems with different fiber types can be compared. Similarly, the woven MI Hi-Nic-S/BN/SiC and the prepreg MI Hi-Nic-S/BN/SiC can be compared for the effect of the processing methodology.

2.3.3.1 Sylramic vs. Sylramic-iBN

The woven MI Syl-*iBN*/BN/SiC and the woven MI Syl/BN/SiC are nearly identical in all aspects except that the former has the very thin in-situ BN layer on the Sylramic fiber. The *iBN* layer keeps the fibers separated and thus prevents the neighboring fibers from welding together [22,40]. By subjecting similar loading conditions, it is possible to evaluate the benefit of the *iBN* coating.

The two material systems are similar to NASA's 01/01 material developed under the Ultra-Efficient Engine Technology (UEET) Program [13] in terms of architecture, layup sequence, constituents and their relative volume fractions. LaRouchelle [13] used the woven MI Syl-*iBN*/BN/SiC to perform studies of its creep-rupture behavior in a furnace environment where temperature and humidity was controlled. This study reported the oxidation embrittlement at intermediate temperature, providing microscopic evidence that the welding between neighboring fibers worsens with increase in water vapor content. Other previous studies using the CMC systems with similar constitutive and chemical makeup found that the slurry cast woven MI CMCs are prone to severe degradation in a burner rig flame [25, 77].

For both the Sylramic based MI CMCs, the architecture involves weaving of fiber tows in the five harness satin pattern, as shown in Figure 12, making it difficult for the crossover points of the fiber tows to be coated uniformly by the CVI process. The crossover points are prone to cracking due to high geometric stress concentration. The non-uniformly coated CVI matrix in the

crack-prone area would make the crossover susceptible to oxidation-induced failure. In case that the CVI matrix that kept two adjacent tows separated is fractured, the oxidation in one tow can carry into the neighboring tow through the crack, creating a cascading effect of multiple adjacent tows being degraded by oxidation. Therefore, crossover points are causes of potential concern for woven MI CMCs.

2.3.3.2 Hi-Nic-S fiber vs. Sylramic or Sylramic-iBN

The comparisons among different fiber types can be extended to include woven MI Hi-Nic-S/BN/SiC using the Hi-Nic-S fiber. With the difference in fiber type, the thermal and chemical properties at high temperature are expected to be different. Thus, it is important to review the properties of the fibers pertinent to this study. The non-stoichiometric (C/Si >1) Hi-Nicalon fiber from Nippon Carbon and the stoichiometric (C/Si ~ 1) Sylramic and Sylramic-*iBN* fibers from ATK (COIC) have small diameters and low oxygen content, and thus provide good thermomechanical reinforcement capability for SiC/SiC composites [22,23,78,79]. The Hi-Nicalon Type S (Hi-Nic-S) is a near stoichiometric variation of the Hi-Nicalon fiber with reduced fiber diameter and improved strength and high temperature properties [79]. In Table 4 [22,23,78,79], the stoichiometric Sylramic-*iBN* shows very similar properties as the near-stoichiometric Hi-Nic-S fiber. It is also notable that Sylramic-*iBN* is the only fiber that does not have thin-carbon surface finish. A thin carbon layer on non- or near-stoichiometric fibers can quickly oxidize at intermediate temperature via pipeline oxidation, opening a path for subsequent oxidation of the overlying BN interphase [32]. Significantly greater thermal conductivity of the Sylramic-*iBN* fiber is the product of improved thermal processing [18], which helps the evolution of *iBN* layer. This increased thermal conductivity reduces the build-up of thermally induced stress,

and improves durability significantly at high temperature [18]. At elevated temperature where creep becomes an important mechanism, small grain size and high oxygen content enhance the thermally activated degradation [23]. The Sylramic-*iBN* with much more coarse grains shows a greater resistance to creep deformation [23].

Table 4: Properties of Reinforcing Fibers [22,23,78,79]

Trade Name	Sylramic	Sylramic-iBN	Hi-Nicalon Type S
Manufacturer	COIC	COIC/NASA	Nippon Carbon
Average Diameter (*μm*)	10	10	12
Fibers Per Tow	800	800	500
Average Grain Size (*nm*)	100	>100	100
Elemental Composition, *wt %*	67 Si + 29 C + 0.8 O + 2.3 B + 0.4 N + 2.1 Ti	N/A	69 Si + 31 C + 0.2 O
Surface Composition	Thin-carbon + B + Ti	Thin iBN (~100 nm)	Thin carbon
Density (*g/cm3*)	3.05	3.05	3.05
Avg. R.T. Tensile Strength (*GPa*)	3.2	3.2	~2.5
RT Tensile Modulus (*GPa*)	~400	~400	400~420
Coefficient of Thermal Expansion ($10^{-6}/K$)	5.4	5.4	3.5
Thermal Conductivity at RT (W/m^2C)	46	>46	18

2.3.3.3 Prepreg MI vs. Slurry Cast MI

The woven MI Hi-Nic-S/BN/SiC and the prepreg MI Hi-Nic-S/BN/SiC differ by the fiber architecture and processing method. The low residual porosity is the concept employed to develop the prepreg MI process. The ultimate strength is limited by its relatively low fiber volume fraction. The low fiber volume fraction of the prepreg MI contributes to a relatively high thermal conductivity, minimizing the thermally induced stress [76]. The prepreg MI has nominally 20-25 *vol %* fiber whereas the slurry cast materials has 35.7 *vol %* fibers [75]. In principle, different modes of composite failure can occur for two CMCs with relatively difference in fiber volume fraction, i.e. 20~25 *vol %* vs. 35.7 *vol %*. The strength of the CMC with lower fiber volume would

be more likely to be determined by the matrix-dominated failure, because the stresses required for matrix failure may exceed those required for fiber failure. The difference in failure mode may lead to a different fracture surface appearance. Still, the two CMCs differ by more than just the fiber volume; they are made using different processing methods.

For example, the prepreg MI CMCs, even with significantly less fibers, have similar tensile properties to the slurry cast MI CMCs [76]. This is believed to be primarily attributed to an even distribution of fibers of less number throughout the matrix, thus avoiding detrimental interactions between contacting fibers [40]. In addition, the prepreg MI process yields composites with much lower (< 1.0 %) residual porosity than those fabricated using the slurry cast MI process. Therefore, the prepreg MI composites should have superior mechanical and thermal properties. This is to be determined by the experimental work performed in this study.

Table 5: Composite Architectures and Properties at Room Temperature [22,74,76,79-81]

CMC type	Description	Fiber vol %	Porosity (%)	*UTS* (MPa)	Strain at UTS (%)	*PL* (MPa)	*E* (GPa)	Thermal Expansion $(10^{-6}/^{o}K)$ @ $1200^{o}C$
Woven MI Syl/BN/SiC	5HS, 6 plies, 0/90 warp aligned	38~40	4.5 ± 0.5	431	0.57	167	207	5.2* (IP) 4.6* (TT)
Woven MI Syl-iBN/BN/SiC	5HS, 6 plies, 0/90 warp aligned	38~40	4.0 ± 0.5	271	0.29	153	210	5.2* (IP) 4.6* (TT)
Woven MI Hi-Nic-S/BN/SiC	5HS, 8 plies, 0/90 warp aligned	35.7	8.0 ± 0.5	334	0.54	121	195	5.4* (IP); 2.9** (TT)
Prepreg MI Hi-Nic-S/BN/SiC	Tape Prepreg, 8 plies $[0/90/90/0]_s$	20~25	< 1.0	340	0.71	197	264	3.9* (IP); 4.1* (TT)

IP = In-plane. TT = Thru Thickness
* CTEs extracted from Figure 5 of Ref [76] and Figure 6 of Ref [22]
** CTE at approximately 1000°C.

Finally, Table 5 summarizes the composite architectures and typical properties of all four CMCs described in this section. The data shown on the table are from the open literature, and no proprietary data are included.

2.4 CMC Degradation by Oxidation

Degradation of CMCs under this investigation is driven by oxidation. Oxidative environments in gas turbine engines have chemicals that react with CMC constituents, degrading the ability of the BN interphase to deflect cracks and deteriorating the debonding and sliding mechanism that provides the CMC the toughness necessary for structural applications. Thus, it is useful to look at chemistry behind the degradation by oxidation and some known degradation types that may relate to the topics in this paper.

2.4.1 Oxidation Chemistry

The SiC/BN/SiC CMCs consist of SiC fibers, BN interphase coating and the SiC matrix. In addition, the melt infiltrated (MI) CMCs considered in this study incorporate Si in the matrix to reduce porosity in the matrix [73] and improve conductivity. Pores usually form during material processing [82] in the matrix, and cracks initiate from the pores in response to applied mechanical load. Both the pores and cracks serve as ingress routes for the oxidants to reach the various parts of the CMCs. The CMC constituents have varying degrees of chemical affinities for oxidation reactions with agents such as O_2, H_2O, CO, and CO_2. For Si and SiC that presents in the MI composite matrix [47,45,83-85],

$$Si + O_2 \rightarrow SiO_2(s) \tag{1}$$

$$Si(s) + 2H_2O(g) \rightarrow SiO_2(s) + 2H_2(g) \tag{2}$$

$$SiC(s) + \frac{3}{2}O_2(g) \rightarrow SiO_2(s) + CO(g) \qquad (3)$$

$$SiC(s) + 3H_2O(g) \rightarrow SiO_2(s) + CO(g) + 3H_2(g) \qquad (4)$$

$$SiC(s) + CO_2(g) \rightarrow SiO_2(s) + 2C \qquad (5)$$
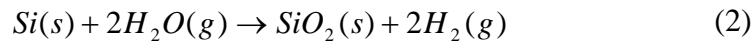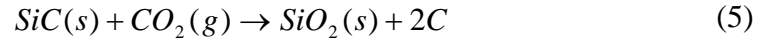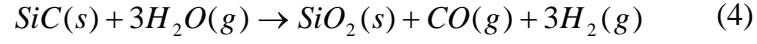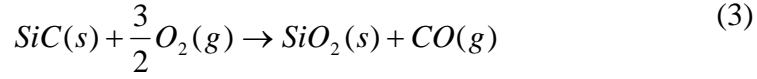
The chemical interactions between the Si-based constituents and the oxidizing agents result in the formation of the protective SiO_2 scales. The silica forms as a thin film, which is highly stable, dense, and self-healing [83]. At 1200°C, the silica formed begins in an amorphous state and develops into a crystalline state slowly with time [86]. Depending on the pressure, the phase of the silica scale may be either solid or viscous liquid, and it is highly sensitive to both temperature and the concentration of hydroxyl (*OH*) [87,88]. Elevated temperature lowers the activation energy for the reactions that cause the viscous flow of silica [87,89]. The *OH* content reduces the viscosity of the silica, such that its glass transition temperature is lowered. As a result, the temperature below which the silica exists in a solid state is lowered. Therefore, the likelihood of the silica scales to behave as viscous liquid increases in a high temperature, *OH*-containing oxidizing environment. In addition, the water vapor that exists in relative abundance decomposes at the combustion temperature approaching 2500°C, releasing more *OH* species into the flow to interface with the silica scale. This further lowers the viscosity of the silica and reduces the glass transition temperature, increasing the probability of the scales to be in viscous liquid at the temperature below 1185°C [90]. It is not known if water vapor has this effect on crystalline SiO_2 [91].
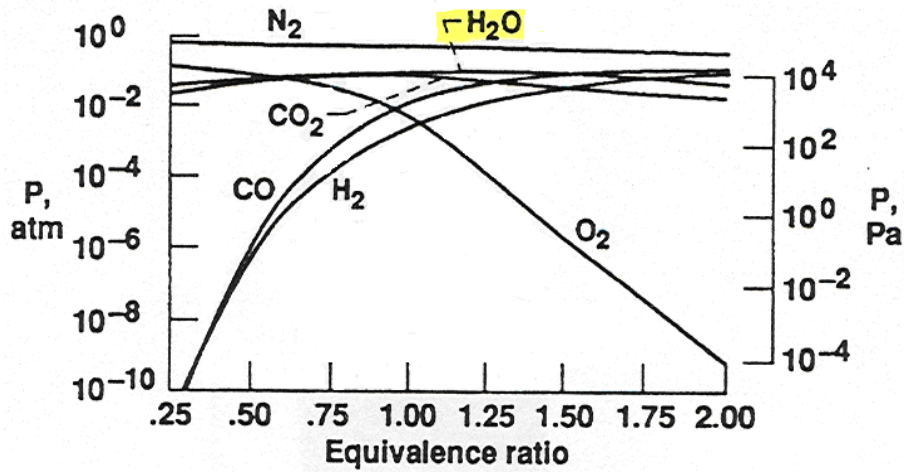
Figure 16: Equilibrium gas composition as a function of equivalence ratio [83]

The growth of this oxide film is described to be parabolic with time [47,83-92]. In combustion environments, however, silica scales react with the combustion gas species and degrade in the form of volatilization. The gas composition, which varies with equivalence ratio as shown in Figure 16 [83], features a number of chemical species that affects the volatility of the silica scales. Four types of gaseous volatile species are known to form as a result of the silica volatilizing reactions shown below [13,47,83,85,92].

$$SiO_2(s) + CO(g) \rightarrow SiO(g) + CO_2(g) \tag{6}$$

$$SiO_2(s) + H_2(g) \rightarrow SiO(g) + H_2O(g) \tag{7}$$

$$SiO_2(s) + 2H_2O(g) \rightarrow Si(OH)_4(g) \tag{8}$$

$$SiO_2(s) + H_2O(g) \rightarrow SiO(OH)_2(g) \tag{9}$$

$$SiO_2(s) + 3H_2O(g) \rightarrow Si_2O(OH)_6(g) \tag{10}$$
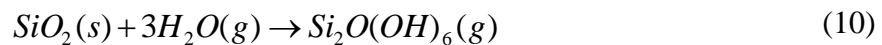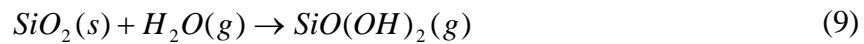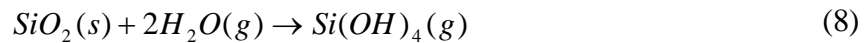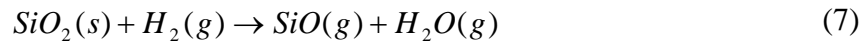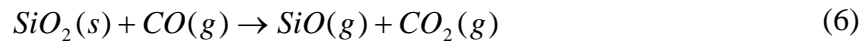
The loss of material due to these concurrent reactions occurs at a linear kinetic rate simultaneously, as the silica grows in a parabolic manner with time. The resulting balance

between the two competing kinetics is described as "paralinear" [47,83-92], and the thickness of silica scales varies with time in a paralinear fashion. Formation of silica scales in this manner consumes the *Si* and *SiC* matrix material. This changes the morphology of the matrix surface exposed to the environment and reduces the structural integrity of the material system. If pre-existing pores and newly nucleated cracks in the matrix develop under load and extend to the interphase surrounding fibers, the oxidizers gain access to the BN interphase and readily react to form the liquid-phase B_2O_3 according to as follows [13, 45, 83]:

$$2BN(s) + \frac{3}{2}O_2(g) \rightarrow B_2O_3(l) + N_2(g) \qquad (11)$$

$$2BN(s) + 3H_2O(g) \rightarrow B_2O_3(l) + N_2 + 3H_2(g) \qquad (12)$$
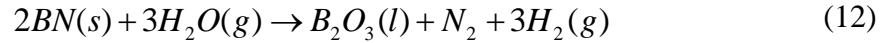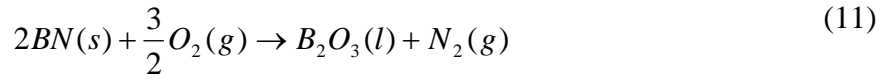
Simultaneously as the formation of B_2O_3 is occurring, *SiC/Si* in the matrix surface in contact with the interphase and the Si doped with the BN interphase also oxidize according to Equations (1) thru (5) and form silica scales in the paralinear fashion. Because the BN fiber coating oxidizes faster than the surrounding *Si* and *SiC*, it acts as a preferred path for the transport of oxidants into the enclosed fiber [45]. Once the BN interphase layer is breached, the SiC fibers oxidize to form silica scales. The liquid B_2O_3 product from Equations (11) and (12) can then become borosilicate glass by reacting with these SiO_2 according to the following reaction [13,45,83]:

$$B_2O_3(l) + SiO_2(s) \rightarrow B_2O_3 \cdot SiO_2(l) \ (borosilicate \ \text{glass}) \qquad (13)$$
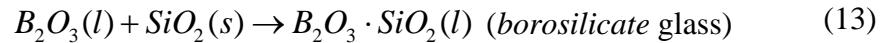
The amount of weight gain observed by Ogbuji [77] does not support the assessment that the SiO_2 comes solely from the oxidation of the *SiC* fiber, *SiC/Si* matrix and Si in the interphase. He suggests the B_2O_3 dissolves the *SiC* matrix and possibly the fiber, predominantly the former by the following reaction [77]:

$$B_2O_3(l) + SiC(s) \rightarrow B_2O_3 \cdot SiO_2(l) + CO(g) \qquad (14)$$
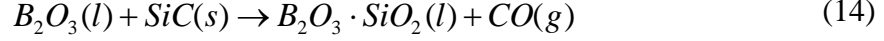
The SiO_2 most probably comes from a combination of the above sources [13,77]. The end result is that the B_2O_3 in the liquid phase reacts and produces borosilicate glass that remains in a liquid form [83]. Based on equilibrium thermo-chemical considerations the B_2O_3 is expected to volatilize significantly [45,93,94] in the presence of moisture according to the following reactions [13,45,83]:

$$B_2O_3(l) \rightarrow B_2O_3(g) \qquad (15)$$

$$B_2O_3(l) + H_2O(g) \rightarrow 2HBO_2(g) \qquad (16)$$

$$B_2O_3(l) + 3H_2O(g) \rightarrow 2H_3BO_3(g) \qquad (17)$$

$$3B_2O_3(l) + 3H_2O(g) \rightarrow 2H_3B_3O_6(g) \qquad (18)$$
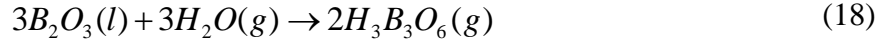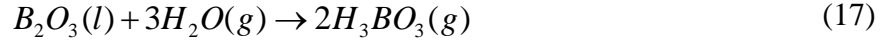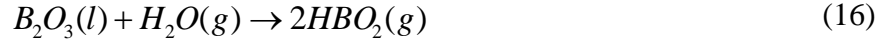
The reactant diffusivities through the borosilicate glass increase with the moisture content, and subsequently increase in the volatility of boria [45,93]. The removal of boron from the borosilicate glass increases the viscosity and eventually freezes the residual SiO_2 glass over time [13]. The viscosity of the glass is not only dependent on the temperature but also on the amount of SiO_2 in the borosilicate glass as well as any impurities that may be present. The resulting adhesion among fibers because of the glass formation has detrimental effects because the attached fibers will experience local load sharing when a neighboring fiber fails [13,25,26,46].

The paralinear kinetics of silica formation has its implication on CMC surface recession, which can be a reliability issue for a long-term application. Appendix A discusses the surface recession in details.

2.4.2 Two types of degradation by oxidation

The degradation that results from the oxidation of the BN interphase described above is commonly understood to occur occurs in two ways. The first, referred to as Type I hereafter, is referred to as a progressive phenomenon, with material degradation advancing inward from the surface and creating a pathway for oxidant ingress as described above. The other type, first reported by Ogbuji [25], referred to as Type II, occurs when the BN interphase is effectively undermined by a continuous thin film of carbon (shown in Figure 17) that can be found on the fibers. This carbon sub-layer can form during melt infiltration of the matrix [82] and oxidizes faster than the BN interphase upon exposure to the ambient [25,45,73]. This differential in the rates of oxidation yields an opening underneath the BN interphase such that both inner and outer walls of the BN interphase are exposed to the environment [25,82].
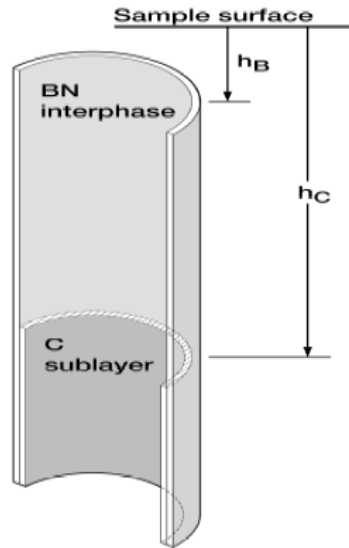
Figure 17: Schematics of Type II degradation in SiC/BN/SiC [25]

Type II degradation is reported to occur orders of magnitude faster than Type I [25]. Type I occurs in all oxidizing media, but Type II has only been observed in the high-velocity flame of a

burner rig [25,77]. The Hi-Nic-S fiber is non-stoichiometric, and thus has the adventitious carbon sub-layer formed during the melt infiltration process. Also, the Sylramic fiber has a thin layer of carbon on the surface, and therefore is subject to Type II degradation. On the other hand, the Sylramic-*iBN* has the in-situ BN layer on the fiber surface, and thus is predicted to be less susceptible to severe oxidation. Based on the microscopic investigation of the fracture surface carried out using SEM and EDS, the extents of oxidation with respect to the time of combustion exposure are analyzed and compared among the four CMCs in Chapter V.

The bridging fibers with silica solidified on the interphase cannot effectively undergo the debonding and sliding mechanism that imparts the fracture toughness to the SiC/BN/SiC CMCs. Therefore, the CMC with the degradation by oxidation will fail in a brittle fashion without exhibiting much inelastic strain. Figure 18 [13,28] is a graphical representation of such degradation that neutralizes the fracture toughening mechanism built in for CMCs by design.
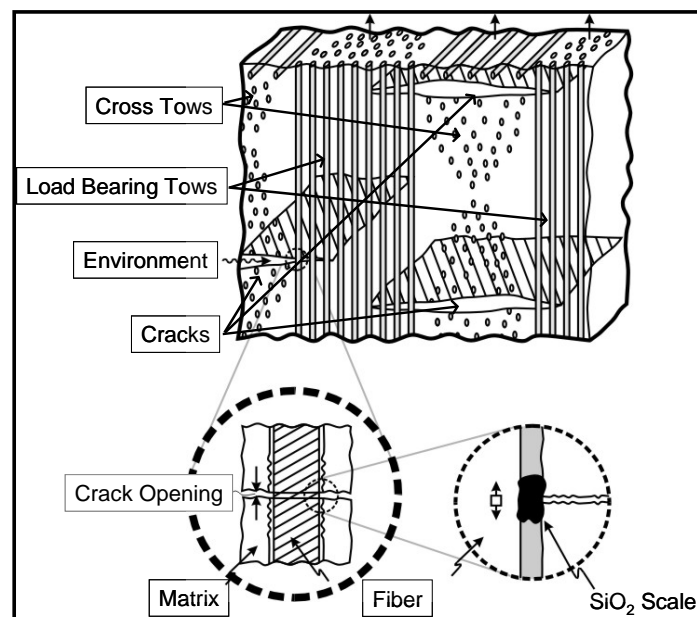
Figure 18: Schematic of Oxidation Embrittlement in CMCs [13,28]

2.5 Fatigue Mechanisms of CMCs

Prior to matrix cracking, constituents of a CMC share the applied load depending on the volume fractions and elastic properties of the constituents [20]. For stress levels above the microcracking threshold of the matrix, the crack density corresponding to the stress level is achieved in the early stage of fatigue loading [95]. Cracks form preferentially at the locations of high stress concentration such as process-induced voids. They can also initiate in the cross tows with higher concentration of pores and matrix flaws or at surface flaws located at the corners or edge surfaces of the machined edge of the specimen. The matrix cracks are initially bridged by the fibers, as illustrated in Figure 19 [52]. The load is no longer shared and is transferred from matrix to fibers such that the stress in the matrix relaxes in the vicinity of the crack. With the subsequent increase in the load carried by the fibers, the probability of fiber fracture increases. The debonding that precedes sliding of the bridging fibers against the matrix may introduce debris that could get in the interphase to increase the probability of the fiber fracture [95]. With fewer fibers to dissipate the crack energy by frictional wear, the crack grows until the energy associated with its propagation is overcome by the energy dissipated at the interphases of the bridging fibers. With continued loading and unloading, the interfacial shear stress decreases by frictional wear, which reduces the bridging stresses. This leads to an increase in the stress intensity at the crack tip and further crack propagation [95,96].
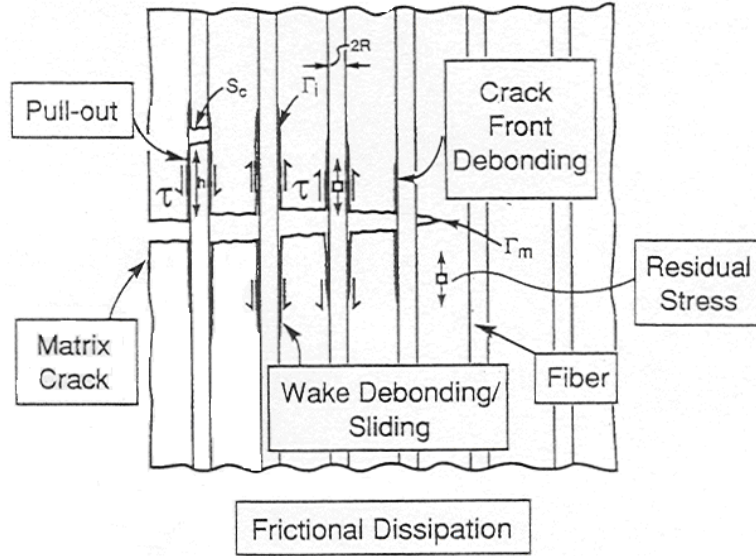
Figure 19: Illustration of Crack Propagation and Fiber Bridging [52]

Other aspects of fatigue that affect the fatigue life include the loading frequency and stress ratio (R). First, the loading frequency can have an effect on the fatigue life. The temperature rises due to frictional heating at the interphase during rapid loading and unloading. For CMC specimens subjected to this type of loading at high frequencies, the temperature rise is steep, and the temperature continues to rise until failure, which was experimentally observed by Staehler et al [97], who evaluated CVI C/SiC at room temperature using two different loading frequencies of 4 *Hz* and 375 *Hz*. The observation that the temperature continues to rise until failure indicates that the damage evolution increases progressively [95]. A study reported by Holmes et al [98] on SiC/CAS composite system showed that fatigue life was sharply reduced as the loading frequency was increased. Loading frequency has also been shown to decrease the fatigue life of woven carbon fiber/SiC matrix composites [99]. For this CMC, the fatigue limit at 10^6 cycles showed moderate decrease from 325 MPa at 10 *Hz* to 300 MPa at 50 *Hz*. The CMCs in the present study is loaded at the frequency of 1 *Hz*.

47

Next, the mean stress or stress ratio (R) is another parameter that could bring the change in fatigue life. Allen and Bowen [100] reported that the Nic/CAS specimens tested at $R = 0.1$ resulted in an S-N curve with a lower fatigue limit than those tested at R = 0.5. Similar results are demonstrated by Sorensen and Holmes [101]. The same Nic/CAS system exhibited a similar trend under the experiments using stress ratios of 0.05 and 0.5.

Because the temperature of the current study is above at which creep may occur, creep and fatigue mechanisms are expected to interact, which may cause the material to fail under the loading conditions in which the same material at room temperature would survive. Moreover, the testing in high-temperature, combustion environment that contains chemical species such as water vapor that has been documented to degrade the strength retention capacity of the CMC by promoting the oxidation embrittlement. The exposed fibers would undergo oxidation that leads to embrittlement and can no longer effectively bridge the matrix crack. Therefore, the oxidation disrupts the fiber bridging mechanism and leads to accelerated failure. The role of oxidation on fatigue is the main focus of the present study, and the topic is explored by subjecting the four types of SiC/BN/SiC CMCs to fatigue loading in a prescribed combustion environment. The details of the experimental are presented in the next chapter.

2.6 Chapter Summary

This chapter provided the background for CMCs in oxidative combustion environment and the other experimental facilities to explore the strength degradation phenomena related to oxidation. Burner rig test facilities are generally used to simulate the gas turbine engines instead of full scale engine tests. The experimental facilities reviewed in this chapter have shortcomings and lack versatilities needed to simulate various thermo-mechanical and mechanical conditions

which components undergo in a combustion engine. Four types of SiC/BN/SiC CMCs under consideration for their potential gas turbine engine applications were introduced as the materials of the present study. The manufacturing process and properties of each CMC were presented. It is understood that the strength retention capacities of the CMCs deteriorate due to the oxidation degradation of the BN interphase in a high-temperature combustion environment. Previous studies investigated this deleterious phenomenon using mostly furnace test facilities, which do not factor in the other parameters of potential significance such as realistic flow velocity and chemical species typical of a real combustion environment. Lastly, the failure mechanism of CMCs under fatigue was reviewed. The discussions in this chapter identified the need for the development of a versatile experimental facility capable of simultaneously applying both mechanical and thermal loading by way of imposing a realistic combustion environment with many controllable physical and chemical parameters such as gas velocity, type and level of mechanical loading, equivalence ratio, gas chemistry and temperature as well as the ability to insert and control the amount of foreign particles or gaseous species to cover a wide range of scenarios encountered during the lifetime of an engine. The AFIT/AFRL Burner Rig was developed to meet these demands and is discussed in details in the following chapter.

III. Experiments

In the preceding chapter, the need was identified and justified for a new versatile test facility. In this chapter, the details of the AFIT/AFRL Burner Rig developed for this research are presented. The discussion in this chapter entails verification of the performance of this facility controlling the interdependent combustion parameters including temperature, gas velocity, equivalence ratio, and gas composition. The High Velocity Oxygen Fuel (HVOF) system was integrated to the MTS mechanical testing system to constitute the AFIT/AFRL Burner Rig system that provides simulated combustion conditions of gas turbine engines. The choice of propane fuel to simulate combustion of aviation fuel is discussed.

The details of the experimental work performed under the current study including the target experimental parameters are described in this chapter. The methods of measurement and calibration of instruments are detailed. In addition to the tests in burner rig, similar fatigue tests were conducted using an electric furnace to access the effects of thermal gradient and moisture. Lastly, the protocols used to perform the experiments and post-test analyses are described.

3.1 Development of the AFIT/AFRL Burner Rig

3.1.1 Description

A unique compact test facility in which a coupon can be tested for mechanical properties in the more realistic combustion conditions was developed. This setup includes a burner rig that produces combustion flames that impinging on a test coupon to simulate a gas turbine engine environment in terms of temperature, humidity, gas flow conditions, thermal gradient, etc. The combustion system is capable of producing flame with the speed up to *Mach 1.0* and temperature

up to approximately 2500°C, thus facilitating the simulation of the thermal cycling conditions involving some of the most severe temperature excursions expected from an advanced turbine engine. The combustion system is combined with a servo-hydraulic fatigue test system (Materials Testing System or MTS hereafter) capable of applying both static and cyclic loading up to 25 *kN* and at the frequencies up to 10 *Hz*. The combined system, shown in Figure 20, is enclosed inside a modular room shown in Figure 21 with dimension of 2.4 m by 3.7 m by 2.3 m to isolate the noise (~140 dB) generated by the high velocity jet. The main setup of the facility was built in the AFIT Combustion Laboratory after meeting rigorous fire and environmental safety regulations. Many safety features were implemented including an extensive ventilation system that incorporates dual exhaust fan systems, automated fire suppression system, pressure regulated shut-off valves, sound-proofing modular room and fire-proof foams and plates to make the laboratory air-tight such that the room is isolated from the rest of the building. Figure 21 shows some of the safety features that facilitated the testing from the fire and environmental safety standpoint. A gas storage facility (Figure 22), which houses the reactant gases such as propane and liquid oxygen as well as an electric propane vaporizer and a manifold valve regulating the flow of the gases, was installed on a concrete pad constructed outside the building, and the gases are carried into the laboratory through tubes. Figure 23 and Figure 24 are the CAD representations of the main test facility in the modular room, illustrating the operation of mechanical actuation system to control thermal cycling on a test specimen.
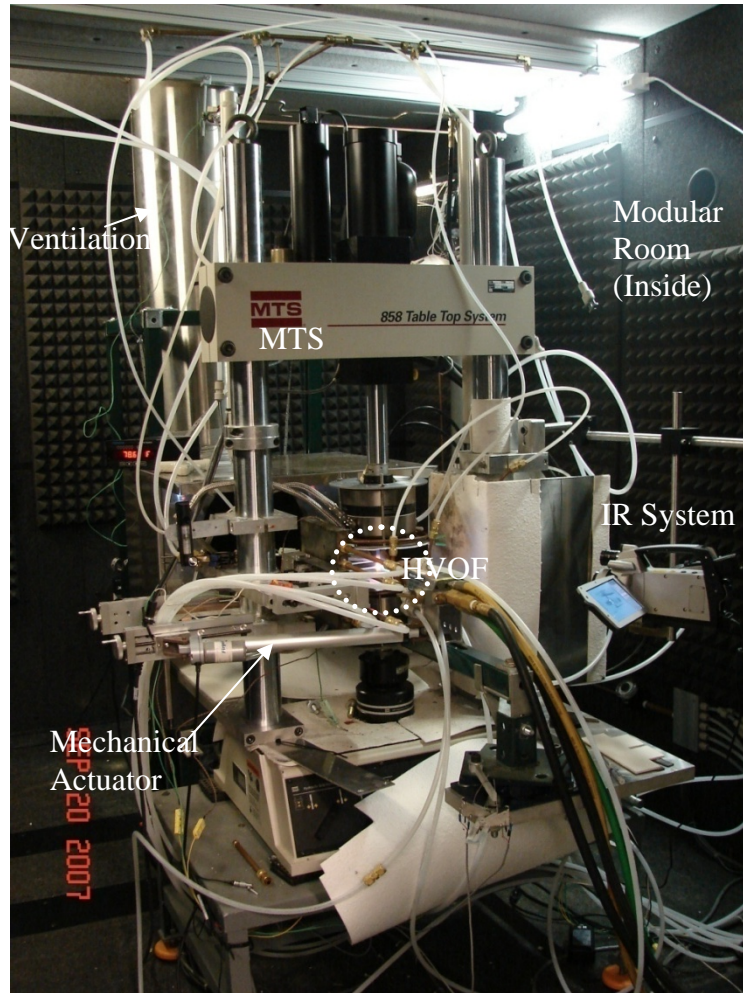
(a)
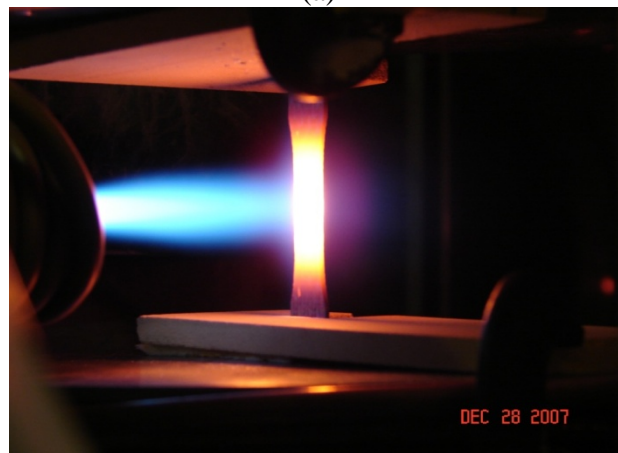
(b)

Figure 20: (a) AFIT/AFRL burner rig in operation; (b) encircled area in (a) zoomed in
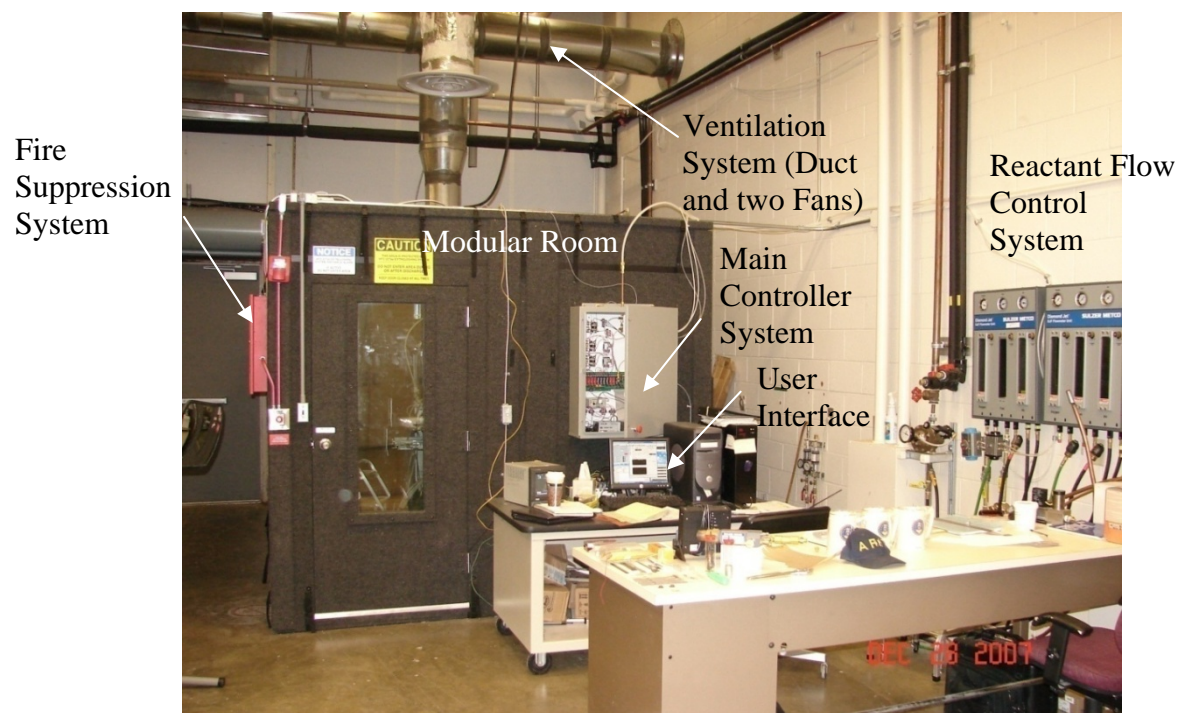
Figure 21: Modular Room enclosing the AFIT/AFRL burner rig inside

Figure 22: Reactant Gas Storage Facility
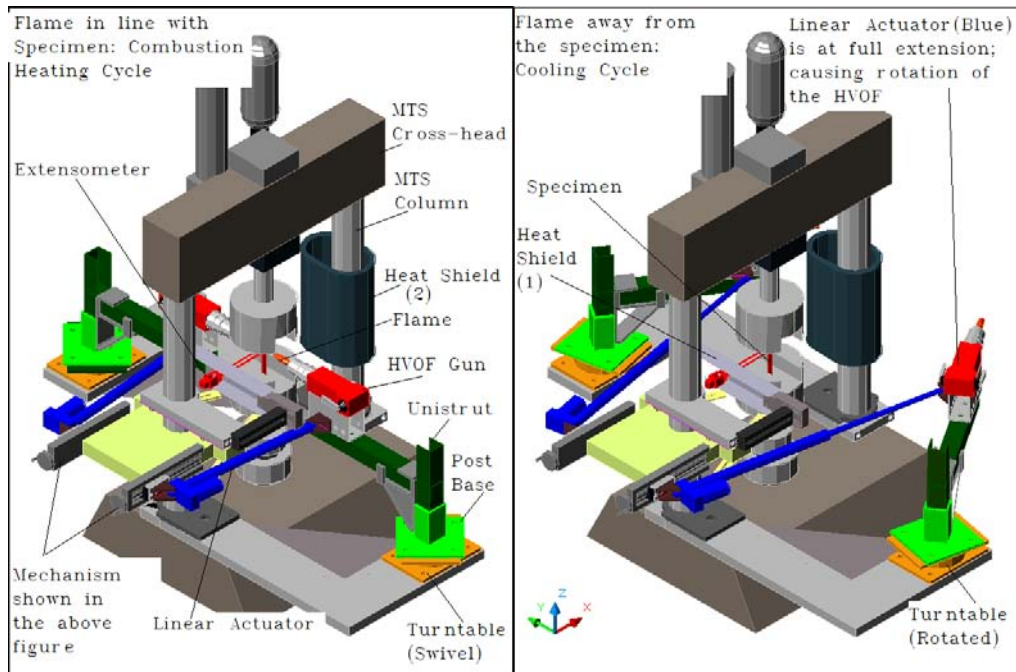
Figure 23: Experimental setup; specimen under impingement (left) and specimen undergoing cooling (right)
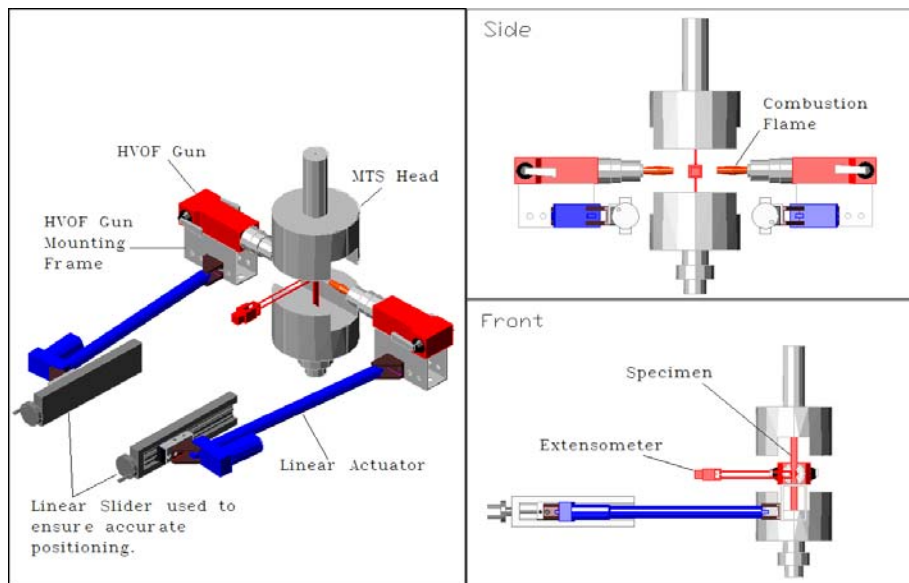
Figure 24: Schematic of Experimental Setup

Each burner consists of a High Velocity Oxygen Fuel (HVOF) gun. The HVOF is commercially available equipment by Sulzer-Metco, Inc. that generates combustion to produce high temperature and velocity for many applications. Each of the two HVOFs can be independently controlled, making it adaptable to an experimental scenario such that two flames of unequal temperature, velocity and gas concentrations can be applied on either side of specimen. In addition, automated thermal cycling was implemented by use of a mechanical system with which the user controls the thermal cycling using the user interface programmed using LabView^{TM}. As illustrated in Figure 23, this mechanical arm system swings the gun exhaust in and out of line with the specimen under test in less than 2 seconds, thus facilitating a rapid thermal fatigue effect. The operation of this thermal cycling system is controlled independently between the two sides, broadening the capability range of thermo-mechanical conditions when combined with mechanical fatigue capability of the servo-hydraulic test machine.

For the present study, the test specimens were under continuous flame impingement from only one side, with the other side open to natural convection. The heating from one side causes thermal gradient effect across the thickness of specimen, which simulates the harsh environment of turbine components under directional impingement of combustion gas.

3.1.2 MTS material testing system and cooling

The MTS 858 material testing system was integrated into the AFIT/AFRL Burner Rig system to facilitate the mechanical loading capability. This servo-hydraulic equipment can exert the load up to 24.5 kN and at frequencies up to 30 Hz. Equipped with TestStar^{TM}, the MTS system can be controlled for loading and frequency. As the MTS was incorporated by the HVOF system that produced high temperature gas, it was necessary for both upper and lower grips to be

designed with channels through which chilled water continuously passes through to quickly dissipate the heat originating from hot flame product impinged on and deflected from the specimen. Copper coils with chilled water running through are placed on top of both the upper and lower fixtures to protect the nearby electronics from the heat. Shop air from a pair of air compressors was used to keep the periphery cool.

3.1.3 High Velocity Oxygen Fuel (HVOF)

The High Velocity Oxygen Fuel (HVOF) is derived from a thermal spray coating technology, which uses compressed air, oxygen and fuel gas to produce a high-velocity gas stream in the gun nozzle. Figure 25 is a schematic flow diagram showing the supply of the reactants to the HVOF system. The gas storage facility in Figure 22 supplied reactant gases to the HVOF flow controllers through tubes. Compressed air was drawn from the building air compressor system. Flow rates of fuel, oxygen, and air were controlled using the volumetric flow controllers shown in Figure 26. Though not explored in this study, there is an inlet for controlled amount of additional chemical, such as H_2O and $NaCl$ to be put through into the combustion. Safety devices including automated fail-safe shut-off valves as well as manual shut-off values were incorporated in the upstream of the flow controllers. In the event of overheating or drop in the cooling air pressure, the system shuts down automatically.
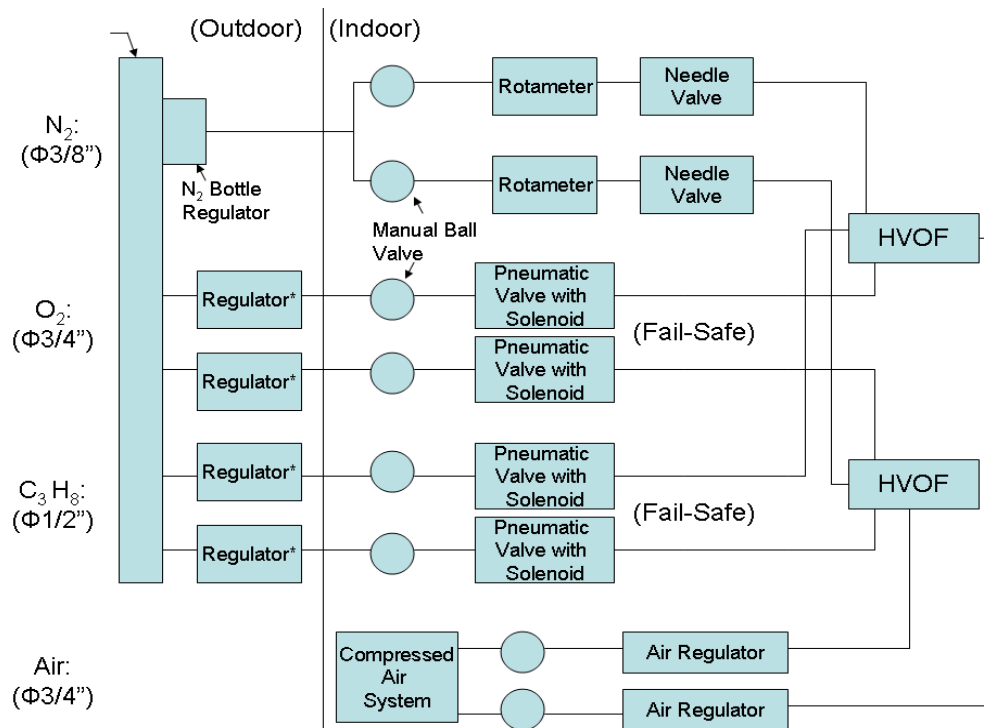
Figure 25: Flow diagram showing the supply of the reactants to the HVOF system

Figure 26: Flow controllers equipped with safety devices

Combustion occurs at the exit of the nozzle that delivers the premixed propane and oxygen out into the atmosphere. Compressed air circulates on the outside of the combustion chamber to protect the HVOF from heating and subsequently enters into the secondary combustion by mixing physically and chemically with the products from the primary combustion. This is illustrated in Figure 27. While the current version of the system was configured for propane as fuel, any other gaseous hydrocarbon can easily replace the propane. Temperature of the combustion of propane with oxygen can be up to $2500^{\circ}C$ [64]. The converging design of the nozzle generates maximum gas velocities of *Mach 1.0* at the nozzle exit. The gas accelerates past *Mach 1.0* in the immediate outside the nozzle and subsequently slows down [102]. The details of the propane combustion relating to the HVOF operation are provided in Appendix B.
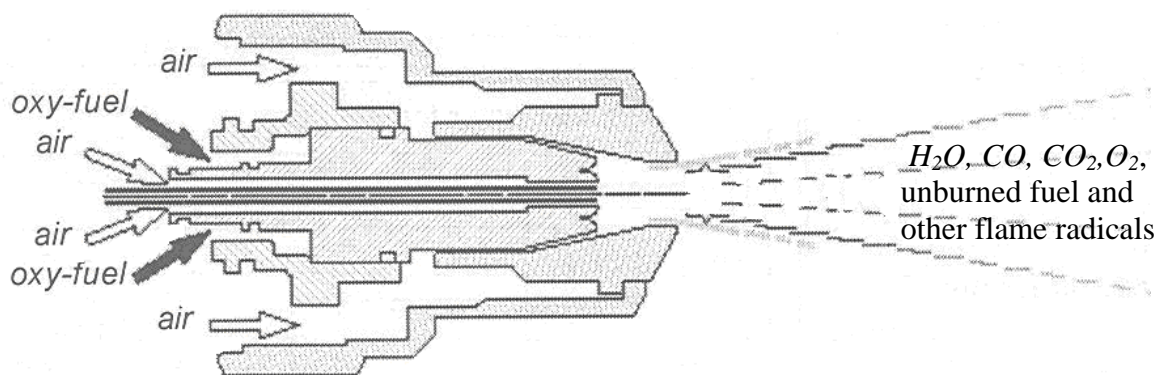
Figure 27: Air-cooled HVOF thermal spray [103]

3.1.3.1 Simulating Combustion of Aviation Fuel using Propane

The combustion of propane was used to simulate that of aviation fuel such as JP-8. Detailed chemical kinetic descriptions of JP-8 are estimated to involve hundreds of chemical species and thousands of reactions occurring simultaneously or in chain [104]. However, CPU time and memory limitations imposed by the available computing power in the present time

prohibit implementation of fully detailed descriptions of this combustion chemistry into 3-D Computational Fluid Dynamics (CFD) simulations of practical devices [105]. For practical purpose, propane, C_3H_8 has been used to simulate the combustion of aviation fuel [106], on the basis that the propane has the similar reaction characteristics as typical practical aviation fuel such as JP-8 [107]. Combustion byproducts such as the chemical species and flame radicals of the propane combustion in the HVOF are similar to those in the gas turbine engines. Full characterization of the propane combustion mechanism is complete and found to involve less complicated reaction mechanisms with 100 species and 539 elementary reactions [108]. Propane is also cheaper and readily available to be used in HVOF. While JP-8 mixing with air results in undoubtedly the most realistic combustion for simulated applications, propane can be used as combustion fuel for these reasons. For the purpose of illustrating propane combustion, Appendix B is provided to demonstrate the computation performed to determine the envelope parameters such as temperature and gas velocity. This preliminary analysis used the global reaction instead of considering all elementary reactions. Using the obtained ranges of temperature and gas velocity as windows of operating conditions, an optimal experimental condition was devised based on our research interests and system limitations imposed by the HVOF system (e.g. limited duration of continuous operation).

3.1.4 Capabilities and Limitations of the AFIT/AFRL Burner Rig

Table 6 shows the types of experiment of which the AFIT/AFRL Burner Rig is capable. The unique capability to apply static and cyclic loadings both mechanically and thermally in a simultaneous manner facilitates the listed types of experiments with various loading scenarios under wide range of temperature excursions.

Table 6: Simulation capabilities of the AFIT/AFRL Burner Rig

Mechanical Loading Type	Thermal Loading Type	Test described as	Simulation of:
Static	Constant (Elevated)	Creep or Creep-rupture	Turbine rotor blades under constant stress in radial direction
Cyclic	Constant (Elevated)	Mechanical Fatigue Interacting with creep	Hot-section components undergoing take-off and landing as well as maneuvering
Static	Cyclic	Thermal Fatigue; Dwelling Effects	Operating conditions of high-end engines
Cyclic	Cyclic	In-phase or Out-of-phase Fatigue	Worst case scenario for hot-section components

The rig has its shortcomings due to its atmospheric operating pressure. In modern engine design, increasing the Turbine Inlet Temperature (TIT) to improve gas turbine efficiency is accompanied by an increase in pressure ratio. Advanced turbofan engines have overall pressure ratios as high as mid forties to one [109]. In terms of chemical kinetics, increasing pressure shifts the chemical equilibrium of the combustion reaction toward the side with fewer moles of gas [64]. Assuming stoichiometric condition, this increases the rate of combustion reaction and promotes the formation of more gas products such as moisture for the same rate of fuel consumption, resulting in the increased overall thrust and thermal efficiency. Hence, the rate of reactions for equations (1) through (19) in Chapter II increases with pressure, causing the BN and SiC in CMCs to oxidize faster than in atmospheric pressure. This aspect of the pressure limitation, however, is partially mitigated by the ability of the propane combustion to generate a flame with high gas velocity and considerably higher moisture contents than the combustion of an aviation fuel.

The rate of material recession by means of formation and subsequent volatilization of gaseous species such as $Si(OH)_4$ occurs predominantly when partial pressures of oxidants (e.g. O_2 and H_2O) are high [47,83-85,91,92], and thus it remains as a challenge to simulate such high pressure oxidation phenomenon with this atmospheric burner rig. The AFIT/AFRL Burner Rig is

capable of circumventing this inherent difficulty by pumping in an increased amount of H_2O into the combustion chamber, thereby increasing its partial pressure in the gas products to the level that the degradation of SiC/SiC composites due to moisture content is properly addressed.

The other aspect of concern in regard to the pressure limitation is its inability to simulate the hydrostatic stress due to pressure. However, this hydrostatic stress is insignificant when compared with the high stress induced by thermal gradients and the mechanical stress exerted on the component attachments as a result of maneuvering of the aircraft [18,70]. The change in the amount of dissociation of the combustion products with pressure variation is another important consideration, as the dissociation causes variation in chemical species and temperature. Below temperatures less than 1000 K, the combustion products are CO_2, H_2O, O_2, CO, and H_2 with exact concentrations depending on the reaction temperature and equivalence ratio. At temperature range greater than 1000 K, however, dissociation reactions during the combustion process will result in flame radicals such as OH, H, and O. As the pressure is increased in a combustion system, the amount of dissociation decreases and the temperature rises, as described in Table 7 [64], which shows a substantial degree of dissociation and about a 15% rise in temperature as the pressure increases from 1 to 10 atm. However, the effect is less significant in very lean operation ($\Phi = 0.6$) where the amounts of dissociation is approximately 50% of those at stoichiometric fuel-oxygen mixture ratio ($\Phi = 1.0$).

Table 7: Equilibrium Product Combustion of Propane-Oxygen Combustion [64].

Φ	0.6	0.6	1.0	1.0	1.5	1.5
P (atm)	1	10	1	10	1	10
CO	.090	.078	.200	.194	.307	.313
CO_2	.165	.184	.135	.151	.084	.088
H	.020	.012	.052	.035	.071	.048
H_2	.023	.016	.063	.056	.154	.155
H_2O	.265	.283	.311	.338	.307	.334
O	.054	.041	.047	.037	.014	.008
OH	.084	.089	.095	.098	.051	.046
O_2	.294	.299	.097	.091	.012	.008
T (K)	2970	3236	3094	3411	3049	3331
Dissociation (%)	27	23	55	51		

Because the burner rig system of the AFIT/AFRL facility is used to create a simulated environment for the vanes and turbine blades, which are located in the downstream and therefore are subjected to predominantly lean burn conditions, the variation of chemical species and temperature with pressure change is smaller compared with those at the stoichiometric conditions. The presence of air as a coolant also reduces the amount of dissociation [64]. Still, the discrepancy in the chemical species and temperature between an ambient pressure operation of the burner rig and the high pressure operations of a real engine may not be trivial. Gas composition and temperature are analyzed to characterize the amount of dissociation experienced in the operating condition of the present study.

3.2 Calibration of the AFIT/AFRL Burner Rig

Gas and surface temperature, gas velocity and composition as well as equivalence ratio are all important parameters that could affect the degradation mechanism of the CMCs in combustion

environment of the AFIT/AFRL Burner Rig. For the facility to serve the purpose of simulating a realistic gas turbine engine environment, it is important that the parameters attainable through the facility are not only controllable to the extent of facilitating a study of the overall effect of varying one or more controlled parameters, but the parameters should also be relatively similar to those of a real gas turbine engine in operation. A specific combustion condition was chosen for this study based on the knowledge of typical operating environment inside gas turbine engine for the present study. The selection was made to simulate an upper bound of operating conditions of advanced engines in terms of gas temperature, velocity, composition and equivalence ratio. Table 8 shows the combustion parameters used in this study.

Table 8: Test Parameters

Test Parameter	Condition	Calibration Tool(s)
Surface Temperature	$\sim 1250^{\circ}C$	Furnace, R-type TC & IR
Gas Temperature	$< 1800^{\circ}C$	R-type TC
Gas Velocity	$\sim$ Mach 0.5	XS-4 High Speed Camera
Equivalence Ratio	~ 0.9	HVOF^{TM} Flow Controller
Gas Composition	H_2O, O_2, CO_2, CO, NOx	Testo XL 350 Gas Analyzer
Mechanical Loading	Fatigue (1 Hz & $R = 0.05$)	MTS
Test Duration	Up to 25 hours	N/A

Preliminary calculations of these parameters were performed using simplifying assumptions involving a single governing combustion reaction for the combustion of propane, as discussed in Appendix B. This step was necessary to determine the flow rates for each reactant gases as well as the distance of the nozzle with respect to specimen that correspond to the gas temperature, velocity and composition in Table 8. Actual combustion of propane, however, involves hundreds of chemical species and more than five hundred elementary reactions occurring simultaneously or in chain. Immediate species produced in such reactions include unstable free

63

radicals such as CH_3 and C_2H_5. These radicals are produced by decomposition of propane fuel, and serve as the chain carriers. The chain reactions terminate upon the elimination of these radicals. Some chain reactions involve reactions between unstable free atoms (e.g. H and O) and the stable chemical products such as H_2O, decomposing into OH and H_2. These reactions, therefore, cause variations in the overall species composition. Due to the presence of the chain reactions and free radicals, the observed parameters such as temperature and velocity may differ slightly from those calculated on the basis of the overall stoichiometric equation [104]. Thus, the actual flame temperature and velocity of the HVOF combustion were experimentally measured, based on which the flow rates of reactants were tuned to attain the prescribed combustion condition for the present study.

The measurement of each combustion parameter was performed using the device and method shown in Table 8. Non-contact methods are preferred due to the turbulence of combustion flame that interferes with the sensitivity of a measuring device requiring its presence in the flame. The calibrations of the measuring devices were done for the specific value of each parameter to ensure the accuracy of measurement.

3.2.1 Surface and Gas Temperature

3.2.1. Surface Temperature

The specimen surface temperature is a temperature of reference in many previous and current research involving burner rigs, facilitating the comparison with the results obtained using a different experimental setup. Surface temperature is different from the gas temperature. It is usually hundreds of degree C below the gas temperature, because not all the heat flux from the hot gas can go into heating the specimen, which is largely because of a single sided heating. The

temperature obtained using a thin-wire mounted on the surface is unreliable as it introduce the height differential that accompanies differential flame residual time and therefore results in preferential surface heating on the protruding mound under the heating exerted by the combustion flame.

As the direct measurement of the front surface temperature using a thin-wire thermocouple would result in an erroneous value, a two-step approach was implemented to measure the surface temperature. This approach involved the calibration of an infrared imaging device to determine surface temperature. The first step is to measure the emissivity of the test specimen. To do this, the specimen was placed in a static air furnace, which is subsequently heated to the temperature of $1235 \pm 50^{\circ}C$. The furnace was a two-part component, in which there was a natural opening between the left and right parts. This opening was used to provide a clear line-of-sight between the surface of enclosed specimen and the infrared imaging system by FLIR. The specimen has an R-type thermocouple adhered at a location on the surface in the immediately adjacent to the spot focused onto by the IR system. Assuming the temperature is the same at the two adjacent locations, the emissivity input on the IR system was adjusted until the IR system and the R-type thermocouple read the same temperature. The setup for this experiment is shown in Figure 28.

Emissivity is a surface radiation property defined as the ratio of the radiation emitted by the surface to the radiation emitted by a blackbody at the same temperature. This property varies with the type and structure of a material. Although all four CMCs in this study are similar in terms of chemical constituents, it should be noted that the surface patterns and their scales, with which the emissivity changes, differ vastly from a woven-cloth MI SiC/SiC CMC with large scale weaving pattern to a prepreg MI SiC/SiC CMC with a much finer weaving pattern. The emissivity is also known to be a property with directional dependence, with the highest intensity emitted in

perpendicular directions to any given point on a woven pattern of material surface. To reduce the complexity of working with multiple variables, it was decided fix the angular offset of the specimen with respect to the infrared lens to approximately 29 degrees. Thus, the emissivity of both woven-cloth and prepreg MI SiC/SiC CMCs at this angle were measured in the furnace with the length between specimen and lens constant. The emissivity was 0.95 ± 0.02 for the woven MI Syl/BN/SiC and 0.97 ± 0.02 for the prepreg MI Hi-Nic/BN/SiC, and they were entered into the FLIR IR system for the second step. In the temperature range of this study's interest, the change in the emissivity of 0.01 translates to about 10°C. Hence, the uncertainty that stems from this measurement is approximately $\pm 20^{\circ}$C.
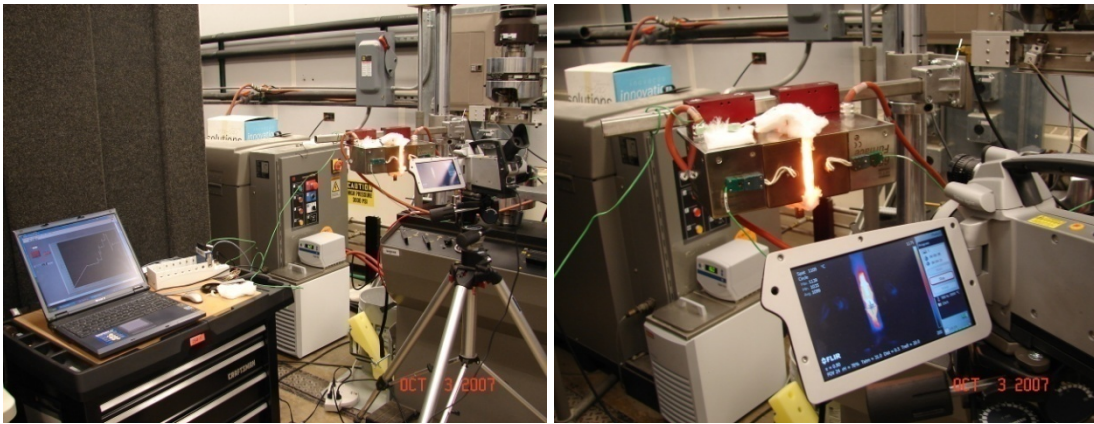
Figure 28: Test setup to determine emissivity

The second step of the calibration to measure the surface temperature using the IR device involved the use of the emissivity measured from the first step dialed into the IR system, which is positioned at the same relative location with respect to the specimen in terms of distance and angle, but this time with the HVOF heating the specimen. Therefore, the flame now exists in the line-of-sight between the specimen surface and the IR system. Under rich-burn condition, the specimen surface may not be visible due to the intense luminosity of the flame [58]. Thus, the

66

temperatures cannot be measured directly using the optical device. Fortuitously, the optical method of measuring the surface temperature works under the lean-burn condition of this study. Still, the line-of-sight catches the underdeveloped zone of the flame, immediately outside the nozzle, as shown in Figure 29, which may contain unreacted fuel that combust in the downstream. The combustion here can be richer than the rest of the flame. Therefore, it was necessary to verify the effect of the flame as radiation absorbing medium.

A built-in function of the IR system that recorded the images at the rate of 30 frames per second was used to capture the event of shutting off the flame. The difference in surface temperature before and after the flame shutoff was recorded. After the post-processing that compares the surface temperature immediately before and after the removal of the flame from the line-of-sight, it was determined that the flame has little skewing effect on the surface temperature measurement. Figure 29 depicts one of the IR images taken during this calibration process, along with the temperature profile during the shutoff. The fact that the highest temperature measured after removal of the flame is lower than the temperature before suggests no absorption of radiation by the presence of the flame. The combustion flame of the study contains up to 32 *vol %* of water vapor, which is known as a main absorber of radiation. The 32 *vol %* of water vapor for the input mass flow rate used in this study, i.e. approximately 5 grams/sec is about 1.5 grams/sec for the flame with cross-sectional area normal to the path of radiation perpendicular transmission of approximately 50 mm^2. This translates to the water vapor content of 0.03 precipitable millimeters (*pr·*mm). For the long wavelength IR system used (i.e. 7.5 *μm* to 13 *μm*), the transmissivity that corresponds to 0.03 *pr·*mm of water vapor is greater than 0.997 [110], which implies minimal loss of radiation due to the absorption by the flame, thus explaining the experimental results shown in Figure 29.
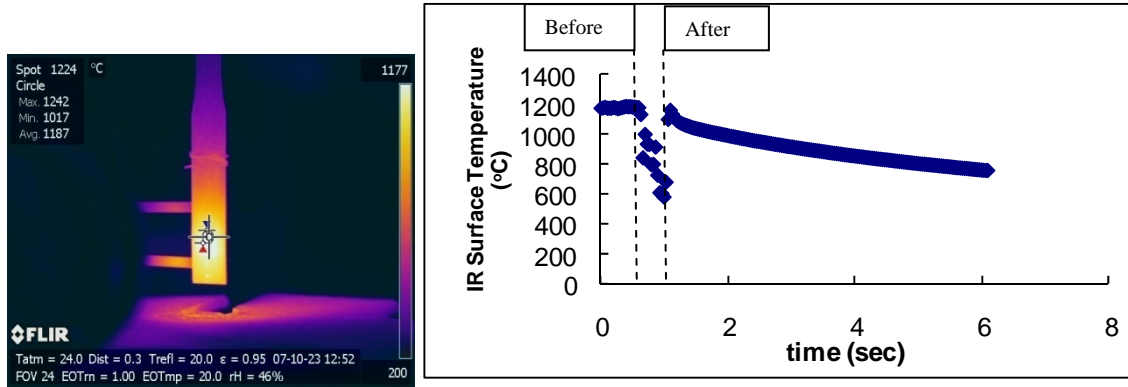
Figure 29: No absorption of radiation by flame

To further validate the described two step method of measuring the surface temperature, it was decided to measure the material temperature, or the temperature of the back side of the first ply from the flame-impinged surface. A blind hole with the depth equivalent to $85 \pm 3\%$ of the specimen thickness was introduced from the back surface, such that the bottom of the hole is in contact with the back of the intact first ply. Then, a thin-wire thermocouple was inserted and adhered such that the bead was bonded to the back of the first ply. Another thin-wire thermocouple was adhered to the back surface at a location slightly away from the entry of the blind hole. Then, the front surface of a specimen was subjected to the flame condition of this study. The temperatures measured by the two thermocouples, assuming a linear temperature profile across the thickness, were used to extrapolate the front surface temperature. The extrapolated temperature was in good agreement with the IR measurement. For the woven MI Syl/BN/SiC, the front surface temperature extrapolated from the measured material and back surface temperature of $1150^{o}C$ and $855^{o}C$ was $1190^{o}C$, which is off only by $20^{o}C$ from $1170^{o}C$, the IR measurement of approximately the same area of the front surface made using the emissivity of 0.95. The difference of $20^{o}C$ falls inside the temperature range corresponding to the uncertainty of the measured emissivity of ± 0.02. Similarly, for the prepreg MI Hi-Nic/BN/SiC

sample, the surface temperature of 1142°C was extrapolated from the material temperature of 1115°C and back surface temperature of 940°C, whereas the IR surface temperature read at 1186°C. The difference between 1142°C and 1186°C is close to what the scatter in emissivity data can account for. These results validate the IR measurement of surface temperature, and, therefore, the emissivities remain 0.95 $\pm$ 0.02 and 0.97 $\pm$ 0.02 for the woven MI Syl/BN/SiC and the prepreg MI Hi-Nic/BN/SiC, respectively.

3.2.1.2 Gas Temperature

Determination of gas temperature is important as it permits an indirect access to other physical parameters such as gas density which could not be measured. It may also allow one to predict a local chemical composition. The gas temperature profile was obtained by inserting an R-type thermocouple into the flame and taking the measurement from the digital gauge that reads the thermocouple. The resulting profile is as shown on Figure 30 without a sample in place. From the nozzle located on the left, the flame is produced and propagates towards the downstream, while the temperature drops quickly as the air in the ambient gets entrained into the flame. At 60 $\pm$ 5 *mm* downstream of the nozzle, an underdeveloped temperature profile is evident with a large temperature gradient from the hot core to cool periphery. The profile develops into a steadier laminar flow in the downstream. The measurement was made for the flow rates that corresponded to the surface temperature of 1200°C.

As the thermocouple would interfere with the flame impingement on specimen if placed in the upstream during test, a thermocouple was placed behind the specimen for the test to monitor the steadiness of the gas temperature. The temperature at about 10 *mm* behind the specimen, located 60 $\pm$ 5 *mm* in the downstream from the nozzle, for the conditions corresponding to the

temperature shown in Figure 30, was considerably lower at approximately 500 ± 25°C. This is because the specimen shielded off and redirected the high-velocity flame to flow around the specimen, creating a cooler environment in the area directly behind the specimen. However, our experiment showed that this temperature changed with the flame temperature, thus making it adequate for qualitatively monitoring the flame temperature.
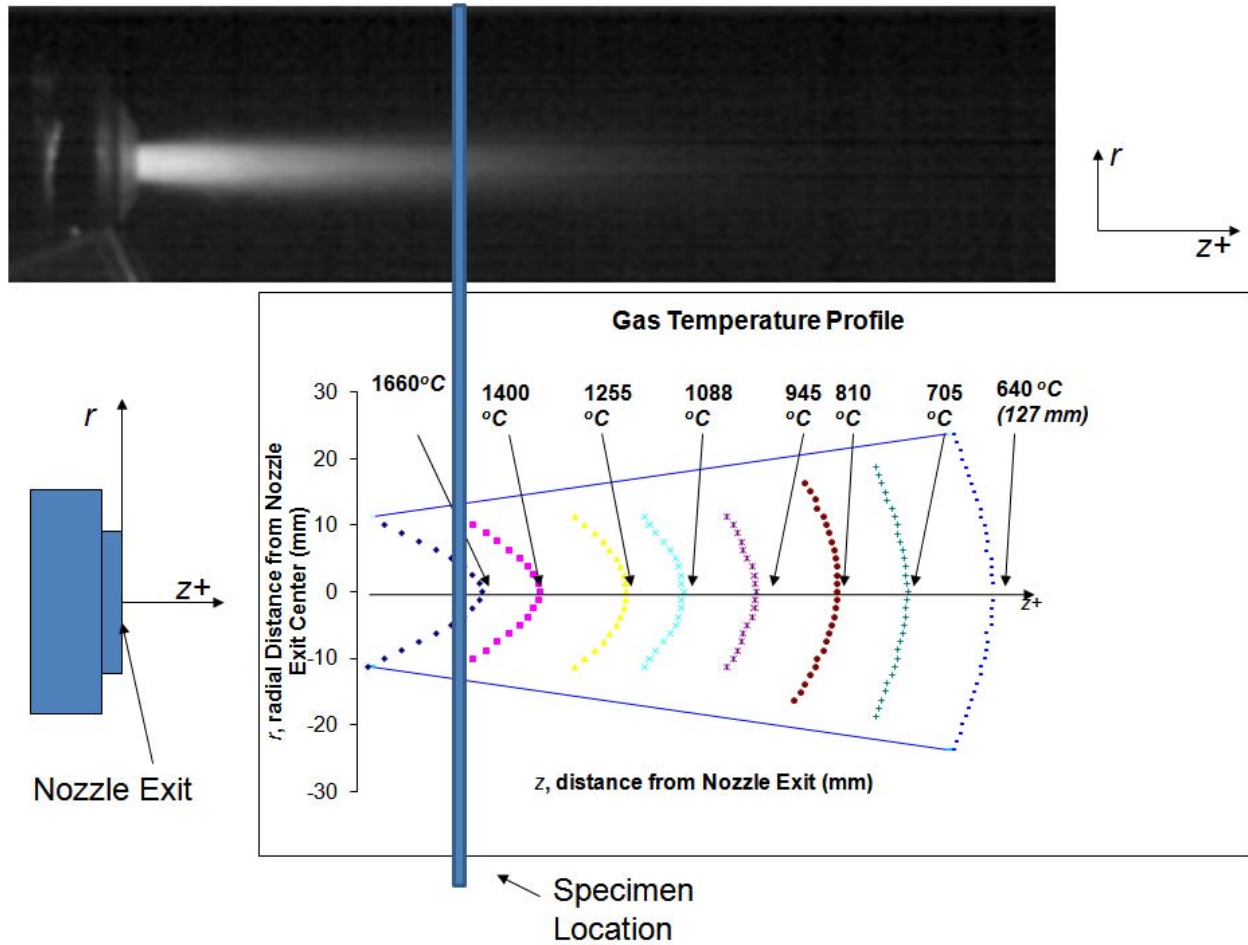
Figure 30: Gas temperature distribution

3.2.2 Gas Velocity

Gas velocity was of interest to find out to determine if it simulates an operating condition of a gas turbine engine. The use of Particle Image Velocimetry (PIV) or Laser Doppler

Vibrometer (LDV) would be ideal for this measurement. Due to their unavailability, however, gas velocity was measured using the X-Stream^{TM} XS-4 High Speed Camera. The range of our interest was the velocity in the upstream of a specimen, and the measurement was done without a specimen in place. The camera was programmed to record images of the flame at 44000 frames per second, as the flame propagates downstream from the nozzle. The post-processing of the images included finding the characteristic features such as flame front, which is indicative of secondary combustion, and tracking their positions between successive images. The convective flame velocity was obtained by taking the difference in the positions of a characteristic feature between two successive images, as depicted in Figure 31. The average distance in position of 11 *mm*, which corresponds to the 1.4 times the diameter of nozzle, is covered in 22.7 *μsec*. The convective gas velocity that corresponds to this measurement was 483 *m/sec*, which is approximately *Mach 0.5*, assuming the local gas temperature of 2300°C. The speed of sound, on which the velocity in Mach number was based, was computed assuming the gas constant of 1.2 and the local flame temperature of 2000°C. The gas speed of *Mach* 0.5 at 11 mm appears reasonable considering the known exponential decay in gas velocity at the exit of the converging nozzle of the HVOF. It would be a topic of a valuable future study to verify the convective gas velocity estimated as described above by comparing with those measured using more widely accepted PIV or LDV.

3.2.3 Gas Composition

A Testo 350 Gas Analyzer^{TM} was used to measure the gas composition. The analyzer has a probe that gets inserted into the flame and built-in filters and chemical sensors that analyze the sampled gas in terms of species and their relative amounts. Chemical products determined by this

measurement were used to validate those estimated Chemical Equilibrium with Applications (CEA) [111]. Codes such as CEA assume chemical equilibrium, which may not be the case in the gas flow. However, the measurement of gas composition in high-temperature, high-velocity flow environment has been challenging and is still the area of active research [112]. Hence, the discussion beyond the equilibrium paradigm would be out of the scope of the current study. For the purpose of this study, the equilibrium is assumed and the chemical species determined using the CEA adequately reflect the chemical conditions corresponding to the local physical conditions such as temperature and pressure in the flame, on the basis that the CO_2 and O_2 as well as NO measured using the analyzer and showed good agreement with the code, as shown in Table 9.
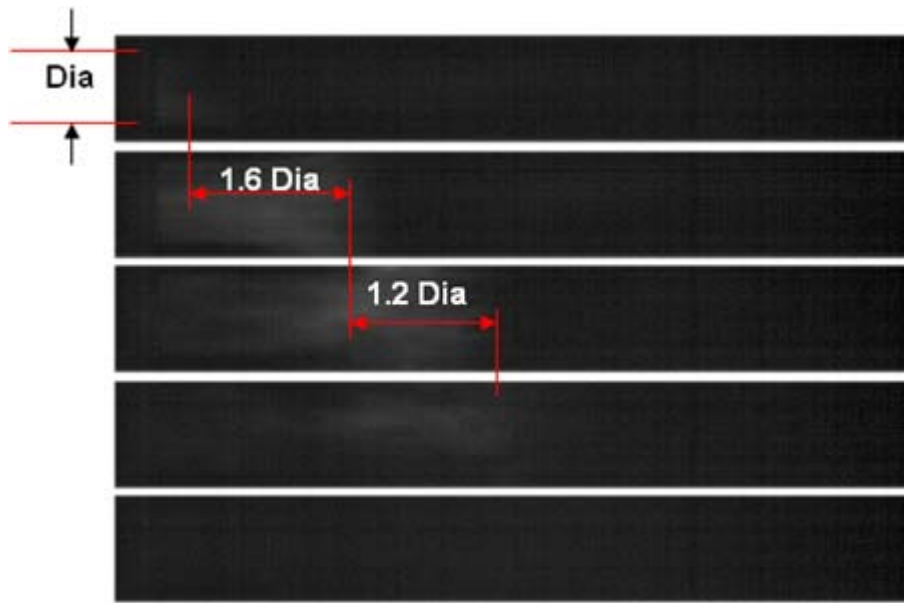
Figure 31: Determination of convective flame velocity using high speed camera

As discussed previously, the propane combustion consists of hundreds of species, and is nearly impossible to track each and every species. Because CO_2 and O_2 are highly stable chemicals that do not decompose or recombine easily, they can be reliable reference for chemical

state of combustion gas. More details of the chemistry of the combustion environment, as it compares to the measured species contents, are provided in Appendix C.

Table 9: Comparisons of species between predicted and measured at T_{gas} of 850°C

Species	CEA (%)	Testo 350 Gas Analyzer (%)
O_2	18.4	18.7
CO_2	3.94	4.52
CO	N/A	0.20
NO	9.0×10^{-6}	5.3×10^{-3}
NO_2	N/A	1.3×10^{-3}

The major species not represented in Table are H_2O and N_2, which could not be measured using the Testo Analyzer. However, based on good agreement of CO and CO_2 contents between the code results and measured, the moisture content was estimated to be 11.5 *vol %*, as illustrated in Appendix C. However, this value could be an underestimation, as the measurement for gas composition calibration was done in a farther downstream location from the inviscid core that produce much higher moisture contents from the primary combustion of premixed flame and oxygen. Direct translation of species without chemical reactions should also be considered. The disparity in the H_2O contents between the primary and secondary combustions will be there, unlike CO_2, which are produced by relatively similar amounts in both primary and secondary combustions. More details of moisture content will be covered as part of the discussion that analyzes the failure of CMCs in Chapter VI.

From the calibration of the instruments to measure and verify the surface and gas temperature, gas velocity and gas composition as prescribed in the test condition, it was determined that the flow rates of the reactants resulting in the surface temperature of 1235 ± 50^oC on the specimen positioned at 60 ± 5 *mm* downstream from the nozzle were 0.72 ± 0.04 gra*m/s* for C_3H_8, 2.2 ± 0.3 gra*m/s* for oxygen, and 3.5 ± 0.3 gra*m/s*ec for compressed air. The corresponding equivalence ratio is 0.9 ± 0.1.

3.2.4 Accelerated Durability Testing and Test Matrix

The combustion environment considered in this study must simulate those encountered in gas turbine hot-section components. These components are also under the application of mechanical load from the attachments as well as pressure load for operating in a pressurized environment. They must survive thousands of hours in such demanding conditions. However, conducting a burner rig test for such a long period of time to validate the durability potential of a test material is simply impractical, especially with expected statistical variations among the same type of material. Therefore, accelerated durability tests are called upon to provide the basis for the material evaluation. The test matrix developed based on this consideration was designed to facilitate systematic assessment of the long-term degradation mechanisms caused by simultaneously unfolding degradation factors such as thermal gradient stress, chemical environment and mechanical loading. This was accomplished by imposing higher mechanical and/or thermal stresses than exist in actual component use, which forces failures to occur in significantly less time.

In addition to mechanical loading, thermal stress was induced by creating high thermal gradients between the front and back surface of a test specimen. This was done by having the combustion flame impinge on a single side of the specimen; while the other side is being open to the ambient air environment. The applied gas temperature to induce the thermal gradient stress was well beyond the maximum service temperature of any modern advanced turbine engine, for which the four CMCs are being considered. Considering that most engines run at the maximum operating condition that includes the highest temperature for no longer than 30 to 60 hours [40], the burner rig test involving the exposure of a specimen to this severe experimental environment for even as short as 25 hours should allow us to investigate on the long-term degradation

phenomena and to study the potential of the proposed materials for the applications that require durability.

In the test phase, fatigue loading with peak stress equivalent to 50 to 125 % of the proportional limit (*PL*) was applied. The *PL* is determined here as the highest stress which a CMC can sustain without deviating from proportionality of stress-strain curve and is determined here as the stress at which the strain deviates by 5×10^{-5} from linear loading [49,75,76]. Another method of determining the *PL* would have the stress at 5% deviation from the extrapolated linear segment used for the modulus determination [113]. The *PLs* of the CMCs in this study obtained using this method were in good agreement with those obtained using the 5×10^{-5} offset method. The differences in *PLs* resulted from the two methods were small, and the *PLs* of the four CMCs were in the same order with similar margins between them regardless of the method used. For consistency, the 0.005% offset method was used throughout the study to determine the *PL*.

The applied stress range ensures that various levels of matrix cracking are captured. For the woven MI Syl-*iBN*/BN/SiC system, for example, 50% of *PL*, the lower value in the applied stress level, is approximately 85 MPa and is below the maximum stress conditions for turbine vanes and blades (i.e. 100 MPa), while 125% of the *PL*, on the other hand, is significantly above the maximum service stress. This approach captures the capability of test material over the stress range beyond the current design stress envelope. As peak stress level increases, test duration decreases, which facilitates the accelerated durability method.

3.3 Specimen

The details of each of the four SiC/BN/SiC CMCs including the constituents, fiber architecture, layup sequence, processing information as well as their room temperature properties are provided

in Table 5 of Chapter II. Every specimen tested used the same dog-bone geometry. The woven MI Syl/BN/SiC and the woven MI Syl-*iBN*/SiC are received from Larry Zawada of AFRL/RX, Wright-Patterson Air Force Base, *OH*, and the woven MI Hi-Nic-S/BN/SiC and the prepreg MI Hi-Nic-S/BN/SiC were received from Dr. Micheal J. Verrilli of GE Aviation. Table 10 shows the number of specimens and the dimensions of the reduced section of each CMC.

Table 10: Specimen dimension and quantity

Type	Length (mm)	Cross-sectional dimension (mm^2)		Quantity
		Thickness (mm)	Width (mm)	
Woven MI Syl/BN/SiC	150.4	1.54 ± 0.03	7.99 ± 0.02	5
Woven MI Syl-iBN/BN/SiC	150.4	1.57 ± 0.04	8.01 ± 0.07	5
Woven MI Hi-Nic-S/BN/SiC	150.4	2.31 ± 0.03	10.16 ± 0.04	6
Prepreg MI Hi-Nic-S/BN/SiC	150.4	2.00 ± 0.01	10.11 ± 0.02	5
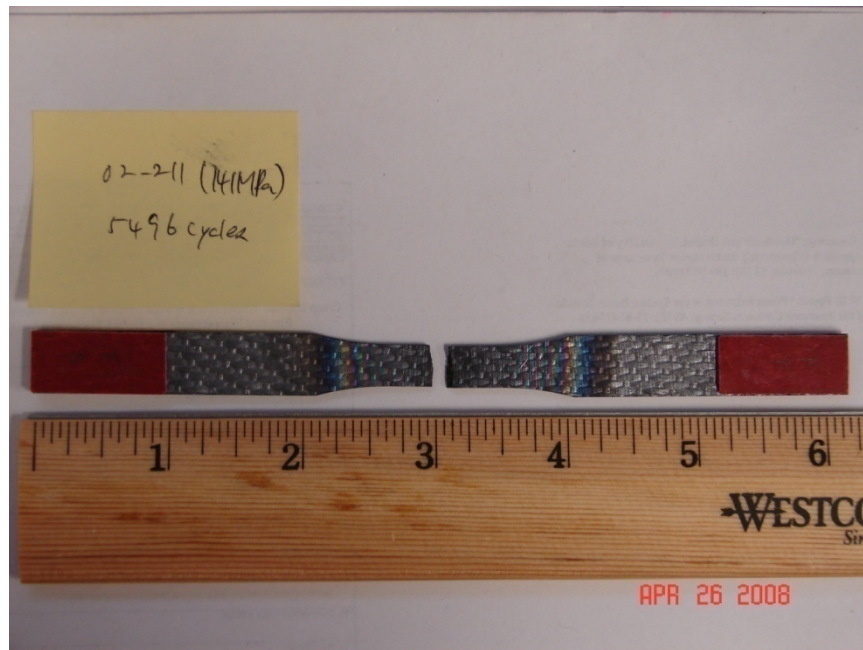
Figure 32: Fractured specimen after test (woven MI Syl-*iBN*/BN/SiC shown)

Figure 32 shows a specimen fractured during the fatigue test. Nearly all specimens failed within ± 3.2 *mm* from the geometric center of the specimen. Both the upper and bottom pieces were subjected to identical heating condition, as the combustion system was programmed to put off the flame as soon as the specimen failure caused the displacement to exceed a user-specified level, which was only slightly different from the peak displacement. However, the upper portion of the failed specimen was used in every case to get fracture surface data to have consistency in the orientation with regard to the flame direction in the data analysis.

The fracture surfaces were cut using a Buehler Isomet Low Speed Saw with a Buehler Diamond wafer blade and kerosene as lubricant. The sectioning was made approximately 3.0 ± 1.0 *mm* from the fracture surface. The sectioned piece containing the fracture surface was mounted on a silver stub using either double-sided carbon tape or silver paste to increase the conductivity for scanning electron microscopy (SEM). The other piece was subsequently cut to a small depth, i.e. 5.0 *mm*, for sectioned surface analysis. For those specimens that fractured outside the gauge section, the sectioning was made inside the gauge area such that the effect of combustion heating could be reflected. The resulting pieces from this step spanned by about 20 *mm* from one end representing the fracture surface to the sectioned surface on the opposite end and one of the pieces was further sectioned by one-fourth of the specimen width in the direction parallel to the loading so as to investigate them for the penetration of oxidation as well as secondary cracking phenomena.

In addition, for each of the four CMCs, an unused portion of the specimen was cut at a 45$^{\text{o}}$ angle to the loading direction for the verification of fiber volume fraction. After polishing, the Reichert-Jung MEF3A optical microscope was used to take images, on which intersection counting was performed using a square grid overlay to verify the fiber volume fractions supplied

77

by the manufacturers. Despite the use of a different method from the manufacturers and the limited size of data collected, the agreement was good.

Sectioned surfaces were made from both the fractured and as-received samples. They were mounted in conductive Polyfast^{TM} mounting compound using either Buehler Simplimet 2000 or Buehler/Metasery Pneumet Mounting press and then polished using diamond paste polishing compound and polycrystanlline diamond suspension and Buehler Perforated Textmet polishing pads on either Pheonix 1000 or Ecomet 4 variable speed grinder polisher. The diamond particle size in the paste or slurry was 45 μm to begin polishing and progressively decreased to involve 9, 6, 3, 1, 0.05 μm in sequence, using the appropriate number of polishing pads designated for each size. As a final step, the polished surface was put in a Buehler Vibromet I polisher filled with colloidal silica slurry and Hyprez oil soluble (OZ) lubricant for 2 or 3 days. The finished surface was cleaned in distilled water and then cleansed using ultrasonic sonicater in acetone, followed by its immersion in distilled water before drying the surface using compressed air. Figure 33 shows two mounts embedding multiple sectioned surfaces of test specimens.

Figure 33: Polished specimen embedded in the mount

78

3.4 Microscopic Analysis

Both fracture and polished surfaces were analyzed under optical and SEM. For optical microscopy, the Reichert-Jung MEF3A was used to inspect the fractured and sectioned surfaces for fiber pullout, matrix quality and cracking phenomena at magnification up to 1000X. For SEM, five different systems were used throughout this study due to limited availability of any one system. Three of the five units, Leica 360 FESEM, FEI Sirion SEM and FEI Quanta Mk II ESEM were field emission SEMs, or FESEM, and the other two FEI Quanta 3-D units were tungsten-filament SEMs. Generally, higher voltage, i.e. 20 or 25 kV was required with tungsten filament SEMs, as compared to 10 or 15 kV used with FESEMs. Leica 360 FESEM, FEI Quanta Mk II ESEM and one of the two FEI Quanta 3-D tungsten-filament SEM were each equipped with Energy Dispersive Spectroscopy (EDS), which measures the elemental composition of the subject area. The EDS was used in conjunction with SEM to substantiate the visual determination of oxidation made using SEM. Low accelerating voltage (5~10 kV) was used to ensure that the composition identified by EDS was that of the surface level. For higher magnification imaging, i.e. beyond 20,000X, the FEI Sirion SEM with ultra high resolution capability was used at 5kV for detailed imaging. To ensure the consistency of imaging quality, a randomly selected location near the center of each surface was calibrated to a reference image representing each type of CMCs before every session of each different SEM.

3.5 Procedures

3.5.1 Fatigue Testing in Combustion Environment

First, the axial alignment of the MTS grips was performed using the alignment sample with stain gauge attached on its surface and the MTS alignment software program. After the

alignment was finished, the MTS grips were thermally protected by attaching the copper coil for chilled water passage and the contacting steel plate designed to aid with active cooling provided by the chilled water. The spatial limitation by the cooling components made it difficult to ensure the vertical alignment of a specimen every time one was loaded. To ensure proper alignment of a specimen, extra measures were implemented. A mechanical stop was positioned and affixed onto each MTS grip according to the alignment checked with no cooling components using the MTS certified calibration equipment. Using the prepositioned mechanical stop, the axial alignment of a specimen was attained by subjecting the edges of the specimen against the stops. An additional check on alignment was performed by subjecting a bubble level against a straight edge of each specimen.

The next step in the pretest procedure was to set up the test specimen. After measuring the dimensions of the specimen, the upper one-sixth of the specimen was gripped by the upper hydraulic grip, an actuating grip of the MTS system. Then the specimen was lowered in displacement control mode until the bottom one-sixth of the specimen could be gripped by the lower stationary MTS grip. Doing this ensured that the center of the specimen gauge section was at the same height as the nozzle of the HVOF system. Before gripping the lower portion, the mode of control was changed from displacement-control to force-control such that the force to be applied on the specimen once the lower section was zero. Using the stops attached on the MTS grips, along with a bubble level, extra care was taken to ensure that the specimen axes aligned properly with those of the load frame. The second step ends with tuning the installed specimen for the load level and frequency. This was accomplished through the auto-tuning command built into the program that controlled the MTS with the load and operating frequency specified as input.

80

The third step was to install the rest of the thermal protection system that thermally isolated the MTS from the heated zone of the specimen. The wedges of the MTS grips were equipped with chilled water passage and fittings for high temperature operation. In addition to the spiral copper tubes, through which the chilled water was pumped, placed between the MTS grip and a steel plate, attached mechanically to either the upper or lower MTS grip, an additional layer of thermal protection was provided by the zirconia-based heat shielding block positioned tightly around the specimen and clamped onto the plate. As an extra measure, compressed air was passed through an opening created by the spiral coils as well as any gaps in the grip area on the cooled side of the steel plate such that proper cooling of the MTS and other periphery equipment can be attained. Such cooling was done on the thermally protected side of the plate to mitigate the possibility of disrupting the thermal profile that developed by combustion heating.

The third step consisted of igniting the combustion flame and adjusting the flow rates of all reactants to their calibrated levels such that the consistent flame was attained. Ignition was accomplished with the HVOF system slid as far back as possible from the specimen and at an off-angle from the position of flame impingement on the specimen. After the flow rates stabilized at the desired levels, the HVOF system was swung into the alignment with the specimen. Before this step, the MTS control was confirmed to be in force control at zero force, so that the thermal expansion caused by the heating did not exert any load on the specimen. At the distance that the flame was first introduced, the surface temperature measured using the IR system read the surface temperature of $700 \pm 50^{\text{o}}$C.

Then, the nozzle was brought in closer to the specimen slowly and incrementally using the linear slider installed on the base of the HVOF system until the surface impinged approached steadily to the temperature of $1235 \pm 50^{\text{o}}$C. The rate of temperature ramp-up is a function of heat

flux applied. Due to the ambient condition and probably air cooling, it took as long as 30 minutes to reach at the target temperature, using the heat flux consistent throughout the test. Once the temperature was reached, the programmed mechanical loading was applied at the frequency of 1 *Hz* and a stress ratio of 0.05.

Due to concerns with fire safety, the operation of the system was limited to 8 or 9 hours per day. Hence, the 25 hour-long tests consisted of two forced interruptions; once after the first 8 hours and the other after the next 8 hours. At each interruption, caution was taken to minimize any shock effect by making sure that the MTS load frame was under force control to zero force, as the combustion flame was slowly and incrementally removed from the specimen. Then the third step in the pre-test is repeated on the next day to resume testing.

If the specimen failed at any point during the test, the combustion system shut down immediately as programmed in the Labview^{TM} user interface. The fractured specimen was then dismounted from the grips. If the specimen survived the test without fracture, the combustion was terminated manually at the end of the prescribed number of cycles as described for the forced interruption and then the specimen was dismounted. In addition, the data collected from the MTS and the Labview^{TM} program were saved along with the test diary that recorded the log information and other details from observations during the test.

3.5.1 Fatigue Tests in Furnace

In addition to the fatigue tests in burner rig, similar fatigue tests were conducted using a laboratory air furnace to demonstrate the effect of temperature gradient and moisture contents in burner rig. This was a demonstrator experiment, for which only one material was selected out of four CMCs. Three woven MI Hi-Nic-S/BN/SiC were used in this demonstration experiment, and

their test results were compared with the fatigue test data for the same material obtained in burner rig exposures. Specimens with geometry and dimensions identical to those in burner rig tests were used. The temparature of the furnace was calibrated prior to the actual testing of the woven MI Hi-Nic-S/BN/SiC specimens. A standard electric furnace from MTS was calibrated to maintain a specimen temperature of $1235 \pm 5^{o}C$, which is equal to the surface temperature in the direct flame impingement area of specimen in the AFIT/AFRL burner rig. R-type thermocouple, the same type used during the calibration of the temperature in the burner rig test, was used to calibrate for the targeted surface temperature. Gas composition inside the furnace was assumed to be that of laboaratory air, i.e. 79 vol % of N_2 and 21 vol % of O_2, as the furnace was open to the air in the laboratory. The relative humidity in the room at the time of testing was $55 \pm 5\%$, which translates approximately to less than 2 *vol %* of *H_2O*.

The rest of the test procedure in furnace testing was identical to that of the burner rig testing. The same stress ratio and cyclic frequency (R = 0.05 and 1 *Hz*) were used. Peak stress applied to each of the three woven MI Hi-Nic-S/BN/SiC specimens were 135, 125 and 100 MPa, respectively, and the corresponding number of cycles at failure at each stress level was obtained. The test runout condition was again set at 90,000, or 25 hours.

IV. Fatigue behavior of CMCs in a combustion environment

The experimental results of this study are presented in this chapter. The results are from the mechanical fatigue testing of four different SiC/BN/SiC CMCs performed in a high temperature combustion environment, using the mechanical and combustion parameters predetermined and calibrated to simulate a realistic high temperature combustion environment. The four CMCs under investigation are (1) woven MI Syl-*iBN*/BN/SiC, (2) woven MI Syl/BN/SiC, (3) woven MI Hi-Nic-S/BN/SiC and (4) prepreg MI Hi-Nic-S/BN/SiC.

For each CMC, the results from room temperature monotonic tension tests are presented. The ultimate tensile strength (*UTS*) and proportional limit (*PL*) collected from the monotonic results serve as bases for comparisons. Using *UTS* or *PL* as reference, the mechanical fatigue test data are presented and discussed in details from both mechanistic and microscopic viewpoints.

This chapter is focused on the test results and the microscopic analysis for each CMC. In-depth discussion is presented for each CMC system in light of fatigue strength in terms of peak stress as well as strength degradation caused by the combined loadings of the mechanical fatigue and the combustion environment. For each material system, the S-N data and relevant discussion are presented first, followed by the microscopic analysis of fracture and sectioned surfaces with the emphasis on the development and effects of oxidation with changing peak stress. The fractographic analysis is followed by the discussion of strength retention test results. Detailed analysis of the fatigue behaviors of each CMC system presented in this chapter not only increases the understanding of fatigue in combustion environment for each material system, but it also lays a foundation for the comparisons between and among different CMC systems, which will be the theme of the next chapter.

4.1 Monotonic tension at room temperature

The stress-strain behavior of the four CMCs under room temperature monotonic tension was investigated and the results are listed in Table 11. Due to the limited specimen availability of the four CMCs, the majority of the room temperature monotonic test data shown are obtained from previous studies performed on the same materials [80,81]. As defined in Chapter III, the proportional limit (*PL*) is the stress at the point of intersection between the stress-strain curve and the line drawn parallelly to the linear portion of the curve from the 0.005% offset in strain from the origin. From Table 11, it is noticed that the MI prepreg Hi-Nic-S/BN/SiC has higher modulus of elasticity (*E)* and *PL* than the other three CMCs. Among the woven CMCs, the MI woven Hi-Nic-S/BN/SiC shows the lowest *E* and *PL*. The two Sylramic fiber woven CMCs are similar in elastic modulus, though the Sylramic CMC with in-situ boron nitride (*iBN*) coated on the fiber exhibits much greater *UTS* and a larger strain at failure. The woven MI Syl-*iBN*/BN/SiC also has a slightly higher *PL* than the woven MI MI Syl/BN/SiC. Representative monotonic stress-strain curves for all three CMCs are plotted in Figure 34. The curve for the prepreg MI Hi-Nic-S/BN/SiC is not available. It is evident that the two Sylramic CMCs behave nearly identically up to the fracture of the woven MI Syl/BN/SiC, suggesting that the in-situ BN layer may have contributed to an increased strain at failure. The highest ultimate stress is attained by the woven MI Syl-*iBN*/BN/SiC, while, though not shown in the figure, the highest ultimate strain is reached by the prepreg MI Hi-Nic-S/BN/SiC at 0.71% (Table 11). The curve representing the woven MI Hi-Nic-S/BN/SiC enters nonlinearity at lower stress, supporting the observation from Table 11 that it has lower *PL* than either of the Sylramic based CMCs. The woven MI Hi-Nic-S/BN/SiC has the *UTS* greater than that of the woven MI Syl/BN/SiC and smaller than that of the woven MI Syl-*iBN*/BN/SiC. The strain at failure for the woven MI Hi-Nic-S/BN/SiC is comparable to that of

the woven MI Syl-*iBN*/BN/SiC. In comparing the two Hi-Nic-S fiber-reinforced CMCs, the prepreg MI Hi-Nic-S/BN/SiC shows a greater modulus of elasticity than the woven Hi-Nic-S/BN/SiC, and thus the slope of the stress-strain curve is with a larger gradient than that shown from the curve for the woven MI Hi-Nic-S/BN/SiC.

Table 11: Room Temperature Monotonic Test Data [80,81]

Specimen ID	Elastic Modulus (GPa)	PL (MPa)	UTS (MPa)	Failure strain (%)
Woven MI Sylramic/BN/SiC				
1228-01-003-16	218	146	250	0.2588
1228-01-003-17	202	159	292	0.3234
Avg. (± St. Dev.)	210 (± 12)	153 (± 9)	271 (± 29)	0.2911 (± 0.046)
Woven MI Sylramic-iBN/BN/SiC				
02-236	200	161	421	0.5571
02-237	221	167	466	0.6007
1228-01-001-16	207	179	447	0.5814
1228-01-001-17	207	163	398	0.5384
1228-01-002-13	200	163	421	0.5571
Avg. (± St. Dev.)	207 (± 9)	167 (± 7)	431 (± 26)	0.5669 (± 0.024)
Woven MI Hi-Nic-S/BN/SiC				
08-501*	195	121	334	0.5379
Prepreg MI Hi-Nic-S/BN/SiC				
18-19-20-5	268	170	363	0.8200
23s/24s-4	257	160	354	0.8600
25s-4	276	190	339	0.7350
28s-4	251	193	305	0.7150
31s-4	258	205	330	0.7400
32s/33s-4	243	208	357	0.6750
38s/39s-4	275	222	346	0.6800
40/s/41s-4	281	228	324	0.4700
Avg. (± St. Dev.)	264 (± 13)	197 (±23)	340 (± 19)	0.7100 (± 0.12)
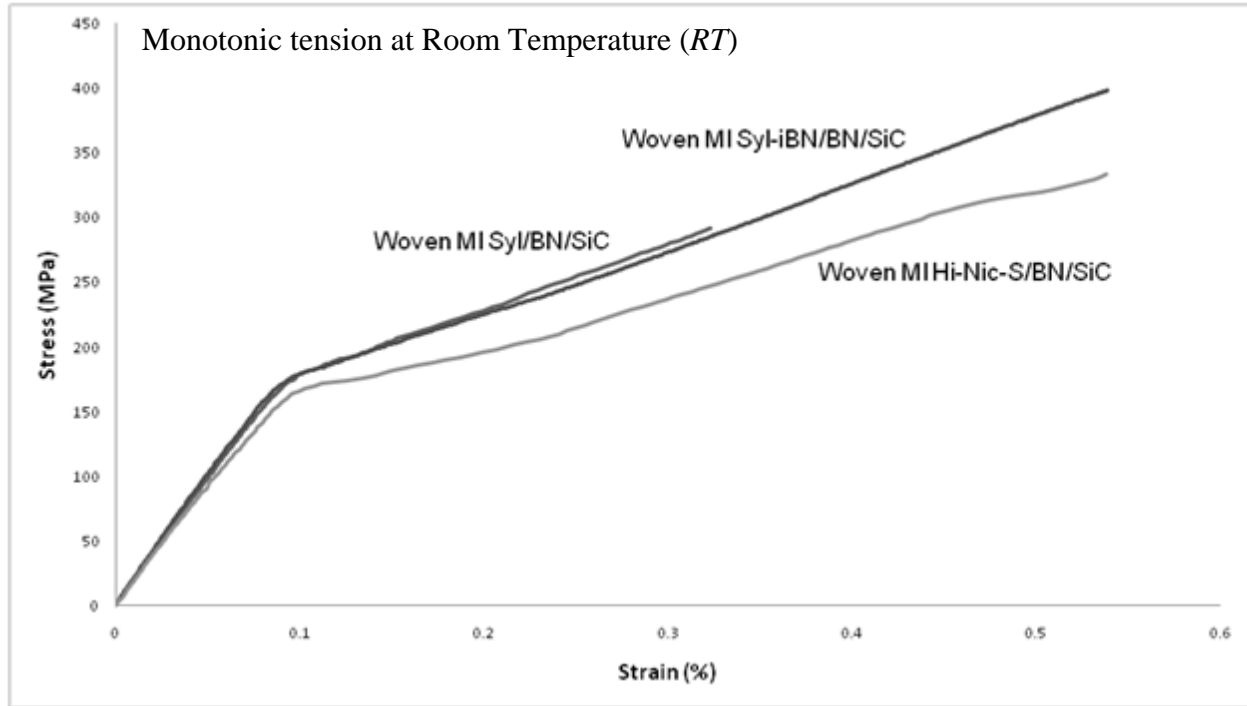
Figure 34: Room temperature monotonic stress-versus-strain curves [80,81]

The room temperature data of the four CMCs are discussed above for the purpose of identifying the material properties, which will serve as the basis for interpreting the fatigue strength relative to the ultimate tensile strength (*UTS*). Normalizing the stress against the material properties such as the *UTS* and proportional limit (*PL*) provides a means to link the experimental data to the physical phenomenon uniquely associated with the properties, such as matrix cracking. It also becomes useful when comparing two different materials with different properties, especially in which the relative change caused by an experimental parameter is to be investigated and compared among several materials with different properties.

The four sections presented below discuss the results and analyses from the mechanical fatigue tests of each of the four SiC/BN/SiC CMC systems in the prescribed combustion environment, applied to each specimen along with simultaneously a mechanical fatigue loading

with the fixed loading parameters of 1 *Hz* and *R* = 0.05. The area on the front surface of the specimen under direct impingement of the combustion flame is referred to as the heated zone, which was 1235 ± 50$^{\mathrm{o}}$C in temperature during test. While the chemical, thermal and fatigue parameters remain constant throughout the entire testing phase, the peak stress was changed between each test such that the fatigue life data for each CMC system is collected over a range of peak stresses. Microscopic analysis was performed on both fractured and sectioned surfaces to investigate for the failure mechanisms in terms of oxidation.

4.2 MI woven Syl-iBN/BN/SiC

The woven MI Syl-*iBN*/BN/SiC was tested under cyclic fatigue at different peak stress levels in the prescribed combustion condition described in the previous chapter. The peak stress was changed between each test such that the corresponding fatigue life of the tested specimens spanned from about 1,000 cycles to over 90,000 cycles. A test was terminated manually if the specimen survived past 90,000 cycles or 25 hours at 1 *Hz*. This was referred to as a runout test in this study.

4.2.1 S-N Data

Table 12 summarizes the data obtained from the tests. Each applied peak stress was plotted against the corresponding cycles-to-failure to obtain the S-N curve, shown in Figure 35. The abscissa represents number of cycles-to-failure in logarithmic scale. The *PL*, represented by a dashed line parallel to the horizontal axis, was denoted on the S-N plot for comparison with applied peak stresses. A normalized S-N curve was obtained by dividing each peak stress by the room temperature ultimate tensile strength (*UTS*) as discussed earlier. The normalized curve indicates the percentage of knockdown in *UTS* experienced by the applied test condition.

Table 12: Fatigue test in combustion for MI woven Syl-*iBN*/BN/SiC

Specimen ID	Applied Peak Stress (MPa)	AppliedPeak Stress (% *UTS*)	Applied Peak Stress (% *PL*)	Number of Cycles	Fractured spot (Distance from center , mm)	Temperature at Fracture (^{o}C)		
						Front	Side	Back
02-207	187	44 ± 3	112 ± 5	1014	3±3	1210±30	960±50	N/A
02-209	169	40 ± 3	102 ± 5	7637	6±3	1135±35	900±50	N/A
02-211	141	33 ± 2	85 ± 4	5496	6±3	1160±40	970±50	810±10
02-212	125	29 ± 2	75 ± 3	17384	0±3	1235±35	980±50	830±10
02-208	110	26 ± 2	66 ± 3	90115	No Fracture	1188±38	920±50	800±10

With the decrease in applied peak stress, the number of cycles-to-failure increases. The fractures occurred in the reduced sections for all specimens except the one test that resulted in runout. A few specimens failed inside and the other two just outside the heated zone, where the highest temperature and the largest thru-thickness gradient were apparent. The location of fracture could aid in the determination of failure mode due to the asymmetric thermal and stress profile, brought about by the directional heating of this study. The runout specimen was later tested monotonically under tension at room temperature condition for the determination of retained strength. The temperature at the fractured cross-section was estimated from the infrared image taken during testing using the calibrated IR system. The ranges in the surface temperature data are primarily due to the parabolic thermal profile with radial gradient in heat flux of the underdeveloped combustion flame, as shown in Figure 30 of Chapter III. The uncertainty in the surface temperature of the side surface with relatively small dimension stems from a large temperature drop experienced across a small dimension of thickness as well as the limitation in the dimensional resolution of the infrared system used in this study.
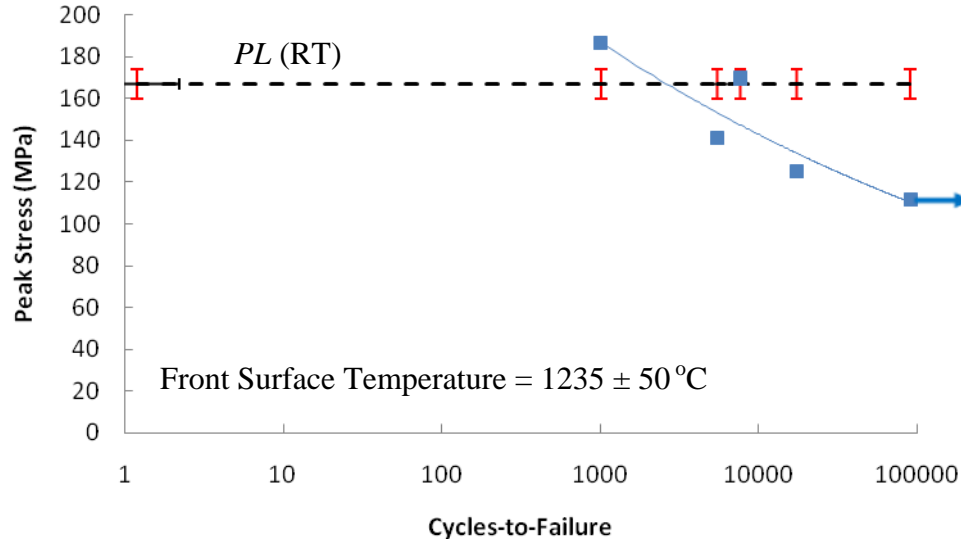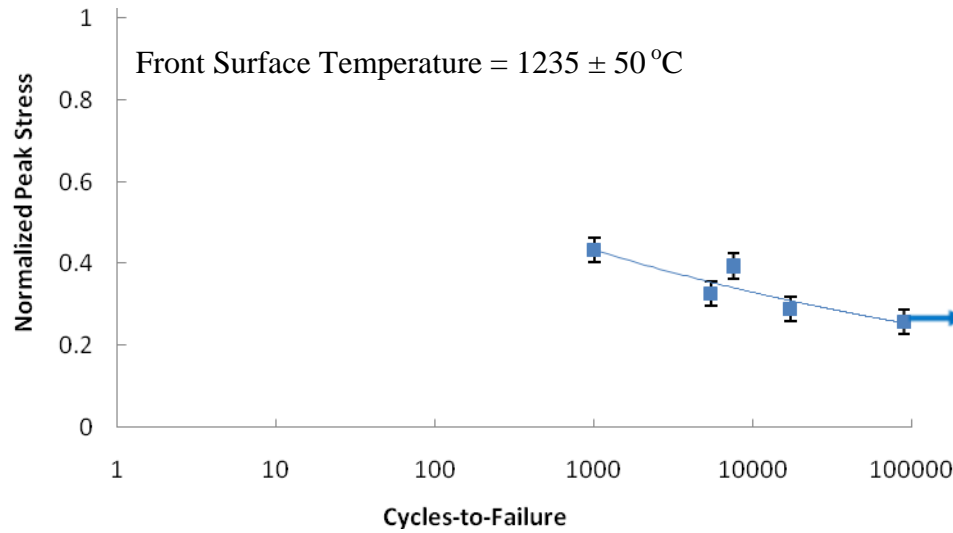
Figure 35: S-N curves for MI woven Syl-*iBN*/BN/SiC with stress (A) in MPa and (B) normalized against *UTS*

The proportional limit (*PL*) for this CMC at room temperature is 167 ± 7 MPa, which is

39 ± 4 % of the room temperature ultimate tensile strength (*UTS*). From Table 12, the applied

peak stress that results in runout was 26 ± 2 % of the *UTS*, or 66 ± 3 % of the *PL*, which is below

the "knee" of the stress-strain curve [48]. While the test with 66 ± 3 % of *PL* as peak stress

resulted in runout, the tests under the peak stress level exceeding 75% of *PL* did not survive past 17,384 cycles. As the 75 ± 3 % of *PL* is below that considered to induce significant microcracking [76], the relatively short fatigue life is consistent with the local stress state being higher than the mechanically applied stress alone due to thermal stresses.

4.2.2 Strength Retention

The specimen which survived the 25 hour or 90,000 cycles of test duration without failure was subsequently tested for the residual strength under room temperature monotonic tension, which found 279 MPa or 65 ± 4 % of the room temperature *UTS*. The stress-strain curves are plotted in Figure 36 for both the runout specimen tested for residual strnegth and the as-received tested under monotonic tension at room temperature.

The stress axis in Figure 36 is represented in two different ways; once with absolute stress scale in MPa and the other using stress scale normalized against the ultimate tensile strength of one of the pristine samples. The proportional limit of the runout specimen tested for residual strength was 167 ± 7 MPa, nearly identical to that of the as-received material tested at room temperature. The modulus of elasticity measured from the runout specimen was 189 GPa, which is smaller than the average modulus of this material at room temperature by two standard deviations. However, this difference could not be assessed for the possible softening of CMC with the test condition due to the absence of additional data as well as statistical scatter in the inherent mechanical properties of this CMC documented in Section 4.1. The modulus that describes the stiffness in the secondary region of the curve is slightly lower than that of a pristine material. With the exception of the small decrease in the moduli of elasticity in both the primary and secondary portions of the two curves, the two curves behaves similarly up to the point of fracture

by the runout specimen. However, the runout specimen failed upon reaching 65 ± 4 % of the *UTS*

(i.e. 279 MPa) at 0.3435, or 61 ± 3 % of the strain at failure for the pristine material. The fact that

the strength retained by the runout specimen is significantly less than the original strength of an

as-received specimen suggests that permanent damage was accumulated during the fatigue

loading in combustion environment.

A

B
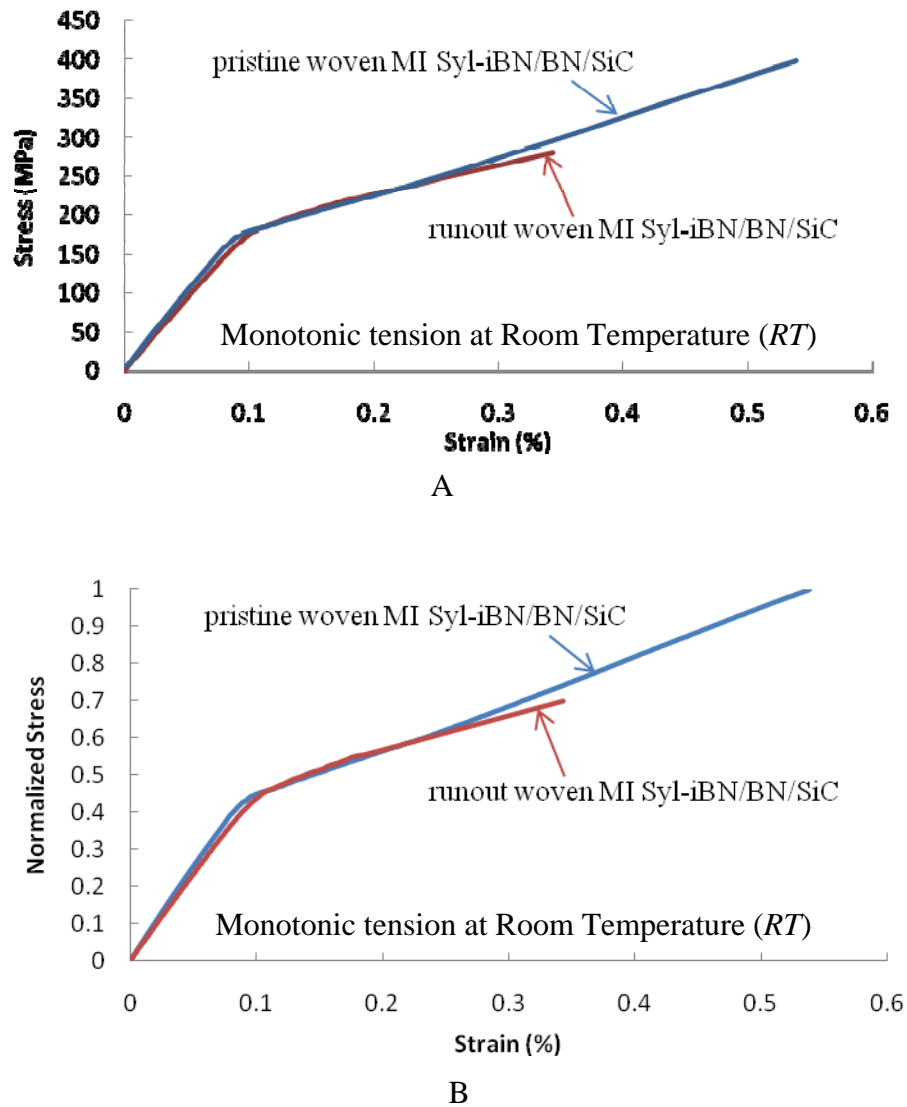
Figure 36: Stress-strain curves of the runout and pristine MI woven Syl-*iBN*/BN/SiC tested under monotonic tension; stress shown (A) in MPa and (B) normalized against *UTS* determined from one of the monotonic tension tests of pristine samples

4.2.3 Microscopic Analysis

The life data presented in Figure 35 revealed an inverse trend in applied peak stress with respect to cycles-to-failure. With the understanding that an oxidizing environment is detrimental to the life of a CMC material, the details of this trend may be interpreted in terms of oxidation. This was done by analyzing the physical and chemical characteristics of both fracture and sectioned surfaces at high magnifications using the Scanning Electron Microscopy (SEM) and the Energy Dispersive Spectroscopy (EDS), respectively.

The microscopic data collected from the fracture and sectioned surfaces of all the tested MI woven Syl-*iBN*/BN/SiC specimens are summarized and presented here. For each fracture specimen, the entire fracture cross-section was scanned thoroughly under either Field Emission SEM (FESEM) or SEM for any evidence of oxidation. EDS was used as supplementary tool for validation. There were two micrographic features suggesting the oxidation. One was the planar fracture surface consisting of fibers with rigid SiO_2 interphase, which often appeared to have failed as a group. The fractographic feature of this type came in small number of the fibers with rigid interphases as well as in a large number sometimes, as demonstrated in Figure 41C. The other micrographic feature suggesting oxidation was the patch or pool of oxide formed on the fracture surface, as shown in Figure 41A & B. The portion of a planar fracture surface with no pullout or very short fiber pullout that contains these features was hence considered to be produced from oxidation and is termed as "*oxidized*." The regions showing the features suggesting oxidation such as patches of oxide layer formed on relatively flat fracture surface are regarded as the areas of secondary effects of oxidation. Both regions are considered to fall under oxidized and are represented by "Ox" on the cross-sectional images of fractured surfaces. The area outside the oxidized regions showing fiber pullouts with no oxidative features is termed

"*non-embrittled*." The failure in this region is described to be due to overload on remaining intact fibers. The oxidized region is separated from the non-embrittled region by dotted lines as shown in Figure 37. As we shall see in the next chapter, the area ratio of the oxidized region to the overall fracture surface permits qualitative assessment of the effects of oxidation on the overall stress state at the time of failure.

4.2.3.1 Fractographic analysis

In fatigue, the level of microcracking is determined by several factors such as the frequency, stress ratio and peak stress. Microcracks induced upon undergoing the applied peak stress in the first few fatigue cycles progressively develop with increasing number of cycles. In all the tests performed in this study, the frequency and stress ratio along with the combustion condition remained constant while the peak stress was changed between tests. Thus, the increase in peak stress can be assumed to bear some correlation to the increase in the level of microcracking. Microcracks then coalesce and evolve, under load, into a main crack or link up with an existing crack that evolved elsewhere. In addition, oxidation is known to occur readily through cracks that are open to the high temperature, high moisture environment. Therefore, the fractographic investigation of oxidation may be related to the mechanical parameters such as peak stress and cycles-to-failure that are interrelated to the cracking phenomenon. These are the basic premises of this study, based on which correlations are attempted between the extent of oxidation observed on a fractured surface and the applied load, the time of combustion exposure and growing number of fatigue cycles.

Figure 37 represents the fracture surfaces obtained from the fatigue tests in the prescribed combustion environment at three different stress levels; 112 ± 5 %, 101 ± 5 % and 75 ± 3 % of *PL*,

for which the corresponding cycles-to-failure are 1,014, 7,637 and 17,384 cycles, respectively. The arrow on each cross-section shows the directly impinged surface from the combustion flame.
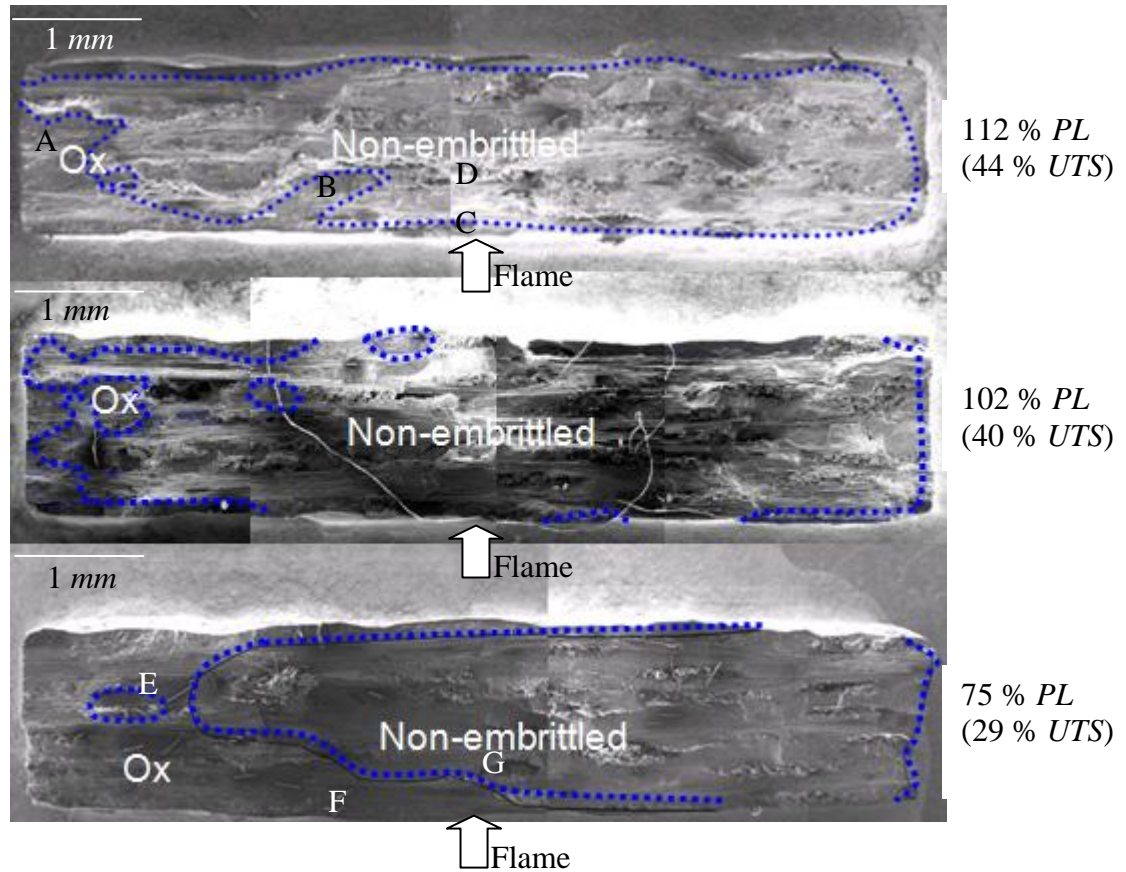
Figure 37: Fracture surfaces at peak stresses of 112%, 101% and 75% of *PL*

The majority of the oxidized regions shown in Figure 37 appear connected to the edge-oxidation developed along the edge on either side. In comparing the oxidized areas of the three fractured surfaces in Figure 37, it is evident that the specimen fatigue loaded at 75 ± 3 % of *PL* shows 2~3 times as large an oxidized area as that of the specimen loaded at 112 ± 5 % of *PL*. Thus, the extent of oxidation observed was smaller at the higher applied peak stress. In addition, the specimen loaded at 75 ± 3 % of *PL* having 3 times larger oxidized area had approximately 17 times longer cycles-to-failure than the other fatigued at 112 ± 5 % of the *PL*. This showed that the extent of oxidation observed was larger with increased cycles.

A closer look at the fracture surface reveals the planar crack plane, fibers with interphases hardened by oxidation, and patches of silica overlayer. The silica observed in the Figure 38 was an example of the patch of overlayer containing silicon and oxygen as the EDS analysis showed. The microstructures commonly observed in the oxidized and non-embrittled regions are depicted in Figure 39 for the specimen fatigued at 112 ± 5 % of the room temperature *PL* and Figure 40 for the specimen fatigued at 75% of the *PL*, respectively. For each of the two cases, four SEM images demonstrating representative micrographic features are provided. The letter designation such as A, B, C or D, etc for each picture in Figure 39 and Figure 40 refers to the corresponding location on the entire fracture surface shown on Figure 37.
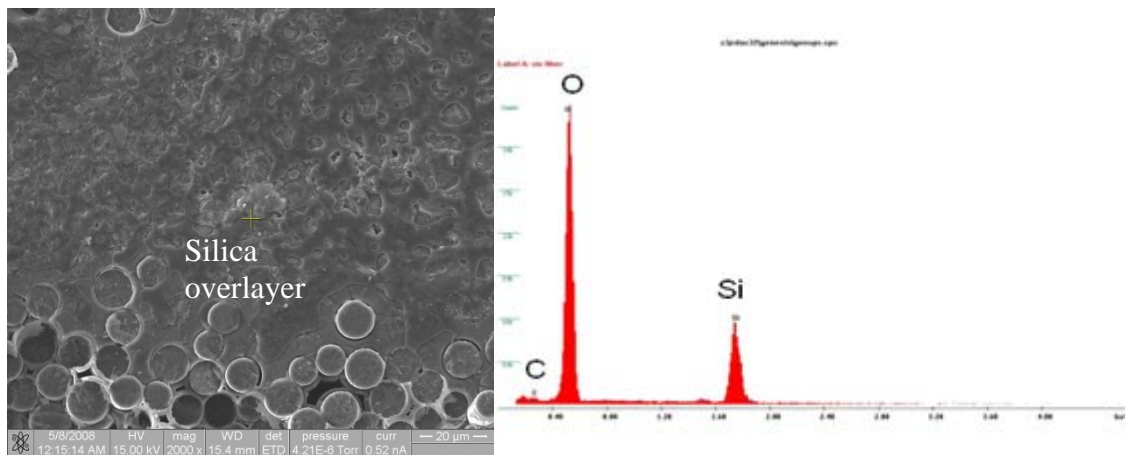
Figure 38: EDS analysis of patch of oxide flown on fracture surface
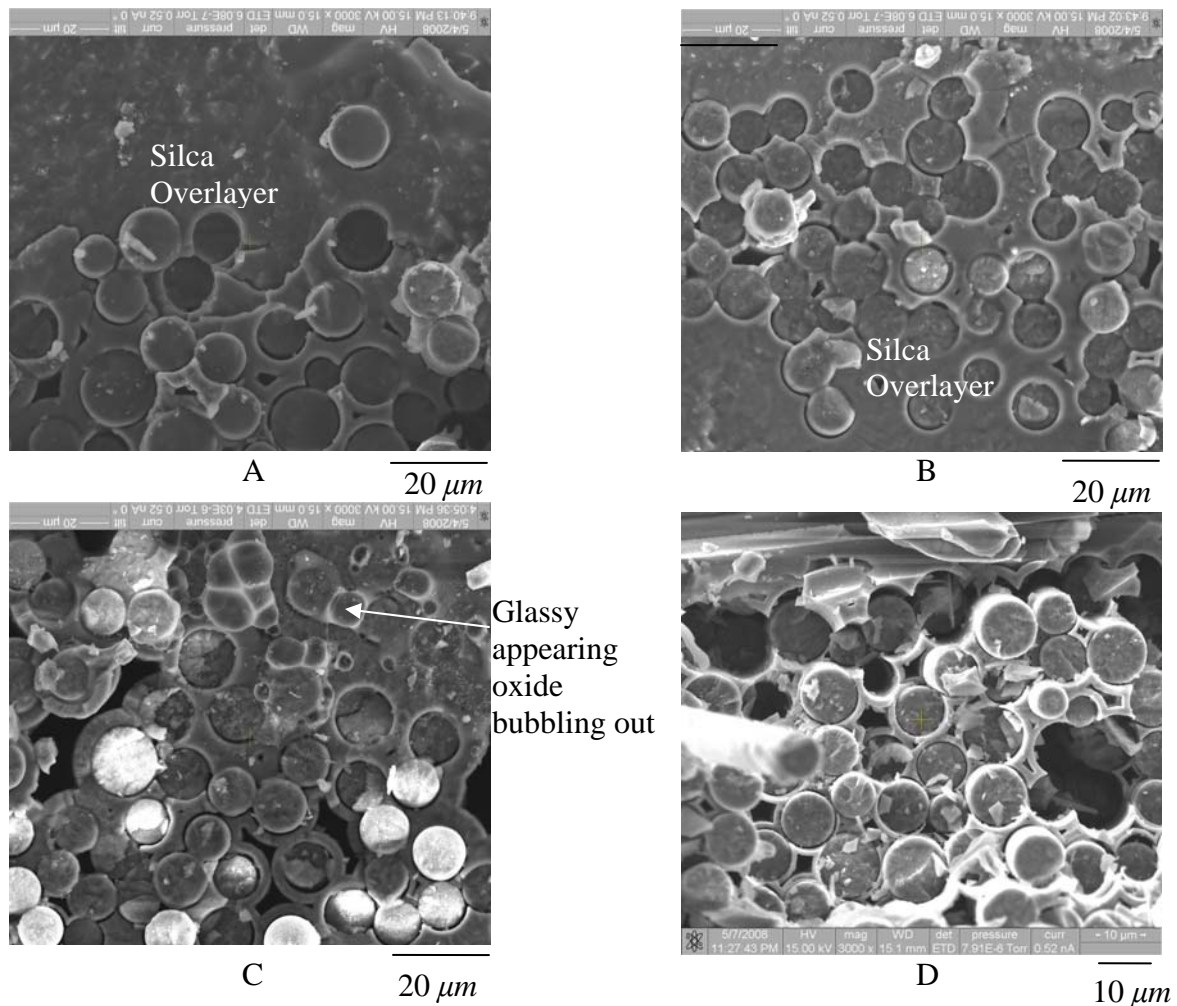
Figure 39: Microstructure of specimen fatigued at 112 % of *PL*: A, B and C are from the oxidized, and D is from the non-embrittled region. Their specific locations are pointed out on the fracture surface as denoted on Figure 37

Commonly on the two surfaces, the oxidized region featured the hardened interphase due to oxidation and the patch of oxide overlayers on the fracture surfaces shown in Figure 39A and B as well as Figure 40E. Both surfaces exhibited the glassy appearing oxides predominantly near the area of direct exposure to hot combustion flame. The glassy appearing features depicted in Figure 39C and Figure 40F appear to have bubbled out from the BN interphase and contains silicon and oxygen according to the EDS analysis. The formation of such glassy features and bubbles was documented in other studies on the oxidation of SiC [91,114] and was found to be more prevalent

with increased water vapor content [91]. Fiber pull-outs were observed in the non-embrittled region, as shown in Figure 39D and Figure 40G.
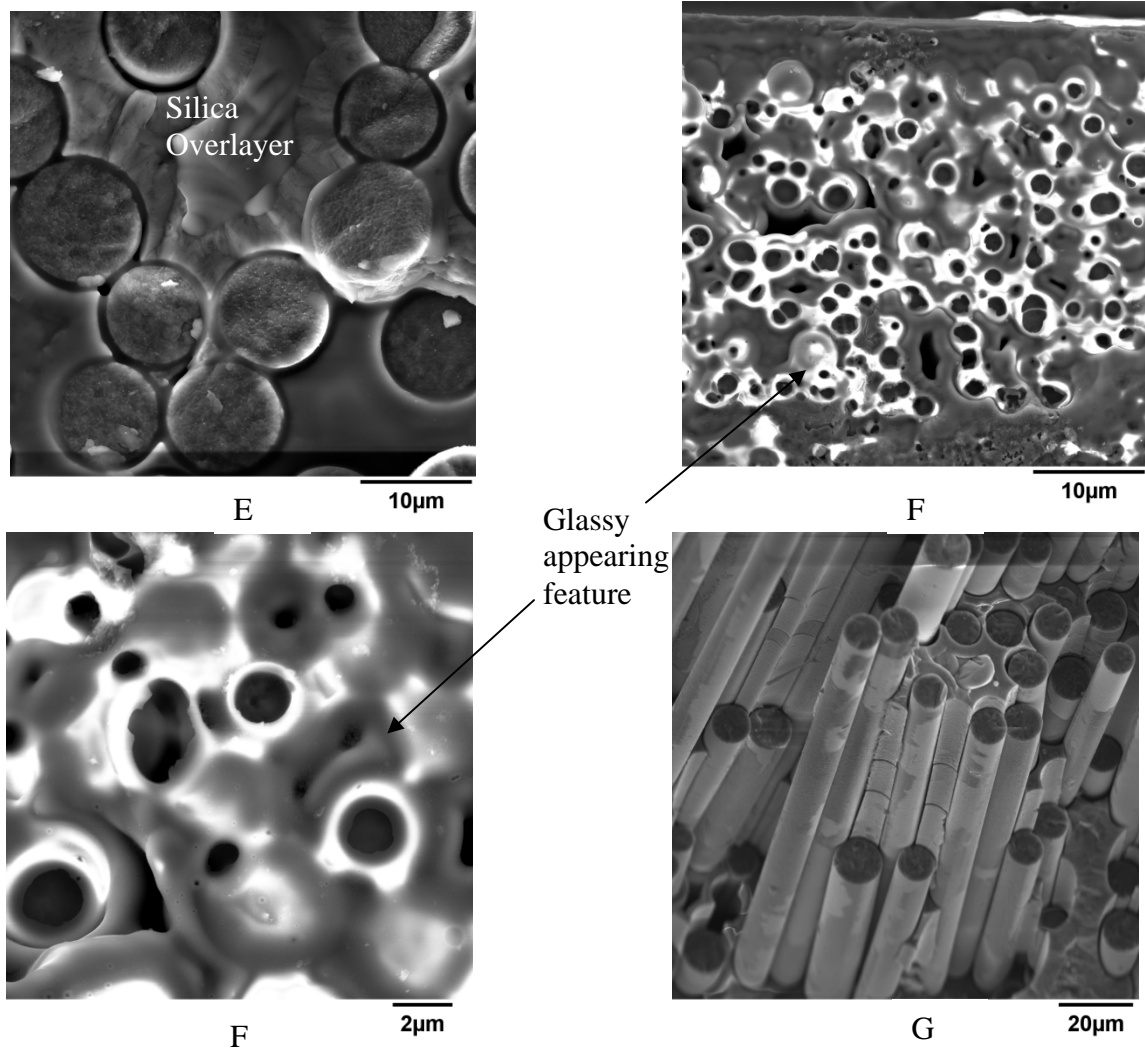
Figure 40: Microstructure of specimen fatigued at 75 % of *PL:* E and F are from the oxidized, and G is from the non-embrittled region on the fracture surface in Figure 37

4.2.3.2 Oxidation of runout specimen

When a woven MI Syl-*iBN*/BN/SiC specimen was loaded cyclically with the peak stress of 110 MPa, which equals to 66 ± 3 % of *PL*, the specimen survived over 90,000 or 25 hour test duration without fracture. The decrease in applied peak stress from 75 ± 3 % to 66 ± 3 % of *PL* resulted in the increase in cycles from 17,384 to above 90,000. Thus, it can be stated within the

tolerance associated with the typical scatter in data that 66 ± 3 % of *PL* is, for the specimen tested in the applied test condition, below the stress level which the specimen accumulated enough degradation to cause failure during the 90,000 test cycles.

4.2.3.2.1 Fracture surface of runout specimen

The fracture cross-section obtained from the residual strength test was at 19 *mm* above the geometric center of the specimen. The surface temperature at the cross-section of this fracture during the combustion test was measured to be $1088 \pm 38^{o}C$, $920 \pm 50^{o}C$ on the side surface, and $800 \pm 10^{o}C$ on the front, side and back surfaces, respectively. The failure occurring outside the heated zone suggests that oxidative degradation may have been facilitated in a lower temperature regime. Figure 41 depicts this fracture surface. The planar fracture surface consisting of fibers with the interphase that appeared to have reacted to join neighboring fibers through solidification was observed on the corners and along the side edges, as shown in Figure 41C. The recession of the BN interphase is also apparent in other location of the oxidized area (Figure 41A). The silica overlayer formed on the surface as a result of the oxidation, shown in Figure 41A & B, observed in the area enclosed by the dotted line in the image showing the overall fracture surface. Finally, Figure 41D depicts the inner core of the material, in which the fiber pull-out was observed. The pullout length was relatively short.
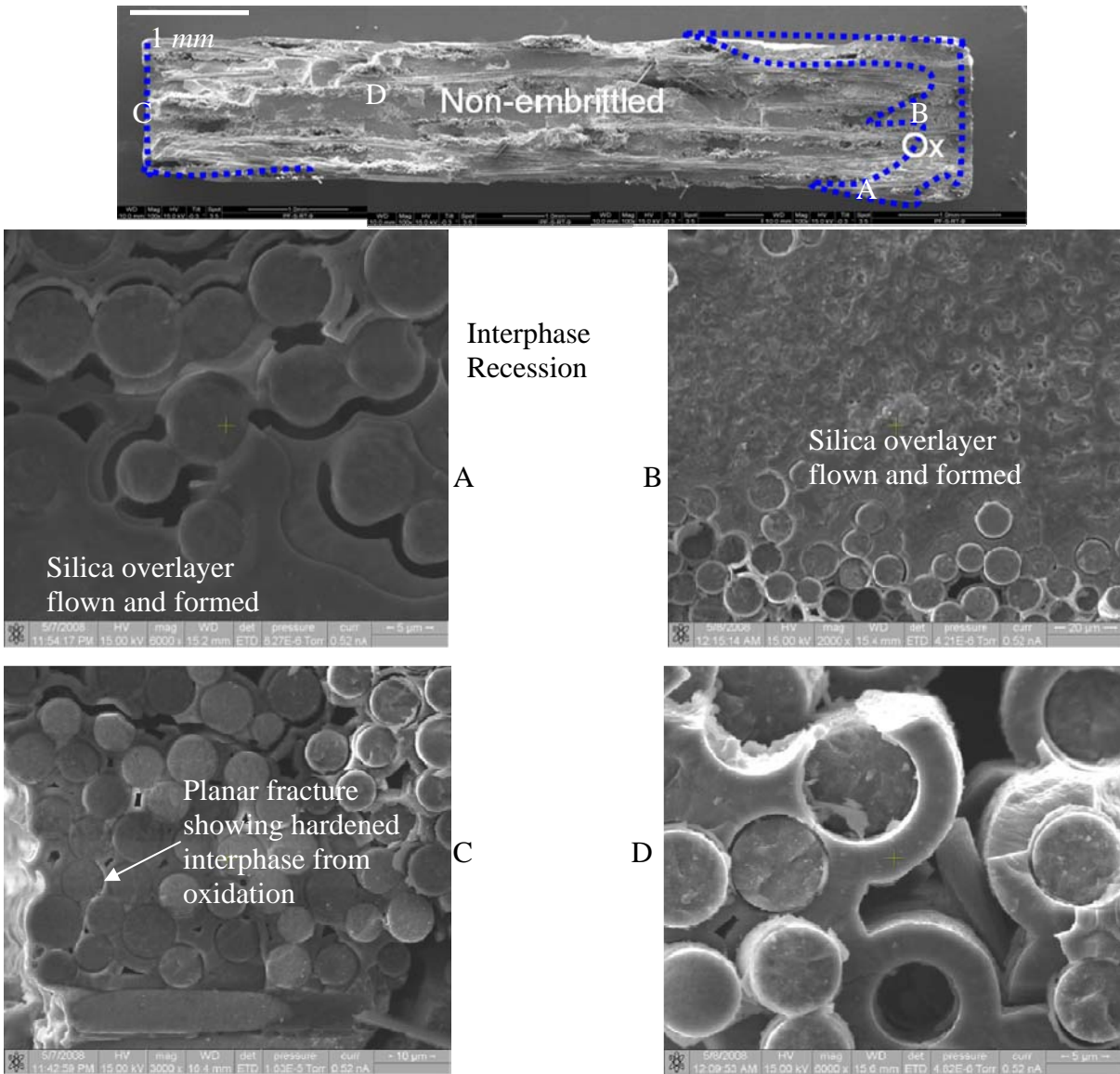
Figure 41: Microstructure of runout woven MI Syl-*iBN*/BN/SiC specimen after residual strength test

4.2.3.2.2 Sectioned surface of runout specimen

4.2.3.2.2.1 Sectioned perpendicular to the loading direction
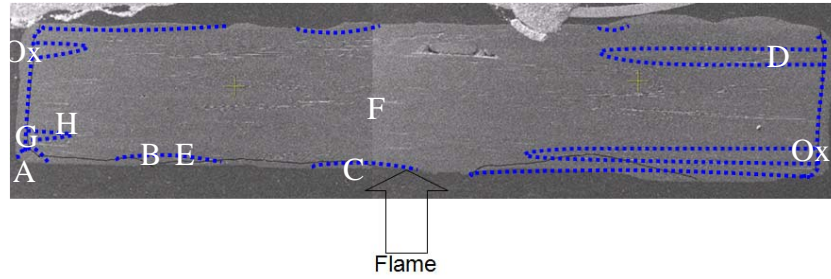
Figure 42: Polished section in the heated zone of runout woven MI Syl-*iBN*/BN/SiC

The runout specimen was tested for residual strength, from which 279 MPa was obtained with fracture at approximately 19 ± 3 *mm* from the center of the specimen. Because the fracture occurred outside the heated zone, unlike all the other test specimens that failed during fatigue testing in combustion, it was necessary to section through the center of the specimen to access and compare the oxidation damage accumulated in the heated zone. Figure 42 represents a section cut from the zone inside the gauge section of the specimen that survived the 25-hour long test under the fatigue cycles at 1 *Hz* and $R = 0.05$. Also shown on the figure is the arrow representing the direction of combustion flame. All the images and illustrations shown from this point on are represented in the orientation shown in Figure 42, unless noted otherwise.

With detailed inspection of the entire sectioned surface for oxidation using SEM and EDS, the region that appeared oxidized was identified and separated from the non-embrittled region by the dotted lines, similarly as done on fracture surfaces earlier. The amount of oxygen content detected decreased with the distance from the surface of the side edge. Also, it was observed that the extent of the oxidation was greater on the 90° tows. Edge oxidation on 0° tows extended up to 100 *μm* from the edge, while the oxidation penetrated up to the depth of approximately 2700 *μm* along the 90° tows. This is believed to be due in part by the oxidation taking place through the trapped voids. Deeper penetration by oxidation along the 90° tows are also due to their low relatively lower mechanical properties including low proportional limit compared to the 0° ply.

A closer look at the oxidized area under the SEM revealed that the oxidation occurred through cracks found in a ply, as seen in Figure 43A, C and E. The cracking that preferentially develops in the plane of a ply is described as ply-splitting [40]. The oxidation also appeared to have taken place diffusively through the BN interphase and trapped voids, as commonly seen on corners and edges. Other features found from the section include the cracking and oxidation captured on Figure 43A and B, and microcracking in the area of high stress concentration in the CVI matrix, as in Figure 43A. Some partial cracks found in the CVI matrix extended to the specimen surface, and some cracks linked paths between load carrying fiber tows and adjacent 90° tows, as seen in Figure 43D. These cracks may have been originated under fatigue due to interfacial shear stress at the location with high stress concentration factor. Voids, flaws and impurities in the MI and CVI matrix with high geometrical irregularities along with the specimen surface especially with high asperities along the machined side surfaces exposing fibers may potentially serve as the initiation sites for these cracks under the mechanical fatigue loading and also from the thermal stress due to elevated temperature. For the non-embrittled regions, Figure 43F, taken from the inner part of the specimen showing oxidation, and it appears pristine.

Some cracks were observed to have partially grown along the plane of 0° tows. Traces of fractured or degraded CVI SiC matrix and debonded interphase are found in the path of these cracks. Many of such cracks were found on the 0° tows near the flame-impinged surface and there was a significantly smaller number of cracks found on 0° tows next near the opposite surface. The cracks were filled with oxides in some cases (Figure 43C & E). Many CVI SiC matrix cracks were found near the primary crack path, as seen in Figure 43A. The number of the fractures in the CVI SiC matrix was greater in the first two plies from the flame-impinged surface, compared to the rest of the cross-sectional area.

Another micrographic feature potentially associated with the degradation of material is the pores in the MI matrix as shown in Figure 43G and H. Imperfect infiltration of molten Si leaves some parts of the MI matrix unfilled, causing process-induced porosity. However, these pores observed here from the runout specimen showed apparent gradient in their distribution with respect to the distance from the flame impinged surface. Higher occurrence of the observed pores was detected from the plies close to the front surface. In addition, these observed pores showed boron, silicon and carbon contents according to the EDS analysis of the pore depicted by a white arrow shown in Figure 43G. Oxygen was also present, suggesting that the pores may have either been a byproduct of oxidative reactions or served as a diffusion path for permeating oxidants. For these reasons, the observed pores appeared to be induced by the applied test conditions and are referred to as "post-test observed pores." Pores, regardless of their origins, introduce deleterious effects to the mechanical properties of a specimen. First, they facilitate the ingress of oxidants, making the material susceptible to oxidation. Secondly, they often have geometry with sharp apex, from which cracks initiated and branch out. Thirdly, they reduce the mechanical properties such as the modulus of elasticity (E) and fracture toughness.
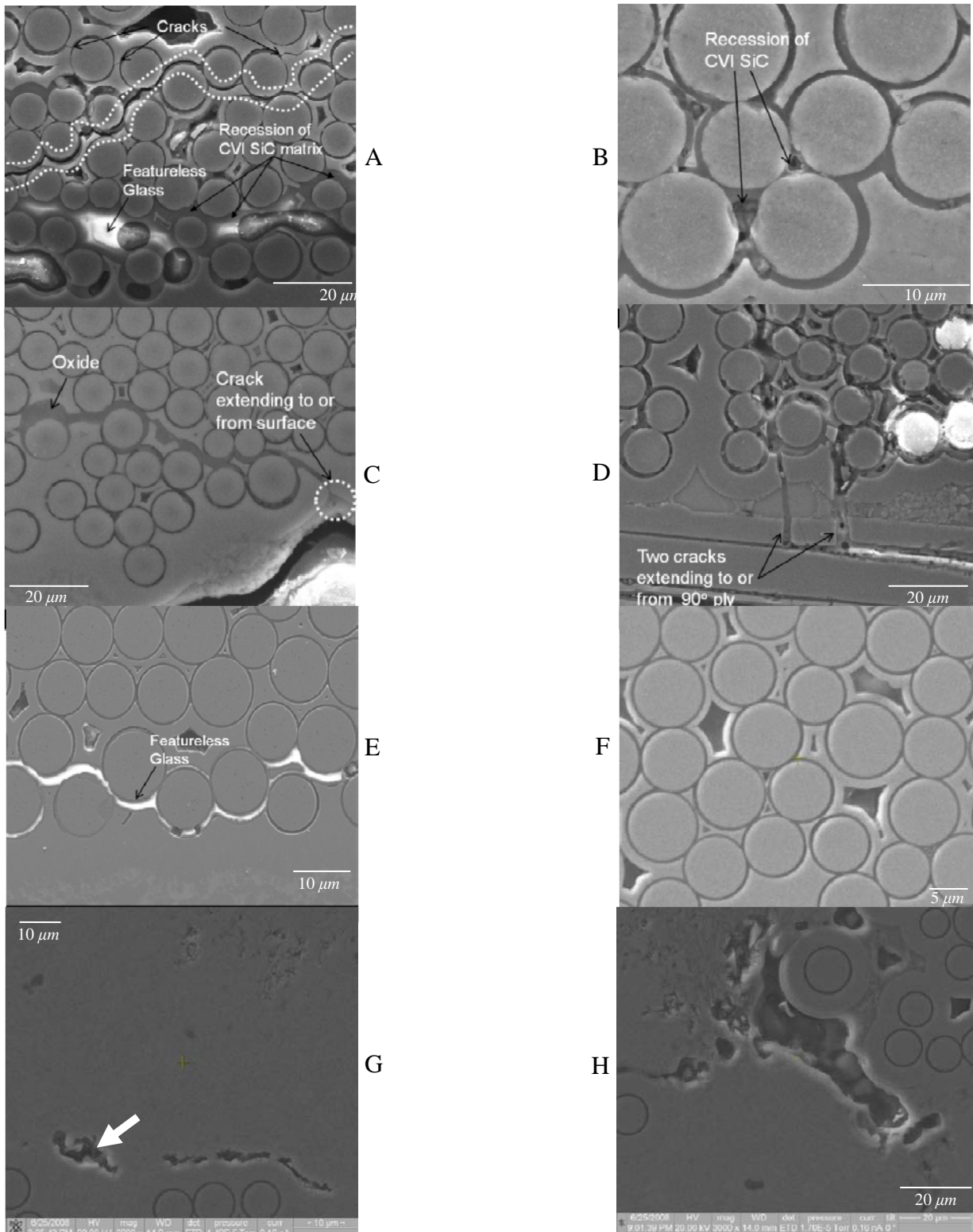
Figure 43: Microstructure of sectioned woven MI Syl-*iBN*/BN/SiC of runout specimen in the heated zone: A through H are from the oxidized and non-embrittled regions of the fracture surface as denoted on Figure 42
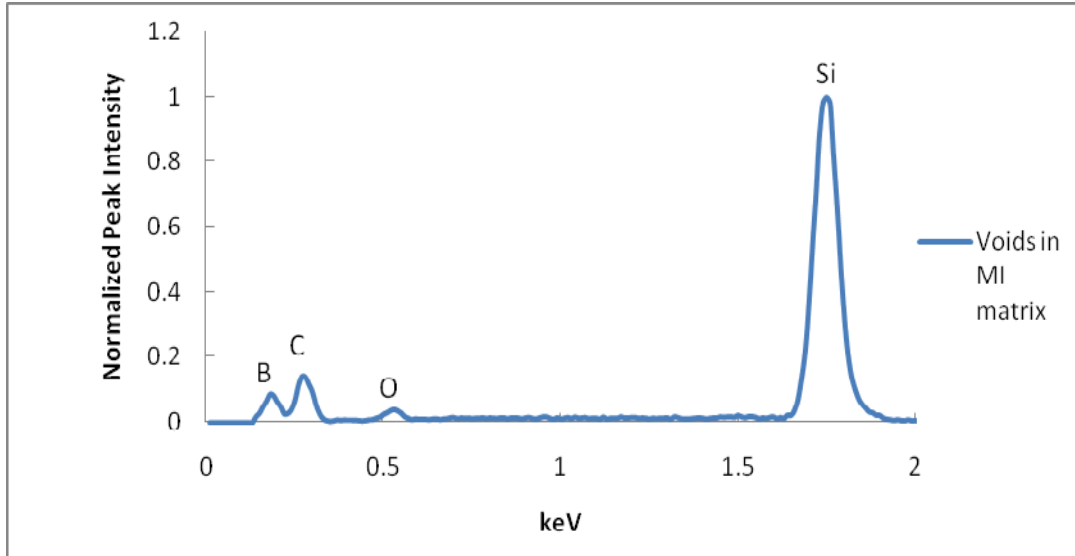
Figure 44: EDS analysis of the void in Figure 43G

4.2.3.2.2.2 Sectioned parallel to loading

The macroscopic and microscopic findings learned from the cross-section cut in the perpendicular direction to the loading axis can be reinforced and enhanced by adding another dimension to the analysis. To do this, the runout woven MI Syl-*iBN*/BN/SiC specimen was sectioned along the loading axis, which is the perpendicular to the polished surface analyzed in the preceding section. A segment including the heated front surface of the specimen sliced along the longitudinal direction into 4 pieces of 2.0 *mm*, producing four sections with the cross-sectional dimension of 2.0 *mm* by 1.6 *mm*. These four sections were polished and analyzed using the optical microscopy and the SEM for crack distribution and oxidation across the dimensions.

An optical image of one of the sections is represented in Figure 45. Cracks in both loading and thru-thickness directions were counted separately on the entire sectioned surfaces including the one shown in Figure 45, and the results are listed on Table 13. In this documentation, the longitudinal direction refers to the direction of axial loading, in which the fatigue loading was

carried out, and the transverse direction is perpendicular to the longitudinal along the axis along the specimen thickness.

A

B
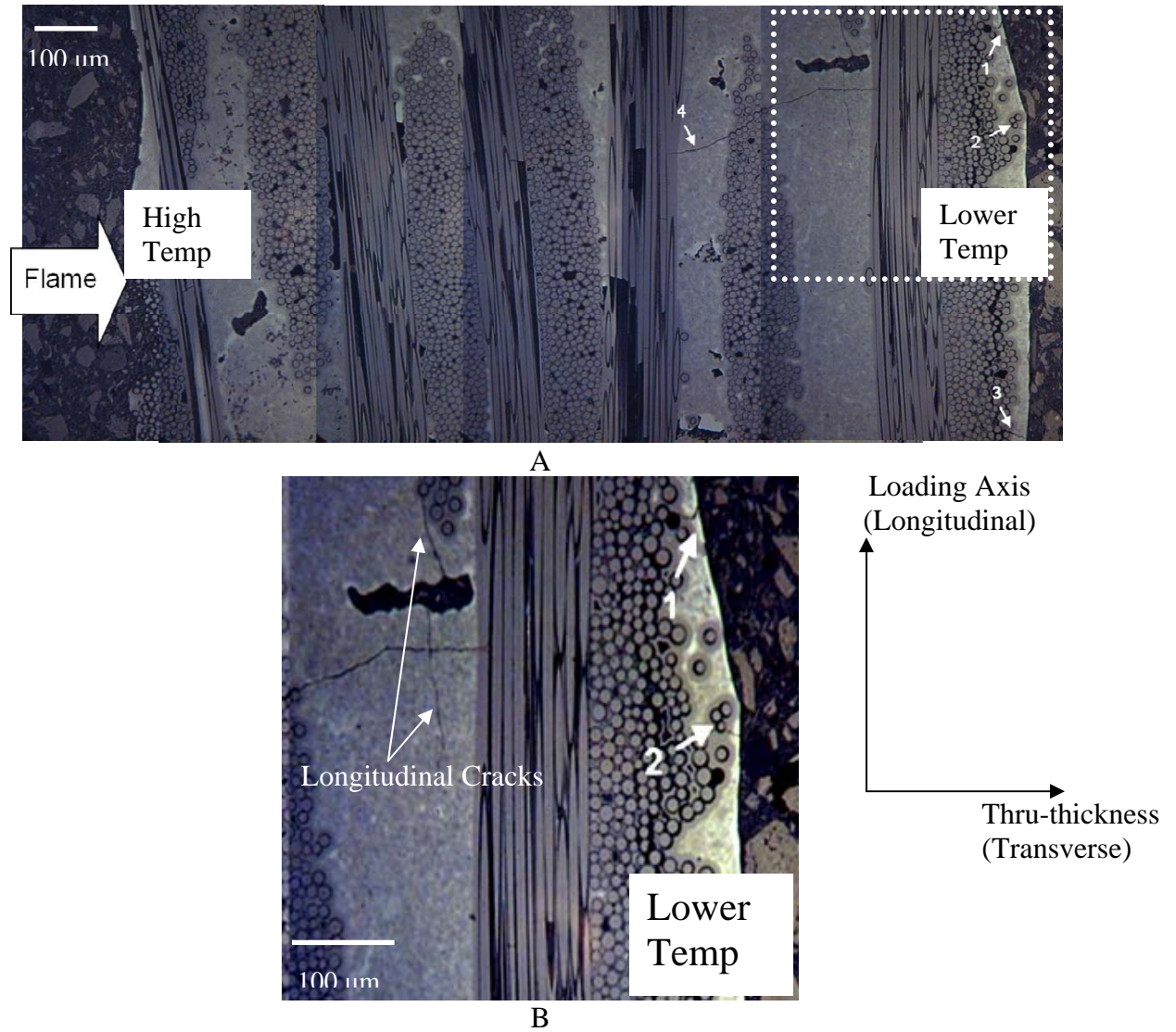
Figure 45: (A) Representative area on one of the four polished surfaces sectioned in parallel to the loading direction: (B) Close up view of the square zone enclosed in dotted line in (A)

Table 13: Crack Distribution across the thickness of the runout MI woven Syl-*iBN*/BN/SiC

Plies	# of Transverse Cracks	# of Longitudinal Cracks
1 and 2	15	1
3 and 4	10	3
5 and 6	48	8

It is evident from both Figure 45 and Table 13 that crack distribution is non-uniform such that majority of the cracks are found in the MI matrix of the 5th and 6th plies, which are the two plies next to the unheated back surface. Two longitudinal and four transverse cracks were found in the 5th and 6th plies, as illustrated in Figure 45. The apparent gradient nature of crack distribution applies to both transverse and longitudinal cracks for this material. Many of the longitudinal cracks appeared to have originated from the voids in the MI matrix, such as the two cracks aligned in the longitudinal directions in Figure 45.

The sectioned surfaces were also studied for oxidation. Because the 8.0-mm wide specimen was sliced into four segments of equal length (i.e. 2.0 *mm*), comparing the oxidation from one section to the next provides the insights into the depth by which the edge-on oxidation penetrates along the 90° ply. SEM pictures were taken from the inside of the heated zone on three different depths from the side surface, exposed directly to the combustion environment. On the surface level, the BN interphase appeared to have reacted away and was replaced by the voids and oxides, as shown in Figure 46A. From this figure, the MI matrix appeared to be more porous, as illustrated by rough morphology of the matrix surface. Oxides also formed on the combustion exposed CVI SiC matrix, especially around the surface of the process-induced voids enclosed by CVI matrix or trapped voids. Similar oxidative features were observed from the next picture that showed the micrograph at the depth of 2.0 *mm* from the side surface, shown in Figure 46B. Interphase oxidation was not as prevalent as in the surface directly exposed to the combustion. Still, many of the trapped voids showed oxide layers formed on their surfaces. The micrograph at the depth of 4.0 *mm* is shown in Figure 46C. Assuming a geometric symmetry of the specimen, this is the midpoint of a specimen width that is the farthest from the combustion-exposed side surface. The oxidation on the surface of trapped voids, though less common, was still observed.

From this, it can be stated that the effect of oxidation along the 90° ply became less with increasing distance from the side surface of direct combustion exposure. As most of the voids have finite depths, the oxidation occurring through them becomes less significant with depth, as evident from the micrographic comparisons at three different depths shown in Figure 46. However, fatigue loading, along with thermal stress, can induce damage in the CVI SiC matrix that can lead to its fracture or the recession of matrix by oxidation, facilitating a deeper ingress of oxidants into the specimen interior. Also, cracks in the MI matrix along the thru-thickness as well as loading directions can be linked by an edge crack that introduces the oxidizing combustion environment into a deeper interior.

Process-induced voids in the MI matrix found on the sections were sizeable with some approaching 400 microns in length, as depicted in Figure 47A. These voids were usually found near outer surface of fiber bundles, where relatively higher concentration of Si impurity was detected from the EDS analysis. This is also the region that the wettability of melt-infiltrated Si can be an issue due to its geometry surrounding fiber tows. The sharp wedged voids shown in Figure 47B makes it difficult to wet slurry particles thoroughly. They are also found commonly near the cross-ply.
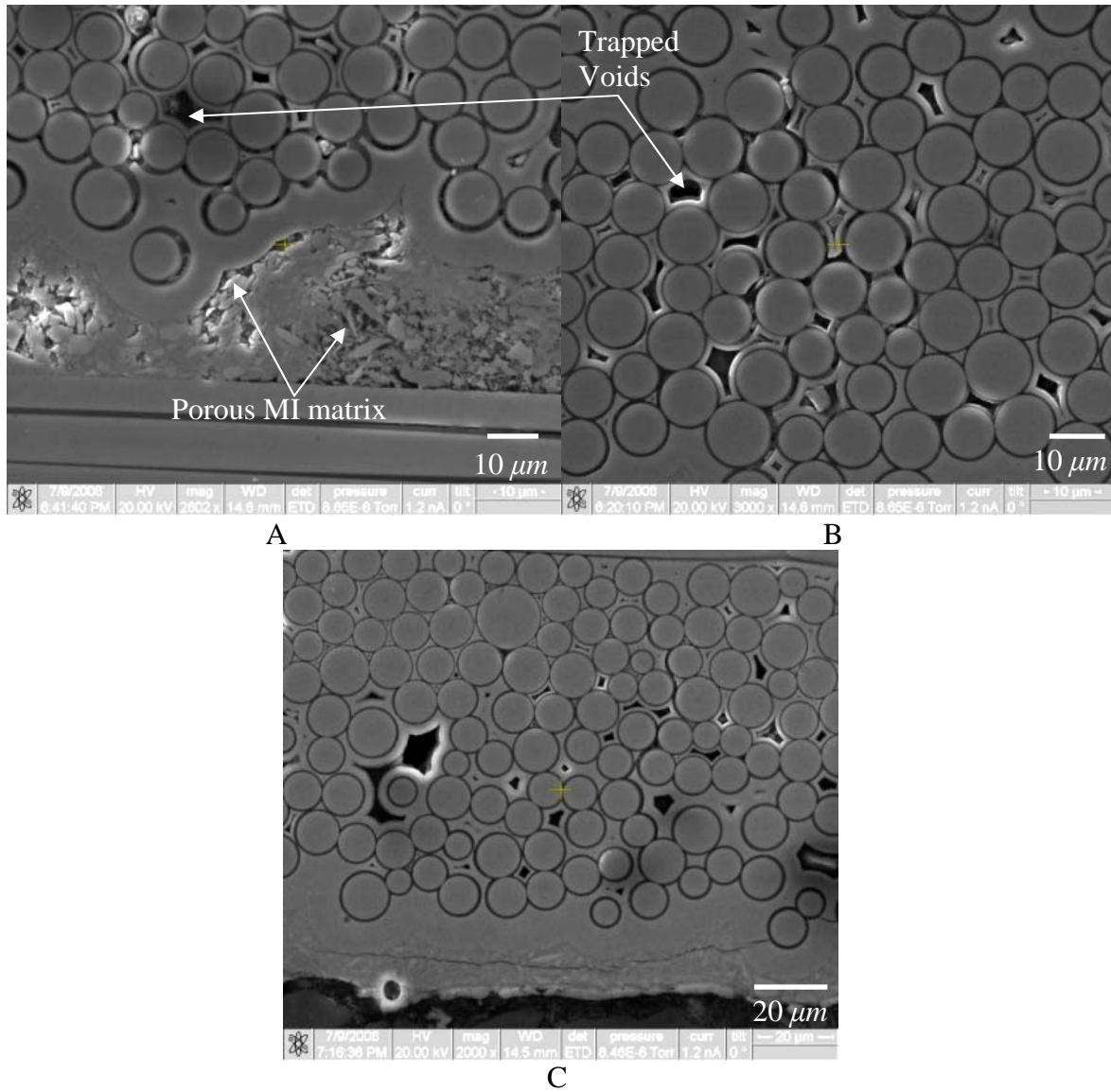
Figure 46: 90° ply at different depths: (A) surface level, (B) 2.0 mm deep and (C) 4.0 mm deep

These voids could serve as the crack initiation sites, as suggested by the two longitudinal cracks that appeared to have originated from a small process-induced void depicted in Figure 45. Large voids with high geometric asperities that reduce the overall load bearing capability of the specimen by increasing the stress intensity level in the adjacent area such that cracks are more likely to nucleate and propagate at an increased rate, thus shortening the number of cycles to reach failure. Cracks nucleated elsewhere that found their paths along such voids can change the

direction of propagation and sometimes branch out into multiple new cracks [115]. With silicon and silicon carbide as well as other impurities such as *Fe* and *B* in physical and chemical contacts, thermal stress may arise from phase transformation of these impurities as well as *Si* in the matrix during heat treatment either during processing or during testing. Similarly, void nucleation may also arise from the phase transformation that may involve volume loss. Residual stress or voids that may result from matrix phase transformations could take part in initiating a new crack or accelerating an existing one under the applied fatigue loading.

A   B
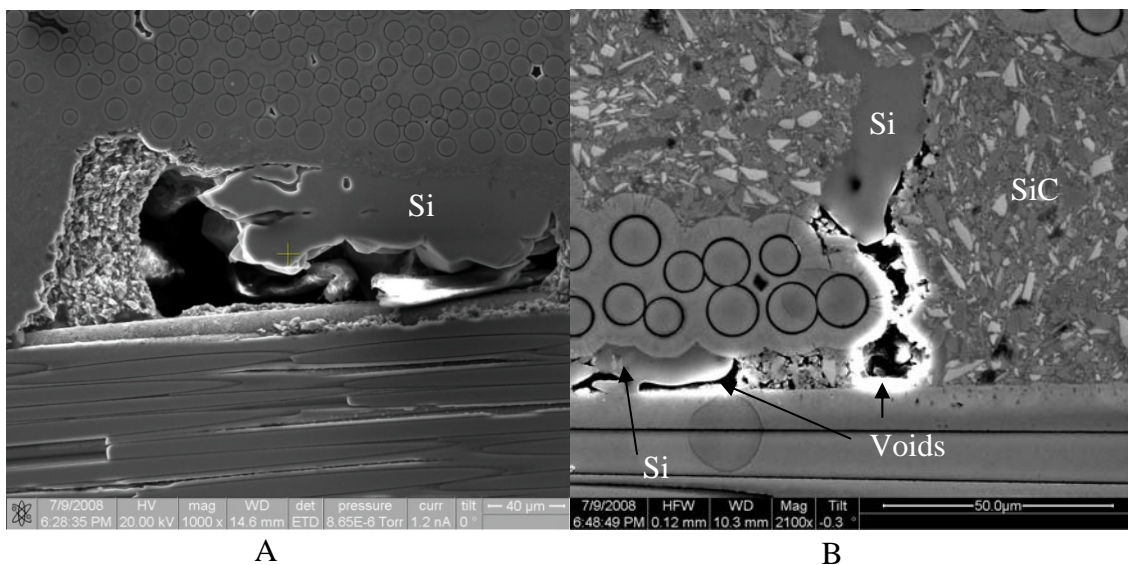
Figure 47: Voids observed from two different angles; (A) on a plane parallel to the loading direction and (B) on a plane perpendicular direction

Some void surfaces contained oxygen, as confirmed by the analysis using EDS. In the presence of oxygen and moisture, stress corrosion reactions can promote the crack growth in the silica formed on the surface of voids. Sub-cracks that form in the brittle oxide could then be linked to the underlying *SiC* or *Si* matrix and, under load, grow into a larger crack that propagates into the bulk material. Such cracks, if open to environment, make the crack paths exposed to oxidation and could lead to environmental degradation of load-bearing fibers in the paths.

On the pristine woven MI Syl-*iBN*/BN/SiC, the unheated back surface was found to have been coated with an extra silicon layer of the thickness as large as 100 *μm*, as shown in Figure 48A. This silicon coating, however, was found to be separated from the underlying MI matrix on the sectioned surface of the runout sample, as shown in Figure 48. Filling the room created by the separation of the two phases were oxides and voids.
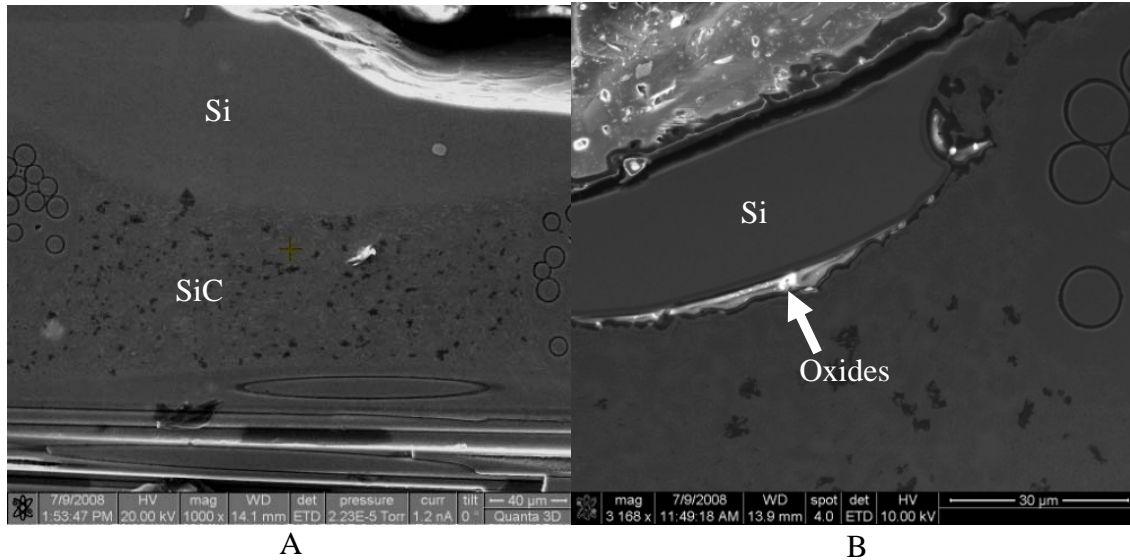
Figure 48: Separation of Si coating and subsequent oxidation: (A) Si coating coated on SiC matrix in pristine sample and (B) the Si coating found separated in the runout sample

4.2.4 Section Summary

In summary, the S-N data and microscopic observations presented in this section provided the qualitative assessment on the effects of the combustion environment on the fatigue life of the woven MI Syl-iBN/BN/SiC CMC. Further, it was obvious from the comparisons of the oxidized regions on fracture surfaces obtained from the tests performed under different peak stresses that the extent of oxidation was larger with the time of combustion exposure and the cycles-to-failure. At a higher peak stress, the time and cycles-to-failure was shorter, and the smaller was the fraction of the fracture surface oxidized before failure. Thus, the extent of oxidation was observed to be lower at a higher applied peak stress. The residual strength test of the specimen that

survived the test duration with the applied peak stress of 110 MPa or 66 ± 3 % of the *PL* resulted

in failure at 19 ± 3 *mm* from the center of the specimen was 279 MPa or 65 ± 4 % of the *UTS* with

39 ± 3 % reduced strain of 0.3534% compared to a pristine specimen. The change in *PL* is within

the scatter band of the room temperature *PL* data, so it is considered unchanged. The residual

modulus of elasticity of 189 GPa was off by two standard deviations from the average modulus of

the pristine samples of the woven MI Syl-*iBN*/BN/SiC. However, the difference could not be

assessed for any material phenomenon based on one data.

4.3 Woven MI Syl/BN/SiC

The same combustion environment as that applied to the woven MI Syl-*iBN*/BN/SiC

specimen was subjected to the woven MI Syl/BN/SiC, which was simultaneously loaded in

fatigue with a peak stress that was varied between each test. As compared to the test condition

applied to the woven MI Syl-*iBN*/BN/SiC, other fatigue parameters stay constant including the

frequency and R-ratio of 1*Hz* and 0.05, respectively. The intent behind applying the same

combustion environment was to facilitate comparisons among different CMC materials. The peak

stress was changed between each test such that an array of fatigue data was obtained with respect

to cycles-to-failure that spans from a very short duration to the runout condition of 90,000 cycles

at the end of 25 hours of applying the fatigue loading in the prescribed combustion environment.

4.3.1 S-N Data

Table 14 shows the data obtained from these tests, based on which the S-N curve was

plotted, as shown in Figure 49. From Table 14 and Figure 49, it can be learned that the applied

peak stress is inversely related to cycles-to-failure. All fractures occurred within ± 3 *mm* from the

geometric center of specimen, where the highest temperature with the largest thru-thickness

gradient was observed. A runout was obtained from the specimen that survived under the peak stress of 81 MPa, equivalent to 53 ± 3 % of the room temperature *PL* and 30 ± 4 % of the room temperature *UTS* of 271 ± 29 MPa.

Table 14: Combustion Test Data for MI woven Syl/BN/SiC

ID #	Peak Stress (*MPa*)	Peak Stress (*%UTS*)	Peak Stress (*%PL)*	Number of Cycles	Fracture location (from center in *mm*)	Temperature at Fracture (°C)		
						Front	Side	Back
02-240	172	63 ± 8	112 ± 7	1979	0 ± 3	1077±44	N/A	N/A
02-239	162	60 ± 7	106 ± 6	2655	0 ± 3	1227±47	N/A	N/A
02-242	124	46 ± 5	81 ± 5	3146	0 ± 3	1235±25	970±50	925±10
02-243	117	43 ± 5	76 ± 5	8059	0 ± 3	1240±25	950±50	N/A
02-238	81	30 ± 4	53 ± 3	90501	No Fracture	1090±30	950±50	830±10

In Table 14, all test specimens showed similar front surface temperatures in the heated zone, except the one fatigued at the peak stress of 172 MPa. This was one of the first specimens to be tested among all specimens of four CMCs. For this specimen, the fatigue loading was applied before the surface reached the target temperature, in anticipation of a quick ramp-up of the temperature. It was learned from this test that it took longer to ramp up the temperature with the heat flux that corresponded to the prescribed combustion condition. For the rest of the specimens, fatigue loading began after the surface reached at the target temperature.

The *PL* of this CMC at room temperature is 153 MPa, 57 ± 10 % of the room temperature *UTS*. The peak stress of 81 MPa, with which a runout was attained, is 53 ± 3 % of the *PL*, well below the knee of the stress-versus-strain curve. A specimen under the stress level significantly below the *PL* has been thought not to nucleate high enough level of microcracking to trigger a crack growth to failure. The observed failure of the CMC with peak stress of 76 ± 5 % of *PL* after

8,059 cycles is again consistent with the idea that the thermal gradient stress adds to the mechanically applied stress, which elevates the stress state to the level beyond the proportional limit.
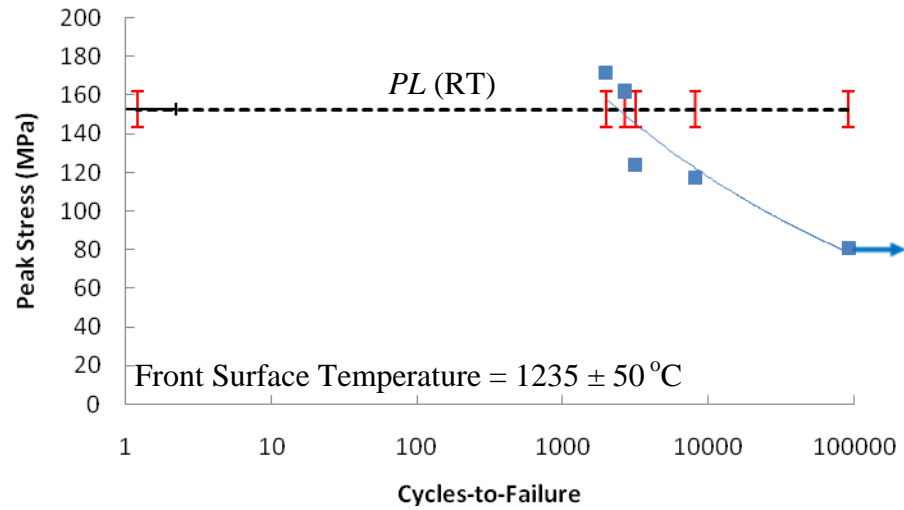
A
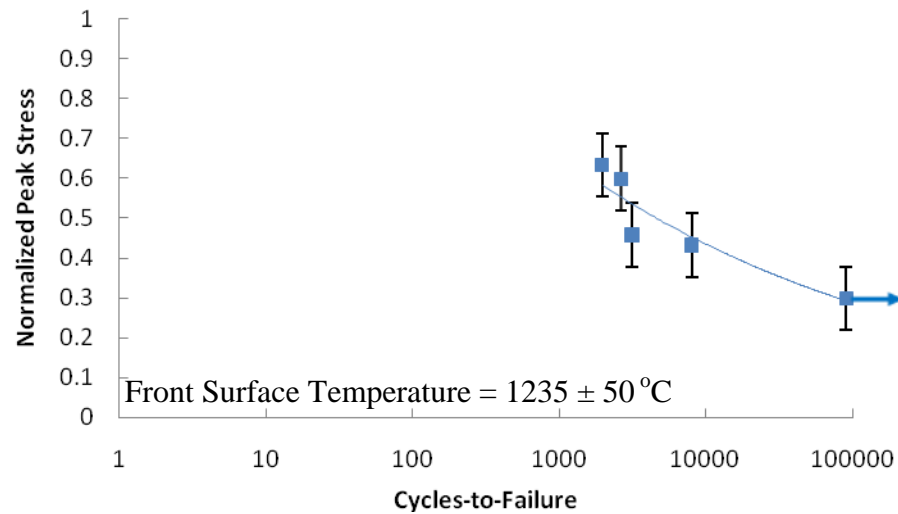
B

Figure 49: S-N represented for woven MI Syl/BN/SiC with peak stress; (A) in MPa and (B) normalized against *UTS*

4.3.2 Strength Retention

The runout specimen tested for residual strength failed at 171 MPa, which is equivalent to 63 ± 8 % of the room temperature *UTS* of a pristine woven MI Syl/BN/SiC tested under monotonic tension at room temperature, as shown in Figure 50.

A

B
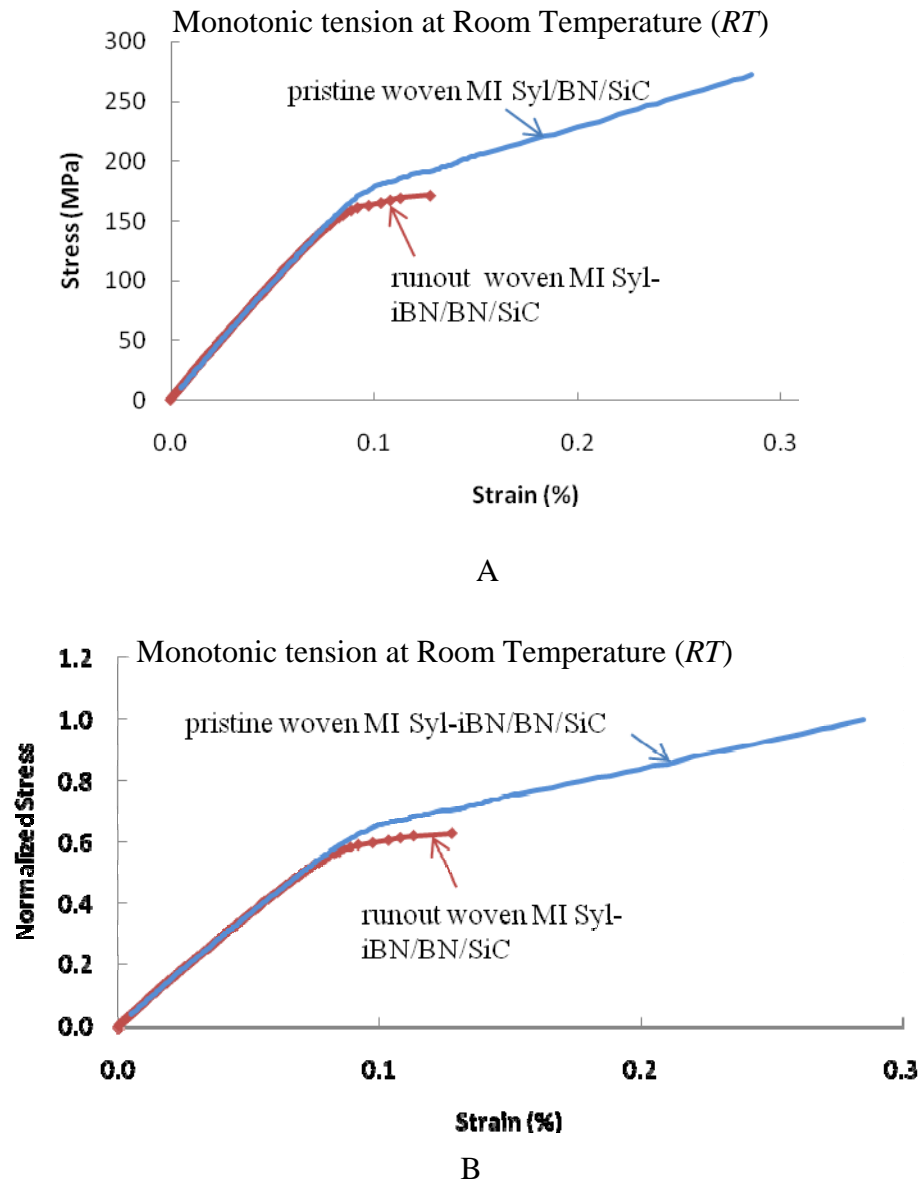
Figure 50: Stress-strain curves of the runout and pristine MI woven Syl/BN/SiC tested under monotonic tension; stress shown (A) in MPa and (B) normalized against *UTS*

From Figure 50, the two curves nearly coincide until the curve representing strength retention behavior of the runout specimen started deviating. Thus, the moduli of elasticity of the two curves was nearly identical, implying that there was no change in stiffness caused by the combined combustion and mechanical fatigue loadings for 25 hours. The proportional limit of the runout specimen was 147 MPa, within the scatter of the 153 ± 9 MPa of the pristine material. The secondary portions of the two curves show much different behaviors, however, as in the woven MI Syl-*iBN*/BN/SiC, the runout material experiences a larger reduction in the strain at failure; the runout woven MI Syl/BN/SiC specimen tested for residual strength failed at 0.1274, 45 ± 7 % of the failure strain experienced by the pristine material. This makes it clear that the specimen experienced permanent degradation, even if it survived the test without failure.

4.3.3 Microscopic Analysis

Using the same microscopic tools and protocols described for the analysis of the woven MI Syl-*iBN*/BN/SiC, the microscopic analysis was performed on fracture and sectioned surfaces from all the woven MI Syl/BN/SiC specimens tested. The analysis presented here leads to an increased understanding of the degradation phenomena of this material involving oxidation under the applied condition.

4.3.3.1 Fractographic analysis

Figure 51 shows the fracture surfaces obtained from the four fatigue tests performed at the peak stress of 112 ± 7 %, 106 ± 6 %, 81 ± 5 % and 76 ± 5 % of the room temperature *PL* of 153 ± 9 MPa (i.e. equivalent to 57 ± 10 % of the *UTS*) respectively. The first two cases involve peak stresses that exceed the *PL* and the latter two involve the peak stresses below the *PL*.
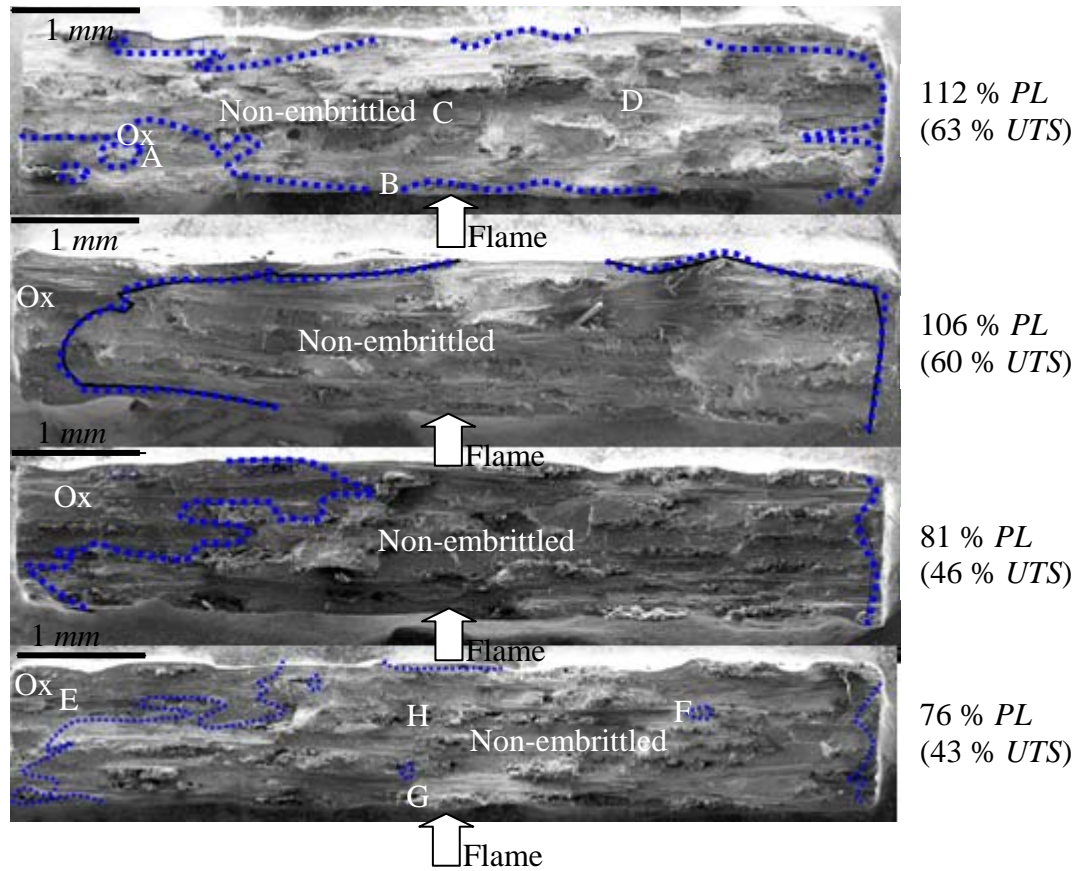
Figure 51: Fracture surfaces at peak stresses of 112 %, 106%, 81% and 76% of *PL*

Comparing between the two cases with peak stresses below the *PL*, first, the specimen fatigue loaded with peak stress that equals to 76 ± 5 % of *PL* survived 8,059 cycles, four times longer cycles-to-failure than the one loaded at 112 ± 7 % of *PL*, which survived 1,917 cycles. However, the difference in the area affected by oxidation is nearly indistinguishable between the two fracture surfaces produced with different peak stresses. For the applied peak stress that exceeds the *PL*, the other two specimens, each fatigued loaded with peak stresses equivalent to, respectively, 112 ± 7 % and 106 ± 6 % of the *PL* were subjected to increased level of matrix cracking, even without the thermal gradient stress factored into the consideration. Therefore for the two cases loaded with peak stresses exceeding the *PL*, greater surface area of the specimen interior must have been open and exposed to the combustion environment prior to its fracture than

for the two specimens loaded with peak stresses under the *PL*. This, with the understanding that interphase oxidation of BN takes place readily with exposure to oxidizing environment at elevated temperature, may explain the similar oxidized area between the two cases. This observation will be substantiated with the qualitative approach using oxidation kinetics in Chapter VI. In addition, every fracture surface commonly exhibited oxidation on edges and corners. In support of this view, the oxidized area on each fractured specimen appears to be extending from the rear left corners. This is most evident from the two surfaces with the history of fatigue loadings with peak stresses of 106 ± 6 % and 81 ± 5 % of *PL.*

Unlike the woven MI Syl-*iBN*/BN/SiC, the difference in the area of the oxidized region between fracture surfaces obtained with different peak stresses was too subtle to make any objective remark on the extent of oxidation in relation to the fatigue strength and cycles-to-failure or the time of combustion exposure. A relatively small window of fatigue life spanned by the four specimens whose fracture surfaces are shown in Figure 51 may account for the subtlety in the comparison of the size of the oxidized regions, as the oxidation develops with time.

A closer examination of each fracture surface revealed oxidative micrographic details in the oxidized regions and fiber pullouts in the non-embrittled regions, respectively. The oxidative features included the fibers with interphases solidified to the matrix and patches of oxide overlayers flown and solidified on crack surface, and they were similar in appearance, morphology and chemical contents to those observed from the woven MI Syl-*iBN*/BN/SiC. On the other hand, the microscopic feature that characterizes non-embrittled area is fiber pullouts of various lengths. The micrographs of both oxidized and non-embrittled regions presented in Figure 52 and Figure 53 were from two specimens fatigue loaded at 112% and 76% of the *PL*,

respectively. The alphabet designated for each image in the figures refers to the location on the fracture surface as indicated on Figure 51.
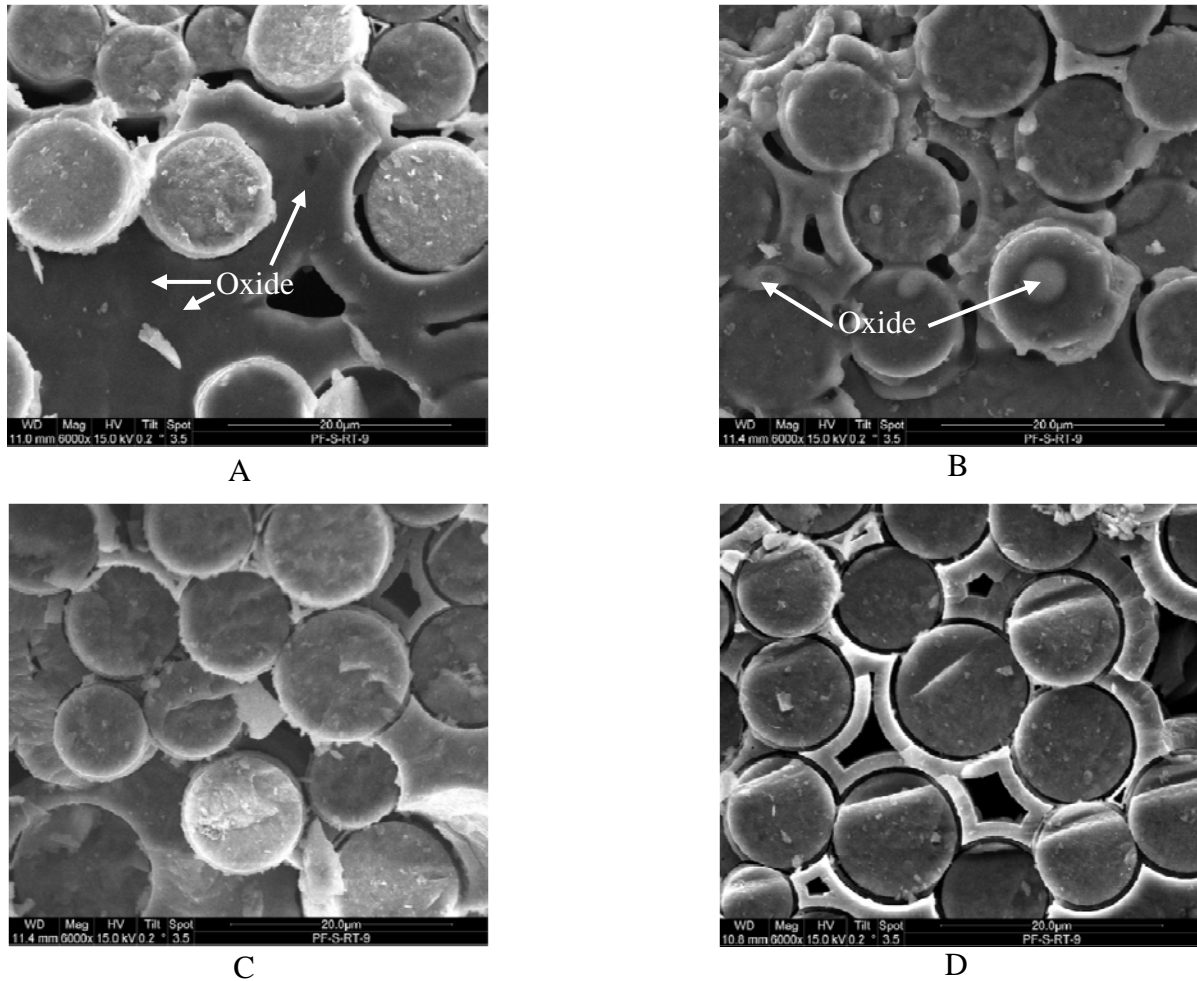
Figure 52: Microstructure of fatigued tested specimen under peak stress of 112% of *PL*: A and B are from the oxidized, C and D are from the non-embrittled regions of the fracture surface. Their specific locations are shown on Figure 51.

In the oxidized regions, fibers were observed to have adhered, through the rigid interphases or oxide overlayer, to neighboring fibers as well as matrix, as shown in Figure 52A & B and Figure 53D & E. Fiber pullouts of varying lengths were observed from the non-embrittled regions, as shown in Figure 52C & D and Figure 53H. Spherical or bubble-shaped features depicted on Figure 53G were found on the fracture surface exposed to the hot gas path during the

combustion application. The EDS analysis shown in Figure 54 revealed high silicon content. Silicon impurity with minor boron and oxygen contents are present in large quantity in the MI matrix may have melted and blown into the spherical shape due to the exposure to the local gas temperature that exceeds $1800^{o}C$.
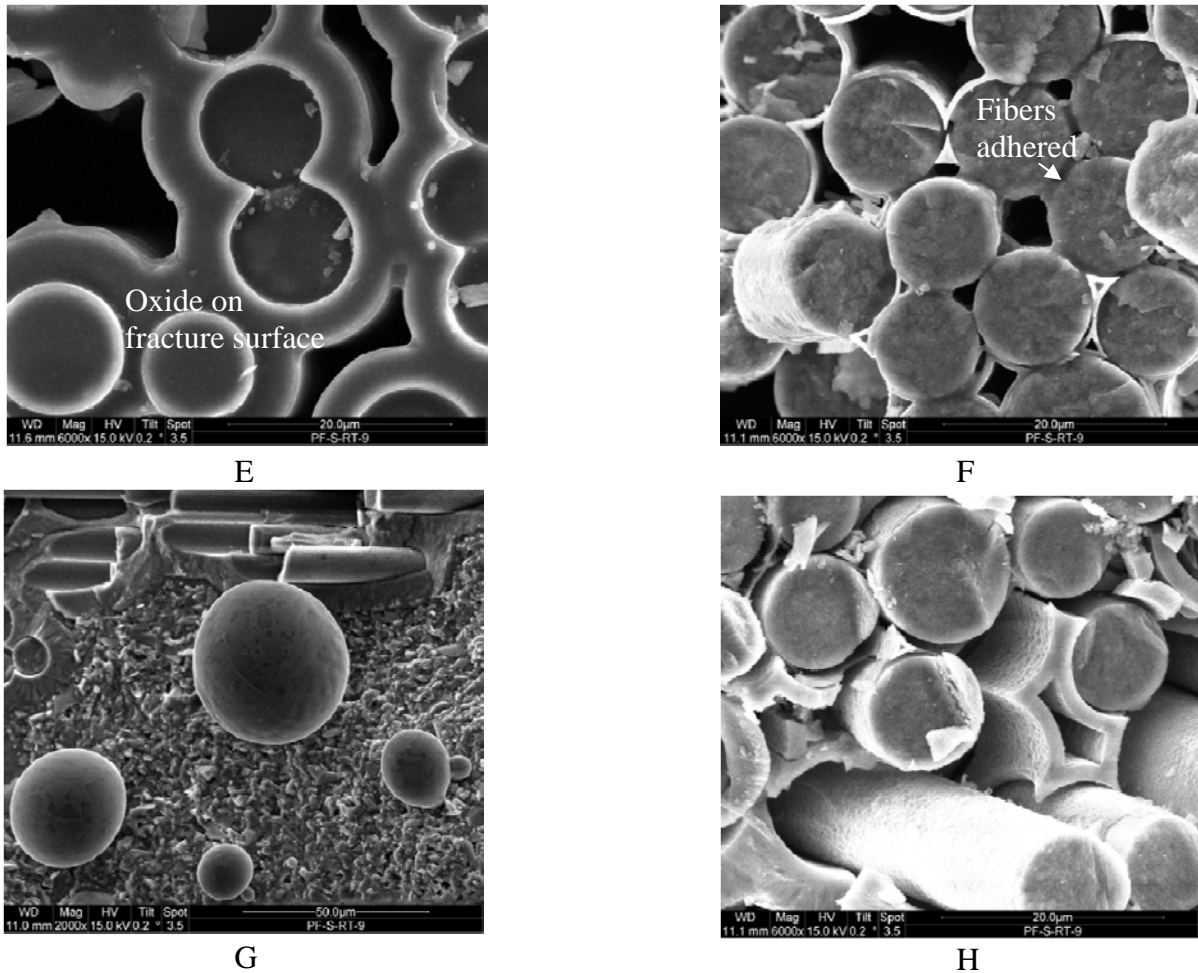
Figure 53: Microstructure of fatigued tested specimen under peak stress of 76% of *PL*: E and F are from the oxidized, G and H are from the non-embrittled regions of the fracture surface. Their specific locations are shown on Figure 51.
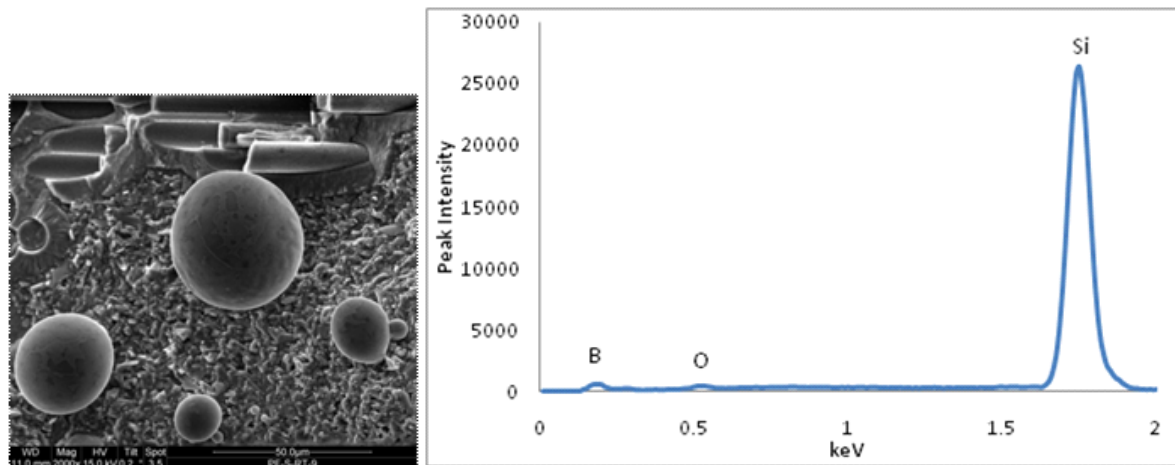
Figure 54: EDS of the spherical features found on the gas path showing predominantly *Si* with minor species containing boron and oxygen

4.3.3.2 Fracture surface of runout specimen

The fracture occurred at 19 ± 3 *mm* from the geometric center of the runout specimen. The surface temperature at this cross-section was recorded using the IR thermal imaging system to be $1090 \pm 30^{o}C$, $950 \pm 50^{o}C$, $830 \pm 10^{o}C$ on the front, side and back surfaces. The failure outside the zone of direct flame impingement suggests that failure mode may have been the permanent degradation that accumulates at lower temperature. The cross-sectional view of this fracture surface is represented in Figure 55. The shape of the oxidized region outlined on the fracture surface shown in Figure 55 suggests that oxidation likely occurred through the cracks that initiated and propagated inwardly from the edge or corners on the left. Micrographic features including the fibers with rigid interphase and silica overlayer were commonly observed throughout the oxidized area, as demonstrated in Figure 55A, B and C. Short pullouts were predominant in the non-embrittled regions (Figure 55D). The pullouts appeared very similar in length to those from the runout woven MI Syl-iBN/BN/SiC. The pervasive oxidation characterized by picture-frame shape of oxidation profile was not observed.
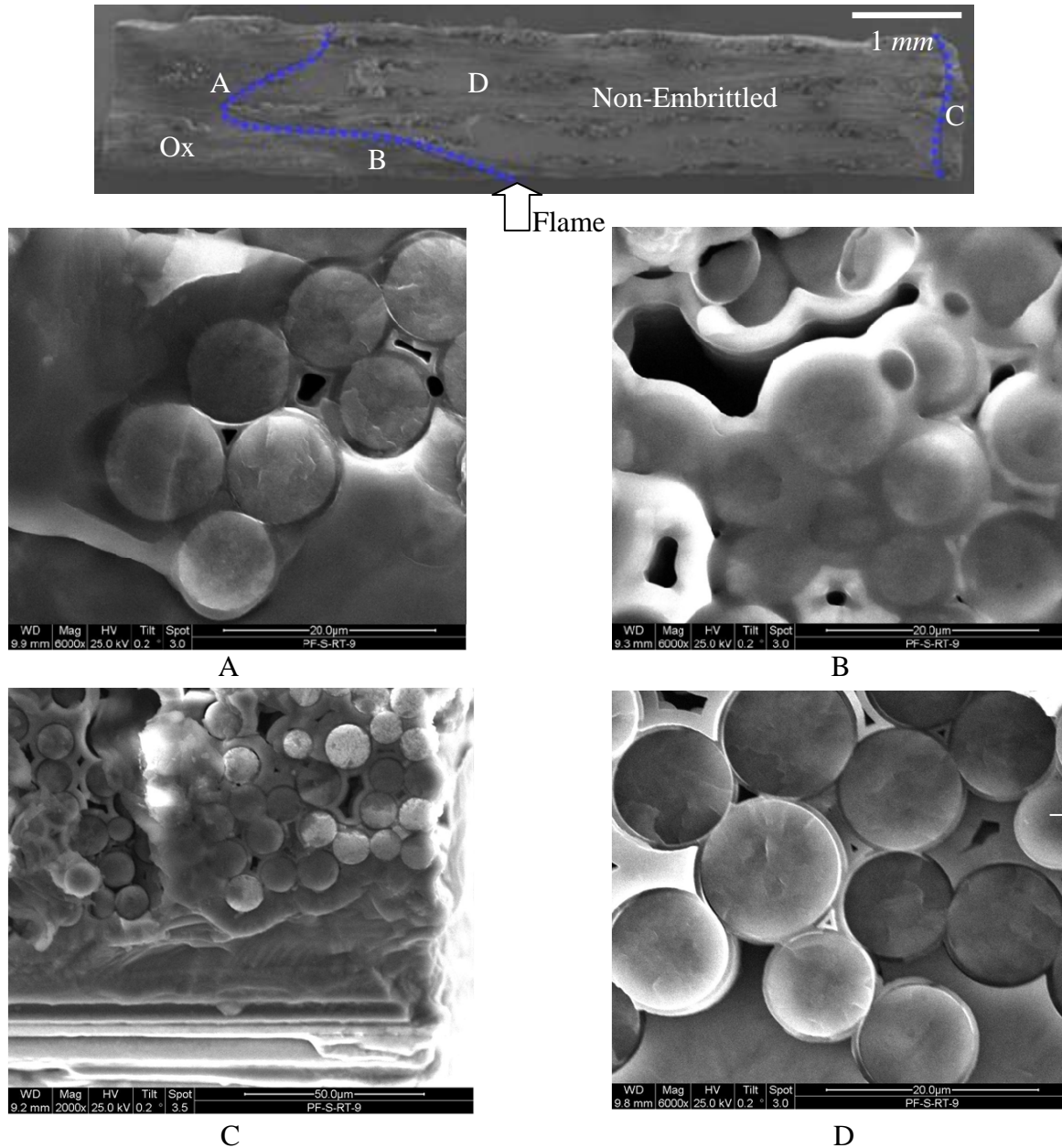
Figure 55: Fracture surface of the runout MI woven Syl/BN/SiC after residual strength test: A thru D are from the oxidized and non-embrittled regions of the fracture surface as denoted on the overall fracture surface shown above.

4.3.3.3 Section surface of runout specimen

The woven MI Syl/BN/SiC specimen loaded cyclically with the peak stress of 53% of the *PL* survived over 90,000 cycles after the 25 hour-long test, and was subsequently tested for

residual strength at room temperature by applying monotonic tension loading on the runout specimen until it failed. After the residual strength test, which resulted in the fracture at 19 *mm* from the geometric center of the specimen, a cross-section was sectioned from the heated zone and polished for microscopic analysis, which is represented in Figure 56.
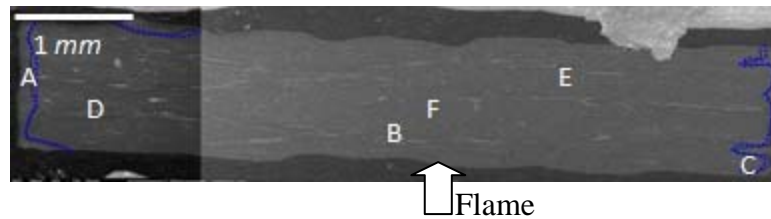
Figure 56: Polished section from the heat zone of the run-out woven MI Syl/BN/SiC

The SEM study showed that the sectioned surface did not experience extensive oxidation. The oxidation that caused the formation of oxide scale was prevalent along the side edges as demonstrated in Figure 57A, but the "picture-frame" oxidation [48] was not observed at this particular plane cut from the heated zone. Corners are among the most heavily oxidized area on the cross-section. From Figure 57B and C, it is apparent that the CVI SiC matrix was at one point deformed into a molten phase. This phase was shown using EDS to contain Si, O and C (Figure 58). It is speculated that B_2O_3 produced by the oxidation of the BN interphase may have dissolved the SiC in the matrix by Equation (14) in Chapter II [77]. The deformed appearance of the CVI SiC matrix were observed in a few other locations including the 2nd ply from the flame-impinged surface near the hot gas path, shown in Figure 57B.

Localized deformation in the CVI SiC matrix with oxide formation at a location isolated by non-oxidized regions, such as region depicted as "B" in Figure 56, could be due to the diffusion of oxidation down along the interphases. With the distance of 19 *mm* from this section to where the fracture occurred, it would also seem plausible to consider an additional path for the

diffusion that can facilitate the transport of oxidants readily, such as a longitudinal crack that created an opening between the CVI matrix and BN interphase for oxidants to travel down along.

Pores were observed in the MI matrix on the surfaces of fiber tows throughout the 1st and 2nd plies, shown in Figure 57D. They appear as fragmentation of the matrix and were found usually surrounding fiber tows. They were more densely populated on those plies located near the side edges. The appearance of porous matrix was noticeably less on the 3rd and 4th plies, suggesting gradient nature of the phenomenon. Such apparent gradient distribution and the fragmented appearance led to the presumed classification of the pores as the post-test observed pores that are different from the process-induced pores showing little discernable distribution pattern.

It could not be determined how the post-test observed porosity evolved in the MI matrix. In most cases, the porous region appears to be extended along delamination that traces around the surface of fiber tows (Figure 57D). Silicon and boron contents were determined in the similar location of the as-received CMC. Boron, which may have been added to enhance the oxidation-resistance of the CMC, is known readily to oxidize and produce a protective oxide that prevents the enclosed bulk from further oxidizing [116]. Boron content was confirmed in several different locations including the tow surface and dark spots in the MI matrix as well as the filler in the trapped voids, the last of which was shown to contain boron using EDS as in Figure 59. The MI matrix surrounding fiber tows are, along with silicon and boron impurity, rich with residual porosity, probably due to a poor melt-infiltration process around the fiber tows with rapid change in curvature. From this observation, it may be presumed that region in the MI matrix containing metal silicon, boron and residual porosity approximately agrees with the region showing the presumably pronounced level of porosity as compared to the rest of the area in the MI matrix.

Lastly, the apparent gradient distribution of such porosity in the presence of the mechanical fatigue may warrant the consideration that the phenomenon may have been assisted by fatigue loading.

4.3.3.2.1 Sectioned parallel to loading

The other fractured piece obtained from the residual strength test the runout MI woven Syl/BN/SiC specimen was sectioned along the loading axis and probed using SEM. In addition to adding to the understanding of the failure, the determination of crack distributions may pertain to the stress distribution, which can vary across the dimension due to thermal stress. Four sections, each representing different depths from side edge surface, were prepared in the similar manner as in the analysis of the woven MI Syl-*iBN*/BN/SiC.
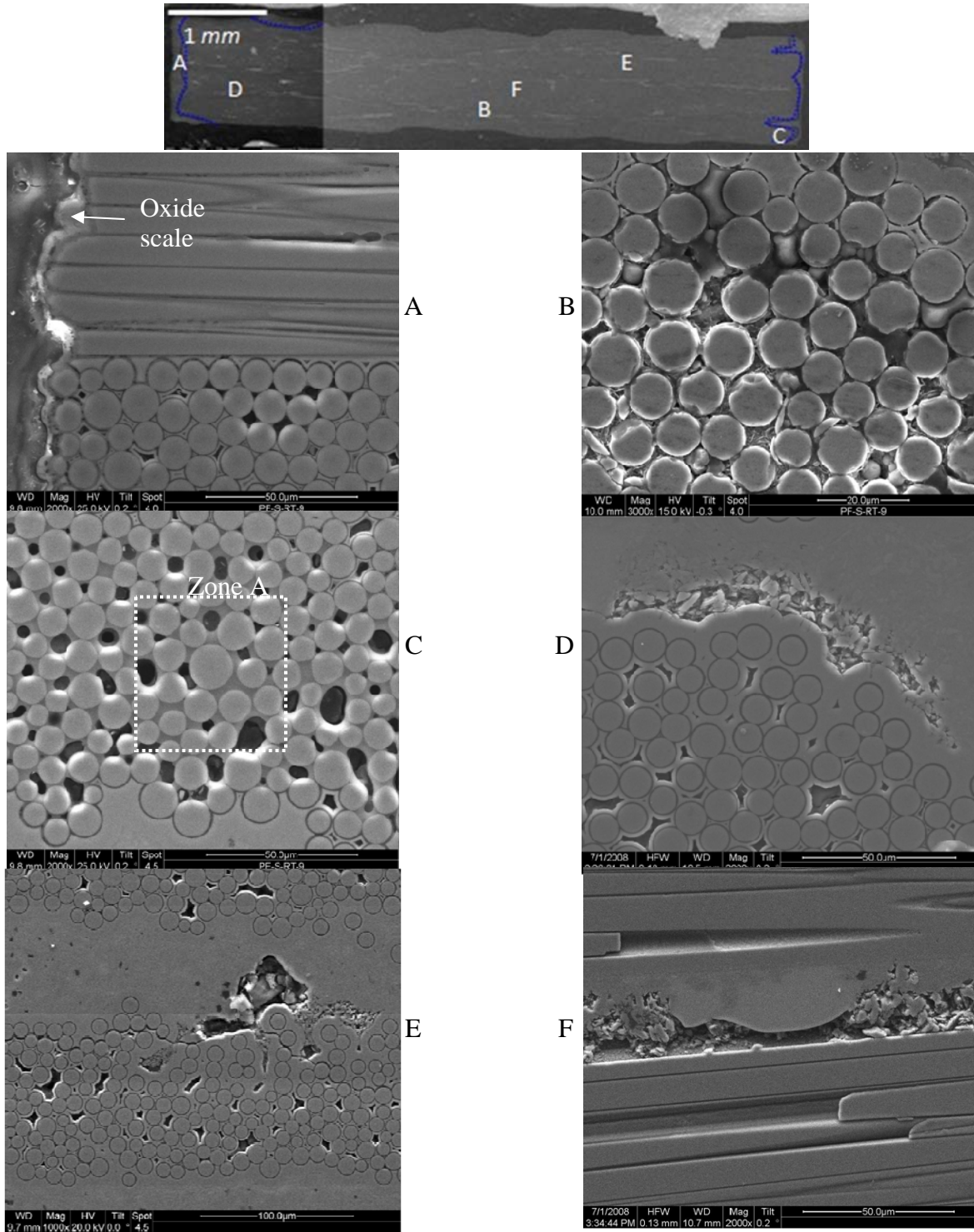
Figure 57: Microscopic features on polished section of the runout woven MI Syl/BN/SiC in the heated zone: Specific location of each image is specified on the sectioned surface above.
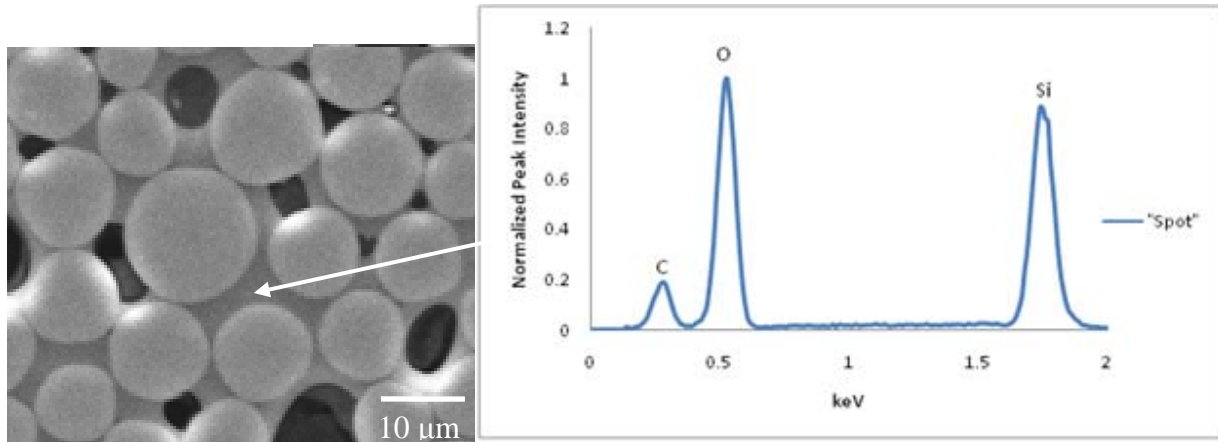
Figure 58: Deformed CVI matrix in the area depicted as Zone A inside rectangle in Figure 57C
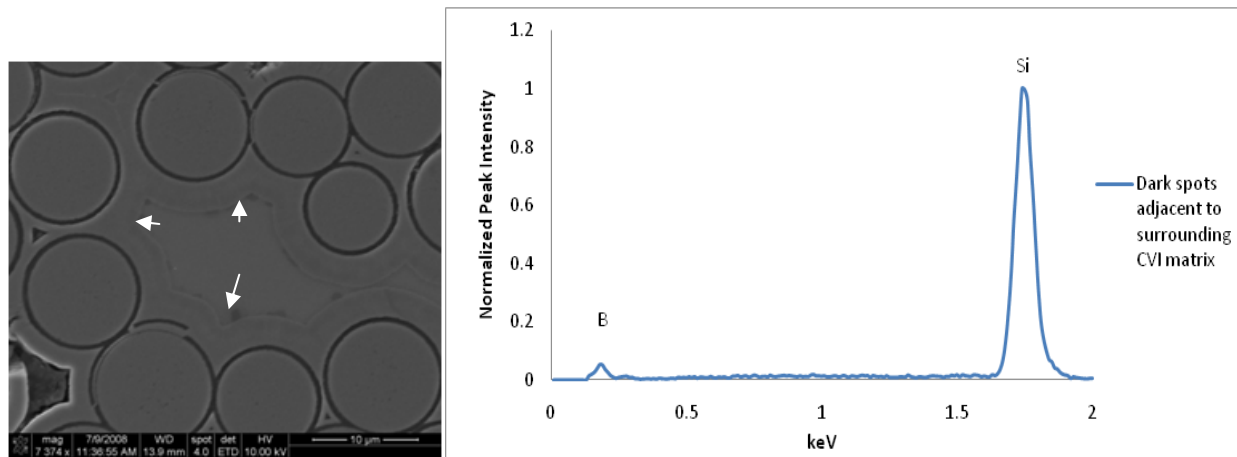
Figure 59: MI matrix contains boron impurity

From the analysis carried out using SEM, transverse cracks were populated on the plies near the back surface, while more longitudinal cracks are found along the plies near either surface than on the plies in the middle. This trend is captured from the data in Table 15.

Table 15: Crack distribution analysis of the runout MI woven Syl/BN/SiC

Ply	Transverse Cracks	Longitudinal Cracks
1 and 2	11	33
3 and 4	24	11
5 and 6	36	20

The density of transverse cracks was larger near the back surface. The majority of longitudinal cracks are observed in the two plies next to the flame-impinged surface. In addition, many of the longitudinal cracks were found near the fracture surface, approximately 19 *mm* away from the geometric center of the runout specimen. The plies near the flame-impinged surface also featured the ply-splitting as well as the separation of two adjacent plies.

4.3.4 Section Summary

From the preceding discussion, it appeared that the extent of oxidation depended on the applied stress level and cycles to failure in combustion. The woven MI Syl/BN/SiC was similar to the woven MI Syl-*iBN*/BN/SiC not only in its S-N behavior and microscopic characteristics, but also in the significantly reduced strain at failure due to oxidation. There were no micrographic details that could be considered unique just to the MI woven Syl/BN/SiC from the MI woven Syl-*iBN*/BN/SiC. Commonly found in the oxidized region were interphase oxidized and adhered to fibers and adjacent matrix, oxide overlayer formed on the fracture surface, similarly as in the woven MI Syl-iBN/BN/SiC on the relatively planar fracture surface, indicative of oxidation occurring in the wake of advancing cracks. Fiber pullouts were predominant in the non-embrittled area of all fracture surfaces, and they were short and brushy, similarly in length and appearance to those observed from the woven MI Syl-iBN/BN/SiC. In addition, the fracture appeared to have emanated from the rear corners. The residual strength test of the runout specimen demonstrated that the elastic properties and the proportional limit did not suffer degradation due to the applied condition in terms of mechanical loading and combustion environment. Substantial reduction in the stress and strain at failure was, however, experienced for this material, as the stress retained

by the runout specimen and its corresponding strain were 63 ± 8 % and 45 ± 7 % of the room temperature *UTS* and its strain exhibited by the pristine specimen, respectively.

4.4 Woven MI Hi-Nic-S/BN/SiC

The woven MI Hi-Nic-S/BN/SiC was also subjected to the same combustion environment as that applied to both the woven MI Sylramic CMCs. Fatigue loading with different peak stresses was applied to each of the 6 specimens, based on which the S-N data in the following discussion were obtained. The test results from the fatigue tests using three woven MI Hi-Nic-S/BN/SiC specimens in the laboratory air furnace to demonstrate the effects of thermal gradient stress and moisture were presented.

Table 16: Combustion test data for MI woven Hi-Nic-S/BN/SiC

Specimen ID	Peak Stress (MPa)	Peak Stress (%UTS)	Peak Stress (%PL)	Number of Cycles	Fractured Location (from center in mm)	Temperature at fracture (^{o}C)		
						Front	Side	Back
Fatigue in Burner Rig								
HNS#2	140	42	116	1047	0 ± 3	1220±52	N/A	N/A
HNS#3	127	38	105	8329	0 ± 3	1222±35	950±50	N/A
HNS#4	93.5	28	77	11858	0 ± 3	1246±29	980±40	880±25
HNS#5	90	27	74	55664	0 ± 3	1266±21	990±50	925±10
HNS#6	80	24	66	53034	0 ± 3	1269±17	950±50	N/A
HNS#7	70	21	58	90059	No Fracture	1185±35	1015±25	910±25
Fatigue in Furnace								
HNS#8	135	40	112	12943	13 ± 3	1235±5		
HNS#9	125	37	103	58838	19 ± 3	1235±5		
HNS#10	100	30	83	94627	No Fracture	1235±5		

4.4.1 S-N Data

Table 16 shows the data obtained from each test and includes the applied peak stress and corresponding cycles-to-failure, fractured location and the apparent surface temperature at that cross-section. Based on the data provided on the table, two S-N curves were plotted; one from the burner rig tests and the other from the furnace tests. The runout conditions occurred at the peak stress of 70 MPa in the burner rig and 100 MPa in the laboratory air of the furnace. All the test specimens that failed during the burner rig fatigue tests fractured in the heated zone, where the highest temperature with the largest thru-thickness gradient was experienced. However, the fracture locations of the furnace tested specimens was off the center of the gauge section by as much as 19 mm, whereas the fractures from the burner rig tests were centered around it, as denoted in Table 16.

4.4.3 Strength Retention

The runout woven MI Hi-Nic-S/BN/SiC specimens, subsequently tested for residual strength, failed upon reaching the ultimate strength of 186 MPa at 0.22 % and 146 MPa at 0.13 % of strain for the runout specimens from the burner rig and furnace exposures, respectively. The stress-strain curves obtained from these tests were plotted along with the curve for a pristine Hi-Nic-S/BN/SiC obtained under monotonic tension at room temperature in Figure 61.
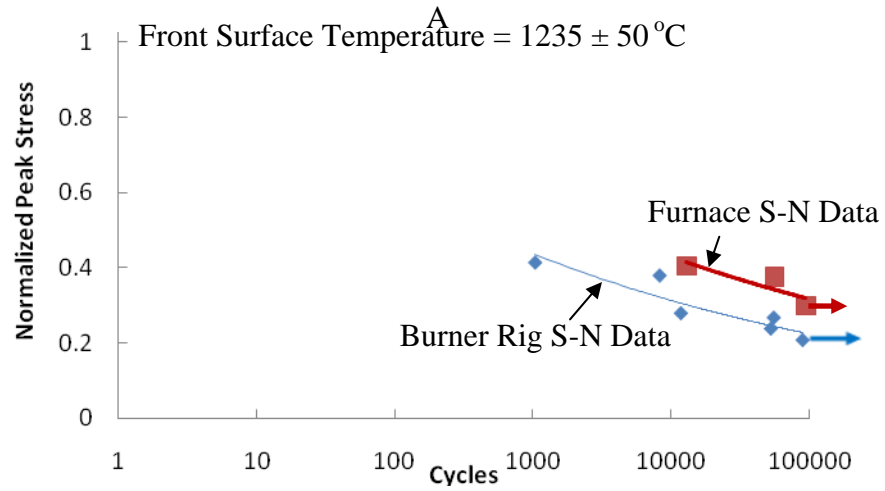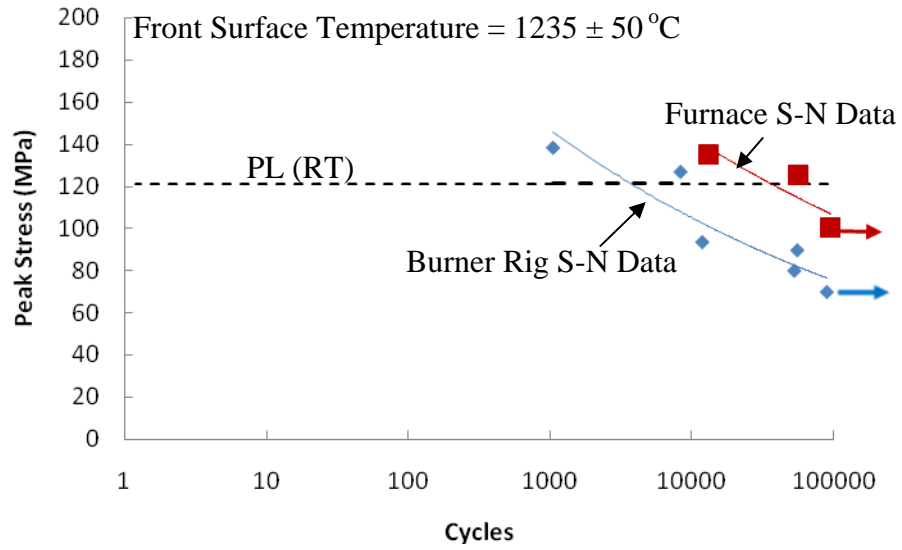
Figure 60: S-N represented for woven MI Hi-Nic-S/BN/SiC with peak stress (A) in MPa and (B) normalized against *UTS*
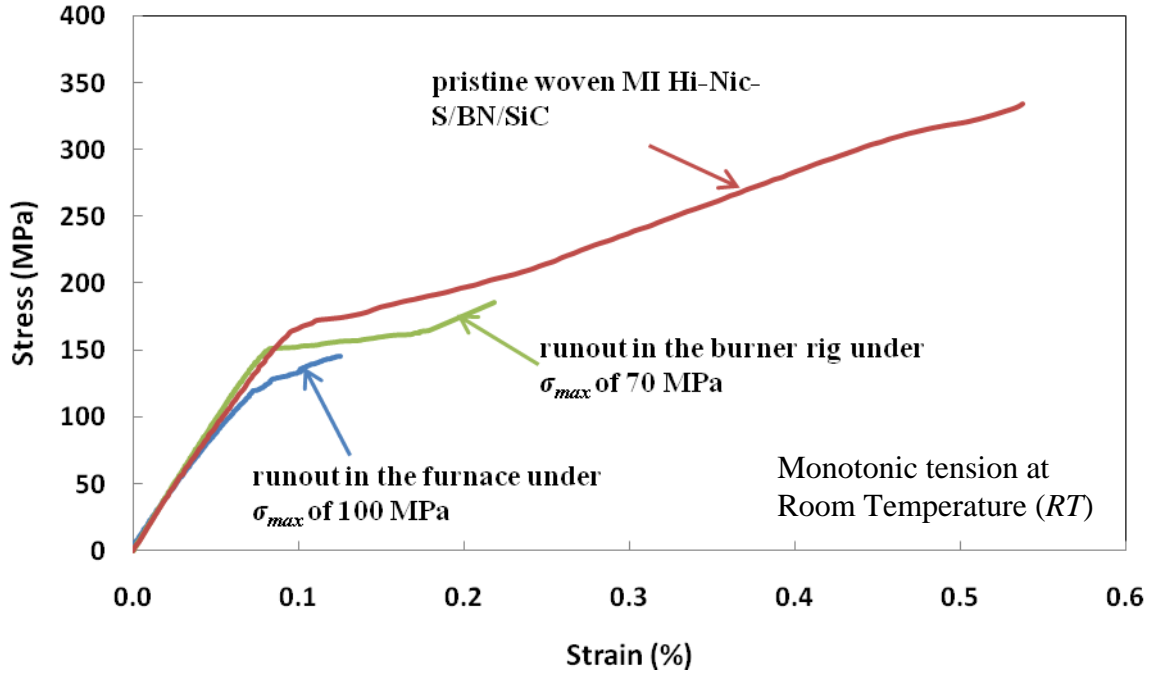
Figure 61: Stress-strain curves of the runout and pristine MI woven Hi-Nic-S tested under monotonic tension

From the comparison in stress-strain behavior between the runout and as-received woven MI Hi-Nic-S/BN/SiC specimens in Figure 61, the modulus of elasticity of the runout specimen from burner rig test was 203 GPa, which is larger than 195 GPa of the pristine specimen. The difference is likely within the scatter of data. The proportional limit (*PL*) of the runout specimen from burner rig test was measured to be 144 MPa, somewhat greater than 121 MPa of the pristine material. On the other hand, the PL of the furnace tested runout specimen is lower than that of the as-received. The difference could be attributed to the permanent changes caused by the 25 hour of fatigue loading that pertain to the interphase sliding such as the residual stress, coefficient to friction, topography, wear property and fracture toughness [35]. For this type of CMC, however, it is not uncommon to have a *PL* or *UTS* that outlies from the average value. Thus, one or two data points could not serve as a valid basis for this comparison, though it could be a point to

consider for a future study. The stress at the point of departure from linearity did not deviate by much among the three curves; 60 MPa for the burner rig runout specimen, compared to 62 MPa for the pristine specimen. The point of delineation is believed to be the stress level at which the fracture of 90° tows initiates. Fractions of the retained strength and the strain at failure for the burner rig runout specimen were 56% and 41% of the respective value obtained from the monotonic tension test of pristine material. Those of the furnace runout specimen are even smaller as evident from Figure 61. Thus, the reduction in fracture toughness was experienced in both test conditions.

With respect to its proportional limits, the runout stress of 70 MPa amounts to 58% of the room temperature *PL* and 49% of the *PL.* from the residual test. This stress level, if no other stress is in effect on the specimen, is low enough to assume no significant nucleation and development of microcracking in the matrix. Consequently, diffusion of oxidizing species through spots other than the edges and corners would be minimal if indeed no other stress were acting on the specimen. However, thermal gradient stress induced by the directional heating added to the applied mechanical stress and probably caused failure at low peak stress. This was evident from Figure that showed the fatigue strengths from the furnace tests to greater by relatively constant amount, i.e. 45 MPa across the entire span of the test cycles. If a time-dependent degradation mechanism such as oxidation were to be a main reason for this difference, the two curves probably would not have been as parallel as observed, because its effects would increase with time and the number of cycles. More in-depth study that incorporates a longer fatigue life would be needed for a more conclusive statement about this observation.

4.4.3.1 Comparison of the residual data between two runout specimens

Keeping in mind that the two test conditions featured different peak stresses that resulted in runout, no definitive conclusion can be deduced from the comparison between the two residual strengths shown in Figure 61. However, the higher strength and strain retained by the burner rig tested specimen, despite relatively similar extent of oxidation [117], points to the possibility that the intact areas of the two runout cases may have undergone different levels of degradation, perhaps in the form of either frictional wear in the interphase under different peak stresses to affect the fatigue strength. The frictional wear could have been accompanied by the interphase oxidation that may have occurred by consuming residual oxygen content. The resulting oxidized interphase could have accompanied a partial or complete change in its physical state that changed in interphase mechanics. In addition, the change in chemical state of interphase through oxidation could have led to its accelerated degradation by friction under cyclic loading. The comparison becomes more convoluted with the consideration of the thermal stress and oxidation. In particular, the non-uniform thermal stress was induced by the directional heating such that a stress level higher than that accounted for by the applied load was imposed on the plies adjacent to the unheated back surface of the specimen, whereas compressive thermal stress acting on the plies near the heated front surface relieved some of the applied stress to reduce the overall stress borne locally. Thus, the gradient nature of the overall stress condition leads to a conjecture that intact fibers in the burner rig test condition may have been subjected to the rates of degradation, such as in the sliding resistance, that varied in gradient along the thickness direction. The discrepancy in residual strength may also be related to the location of the fracture. The furnace tested specimen failed near the grip whereas the burner rig tested one failed within the reduced section. In general,

the failure outside the reduced cross-section occurs at a lower stress. More in-depth studies in this direction are also needed to further investigate the phenomenon.

4.4.2 Microscopic Analysis

The results of the microscopic analysis for the woven MI Hi-Nic-S/BN/SiC are presented in this section. Similarly to the analyses of the two woven MI CMCs using Sylramic-based fibers, the scope of the micrographic study for the woven MI Hi-Nic-S/BN/SiC encompasses both macro-level image analysis of fractured surface which captures the traces and extent of oxidation and micro-level assessment that provides detailed information pertinent to oxidation. First, three fractured surfaces obtained from specimens tested and failed under different peak stresses and in different number of cycles are discussed. Then the analysis of the fracture and sectioned surfaces of the runout specimen was presented.

4.4.2.1 Fractographic Analysis

Figure 62 depicts the fracture surfaces obtained from three fatigue tests performed at the peak stress of 105%, 74%, and 66% of the room temperature *PL* of 121 MPa from top to bottom. The specimen under fatigue loading with peak stress of 66% of the *PL* survived 53,034 cycles, more than 6 times as long as the fatigue life of the specimen loaded at the peak stress of 105% of *PL*. The difference in the test durations and cycles-to-failure translated into the difference in the extent of oxidation on the fracture surfaces. A significantly larger oxidized area was observed on the surface obtained after 53,034 cycles, as compared to the specimen that failed after 8,329 cycles. In addition, the specimen fatigue loaded with peak stress of 74% of *PL* survived 55,664 cycles, which was similar in fatigue life to the specimen subjected to 66% of *PL* The similar

fatigue life was reflected by the similar area fractions of the oxidized regions exhibited on the two fracture surfaces.
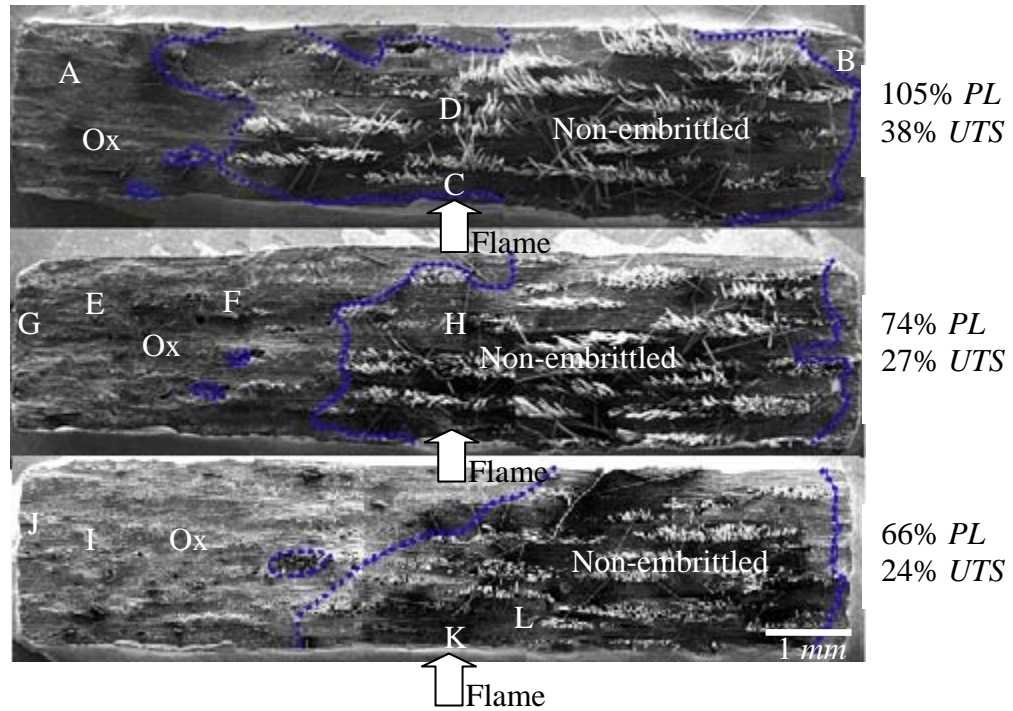
Figure 62: Fracture surface at peak stresses of 105%, 74% and 66% of *PL*

From Figure 62, it is evident that oxidation appears to be initiated from either edge or corners, and permeated into the deeper interior of the specimen with increased cycles, which was determined to be inversely related to the applied peak stress according to the S-N data in Figure 60. The potential causes for the failure appearing to originate preferentially from the left side of the specimen are discussed in Appendix D. One observation of the woven MI Hi-Nic-S/BN/SiC, dissimilar to the other two woven MI CMCs using Sylramic-based fibers (Figure 40G), was that the length of fiber pullout varied markedly with test duration and peak stress, as demonstrated in Figure 63. The difference could be attributed to the difference in the interphase properties, in particular, in the presence of a thin carbon layer on the non-stoichiometric Hi-Nic-S fiber [23,122]. The carbon content on the fiber surface may be attributed to an increased pullout length [49].

The specimen fatigued to failure at the peak stress of 105% of *PL* after 8,329 cycles exhibited the longest fiber pullout length, whereas the shortest pullout length is obtained from the specimen loaded with peak stress of 66% of the *PL*, which survived 53,034 cycles. The observed change in fiber pullout length with the number of cycles and/or applied stress can be attributed to change in interphase properties [53]. Progressive degradation of interphase properties with accumulated fatigue cycles may have caused gradual erosion of the interphase to change its surface roughness, which changed the fiber pullout behavior [33,96]. Given the exposure to oxidative environment, the degradation could also stem from SiO_2 film that may form on SiC fiber [118]. The silica film is believed to grow with time, and a study performed by R. Hay et al [119] showed that fiber strength of Hi-Nic-S fiber depends on the silica thickness. Reduced strength of fibers may have been indicated by the observed difference in fiber pullout length.
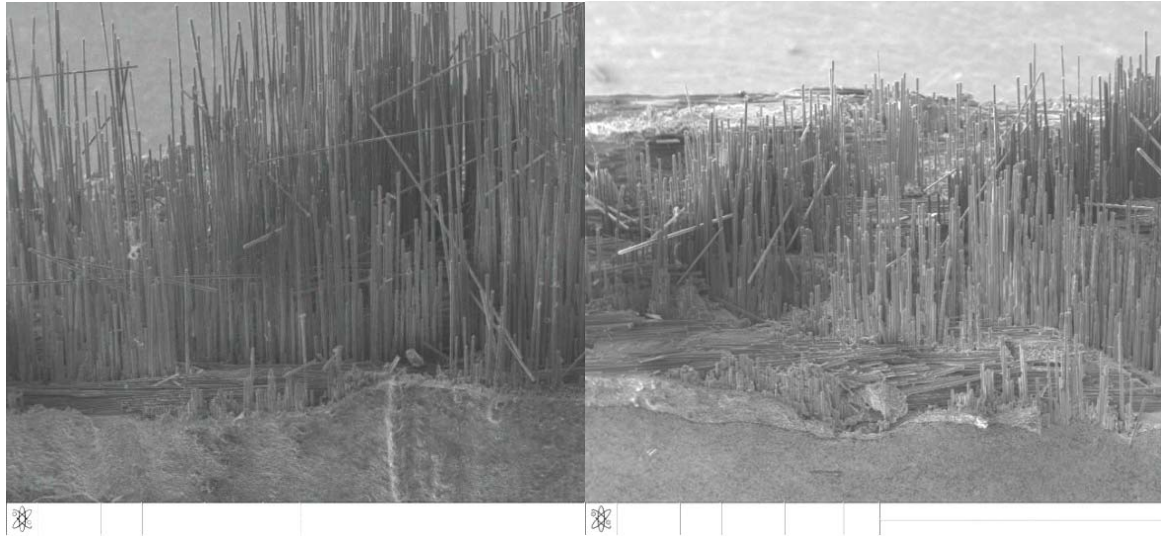
Figure 63: Fiber pullouts on fracture surfaces of the woven MI Hi-Nic-S/BN/SiC failed under the peak stress of 105% (Left) and 66% of the RT *PL* (Right)
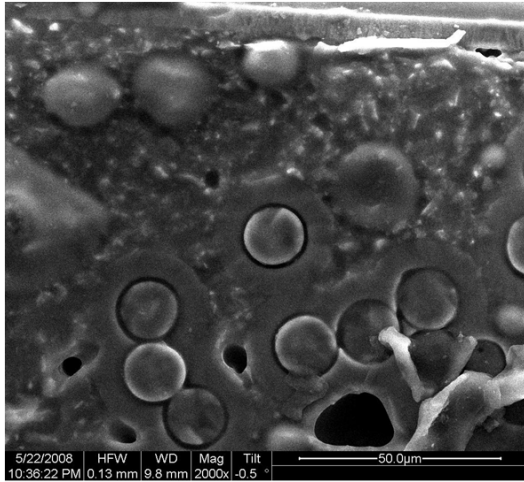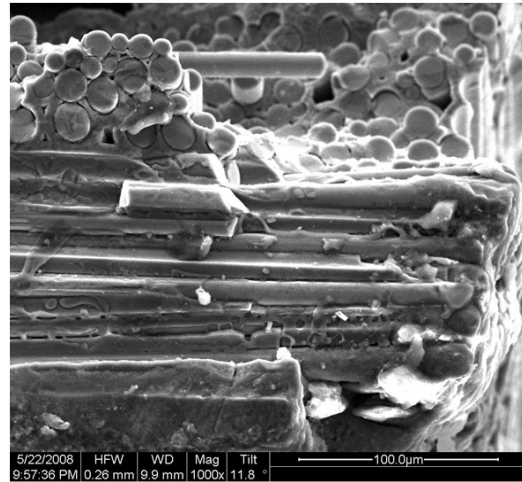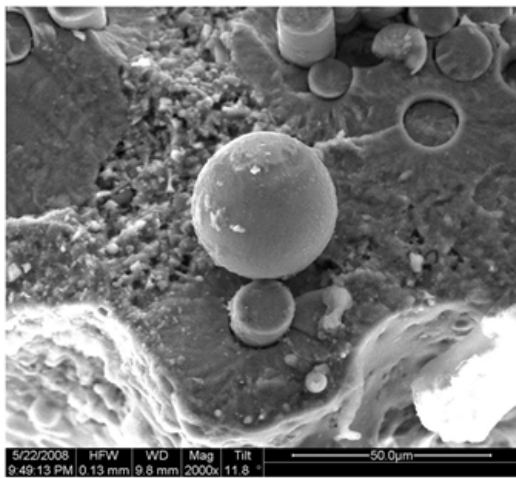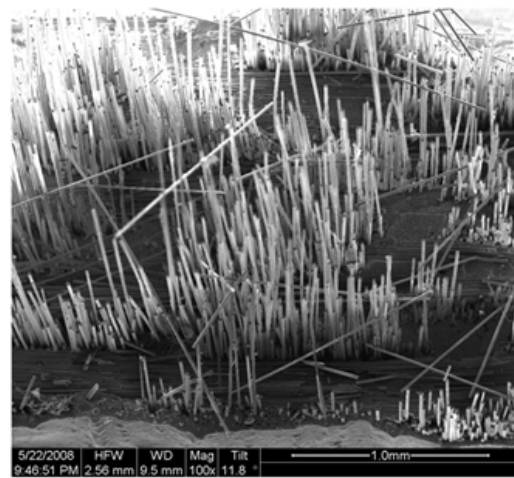
Figure 64: Microstructure of fatigued tested specimen under peak stress of 105% of *PL*: A thru D are from the oxidized and non-embrittled regions of the fracture surface as denoted on Figure 62.

E

F

G

H
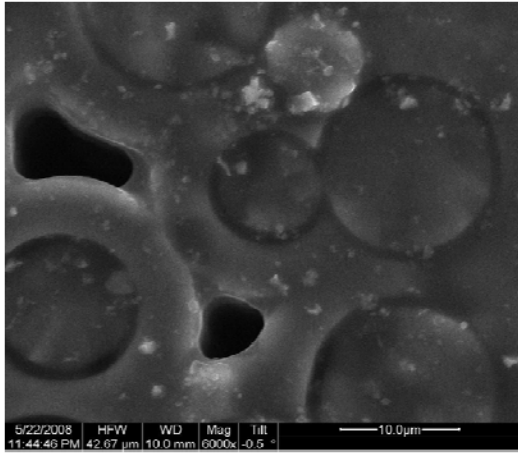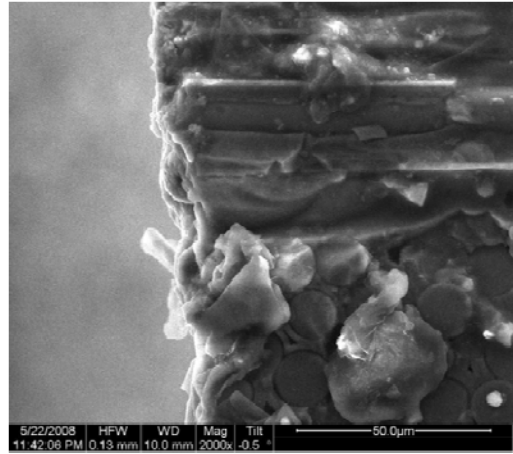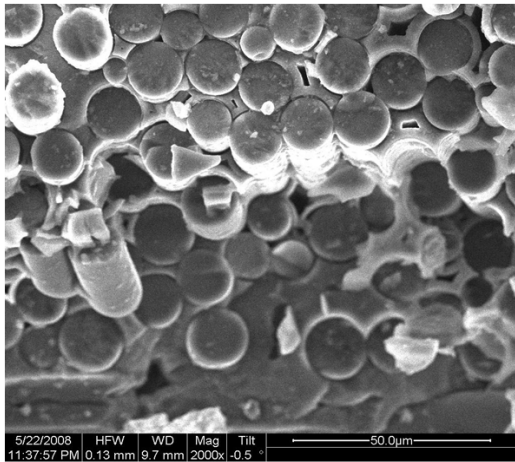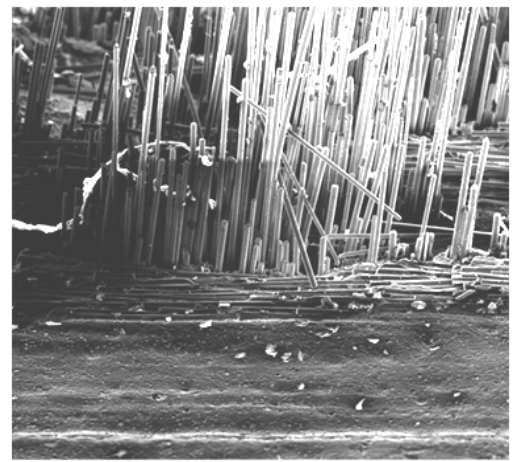
Figure 65: Microstructure of fatigued tested specimen under peak stress of 74% of *PL*: E, F and G are from the oxidized, and H is from the non-embrittled region of the fracture surface. Specific locations imaged are shown on Figure 62.
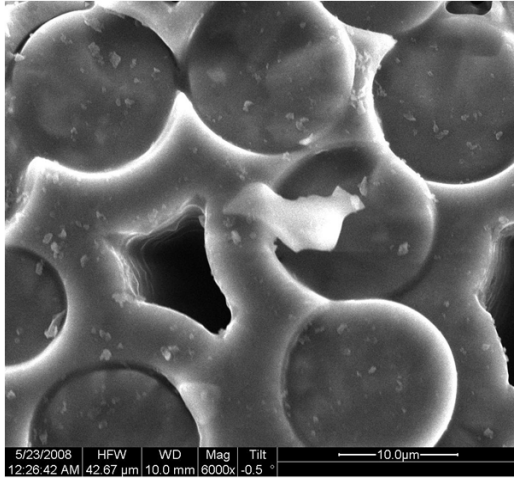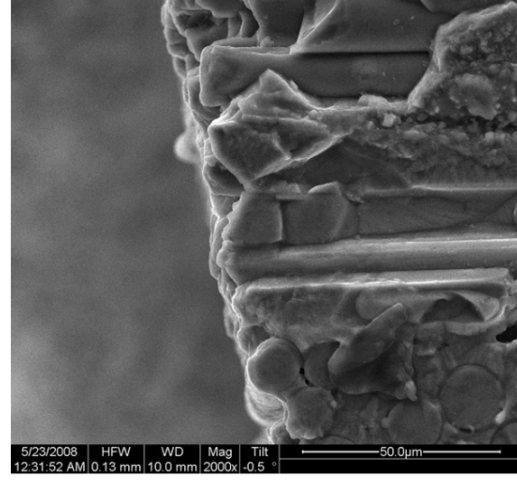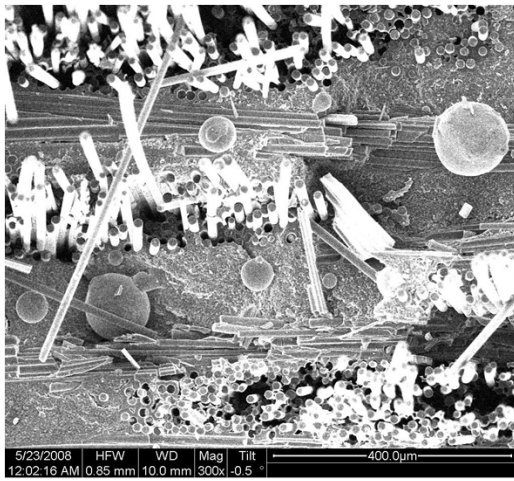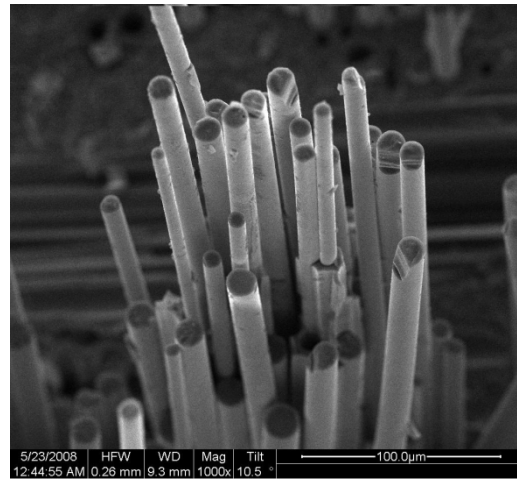
Figure 66: Microstructure of fatigued tested specimen under peak stress of 66% of *PL*: I and J are from the oxidized, and K and L are from the non-embrittled region of the fracture surface. Specific locations imaged are shown on Figure 62.

Detailed micrographs of each fracture surface shown in Figure 62 are represented in Figure 64, Figure 65 and Figure 66. In the oxidized regions, the oxidative features such as grouped fiber failure on relatively flat surfaces showing interphase oxidation as well as patches of oxide overlayer, similarly to the two Sylramic based woven MI CMCs discussed earlier. Among the commonly observed in the oxidized area are captured in Figure 64A, Figure 65E and Figure 66I. Oxidized machined edges are depicted in Figure 64B, Figure 65F and Figure 66J. Fiber

pullouts of much greater lengths than those observed from the Sylramic reinforced CMCs are exhibited in the non-embrittled regions shown in Figure 64D, Figure 65H and Figure 66L Spherical features found in Figure 64C and Figure 66K appear similar to those observed in the woven MI Syl/BN/SiC CMC, which were determined through EDS analysis to be predominantly silicon with very small oxygen content, as was the case in the other CMC.

4.4.2.2 Fracture surface of runout specimen

The residual strength test resulted in a fracture at 25 ± 3 *mm* above the geometric center of the runout specimen. Using the FLIR ThermaCAM^{TM} software, it was possible to re-access IR images taken during test, which allowed the determination of surface temperature at the failed cross-section. Temperature history is important in addressing the cause of fracture potentially related to any degradation mechanisms led by oxidation, as the rate of oxidation varies with temperature. It was found from this analysis that the temperature at the cross-section of fracture was $1185 \pm 35^{o}C$ along the front width, $1015 \pm 25\,^{o}C$ across the thickness on the side, and $910 \pm 25\,^{o}C$ along the width of the back surface. The fracture that occurred outside the heated zone suggests that the rate of degradation may have been higher at lower temperature.

Figure 67 shows the residual fracture surface. It was apparent from overall surface image which outlined the oxidized area by dotted lines that the oxidation front had grown from the proximity of rear left corner of the specimen. In the oxidized area, the planar fracture surface with fibers adhered to adjacent neighbors was observed as shown in Figure 67A. The fracture of 90° fibers in group along the dotted line on Figure 67B was observed near the edge, suggesting the grouped fiber failure as the result of oxidation that led to the adherence of neighboring fibers. The oxide overlayer common in oxidized area suggest that silica or borosilicate may have flown and

sealed off the surface encompassing multiple adjacent tows, as apparent from Figure 67C. Finally,

Figure 67D depicts an image taken in the non-embrittled inner core of the material, in which the

fiber pull-outs were observed.
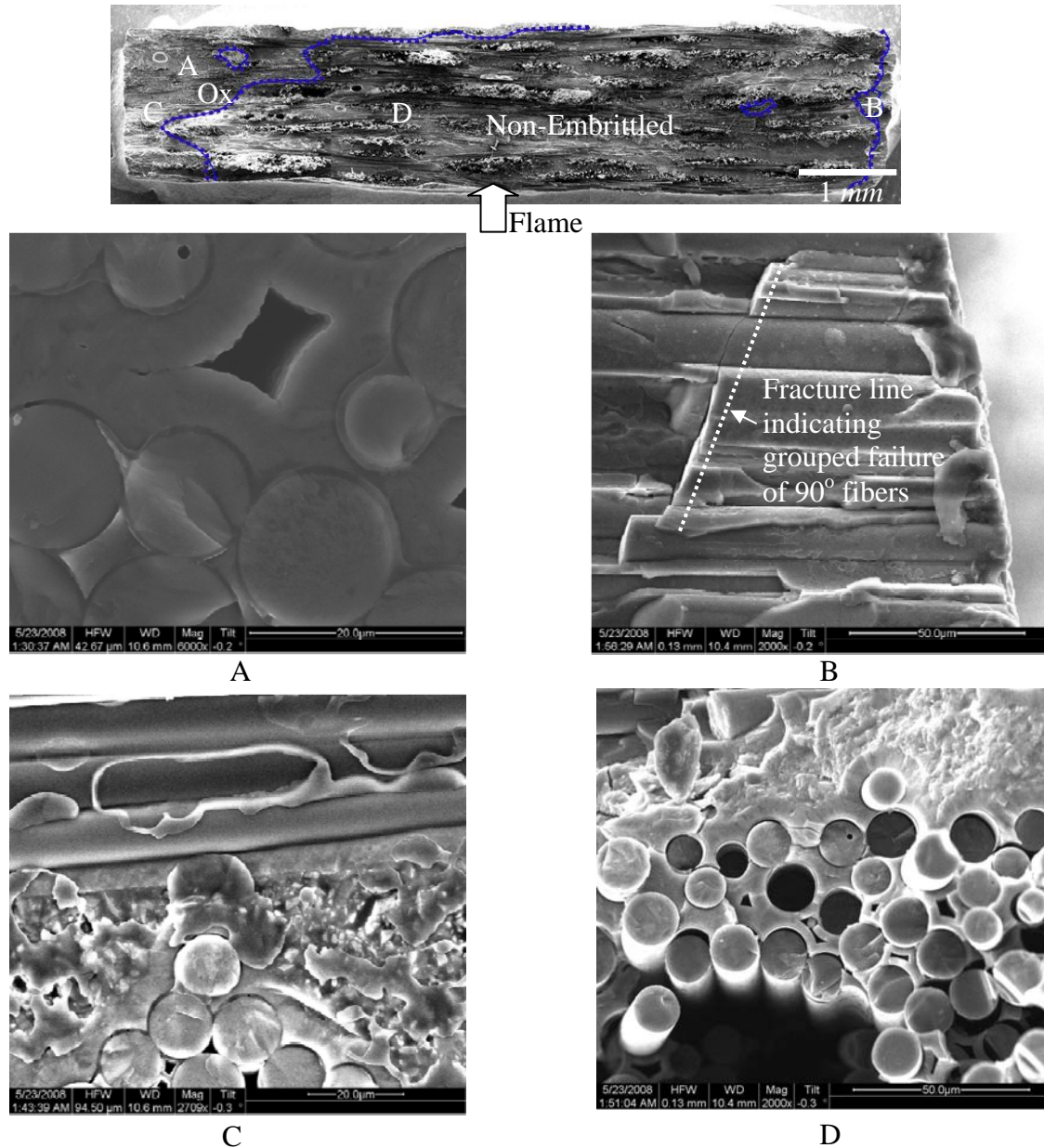
Figure 67: Fracture surface of the runout MI woven Hi-Nic-S/BN/SiC after residual strength test: A thru D are from the oxidized and non-embrittled regions of the residual fracture surface as denoted on the above image.

4.4.2.3 Sectioned surface of runout specimen

A cross-sectional surface sectioned from the heated zone of this specimen was polished and investigated for damage related to oxidation. Overall appearance of the woven MI Hi-Nic-S/BN/SiC microstructures shown in Figure 68 was similar to the two Sylramic fiber based woven MI CMCs. Edge oxidation was evident in Figure 68; deeper penetrating oxidation was observed on more crack-prone 90° tows, suggested by oxidative features found along the interphases leading to deeper interior along 90° tows. The surface quality on the 0° tows near the flame impinged surface was indicative of a degraded form suggested by apparent shrinkage or thinning of some CVI matrix in the adjacent to the observed porosity, as depicted in the circled area of Figure 68B. In addition, the matrix on the plies near the flame-impinged surface appeared to be more porous in the area surrounding the fiber tow surface, as compared to the similar regions on the plies near the unheated back surface. This is evident from the comparison of the pores along the fiber tows in Figure 68C and Figure 68D.

From the inspection of the polished surfaces cut in parallel to the loading direction of the residual strength tested sample, it was apparent that the fibers bundles on 90° tows next to the flame-impinged surface underwent cracking within the plane of the ply in the direction parallel to the loading. This is demonstrated in Figure 69 with the surface opposite to the flame-impinged that showed no such cracking as a comparison.
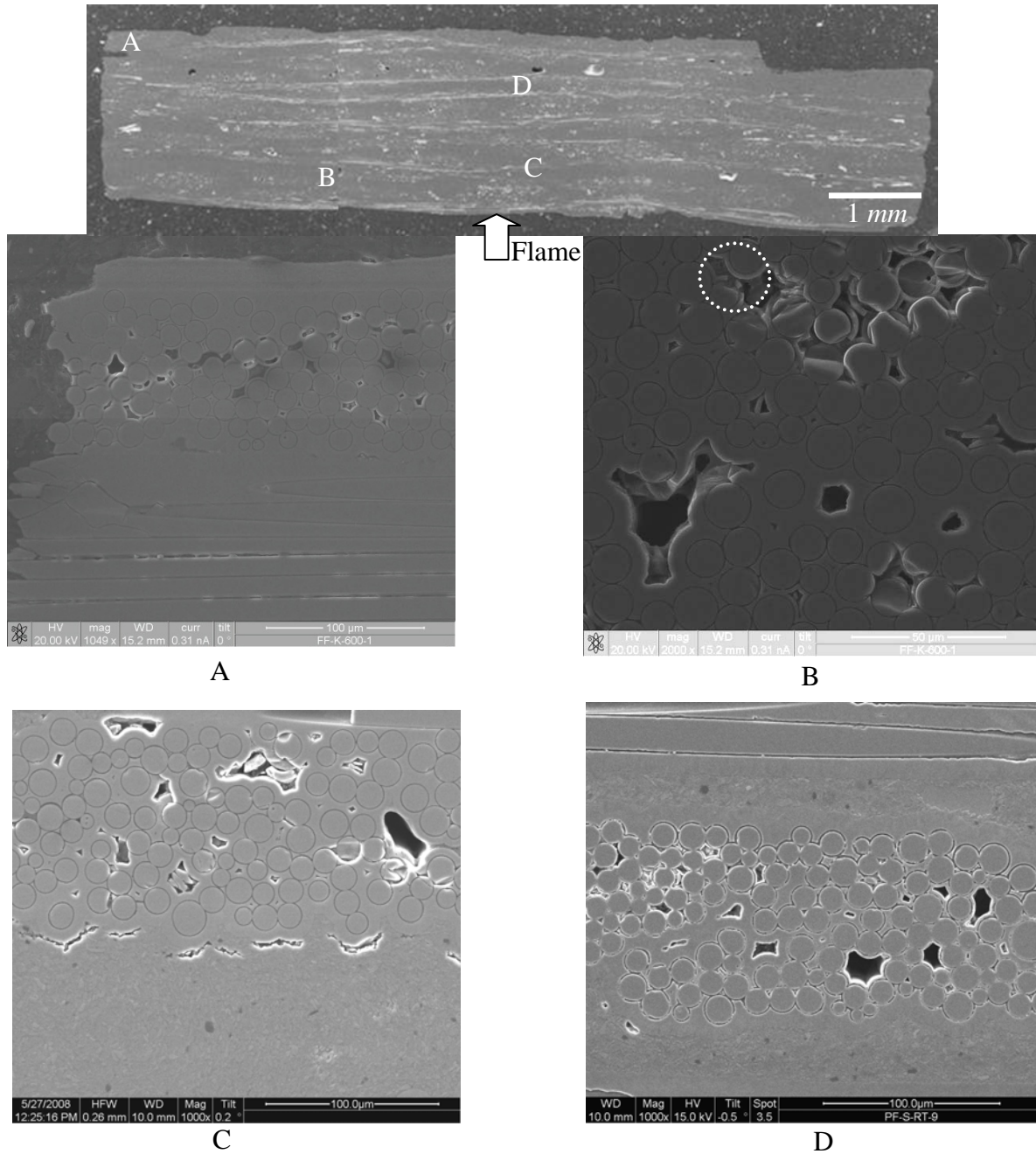
Figure 68: Polished section from heated zone of runout woven MI Hi-Nic-S/BN/SiC: A thru D are from the sectioned surface as denoted on the above.

<div style="text-align:center">Front   Back</div>
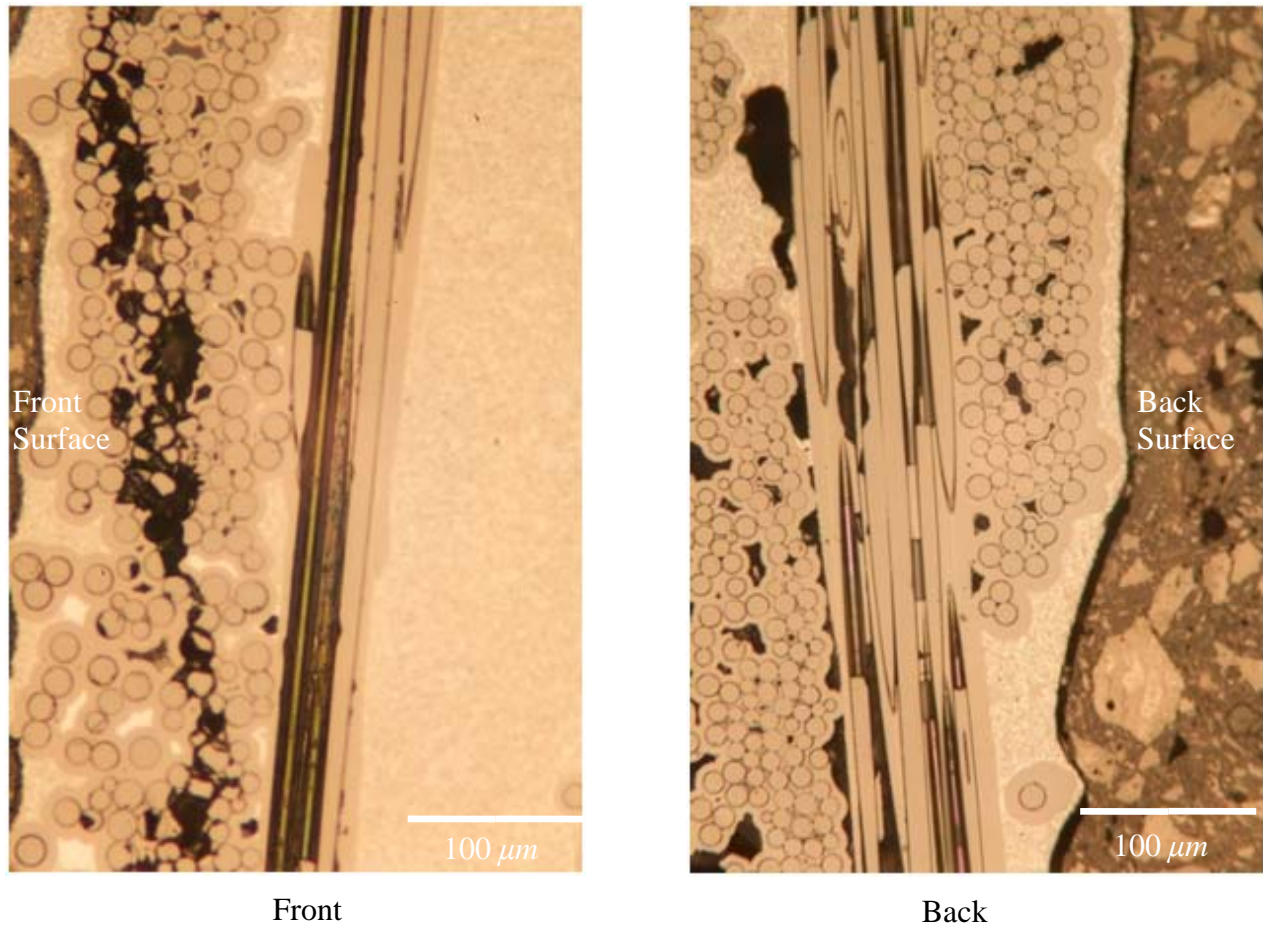
Figure 69: Representative area on polished surface sectioned in parallel to the loading direction splitting on plies closest to flame impinged surface (Left); no splitting on the back surface (Right)

4.4.4 Section Summary

In summary, the preceding section presented the fatigue and residual strength data of the woven MI Hi-Nic-S/BN/SiC CMC and discussed the micrographic observations that provided the qualitative measure of the effects of oxidation in conjunction with the applied stress. The analysis demonstrated that the material exhibited the familiar trends in its relations between the oxidation and the applied stress as well as the number of cycles; a smaller oxidized area was observed on the surface of a specimen fractured under a higher peak stress, and a larger oxidized area was resulted from the specimen that showed a longer fatigue life. It was evident from the comparisons

between the fractures surfaces of different test specimens that the oxidation initiated from either edge or corners permeated deeper into the bulk specimen with increased cycles, which was inversely related to the peak stress. The pullout lengths exhibited by this CMC were in general much longer than those observed from the other woven MI using Sylramic fibers. The fiber pullout behavior with respect to the applied condition was such that a longer pullout was attained from a specimen fatigued at a lower applied stress that survived a longer life. From the strength retention test of the specimen that survived 90,000 cycles at the end of 25 hours of fatigue loading with the peak stress of 70 MPa in the prescribed combustion environment, it was determined that 56% of the pristine *UTS* was retained at the strain equivalent to 41% of the failure strain of the pristine woven MI Hi-Nic-S/BN/SiC specimen, which implied a significant permanent degradation in its strength retention capability.

For this CMC, similar fatigue tests were carried out on three specimens using furnace heating that does not involve thermal gradient. The fatigue strengths from these tests were greater by relatively constant amount, suggesting that the thermal gradient effect was evident.

4.5 Prepreg MI Hi-Nic-S/BN/SiC

A test matrix similar to those used for the other three CMCs was used to carry out for five MI prepreg Hi-Nic-S/BN/SiC specimens under the same prescribed combustion environment. The frequency and stress ratio or *R*-ratio remained the same as in the other tests at 1 *Hz* and *R* = 0.05, while peak stress was changed from one test to another such that the S-N behavior for the applied condition was attained.

4.5.1 S-N Data

Table 17 shows the data obtained from each test. The three tests carried out at the peak stresses of 145 MPa, 134 MPa and 125 MPa did not survive past 1,000 cycles, and they all resulted in failure, which occurred relatively close to the gauge section. Two runout specimens were obtained for this test matrix; one at the peak stress of 92 MPa and the other at 105 MPa. The fatigue test using 92 MPa for peak stress yielded runout, and this prompted a need for another test at the peak stress between 92 MPa and 125 MPa, the latter of which resulted in failure after less than 1,000 cycles. The highest peak stress applied to a specimen that resulted in runout was 105 MPa, 55% of the room temperature *PL* of the as-received prepreg MI Hi-Nic-S/BN/SiC from the same panel tested under monotonic tensile loading. Based on these results, the applied peak stresses for the five specimens were plotted against their corresponding cycles-to-failure, which is represented in terms of both absolute and normalized stress scales in Figure 70.

Table 17: Fatigue test results in combustion for prepreg MI Hi-Nic-S/BN/SiC

Specimen ID	Peak Stress (*MPa*)	Peak Stress (*%UTS*)	Peak Stress (*%PL*)	Number of Cycles	Fractured location (from center in *mm*)	Temperature at Fracture (^{o}C)		
						Front	Side	Back
Gen II-1	145	48	75	209	0 ± 3	1250±30	N/A	N/A
Gen II-2	134	37	79	926	6 ± 3	1140±25	N/A	N/A
Gen II-3	125	36	56	758	3 ± 3	1175±40	N/A	N/A
Gen II-4	105	31	55	90001	No Fracture	1025±25	950±50	845±5
Gen II-5	92	28	41	90555	No Fracture	1283±23	950±50	830±10
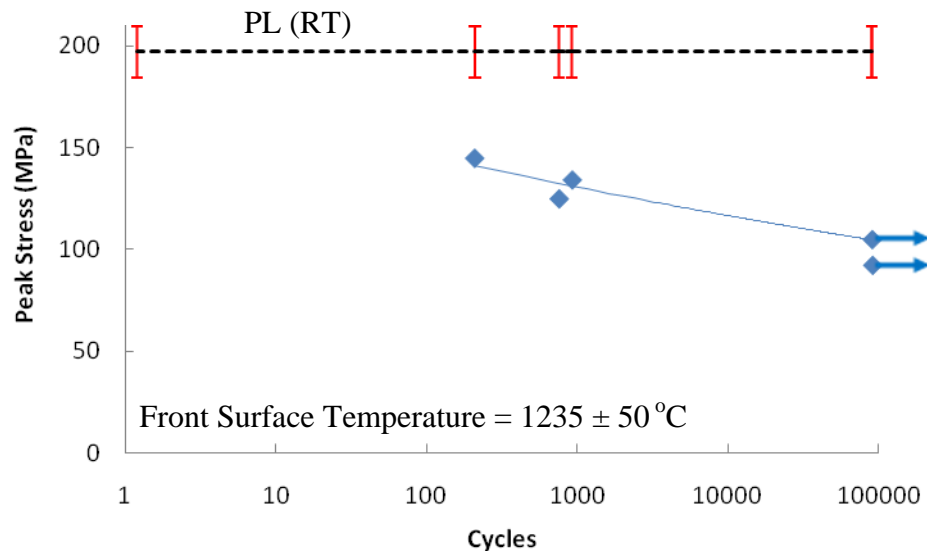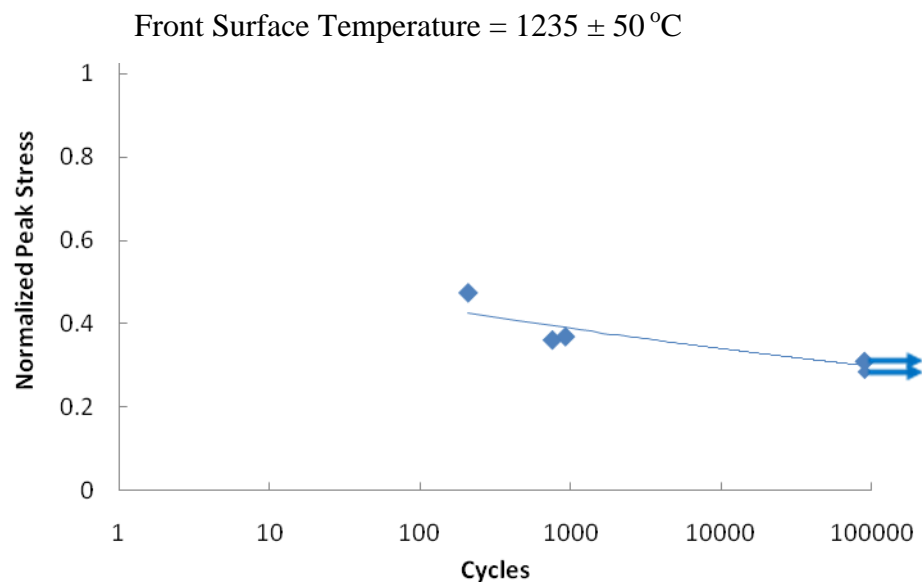
Figure 70: S-N Curves of MI prepreg Hi-Nic-S/BN/SiC with peak stress; (A) in MPa and (B) normalized against *UTS*

It should be noted that five prepreg MI Hi-Nic-S/BN/SiC specimens tested here were each from different panels unlike the other three CMCs tested in this study. To remove scatter caused by variations between panels, each peak stress was normalized by the individual panel's room

temperature ultimate strengths. For a balanced treatment of each material to set up comparisons between CMCs, the peak stresses applied to each of the other three CMCs were also normalized by the room temperature *UTS* of the respective CMC.

With respect to the proportional limit of the prepreg MI Hi-Nic-S/BN/SiC from the same panel, the runout stress of 105 MPa amounts to 55% of the *PL* of a sample from the same panel (i.e. 190 MPa). The specimen that survived only 758 cycles was loaded with peak stress of 125 MPa, equivalent to 56% of the room temperature *PL* of a specimen cut from the same panel (i.e. 222 MPa). The scatter in the *PL* data is quite large ranging from 170 MPa to 222 MPa, which could be due to the relatively large variation in fiber volume fraction from 20 to 25%. The standard deviation of the average *PL* of 197 MPa was ± 23 MPa.

4.5.2 Strength retention

There were two specimens that survived more than 90,000 cycles in the prescribed combustion condition at the end of 25 hour-long tests with peak stresses of 92 MPa and 105 MPa, respectively. These runout specimens were subsequently tested for residual strength by having monotonic tension subjected at room temperature. Figure 71 shows the stress-strain curves for the two runout specimens in response to the monotonic tension loading.

Monotonic tension at Room Temperature (*RT*)

Monotonic tension at Room Temperature (*RT*)
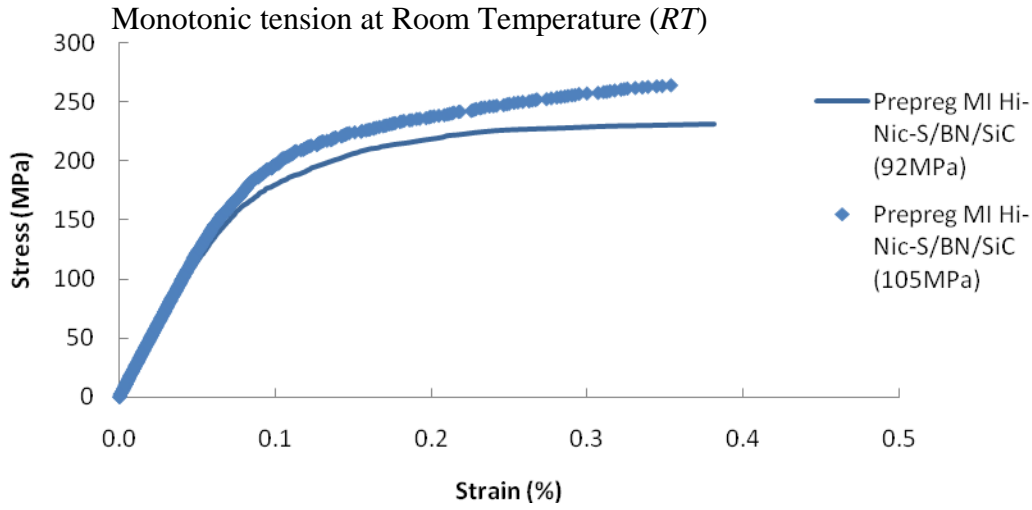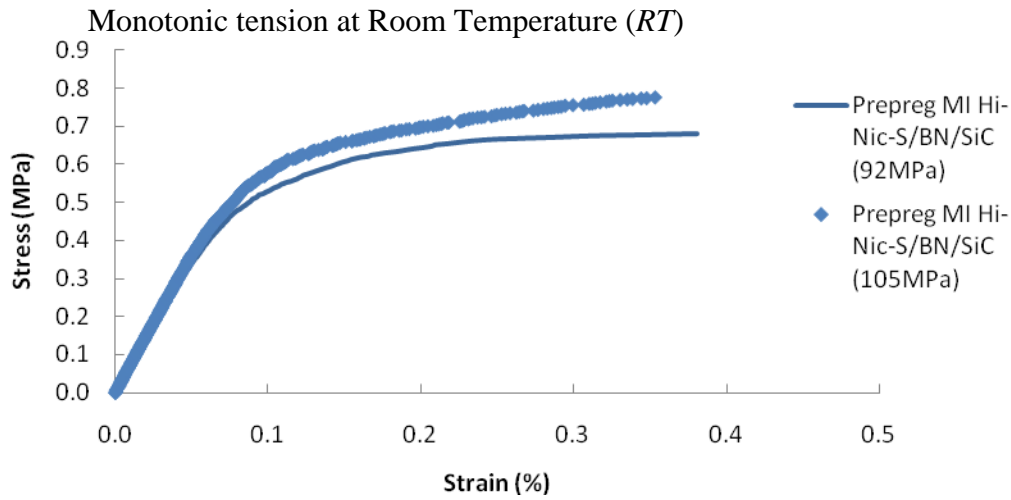
B

Figure 71: Stress-strain curves of two runout prepreg MI Hi-Nic-S tested under monotonic tension; stress shown (A) in MPa and (B) normalized against *UTS*

From Figure 71, the two stress-strain curves have lower elastic moduli of 244 GPa and 247 GPa, which are 93 ± 5 % and 94 ± 4 %, respectively, of the elastic modulus of a pristine specimen, (i.e. 264 ± 13 GPa). The decrease in modulus may be related to the fiber surface finish [120], and the thin carbon layer on the Hi-Nic-S fiber could have dealt the observed loss in modulus [121]. Proportional limits of the runout specimens were 132 MPa and 156 MPa,

respectively in the ascending order of the peak stresses applied. Both the *PLs* are significantly less than 197 ± 23 MPa, the average *PL* of as-received specimens. Reduced *PL* may be the result of the permanent damage accumulated during the fatigue testing in combustion. The retained strength and the corresponding strain are 232 MPa at 0.38% for the one fatigued at the peak stress of 92 MPa and 264 MPa at 0.35% for the other that fatigued at 105 MPa. Compared to 340 ± 19 MPa at 0.71 ± 0.12 %, which is the *UTS* and strain at failure for as-received prepreg MI Hi-Nic-S/BN/SiC specimens tested under monotonic tension at room temperature, the two runout specimens retained 68 ± 4% and 78 ±4% of its original strength at the strain reduced to 55 ± 9 % and 51± 9 % of the original, respectively for the peak stresses of 92 MPa and 105 MPa applied.

Of the two runout prepreg MI Hi-Nic-S/BN/SiC specimens, the one that survived at the peak stress of 105 MPa was primarily discussed because it survived the higher peak stress than the other. This peak stress level is equivalent to 55% of the room temperature *PL* of the same panel, below which a test would likely result in runout, as evident from the specimen that did not fail under the peak stress of 92 MPa or 41% of its *PL*. Considering the next higher peak stress tested was 56% of the *UTS* that ended in failure after 758 cycles, the decrease in the peak stress by 1% of the *PL* caused the lifetime of the specimen to increase by in excess of 90,000 cycles. As compared to the woven MI CMCs discussed above, the rate of change in cycles-to-failure with respect to the change in the applied stress is relatively high.

The residual strength tests of the two runout specimens resulted in the fractures at 25 ± 3 *mm* and 0 ± 3 *mm* from the geometric center of each specimen for the two specimens fatigued under 105 MPa and 92 MPa, respectively. The latter specimen was the only runout specimen of all four CMC types in this study that demonstrated the fracture inside the heated area.

4.5.3 Microscopic Analysis

The results of the microscopic study carried out using the fracture and sectioned surfaces of the five prepreg MI Hi-Nic-S/BN/SiC specimens are presented in this section. The analysis was carried out using the standards and methodology applied for the other three CMCs in order to facilitate comparison in the next chapter

4.5.3.1 Fractographic Analysis

Figure 72 represents three fracture surfaces obtained from the three tests performed under fatigue loading with the peak stresses equivalent to 79%, 75% and 56% of the room temperature *PL* of their respective panels.
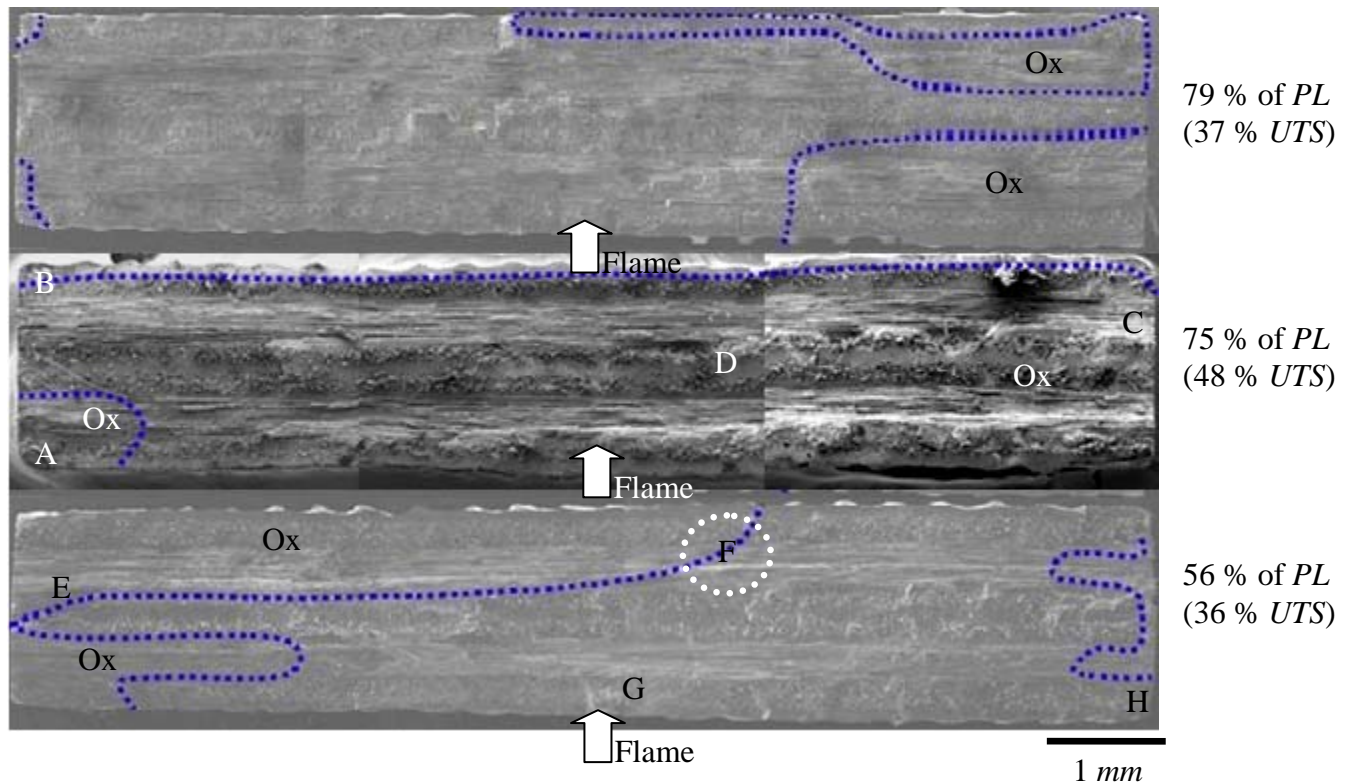
Figure 72: Fracture surfaces of the prepreg MI Hi-Nic-S/BN/SiC CMCs fatigued at 79%, 75% and 52% of *PL*

For each of the three fracture surfaces, the entire surface cross-section was probed under the SEM. With the aid of the EDS, the oxidized regions, shown outside the dotted lines on each fracture surface in Figure 72, were identified and separated from the rest of the surface area that did not show oxidative features. From the visual comparison, it appeared that the oxidized surface area was larger for the lower peak stress applied. The cycles-to-failure for the three cases were 926, 206 and 758 cycles in the descending order of the normalized peak stress applied. The extent of oxidation did not show a consistent trend with respect to the number of cycles. Separated only by 720 cycles, the change in fatigue life was probably too small to see any difference in the effects of oxidation.

The microstructures commonly observed throughout the oxidized and non-embrittled regions of the two specimens fatigued at 75% and 56% of their respective *PL* are presented in Figure 73 and Figure 74, respectively. Fibers adhered to their neighbors through the contacting interphases that became rigid by oxidation were observed as shown in Figure 73A, though not as common as in the woven MI CMCs. Oxide overlayers formed on the fracture surface were observed throughout the oxidized regions on the fracture surfaces characterized as single-and multi-planar crack planes, as shown in Figure 73A and B & Figure 74. Unlike the woven MI CMCs, the prepreg MI CMC with much shorter combustion exposure did not exhibit much edge oxidation. In the non-embrittled region, fiber pullouts showing no interphase oxidation were observed as shown in Figure 73C and D & Figure 74H. As compared to the woven MI CMCs, the prepreg MI Hi-Nic-S/BN/SiC showed much shorter pullouts, suggesting different modes of governing the fiber-interphase and matrix-interphase interactions under fatigue than those in the woven MI CMCs.
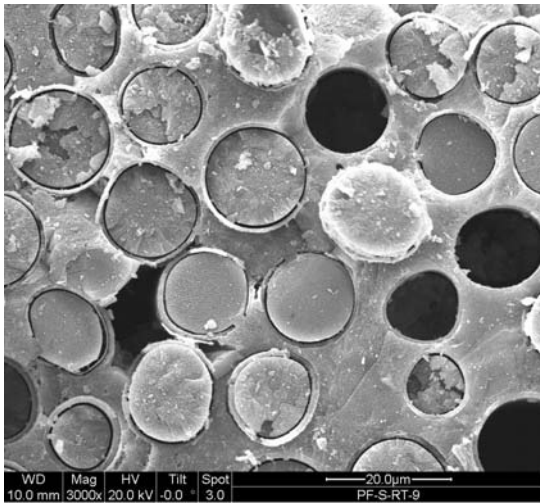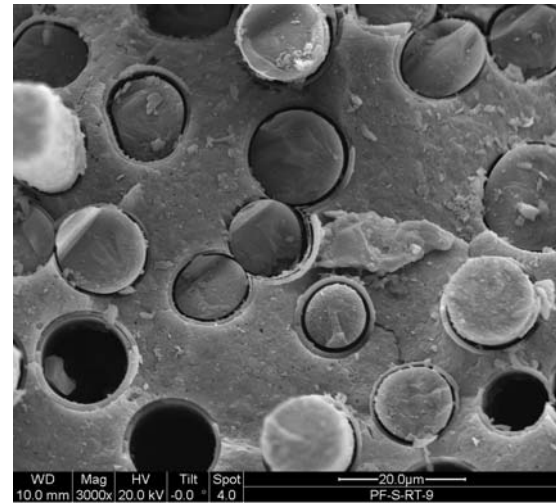
Figure 73: Microstructure of the MI prepreg Hi-Nic-S/BN/SiC fatigued at peak stress of 75% of *PL*: A thru D are from the fracture surface as shown on Figure 72.
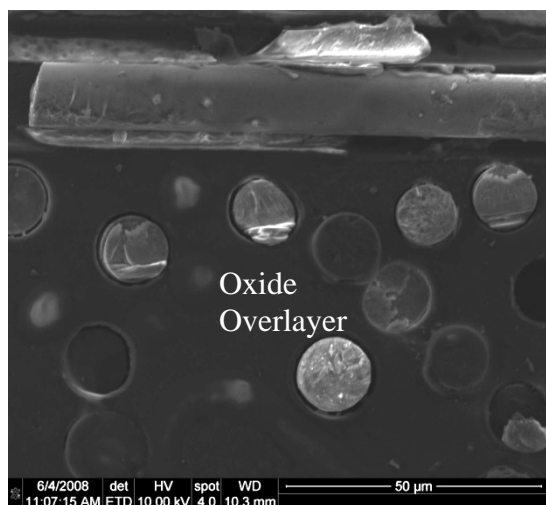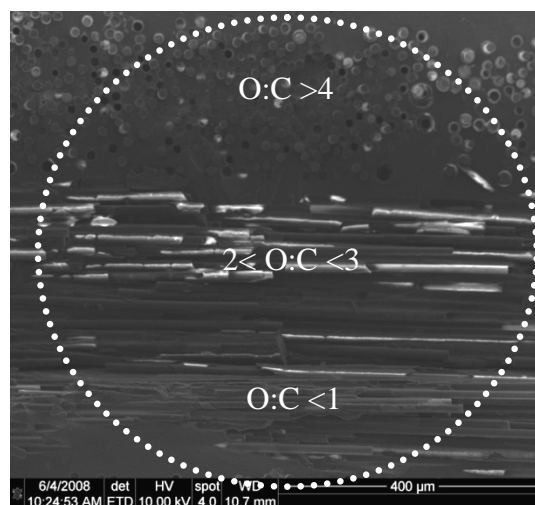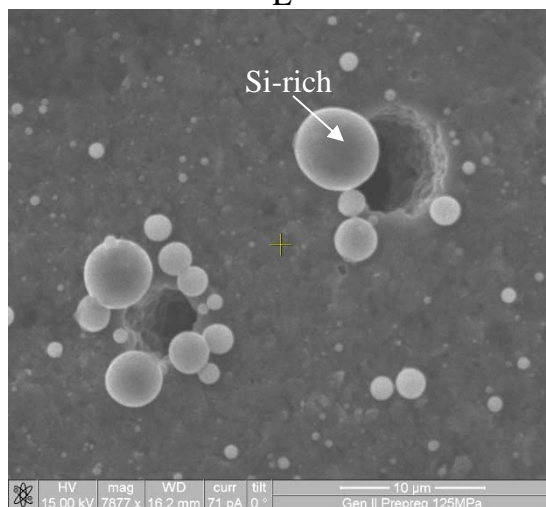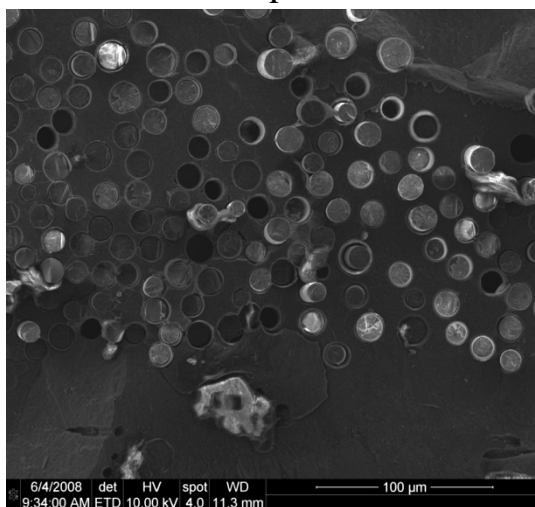
Figure 74: Microstructure of the MI prepreg Hi-Nic-S/BN/SiC fatigued at peak stress of 56% of *PL*: E thru H are from the fracture surface as shown on Figure 72.

Spherical features shown in Figure 74G were observed to be populated around the pores located on the plies adjacent to the flame impinged surface of the fractured surface. These features were similar in chemical content as the spherical ones observed from the woven MI Syl/BN/SiC and woven MI Hi-Nic-S/BN/SiC, which consisted predominantly of Silicon for both instances. In addition, they were found in a similar relative location as those of the woven MI CMCs.

Figure 74F illustrates the EDS analysis results for the area on the fracture surface close to the back surface as located at the encircled 'F' on Figure 72. The oxygen-to-carbon content ratio was a measure of the level of oxidation and was presented to demonstrate the oxidation gradient that existed across the thickness. The depicted region was transitioning from the oxidized to non-embrittled zones from the top and downward, suggesting that the rear part of the surface may have cracked opened to the environment before the front surface. This matches with the observation made in the encircled area in Figure 74F, which shows the oxygen gradient with decreases in concentration as it gets closer to the front surface. For this measurement, the oxygen-to-carbon ratio was taken as illustrated on Figure 74F using the EDS at discrete intervals from the rear surface.

4.5.3.2 Fracture surface of runout specimens

The cross-section at which the fracture occurred during residual strength test was 0 ± 3 *mm* for the one fatigue loaded with the peak stress of 92 MPa and 25 ± 3 *mm* for the other loaded with 105 MPa when measured from the specimen center, to which the direct heating was applied. The surface temperature at this cross-section was $1283 \pm 23^{o}C$ on the front, $950 \pm 5^{o}C$ on the side and $830 \pm 10^{o}C$ on the back for the former that failed at the specimen center, and $1025 \pm 25^{o}C$ on the front, $950 \pm 50^{o}C$ on the side and $845 \pm 5^{o}C$ on the back at the cross-section located at 25 ± 3 *mm* from the specimen center. Figure 75 and Figure 76 depict common microscopic features observed on the fracture surfaces obtained from the residual strength test of the runout specimens that survived the peak stresses of 92 MPa and 105 MPa, respectively.
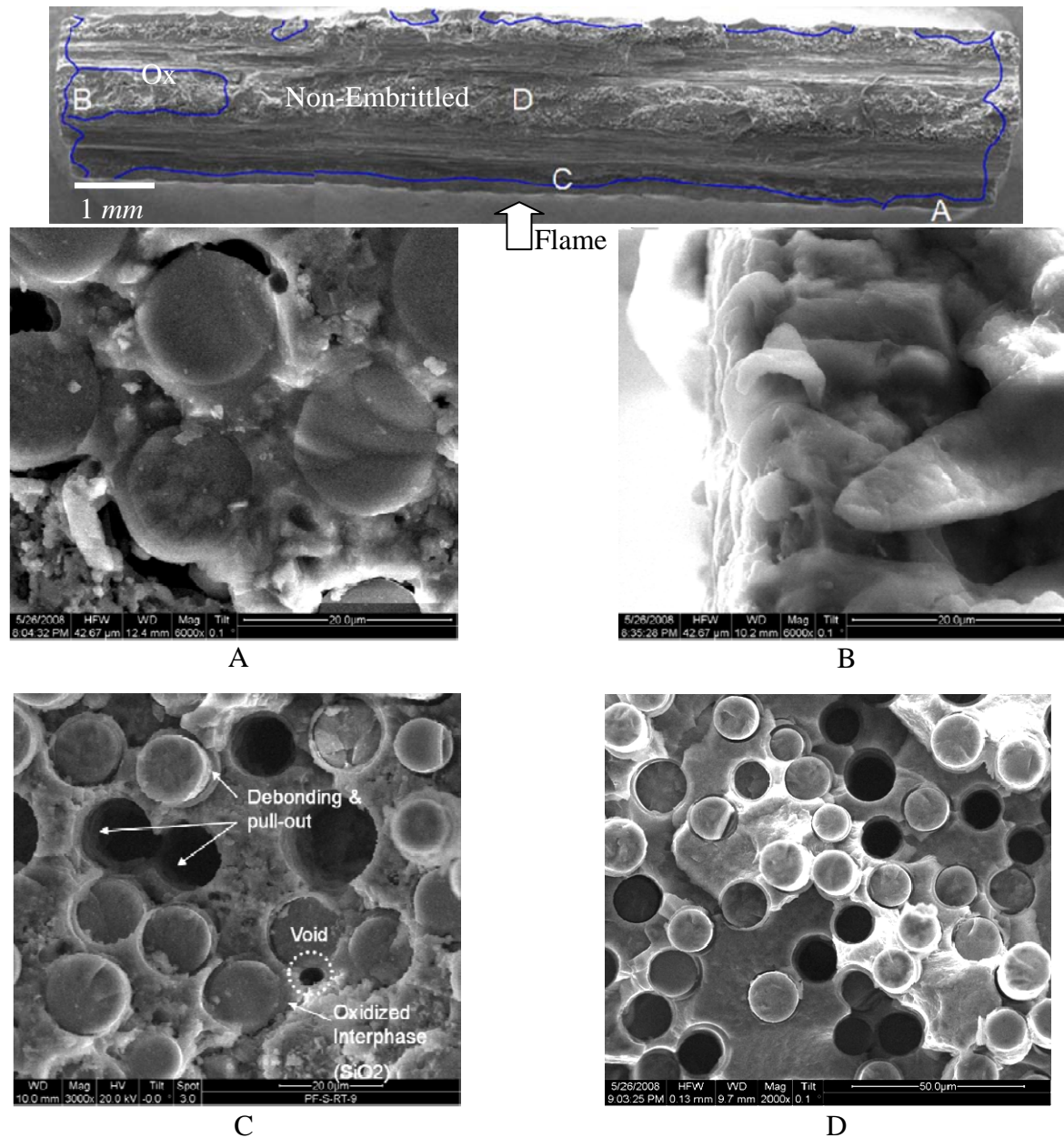
Figure 75: Fracture surface of the prepreg MI Hi-Nic-S/BN/SiC that survived peak stress of 92 MPa after residual strength test: A thru D are from the residual fracture surface as shown and denoted on the above figure.

157
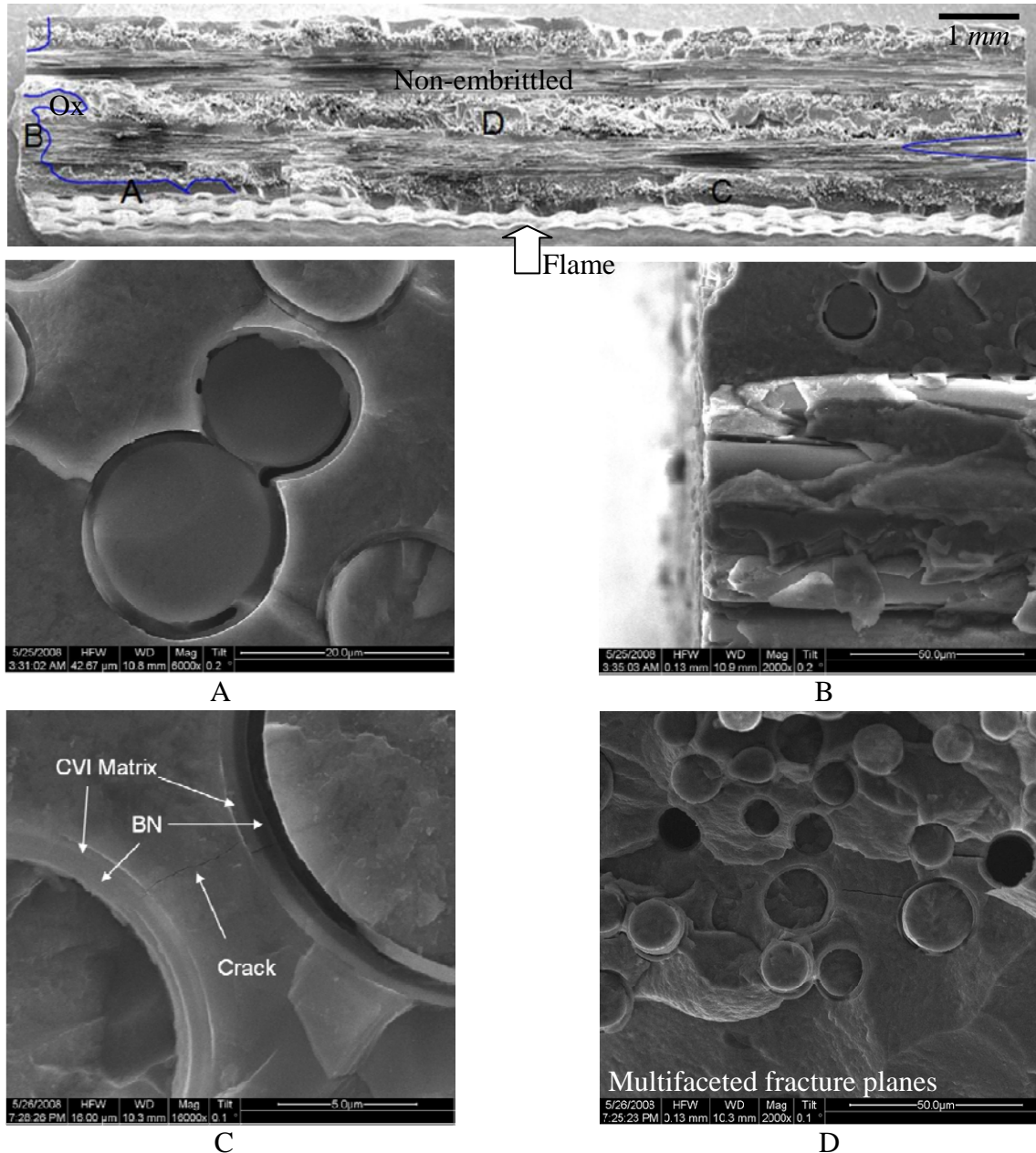
Figure 76: Fracture surface of the prepreg MI Hi-Nic-S/BN/SiC that survived peak stress of 105 MPa after residual strength test: A thru D are from the residual fracture surface as shown and denoted on the above figure.

Interphase oxidation was evident in Figure 75A and Figure 76A, and the edges and corners were seen oxidized as shown in Figure 75B and Figure 76B. The oxide overlayer was observed and confirmed using EDS. The MI matrix on the plies adjacent to the heated zone shown in Figure 75A and C has higher concentration of voids. The MI matrix on the fracture

surface of the runout specimen that survived under 105 MPa did not show as much spalled appearance in the matrix. This is likely due to substantially higher temperature at the cross-section of the residual fracture for the runout specimen that survived the peak stress of 92 MPa. As the higher moisture content at higher temperature increases the oxidation potential, the porosity, similar as those observed from the sectioned surface shown in Figure 78C, was observed to be more prevalent over the plies adjacent to the zone of direct flame impingement.

Pullout in the non-embrittled regions were very short as shown in Figure 75D and Figure 76D. Fracture planes surrounding fibers in the non-embrittled zone were often multifaceted as shown in Figure 76D, unlike planar crack surfaces of the woven MI CMCs. It appeared as if multiple cracks of different plane orientations have developed from the interphase of the fibers showing the multi-faceted crack planes. Figure 76C shows a crack in the MI matrix that appears to have linked with a fracture in the BN interphase. Such cracks are densely populated on fracture surfaces of both the runout specimens.

4.5.3.2 Oxidation on runout specimen

After the residual strength test of the runout specimen that survived under 105 MPa, the fractured piece that contained the heated zone was sectioned across the thickness in the area that experienced the direct flame impingement. The remaining of this piece encompassing the residual fracture surface and the sectioned surface was sectioned into four pieces along the longitudinal axis, in a similar way as done for the three woven MI CMCs. Micrographic observations made from these sectioned surfaces are discussed in the following section.

4.5.2.2.1 Sectioned perpendicular to loading

Figure 77 represents a cross-section cut along the width inside the gauge section of the runout specimen, which survived over 90,000 cycles under the fatigue loading with the peak stress of 105 MPa. Similarly to all the figures represented in the shown orientation, the flame was applied from the bottom of the image, and it impinged on the surface as indicated by the arrow.
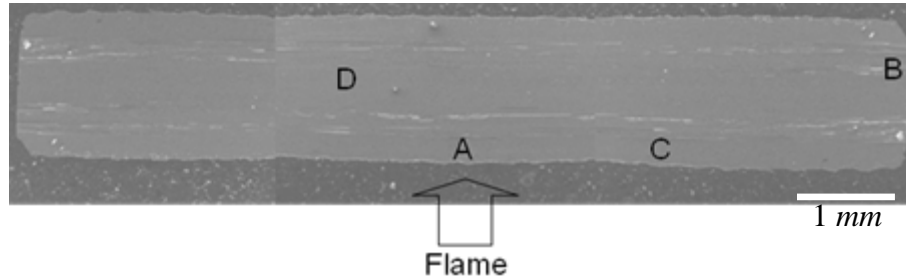
Figure 77: Polished section from heated zone of runout prepreg MI Hi-Nic-S/BN/SiC fatigued at 105 MPa

Detailed micrographic analyses using SEM and EDS revealed that glassy appearing oxides partially filled pores in the surrounding area of some fibers, as depicted in Figure 78A. Oxidation reactions involving formation of the oxides and outgassing of gaseous products could be speculated for the causes of the observed features. Edge oxidation was seen along the interphase in Figure 78B, although it was not as extensive and deep as in the cases with the woven CMCs.

The pores found in the MI matrix, such as the ones shown in Figure 78A and C, were observed to be more densely populated on the plies located closer to the flame impinged side, and the density of such pores in the matrix appeared to lessen with distance from the flame-impinged surface along the thickness direction in a gradient. This is illustrated in Figure 79, which compares three different states of the MI matrix representing different distances with respect to the flame impinged surface. There appeared to be debonding between the Si_3N_4 layer and the MI matrix through pores in Figure 79A. Pores have chemical contents of Si, C and O as in Figure

79D. A lesser degree of debonding was observed on the surface of the Si_3N_4 layer (Figure 79B) on a 0° fiber in the 3rd ply from the flame-impinged surface. A pore can be observed in the MI matrix close to the region where two fibers are joined. No debonding or pores were observed from the similar region on the ply closest to the unheated back surface (Figure 79C). It is noted that the phase of the MI matrix surrounding the fiber in the figure is predominantly Si. The gradient nature of these micrographic features including the post-test observed pores and debonding can potentially be investigated against the chemical, thermal and mechanical conditions, each of which varied in gradient. With this, the post-test observed porosity observed in the prepreg MI CMC and apparent gradient of such pores in distribution are now common characteristics found from all four CMCs.
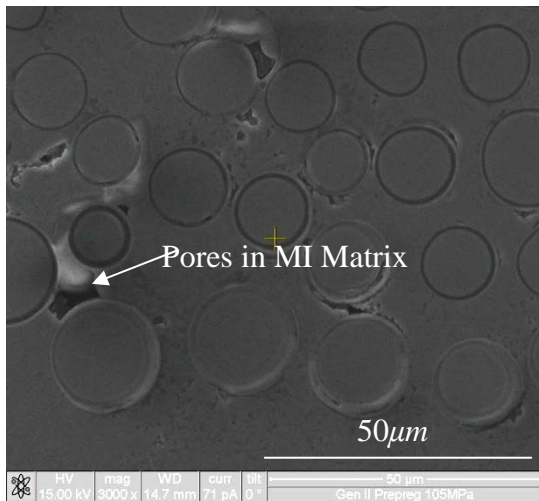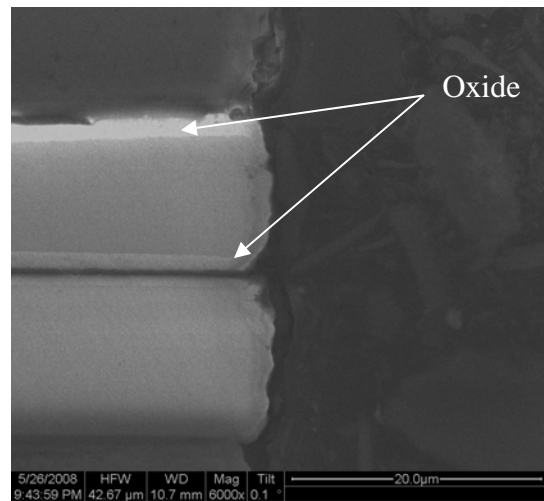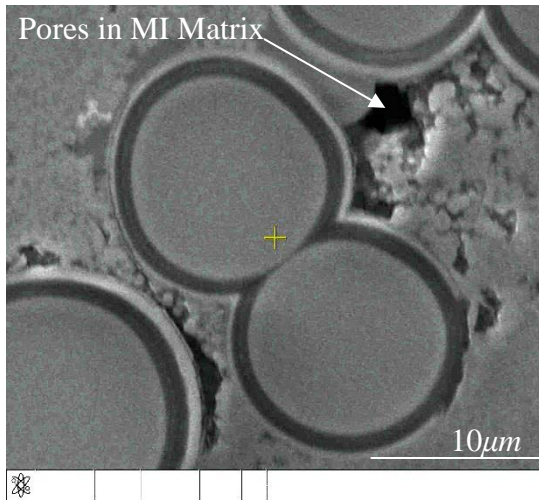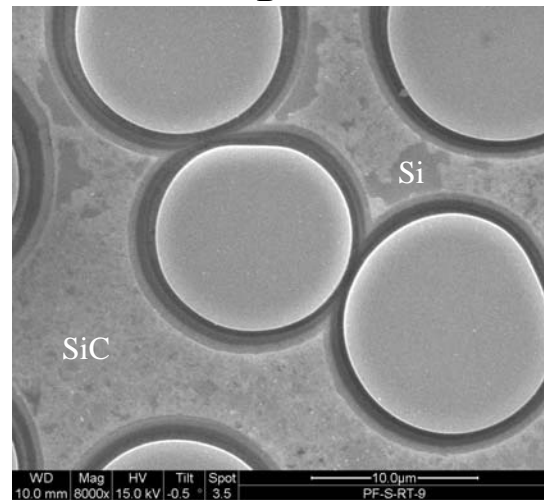
Figure 78: Microstructure of runout prepreg MI Hi-Nic-S/BN/SiC fatigued at 105 MPa sectioned in the heated zone
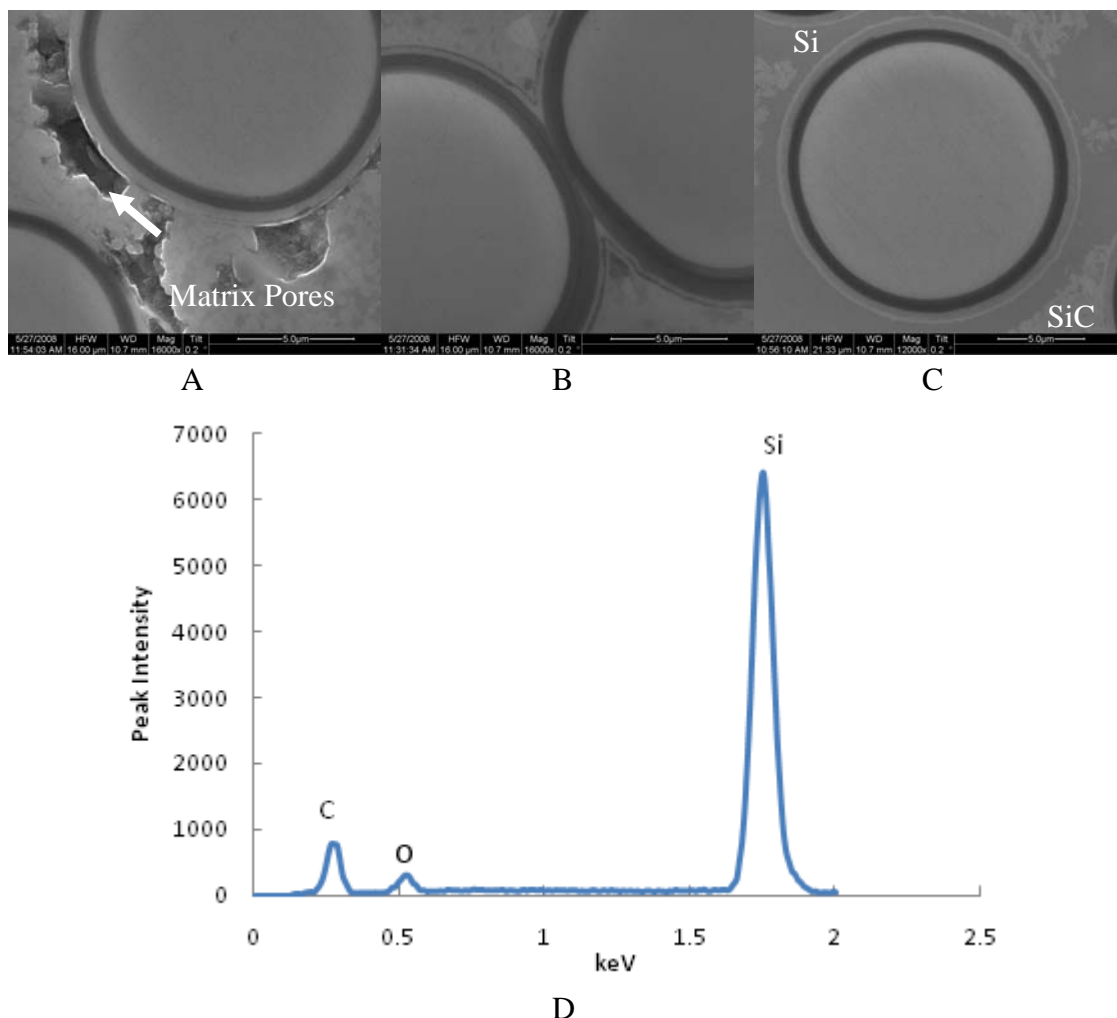
Figure 79: Gradient nature of pores in MI matrix; (A) 1st ply, (B) 4th ply, (C) 8th ply from impinged surface; (D) EDS in the porous area indicated in (A)

The mechanism by which the observed pores evolved is yet to be determined, though the fact that it appeared to involve the evolution of pores in place of the area used to be occupied by silicon metal leads to the speculation that chemical reactions, possibly enhanced by increase in temperature or applied mechanical stress, formed liquid glassy appearing phases (Figure 78A) and volatilized the solid state matrix into gaseous products through such chemical reactions as Equation (14). Oxygen contents in the pores also suggest that they may have been involved in migrating oxidants into the specimen interior.

4.5.2.2.2 Sectioned parallel to loading

Micrographic investigation of the longitudinally sectioned surfaces revealed that the cracks in the runout prepreg MI Hi-Nic-S/BN/SiC were predominant along the loading direction, especially in the 90° plies. The crack distribution from the optical inspection is summarized in Table 18. The longitudinal cracks were very long with the longest one exceeding 10 *mm* in the direction parallel to the loading. A segment of one such crack is represented in Figure 80. It could be that unidirectional plies are less resistant to damage from thermal gradients [118]. It is also notable from Table 18 that the longitudinal cracks are found predominantly on the two plies adjacent to the unheated back surface. Such longitudinal cracks are also referred to as the ply-splitting, as defined previously. Machined edge surface, which was exposed to the flame in the heated segment of a specimen, was used as a reference to describe the depth at which sectioning was made.

Table 18: Transverse (Trans) and Longitudinal (Long) cracks observed using optical microscopy: at different depths from the side surface

Crack Direction	Machined Edge Surface		2.5mm below the edge surface		5mm below the edge surface		7.5mm below the edge surface	
	Trans	Long	Trans	Long	Trans	Long	Trans	Long
1st	19	0	0	0	1	0	7	0
2nd & 3rd	26	0	7	1	5	1	13	0
4th & 5th	30	0	3	0	5	0	1	0
6th & 7th	19	0	0	9	0	4	4	4
8th	19	0	5	0	0	0	2	0
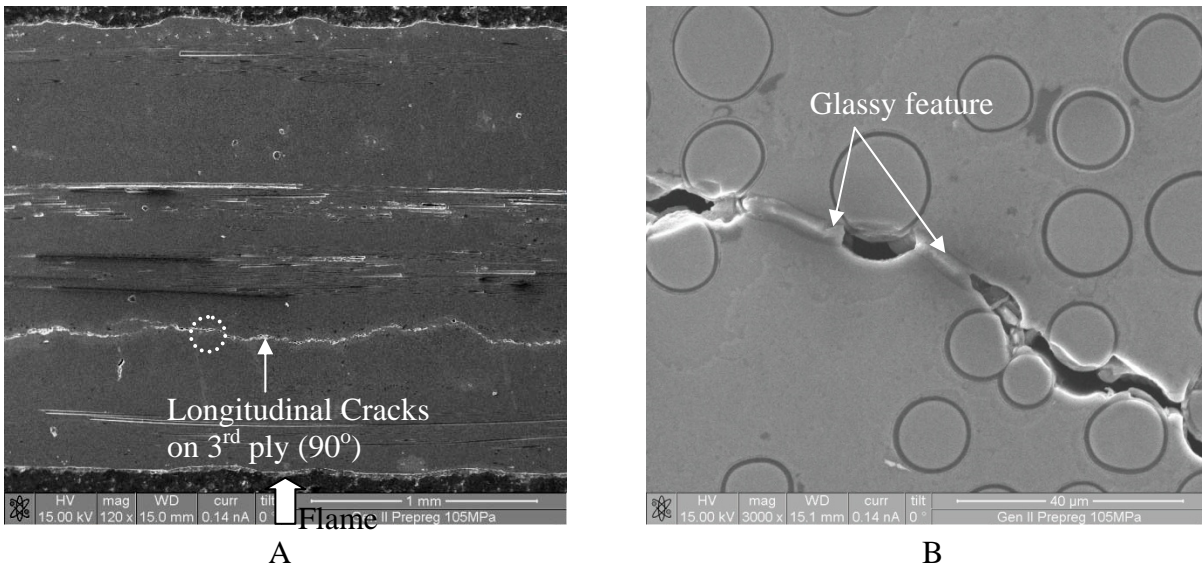
Figure 80: (A) A longitudinal crack found on the 3rd ply from the impinged surface; (B) encircled area in (A) showing glassy feature

Transverse cracks are ones in perpendicular to the loading directions and were populated heavily on the side surface along the edge exposed to combustion. On the other sections at the depths from the edge of 2.5, 5.0 and 7.5 *mm*, respectively, the number of transverse cracks was far less; a few that existed were located in the immediate vicinity of the fracture surface resulted from the residual strength test. No other discernable pattern pertinent to the transverse cracks could be identified from this optical inspection.

Unlike the woven MI CMCs, the prepreg MI Hi-Nic-S/BN/SiC does not have voids in the CVI matrix, and thus it has a very low porosity level, limiting oxidation. This was illustrated in Figure 81 which compares the SEM of the sections at different depths from the machined edge surface of the runout specimen.

| A | B | C |
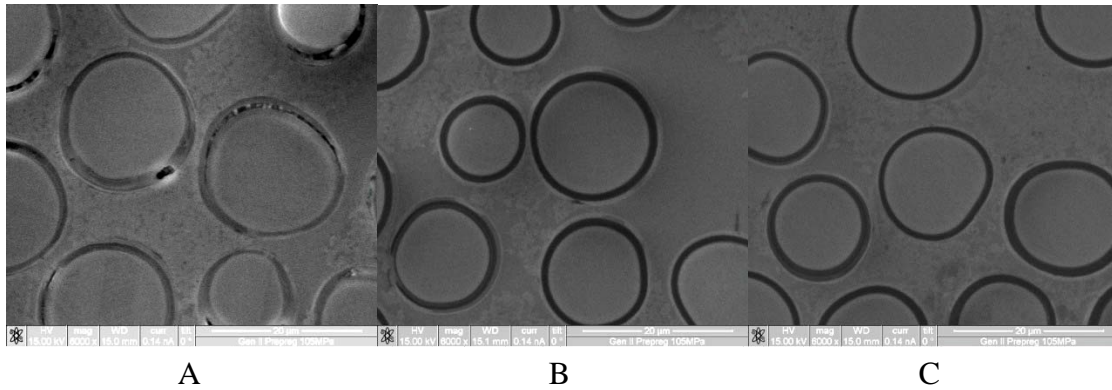
Figure 81: 90$^{\text{o}}$ ply at different depths: (A) side surface, (B), 2.5 *mm* deep, (C) 5.0 *mm* deep

The section representing the surface level with the side edge of the specimen shown on the left of Figure 81 documented oxidized interphase, which agreed with the observation made earlier in Figure 78B, taken perpendicular to the loading direction. The oxidation most likely occurred through the pipelined diffusion along the interphase. Outside of the voids near the front and back surfaces and the glassy appearing features randomly and sporadically found in the longitudinal crack paths, the rest of the specimen did not exhibit significant micrographic evidence that would indicate the level of permeation by oxidation into the material interior. Most of the longitudinal cracks did not show the formation of the glassy appearing features in their path. Instead, the cracks appeared to be a linearly array of voids in the MI matrix, as suggested in Figure 80. Debonding between the MI and CVI matrix appeared to be common over the entire surface investigated including in those area remote from cracks. In particular, the debonding appears to be accompanied by thinning of the CVI matrix. Due to the relative scarcity of the transverse cracks that would have been open to the environment, the interior of the material may have been left isolated from the oxidizing environment on the outside, and this was apparent from near pristine microstructure found in the interior of the runout specimen shown in Figure 77.

4.5.4 Section Summary

The fatigue behavior of the prepreg MI Hi-Nic-S/BN/SiC CMC in the prescribed combustion environment of this study was presented in this section. The S-N data were plotted that showed that the number of cycles to failure was inversely related to the applied peak stress. Two specimens survived at the peak stress of 105 MPa and 92 MPa after 25 hours of fatigue loading. These stresses correspond to 55 % and 41 % of their room temperature *PLs*. Each of the two runout specimens was subsequently tested for its residual strength under monotonic tension and failed after reaching 232 MPa at 0.38 % for the 105 MPa specimen and 264 MPa at 0.35 % for the 92 MPa specimen. The fractures occurred in parallel to the plane of a loading cross-section at 25 ± 3 *mm* and 0 ± 3 *mm* from the geometric center of each specimen, respectively. From the comparison with the failure strength and strain of 340 ± 19 MPa and 0.71 ± 0.12 % of the as-received material, it was evident that the runout specimens, though they did not fracture, underwent permanent degradation from the fatigue and combustion loading in their strength retention capability and its ability to exhibit significant inelastic strain before failure.

The microscopic examination of the fracture and sectioned surfaces from the fatigue testing showed oxidative features such as oxide overlayers, suggesting that the oxidative degradation could be related to the degraded mechanical properties observed. Many cracks were very long and aligned along the loading directions.

The MI matrix was observed, and its gradient nature was demonstrated. The matrix appeared to be spalled around the fibers in the vicinity of the flame-impinged surface, giving it an appearance of spallation. While the mechanism behind the spallation of the MI matrix remains to be determined, the micrographs are documented to suggest that it may not only influence the load carrying capability of the affected fibers, but also facilitate oxidation through the pores found in

the MI matrix. This phenomenon could be linked to the physical conditions of this study that showed similarly gradient nature such as chemical and thermal fields

4.6 Chapter Summary

Experiments were conducted to gain understanding of the degradation in fatigue behaviors of the four types of SiC/SiC CMCs in a combustion environment. Table 19 summarizes the test results and the observations from the fractographic study performed in this chapter. The observations from the monotonic, fatigue and residual strength tests carried out with the four types of SiC/BN/SiC CMCs are presented.

The data obtained from the fatigue and the residual strength tests are also presented in both absolute and relative units, the latter of which were computed by taking the fraction of the fatigue or retained strength with respect to the characteristic strengths such as the ultimate tensile strength (*UTS*) or the proportional limit (*PL*), which are obtained from the room temperature monotonic tension test of a pristine form of each CMC.

For one of the four CMCs, i.e. woven MI Hi-Nic-S/BN/SiC, similar fatigue tests were carried out in laboratory air furnace environment to access comparatively the effect of thermal gradients induced by the burner rig heating. Fatigue strengths from these tests were greater by relatively constant amount, i.e. 45 MPa, than those from the burner rig tests. This suggested that thermally induced stress added to the combined stress that resulted in lower fatigue strengths.

From the microscopic study of both fracture and sectioned specimens of all four CMCs, it was commonly observed that the extent of oxidation was observed to be larger for a lower peak stress applied, which resulted in a higher number of cycles to failure. The oxidized regions of fracture surfaces were characterized by planar fracture surfaces that showed fibers adhering to the

matrix through oxidized interphase. Oxide overlayer was commonly observed on the crack plane in the oxidized region, and they are the byproducts of the BN oxidation. Fiber pullout of various lengths was commonly observed in the non-embrittled portion of fracture surface. It was evident from the woven MI Hi-Nic-S/BN/SiC that fiber pullout length was indicative of the level of oxidation. The pullout length was long for the specimens that were tested at relatively high peak stresses and thus failed early, while the pullout was relatively short for the specimen fatigued at a lower peak stress that survived a longer period of fatigue loading in combustion environment.

Table 19: Summary of Test Results

Test type		Woven MI Syl-iBN/BN/SiC	Woven MI Syl/BN/SiC	Woven MI Hi-Nic-S/BN/SiC	prepreg MI Hi-Nic-S/BN/SiC
Monotonic	E (GPa)	207 ± 9	210 ± 12	195	264 ± 13
	UTS (MPa)	431 ± 26	271 ± 29	334	340 ± 19
	Strain (%)	0.5669 ± 0.024	0.2911 ± 0.046	0.5379	0.71 ± 0.12
	PL (MPa)	167 ± 7	153 ± 9	121	197 ± 23
Fatigue	Runout Peak Stress	110 Mpa	81 MPa	70 MPa	105 MPa
		0.26 *UTS*	0.30 *UTS*	0.21 *UTS*	0.31 *UTS*
		0.66 *PL*	0.53 *PL*	0.58 *PL*	0.55 *PL*
Residual Strength	Retained Modulus	189 GPa	200 GPa	203 GPa	247 GPa
		0.91 E	0.95 E	1.04 E	0.94 E
	Strength Retained	279 MPa	171 MPa	186 MPa	264 MPa
		0.65 *UTS*	0.63 *UTS*	0.56 *UTS*	0.78 *UTS*
	Retained Strain	0.34%	0.13%	0.22%	0.35%
		0.60 Strain	0.44 Strain	0.41 Strain	0.48 Strain
	Proportional limit Retained	167 Mpa	147 MPa	144 MPa	156 MPa
		1.00 *PL*	0.96 *PL*	1.19 *PL*	0.79 *PL*

Pores observed from the four CMCs were induced by either processing or the applied test conditions. Those that showed oxygen contents and demonstrated the concentration gradient that decreases with respect to the distance from the flame-impinged surface were termed post-test observed pores and documented on all four CMCs. Pores can not only reduce the mechanical

properties of a material by lowering stiffness, but also they can serve as preferred path of oxidation into the specimen interior.

V. Comparisons among Four CMCs

This chapter presents the comparisons of the fatigue test data for the four CMCs discussed individually in the previous chapter. To address two of the objectives of this study, comparisons are made with the emphasis on identifying the effects of the characteristic differences among them, which are the presence of *iBN* fiber coating and the different processing methodologies. The comparisons lead to the identification of a material with the highest potential for application in a gas turbine engine environment. Further, based on the insights gained from this comparative analysis, a new material system that would combine the benefits of each material system is also suggested.

5.1 Overall comparison of all the S-N curves
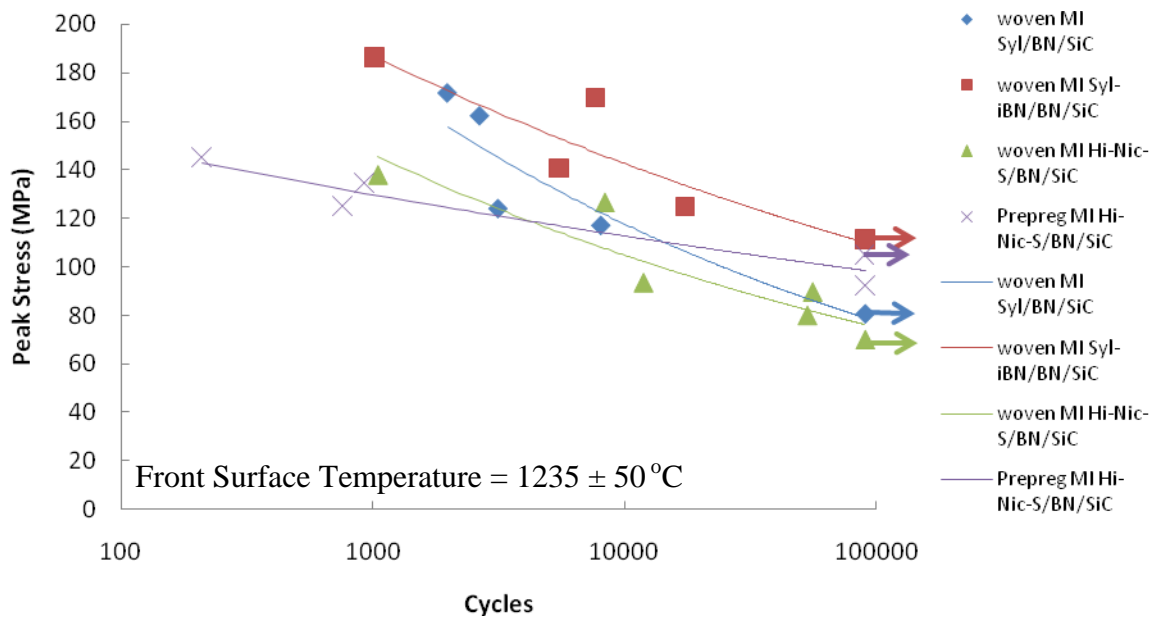
Figure 82: S-N Data for all four CMCs

Shown in Figure 82 are the applied peak stresses plotted against the corresponding cycles at failure for all the specimens tested in this study. For the four CMCs, whose *UTSs* at room temperature differ from 271 ± 29 MPa of the woven MI Syl/BN/SiC to 431 ± 26 MPa of the woven MI Syl-*iBN*/BN/SiC, the fatigue runout strengths converge to a relatively small range of stresses from 70 to 110 MPa, as shown in the plot. In comparing the four S-N curves, the woven MI Syl-*iBN*/BN/SiC demonstrated the longest cycles-to-failure for a given peak stress, while the shortest fatigue life for a given peak stress was attained by the woven MI Hi-Nic-S/BN/SiC. Another interesting observation was that the prepreg MI Hi-Nic-S/BN/SiC showed a distinctly different trend from those exhibited by the three woven MI CMCs. The slope of the S-N curve for the prepreg MI CMC is distinctively lower than those for the three woven MI CMCs. This could be attributed to the dense matrix of the prepreg MI CMC and will be discussed in further details in the section that compares the prepreg and the woven MI Hi-Nic-S/BN/SiC CMCs.

To investigate for a possible correlation of the observed knockdown in fatigue strength caused by the test condition to the mechanical properties, two additional S-N curves were plotted with the peak stresses normalized, for one, with respect to the room temperature ultimate tensile strength (*UTS*) and, for the other, with respect to the proportional limit (*PL*) obtained from the room temperature monotonic tension testing of an as-received specimen of each kind. The two plots are shown in Figure 83 and Figure 84.
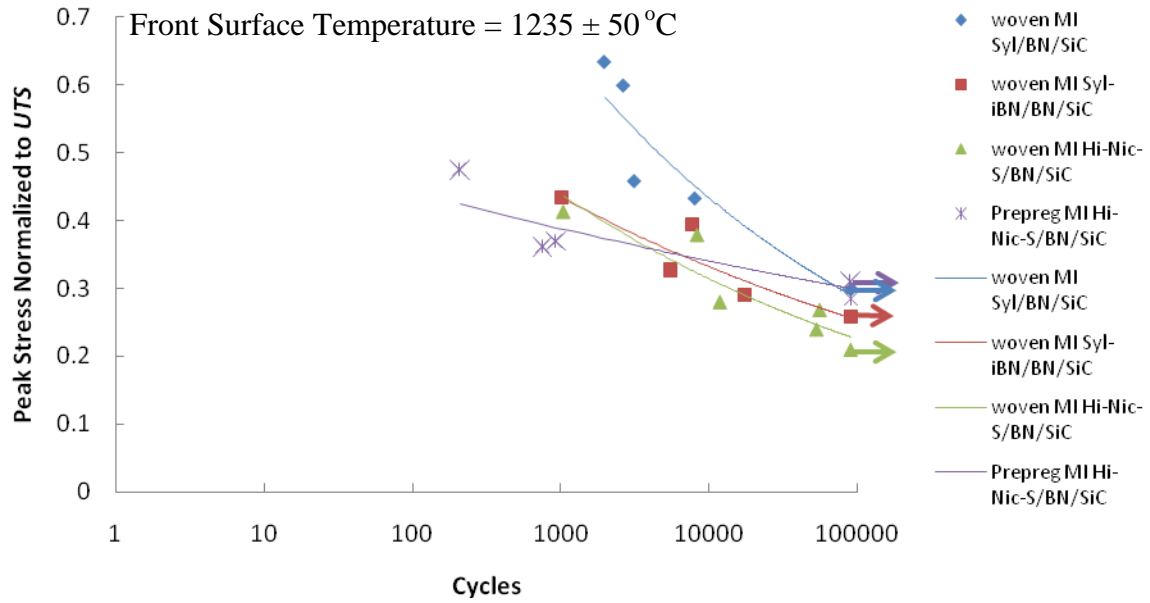
Figure 83: S-N Data with peak stresses normalized against *UTS*
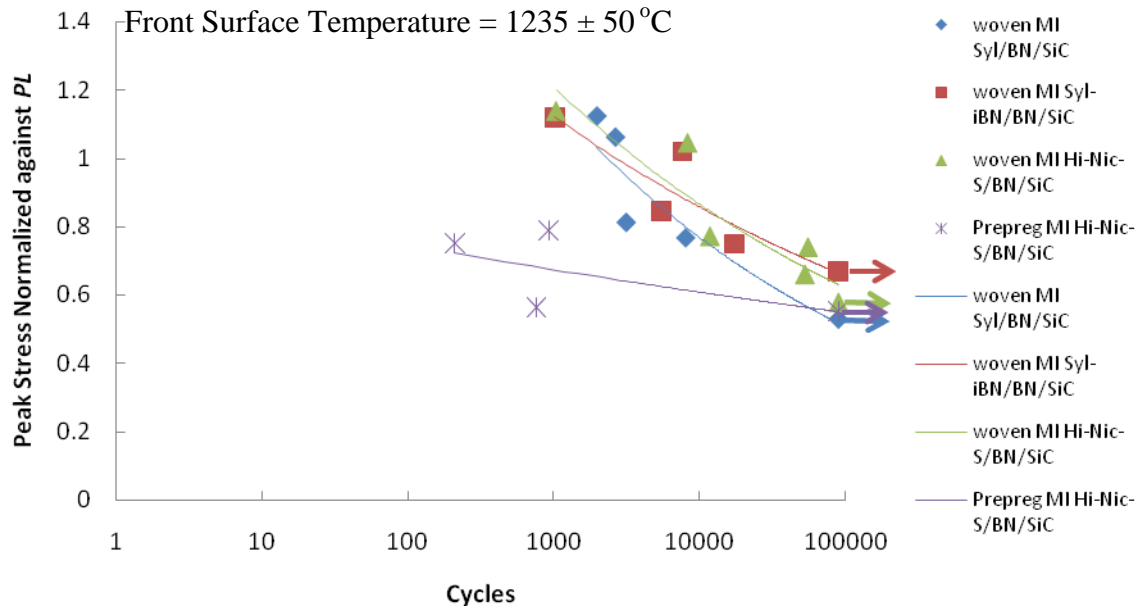
Figure 84: S-N Data with peak stresses normalized against *PL*

From Figure 83, it is difficult to draw any conclusive trend that would suggest a potential correlation between the fatigue strength and the *UTS*. The two CMCs with relatively low *UTSs*,

the woven MI Syl/BN/SiC and the prepreg MI Hi-Nic-S/BN/SiC are the ones with smaller fractions of knockdown in fatigue strength than those with the large *UTSs*. The fatigue strength decreases with increasing number of applied cycles, independently of the oxidation [96]. With oxidation, the bridging fibers undergo oxidative degradation, deteriorating the fracture toughness of the CMC. However, the elastic properties remained relatively unchanged before and after the fatigue test in the combustion condition. This is because the elastic properties are determined largely by the intrinsic properties of the matrix, which is relatively slow to change with respect to time. On the other hand, the reduced fracture toughness is the product of the failure in the fiber-bridging mechanism due to oxidative degradation, which can occur rapidly at a rate determined by the propagation of cracks and the oxidation kinetics. The property associated with the matrix cracking phenomenon is the proportional limit (*PL*). For an applied stress below the "knee" of the stress-strain curve, which ranges from 170 MPa to 200 MPa for the four CMCs of this study, the fatigue behavior may be characterized by partial cracks in the matrix, and the cracks provide environmental access to bridging fibers. Therefore, while the data normalized with respect to the *UTS* remained as an important measure of the change in its strength, it could be the normalization against *PL* that may bear more relevance to the state of cracking in the matrix, through which oxidation occurs.

The peak stresses for all specimens tested normalized against the *PLs* are, therefore, plotted with respect to the cycles-to-failure, as shown in Figure 84. In comparing the fatigue strengths of the four CMC systems at the test runout condition, the woven MI Syl-*iBN*/BN/SiC survived without fracture at the peak stress level equivalent to 67% of its *PL*, while the other three CMCs attained the runout at the stress level equal to 55 ± 3% of their respective room temperature *PLs*. While the stress level that resulted in runout seemed low at first, it was shown

174

that matrix cracks nucleate and develop well below *PLs* [48] In addition, there are thermal gradient stresses, in addition to the applied stress level, which could increase the local stress beyond the matrix cracking stress. Assuming similar thermal gradient stresses and similar cracking behaviors in the matrix for the four CMCs, the woven MI Syl-*iBN*/BN/SiC was subjected to a higher state of matrix cracking among all the test specimens that resulted in runout. This observation indicates for the possibility that the in-situ BN layer coated on the Sylramic fiber of the woven MI Syl-*iBN*/BN/SiC may be accounted for the improved resistance to failure at a higher state of matrix cracking.

The above comparisons of the S-N data among different materials provide an overview of the discussion that follows in the remainder of this chapter, which features detailed comparisons among the four CMCs tested. First, a direct comparison is made between the woven MI Syl/BN/SiC and the woven MI Syl-*iBN*/BN/SiC. This comparison discusses the effectiveness that the in-situ BN fiber coating has on slowing degradation in the combustion environment. Then, the comparison is extended to include the woven MI Hi-Nic-S/BN/SiC. All three woven MI CMCs are compared, which sets up an ensuing comparison between the woven MI Hi-Nic-S/BN/SiC and the prepreg MI Hi-Nic-S/BN/SiC. While the comparisons remain qualitative in nature due to a number of secondary parameters that differ among different CMCs, such as the fiber volume fraction and the number of plies, the discussion is carried out with the understanding that recognizes and examines possible ramifications for the difference in the secondary parameters on the main difference highlighted by the comparisons.

It is important to emphasize that the combustion heating generates a complex three-dimensional field of thermal gradient stress such that it adds to or subtracts from the applied fatigue stress. For instance, there is estimated 100 MPa of the tensile thermal gradient stress

acting on the unheated surface, which adds to the mechanically applied stress of 110 MPa to constitute a local stress condition of 210 MPa on the back surface of specimen. The magnitude of the thermal gradient stress varies with the location on the specimen. For simplicity, however, the thermal gradient stress is not considered in the present discussion, as the similar thermal gradient stress field was subjected to all the CMCs in this study. A more in-depth discussion of the thermal gradient stress is presented in conjunction with the development of a failure mechanism in the next chapter.

5.2 Effect of the iBN layer

The woven MI Syl-*iBN*/BN/SiC and the woven MI Syl/BN/SiC are nearly identical in terms of its composition, architecture as well as the level of matrix porosity and the fiber volume fraction. Both have the silicon-doped boron nitride as the interphase, and their microstructures are nearly identical. A distinct difference that exists between the two CMCs is the pre-treatment that added a thin layer of in-situ BN coating on the fibers for the woven MI Syl-*iBN*/BN/SiC.

5.2.1 Monotonic Results

The room temperature monotonic stress-strain curves for the two CMCs are shown in Figure 85. They show similar stress-strain behaviors until the woven MI Syl/BN/SiC fractures first at the strain of 0.32%. The woven MI Syl-*iBN*/BN/SiC did not fail until the strain of 0.54% was reached. The strengths of the two fibers, Sylramic and Sylramic-*iBN* are almost equal [122]. Thus, the fiber strength is eliminated from consideration as a factor responsible for the observed deviations in the two stress-strain curves. It was suspected that the difference might stem from the different interactions between the fiber and the interphase under tension. The fiber-interphase interaction between the Sylramic-*iBN* fiber has a lower surface roughness, compared to the

176

Sylramic fiber [79], and thus is morphologically more favorable surface to induce a better debonding and sliding mechanism under monotonic tension. This gave rise to a larger strain and an increased strength, as compared to the fiber-matrix interaction between titanium boride (TiB_2) or boron carbide (*BC*) [79, 121] on the Sylramic fiber and the BN interphase of the woven MI Syl/BN/SiC. Due to the proprietary nature of the processing details of these CMCs, the information or experimental work that may validate this observation is not available on a public domain. However, it could be speculated that the surface of the Sylramic fiber with TiB_2 finish may have been rougher than the *iBN* on the Syl-*iBN* fiber, based on the fact that the ultimate tensile stress and the corresponding strain are highly sensitive to the surface finish and roughness of the fiber [120].

In addition to the difference in stress and strain, the two CMCs exhibited slightly different proportional limits; 167 ± 7 MPa for the woven MI Syl-*iBN*/BN/SiC and 153 ± 9 MPa for the woven MI Syl/BN/SiC. The difference could be considered within the scatter. The monotonic stress-strain data not only allow the baseline comparison that increases the understanding of two materials in their pristine state, but they also provide the mechanical properties to which the fatigue data can be related such that a qualitative assessment of the physical implication of the strength knockdown experienced by the applied test condition can be drawn. Physical phenomena or characteristics such as matrix cracking and material strength can be interpreted in reference to the material properties such as proportional limit (*PL*) and the ultimate tensile strength (*UTS*), respectively. Hence, normalizing the applied stress against them facilitates the interpretation of the fatigue test data in terms of matrix cracking and fracture toughness. It also provides common bases in comparing CMCs with different mechanical behaviors.
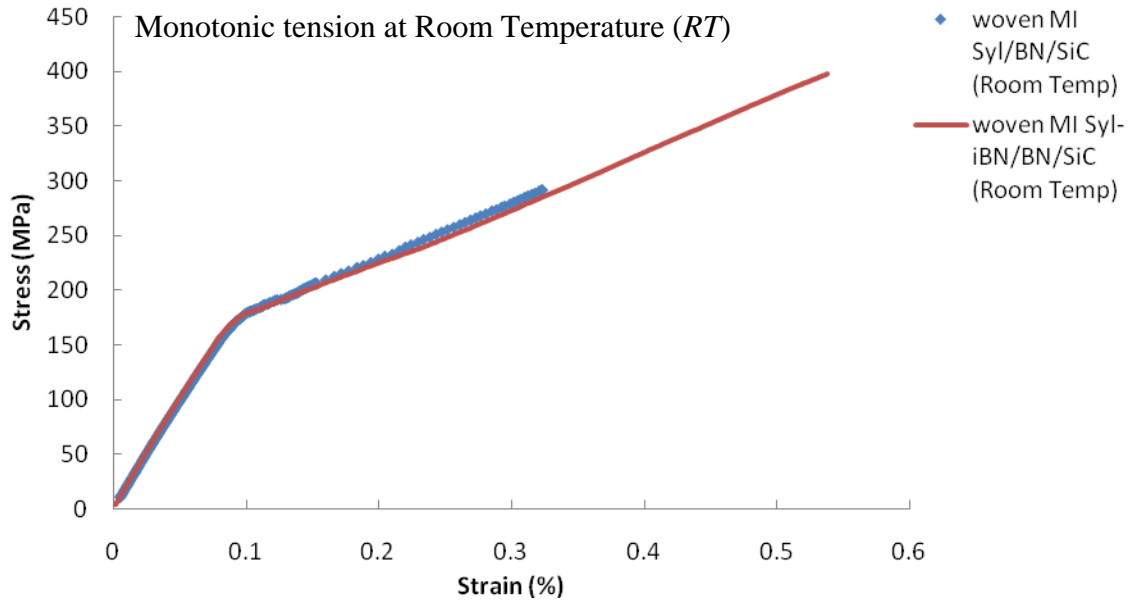
Figure 85: Stress strain curves for the woven MI Syl-*iBN*/BN/SiC and the woven MI Syl/BN/SiC

5.2.2 S-N Curve comparisons

It was evident from Figure 86 that the woven MI Syl-*iBN*/BN/SiC had a higher cycles-to-failure for a given peak stress than the woven MI Syl/BN/SiC. However as illustrated in Figure 87, due to the relatively low *UTS* of the woven MI Syl/BN/SiC, its relative knockdown in strength with respect to the *UTS* was less than the decrease in strength experienced by the woven MI Syl-*iBN*/BN/SiC with relatively large *UTS* of 431 ± 26 MPa. This suggests that *PL* may be a reference that relates better to the fatigue characteristics of a material. On the other hand, the S-N curves plotted with peak stresses normalized against the *PL*, shown in Figure 88, exhibited very similar trends to those in Figure 86. The similarity comes from the relative closeness in their *PLs*. Based on the results shown on Figure 86 and Figure 88, it could be stated that the woven MI Syl-*iBN*/BN/SiC with the higher *PL* of 167 ± 7 MPa survived a higher number of cycles than the

178

woven MI Syl/BN/SiC with the *PL* of 153 ± 9 MPa for a given peak stress as well as for a given

peak stress normalized against *PL*.
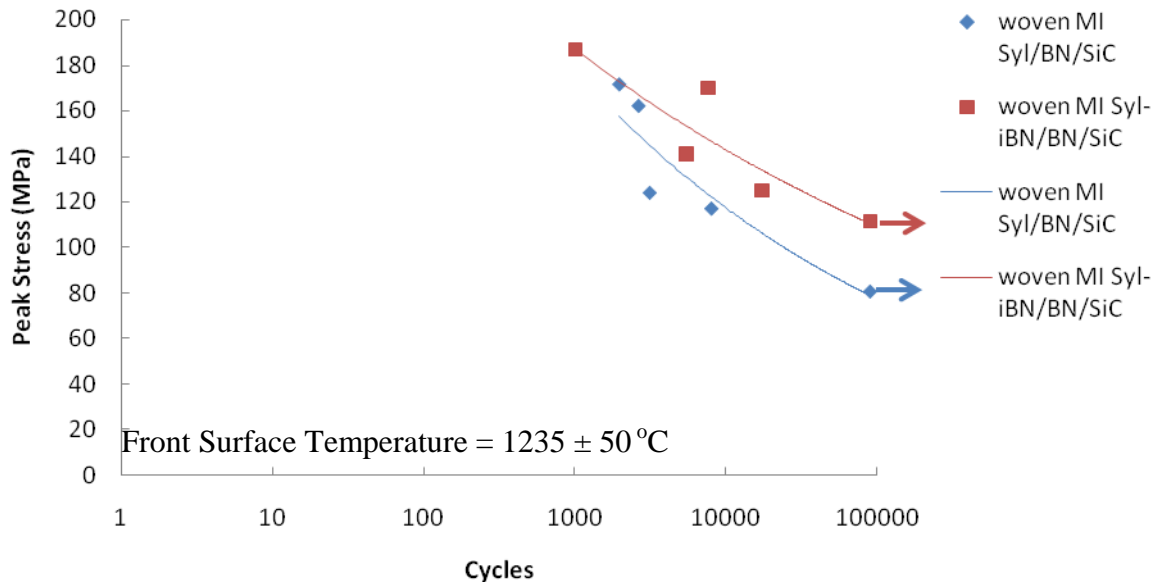
Figure 86: S-N data of the woven MI Syl-*iBN*/BN/SiC and the woven MI Syl/BN/SiC
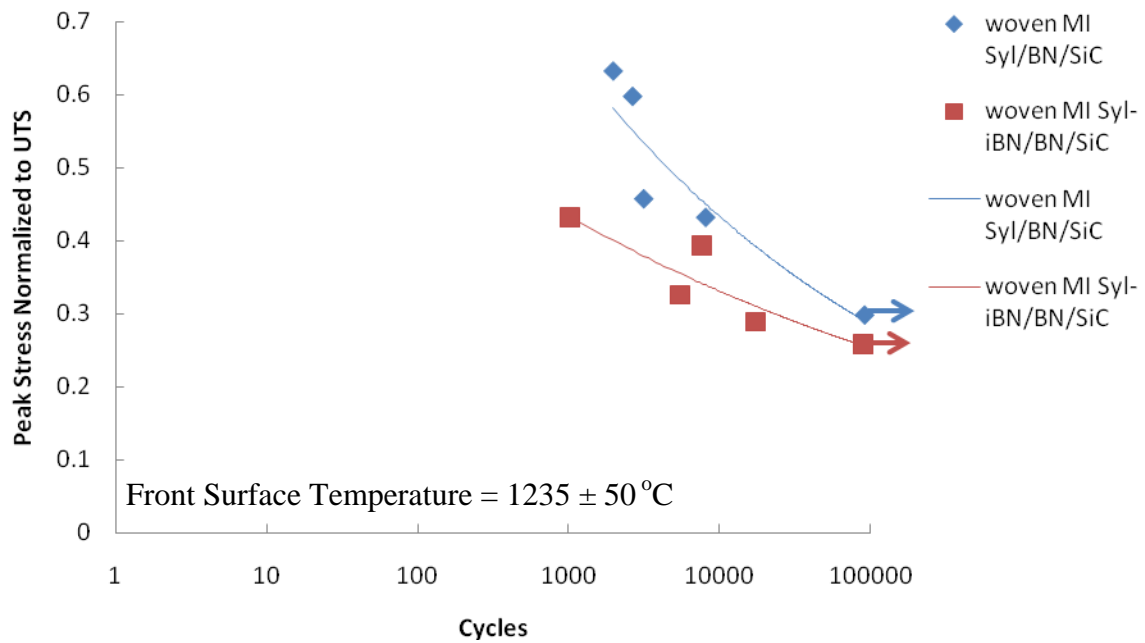
Figure 87: S-N data with peak stress normalized against *UTS*
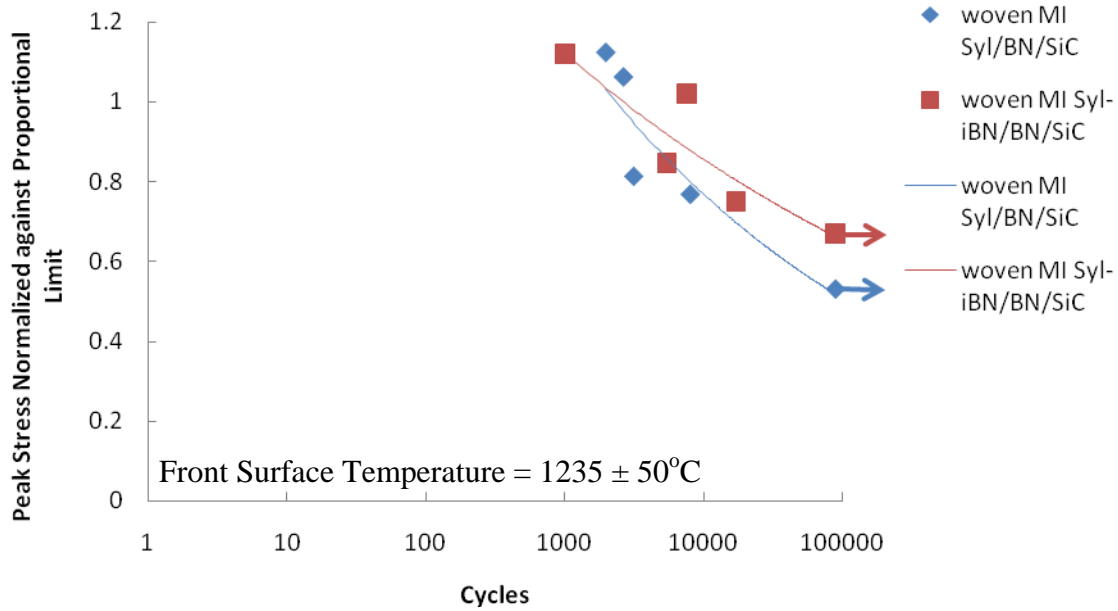
Figure 88: S-N data with peak stress normalized against *PL*

5.2.3 Extent of oxidation

To compare the effects of oxidation in deteriorating the mechanical properties of the two CMCs, analyses were performed for the two materials tested at similar peak stresses. For this, two different stress levels of 170 MPa and 125 MPa were selected, the former of which is higher than the *PL* of either CMC, while 125 MPa is equivalent to 75% of the *PL* for the woven MI Syl-*iBN*/BN/SiC and 81% of the *PL* for the woven MI Syl/BN/SiC.

5.2.3.1 Syl vs. Syl-iBN at the same stress 170 MPa and 125 MPa

At the peak stress of 170 MPa, the size of the oxidized area, marked by "Ox" on each fracture surface on Table 20, appeared to be similar. However, it took approximately 4 times as long for the woven MI Syl-*iBN*/BN/SiC to fail. At the peak stress of 125 MPa, the Sylramic-iBN MI CMC survived nearly 6 times the cycles that the other lasted, with only a slight difference in

the size of the oxidized region between the two surfaces. The size of the oxidized area was assumed to relate with the extent of oxidation under the assumption that the four CMCs are governed by the same oxidation chemical kinetics involving the BN interphase oxidation. Micrographic studies of these surfaces found no features that were unique to either type of CMC; the observations including the adherence of neighboring fibers as well as the formation of oxide overlayers involved no distinguishable difference in appearance, and their fiber pullout in their non-embrittled regions were similar in physical appearance including their lengths. Understanding that the level of matrix cracking under a given stress is similar for the two CMCs with relatively similar proportional limits, the observation that it took several times longer to cause failure to the woven MI Syl-*iBN*/BN/SiC than to cause failure to the woven MI Syl/BN/SiC, which displayed the similar extent of oxidation after having undergone the same test condition, indicates that the in-situ BN fiber coating of the woven MI Syl-*iBN*/BN/SiC not only kept neighboring fibers from coming in direct physical contact with one another and thus lessened the probability of premature failure, but also served as an additional layer that slowed down the oxidation, making it less prone to the degradation of mechanical properties induced by oxidation.

Relatively short time it took for the woven MI Syl/BN/SiC to oxidize the similar size of fracture surface area after four or six times as long an exposure to the same combustion environment suggests the following: First, the woven MI CMC with in-situ BN fiber coating experienced a slower advancement of the oxidation front and thus was less susceptible to oxidation than the woven MI Syl/BN/SiC. Secondly, the woven MI Syl/BN/SiC with a thin carbon layer containing B and Ti between the Sylramic fiber and the BN interphase may have experienced a faster degradation. The carbon-content on the Sylramic fiber of the woven MI Syl/BN/SiC could oxidize and recede faster than the BN interphase on its outer surface, exposing

the inner surface to an oxidizing environment. This could allow the degradation of the deeper part of the material interior. This oxidation was referred to as "Type II" degradation by Ogbuji, and was seen only in high-temperature, high-velocity burner rig environment. [77].

Table 20: Comparisons between the woven MI Syl-*iBN*/BN/SiC and the woven MI Syl/BN/SiC fatigued at peak stress of 170 MPa and 125 MPa

Peak Stress (MPa)	CMC Type	Fracture Surface	Cycles-to-failure
170	Woven MI Sylramic-*iBN*/BN/SiC		7937
	Woven MI Sylramic/BN/SiC		1979
125	Woven MI Sylramic-*iBN*/BN/SiC		17384
	Woven MI Sylramic/BN/SiC		3146

1 mm

5.2.4 Residual Strength Comparisons

The stress-strain curves obtained from the residual strength test of the runout specimens for the two CMCs are plotted in Figure 89. The stress-strain behaviors of the two CMCs in pristine state at room temperature are also shown in semi-transparent lines of the same color.
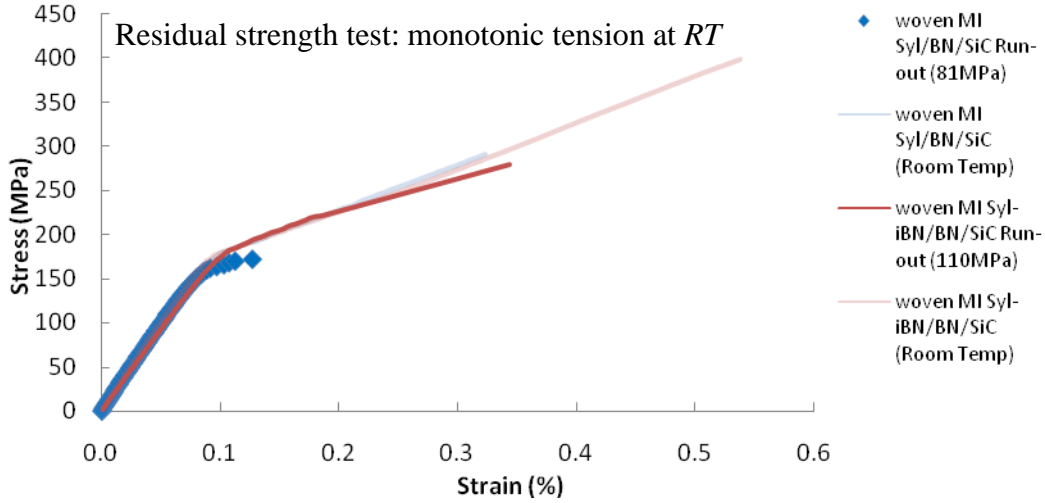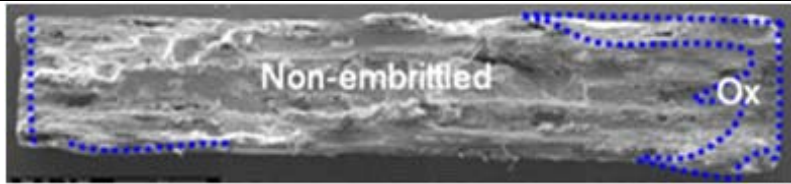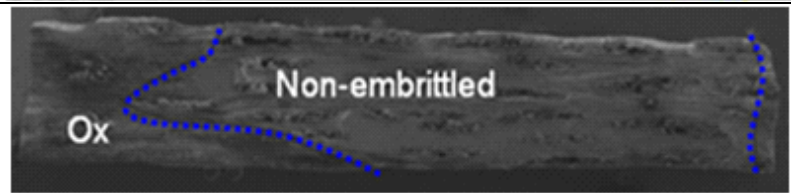
Figure 89: Residual stress-strain curves for the woven MI Syl-*iBN*/BN/SiC and the woven MI Syl/BN/SiC

The runout specimens were obtained at the peak stress equivalent to 67% and 53% of the *PLs* for the woven MI Syl-*iBN*/BN/SiC and the woven MI Syl/BN/SiC, respectively. Assuming similar cracking behaviors and thermal gradient stresses, the woven MI Syl-*iBN*/BN/SiC with 67% of the *PL* applied in fatigue can be assumed to have undergone a greater level of matrix cracking. The two runout specimens were subsequently tested for residual strength, and the strength and strain retained by the runout woven MI Syl-*iBN*/BN/SiC specimen was 279 MPa and 0.34%, which were 65% and 61% of the room temperature *UTS* and its corresponding strain, respectively. In comparison, the strength retained by the runout woven MI Syl/BN/SiC with presumably less matrix cracking was 171 MPa, 63% of the *UTS* at the strain equivalent to only 44% of the strain corresponding to the *UTS*. Based on these results, it can be stated that both the runout specimens have accumulated permanent damage from the fatigue loading. In addition, though the runout MI Syl-*iBN*/BN/SiC retained the higher strength at 279 MPa, the fraction of the *UTS* it retained compares evenly with that of the runout woven MI Syl/BN/SiC despite having undergone the fatigue loading with a higher peak stress. A larger strain retained by the woven MI

Syl-*iBN*/BN/SiC, together with its higher retained strength, makes the woven MI Syl-*iBN*/BN/SiC a material with higher resistance to the degradation than the woven MI Syl/BN/SiC for the applied condition. On the basis of these observations along with the overall higher fatigue strength at a given fatigue life, the woven MI Syl-*iBN*/BN/SiC was a better material for structural application that undergoes fatigue loading in an oxidizing environment similar to the applied condition in this study.

Table 21 shows the fracture surfaces obtained from the residual strength tests of the two runout specimens of the woven MI Syl-*iBN*/BN/SiC and the woven MI Syl/BN/SiC, respectively. Both the runout specimens failed approximately at 19 *mm* from the geometric center, which was outside the zone in which the flame was directly impinged. With the same gas temperature and chemistry assumed to have interfaced with both the specimens at this cross-section during the fatigue tests, oxidation appeared to have been more pervasive in the woven MI Syl/BN/SiC, as indicated by its relatively large oxidized area.

Table 21: Fracture surfaces from residual strength tests of the runout specimens representing the woven MI Syl-*iBN*/BN/SiC and woven MI Syl/BN/SiC

Peak Stress (MPa)	CMC Type	Residual Fracture Surface	Residual Strength (MPa)
110	Woven MI Sylramic-*iBN*/BN/SiC		279
81	Woven MI Sylramic/BN/SiC		171

1 mm

The fraction of the oxidized area to the entire fracture surface was approximately 0.24 for the runout MI Syl-*iBN*/BN/SiC and 0.31 for the MI Syl/BN/SiC. With a simplifying assumption that no stress was carried by the fibers in the oxidized area, the residual strength was estimated by multiplying the room temperature *UTS* to the fraction of the non-embrittled area. The assumption is based on the general understanding of the mechanics of fiber-reinforced composites that involves the intact portion of the cross-section supporting the applied load. There are experimental results from other studies that support this assumption [77,123,124]. The strength supported by the intact fibers outside the oxidized area was estimated to be 327 MPa, which is higher than the actual retained strength of 279 MPa. Similarly, the strength carried by the intact fibers of the runout woven MI Syl/BN/SiC specimen was estimated to be 187 MPa, off by about 9% from the actual retained strength of 171 MPa. The estimated strengths were overestimated by 17% and 9% for the two runout specimens. The overestimations can most likely be attributed to the simplistic approach taken based on the area estimation of the non-embrittled regions on the fracture surface. It is highly probable that a fair amount of oxidation damage could be sustained by interphases before they can be visible on the surface. A conservative estimation of the oxidized area due to the subtlety associated with determining the oxidative microscopic features using the SEM as well as the unaccounted fraction of the weak fibers that are known to fail upon initial loading [50] regardless of matrix cracking may be probable causes for the overestimations. In addition, even a small amount of erosion at the interphase surface during 90,000 cycles of the fatigue loading could have altered the parameters that govern the load transferring between fiber and the interphase (e.g. interphase roughness) and changed the load carrying capability of the fibers in the non-embrittled region. This simplistic methodology using the area fraction on the fracture surface to estimate the retained strength or strength at failure was performed on the

185

majority of the tested specimens as a check to validate the measurements. The analysis suggested a means to correlate the oxidation information obtained from microscopic analysis to the mechanical properties at the time of failure.

The preceding discussions involved the comparisons of the woven MI Syl-*iBN*/BN/SiC and the woven Syl/BN/SiC in the degradation of mechanical properties induced by the simultaneous loadings of mechanical fatigue and an oxidizing combustion environment. The experimental data as well as the comparative analysis of the reduced data such as the oxidation on fracture surface for both materials indicated that the woven Syl-*iBN*/BN/SiC was more resistant to the damage from oxidation and fatigue loading and that it retained a higher strength and strain for a given peak stress.

5.3 Effect of fiber

The comparisons discussed in the preceding section between the two MI CMCs using Sylramic and Sylramic-*iBN* fibers are now expanded in this section to include the third woven MI SiC/BN/SiC using the Hi-Nic Type S fiber or Hi-Nic-S fiber. The comparisons are thus focused on the effect of the fiber type on the performance of the CMCs.
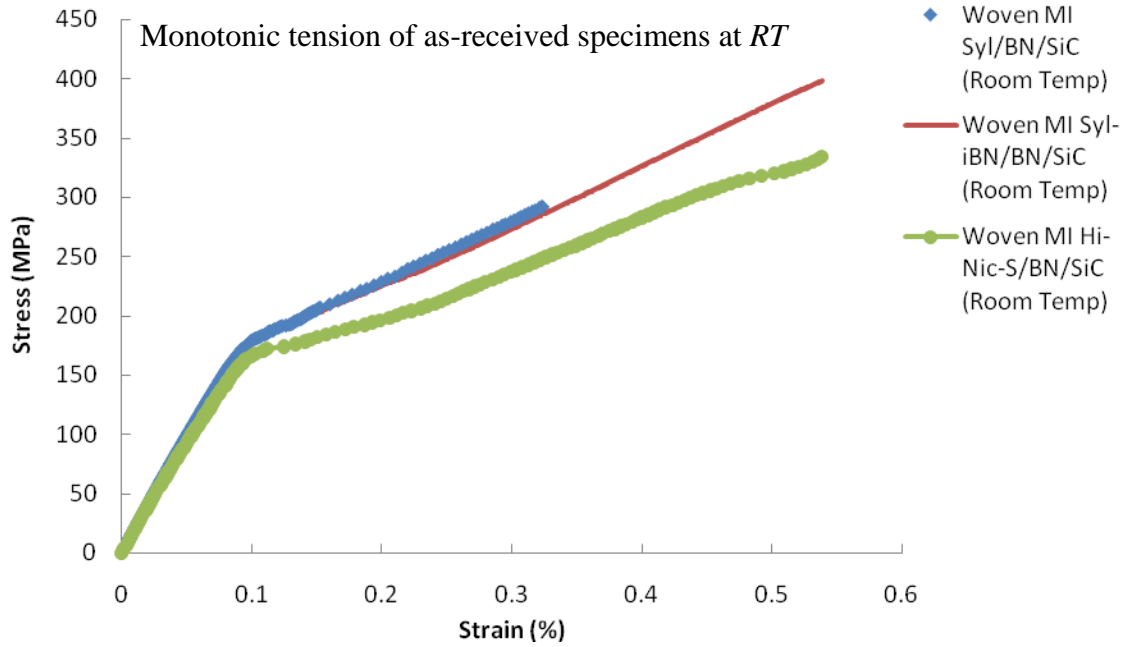
Figure 90: Stress-strain curves representing each of the three woven CMCs under monotonic tension at room temperature

5.3.1 Monotonic Results

Figure 90 shows the monotonic stress-strain curves for three woven MI CMCs under room temperature monotonic tension. In the elastic regime, the woven Hi-Nic-S/BN/SiC CMC shows the modulus of elasticity of 194 GPa, slightly smaller than those of the other two CMCs using Sylramic-based fibers. Its proportional limit is 121 MPa, considerably less than 167 ± 7 MPa and 153 ± 9 MPa of the other two CMCs. The lower proportional limit of the woven MI Hi-Nic-S/BN/SiC CMC could be due to the higher porosity and lower fiber volume fraction. Above the "knee," the stress-strain curve of the woven MI Hi-Nic-S/BN/SiC shows a lower slope as compared to the other two. In addition, its *UTS* is lower than that of the woven MI Syl-*iBN*/BN/SiC, while the strains at failure for the two CMCs are similar.

The woven MI Hi-Nic-S/BN/SiC has the fiber volume fraction of 35.7 vol%, as compared to the 38~40 vol% of the other woven MI CMCs using Sylramic-based fibers. The Hi-Nic-S fiber has the elastic modulus of 410 ± 10 GPa, very similar to 400 GPa of both Sylramic and Sylramic-*iBN* fibers. Due to its slightly lower fiber fraction, the stress borne by each fiber for a given global stress is expected to be somewhat greater. It should also be mentioned that the strength comparison of the strengths of any two CMCs with different dimensions must be considered with the caution that the woven MI Syl/BN/SiC with the surface-to-volume ratio of 1.5 may have a higher strength than the woven MI Hi-Nic-S/BN/SiC with smaller surface-to-volume ratio of 1.1. The defect that initiates fracture is often on the surface of the specimen and the rupture strength increases with increasing the surface-to-volume ratio [125]. With the dimensions of both specimens relatively large, millimeter scale in size as well as with the stress-to-volume ratio that differs by less than 30%, it was assumed that the size effect does not influence the specimen strength.

In addition to slightly different stresses on fiber for the three CMCs that share the similar processing techniques, there may have been other factors that contributed to their different stress-strain behaviors. One such factor is the morphological difference in the fiber surface finish that can change the effectiveness of the fiber-bridging mechanism. The fiber bridging mechanism can also be affected by the difference in interphase properties and conditions such as surface roughness and misfit stress exerted on the fiber and interphase during the MI process. This is suggested by much longer fiber pullout by the woven MI Hi-Nic-S/BN/SiC. The carbon content and the surface roughness associated with the thin carbon layer finish on the Hi-Nic-S fiber surface may have resulted in the observed pullout behavior [49]. Another potential factor is porosity. The difference in the stress-strain response can be dominated by different mechanical

behaviors of the MI matrices of two materials with different porosity. The porosity was determined using the optical microscopy, followed by post-processing of the images using the Photoshop that used its built-in function to detect the fraction of the voids or pores. From this analysis, it was shown that the porosity of the woven MI Hi-Nic-S/BN/SiC was greater than the two Sylramic-fiber reinforced CMCs by approximately 50%. Based on its low proportional limit, the woven MI Hi-Nic-S/BN/SiC can be presumed to develop matrix cracks at lower stress. Pores in the matrix often have the geometry with high stress concentration and thus, nucleating a crack originating from such pores is facilitated at relatively lower stress. The higher porosity of the woven MI Hi-Nic-S/BN/SiC could be due to greater thickness through which the MI infiltration had to occur for the 8-ply system of the woven MI Hi-Nic-S/BN/SiC, as compared to the two Sylramic reinforced CMCs with 6 plies in each [40]. There may be additional small differences such as the impurity types and amounts. However, they are not expected to factor into room temperature mechanical properties. Most of the processing parameters such as the impurities are proprietary information, so that a detailed comparative analysis in regard to the effect of these parameters could not be further investigated in this study.

The fatigue strengths of the three woven MI CMCs at the test runout condition were found to be in the same order as their room temperature *PLs*. The woven MI Syl-*iBN*/BN/SiC with the highest *PL* attained the highest peak stress that resulted in runout, and the woven MI Hi-Nic-S/BN/SiC with the lowest *PL* achieved the lowest fatigue strength at runout. This result indicates that the fatigue strength may be directly related to the proportional limit. While the data may not be substantial to validate this conjectured correlation, further efforts in this direction may be warranted for the tremendous payoff in potentially projecting the results from a simple room

temperature test to those from a more complicated fatigue testing in a burner rig or other representative environments for typical turbine engine operation.

5.3.2 S-N curve comparisons

The life data obtained from the fatigue testing of all three woven SiC/BN/SiC CMCs in a combustion environment are plotted as peak stresses versus cycles at failure as shown in Figure 91. The fatigue life of the woven MI Hi-Nic-S/BN/SiC was the lowest at any applied stress level. Also, its runout fatigue strength of 70 MPa was below the runout stresses of the other two woven MI CMCs.
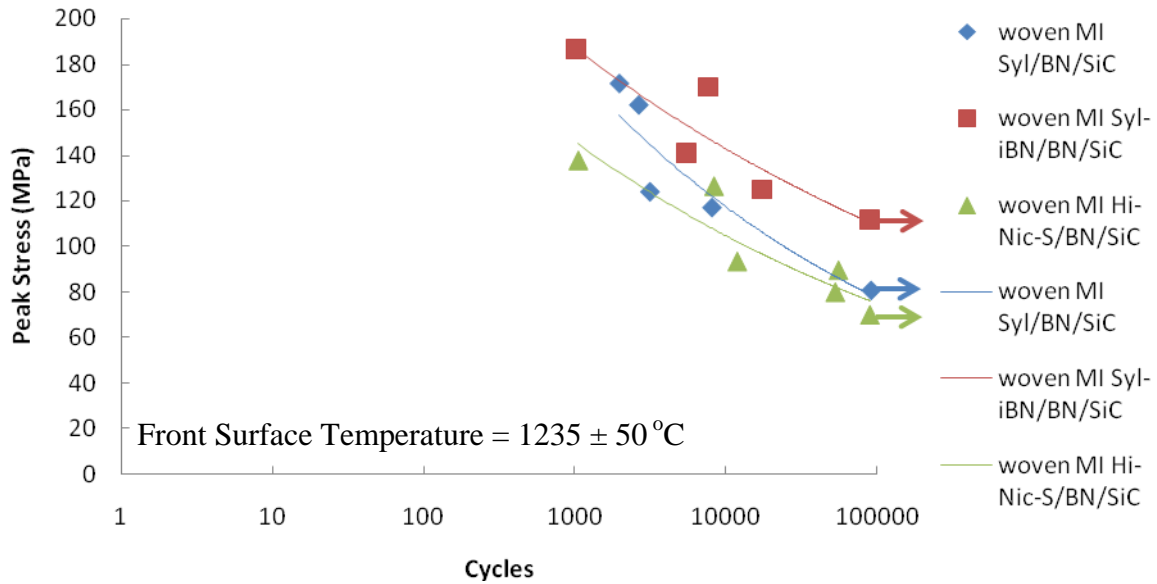
Figure 91: S-N data for the three woven MI CMCs

As discussed in the previous section, the relative fatigue strength with respect to the *UTS* was higher for the woven MI Syl/BN/SiC due to its relatively low *UTS*, as indicated on Figure 92. From the monotonic stress-strain data earlier, it was noted that the failure of the woven MI Syl-*iBN*/BN/SiC and the woven MI Hi-Nic-S/BN/SiC occurred at different *UTSs* with very similar strain-at-failure. Thus, a side-by-side comparison that involves the peak stresses normalized to the

UTS would be more appropriate between the two MI CMCs exhibiting the similar strain behavior, namely the woven MI Syl-iBN/BN/SiC and the woven MI Hi-Nic-S/BN/SiC. From Figure 92, the fatigue life of the latter was slightly lower than that of the former, which suggests that the woven MI Hi-Nic-S/BN/SiC experienced a relatively larger decrease in strength with respect to its *UTS*. The slopes of the two curves are also indicative of the rate of the damage accumulation with respect to the number of cycles, and the S-N curve for the woven MI Hi-Nic-S/BN/SiC with a steeper slope suggests that its degradation occurs faster than that of the woven MI Syl-*iBN*/BN/SiC.
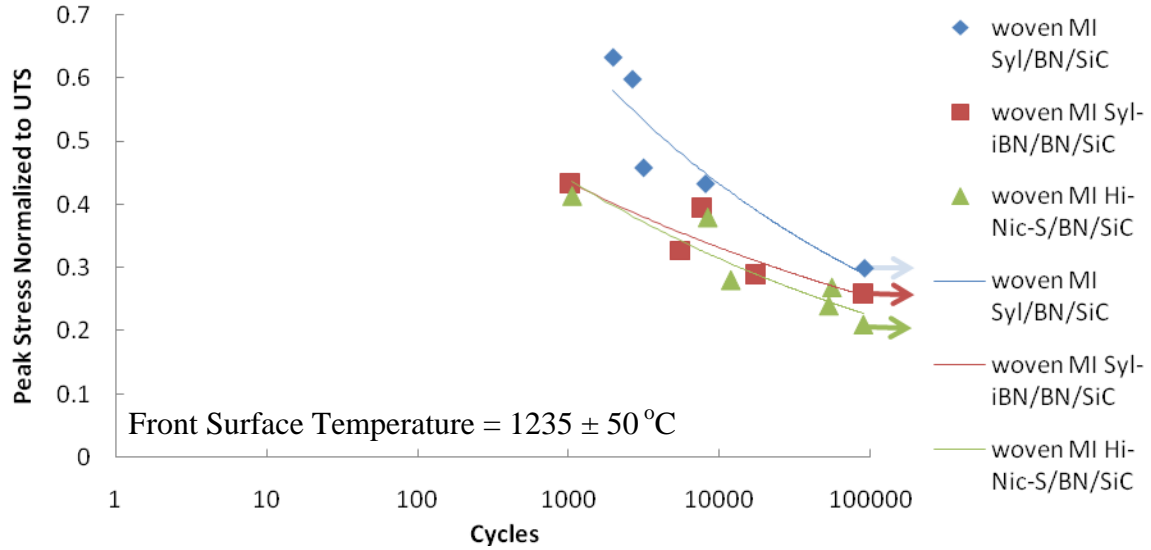
Figure 92: S-N Data with peak stress normalized against *UTS*

Finally, the peak stresses were normalized to the proportional limits (*PL*) of their respective CMCs and were plotted against cycles at failure, as shown in Figure 93. The S-N curves for the woven MI Hi-Nic-S/BN/SiC and the woven MI Syl-*iBN*/BN/SiC CMCs almost lie together, except at the high-cycle end of the curves where the runout of the woven MI Hi-Nic-S/BN/SiC was attained at a lower peak stress. The strain corresponding to a given peak stress would be the highest for the woven MI Hi-Nic-S/BN/SiC than other two systems based on the

monotonic test results in Figure 90. Therefore, the woven MI Hi-Nic-S/BN/SiC is expected to develop relatively more damage during fatigue for a given stress. In addition, the fatigue strength at runout for the two CMCs other than the one with the in-situ BN coating are relatively similar, i.e. 53% and 58% of their respective *PLs*, while the woven MI Syl-*iBN*/BN/SiC with the in-situ BN coating showed considerably higher the peak stress level of 67% of its *PL*. Recalling that the *PL* of the woven MI Syl-*iBN*/BN/SiC was the highest, followed by the woven MI Syl/BN/SiC and the woven MI Hi-Nic-S/BN/SiC, this observation adds to the earlier finding that the woven MI Syl-*iBN*/BN/SiC outperforms the other woven MI CMCs.
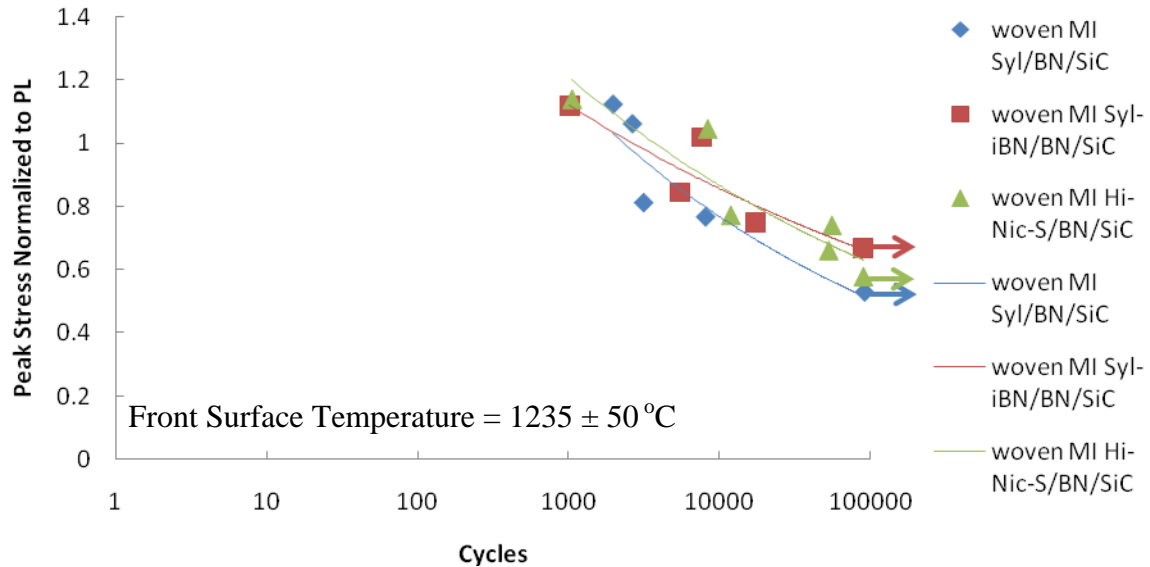
Figure 93: S-N Data with peak stress normalized against *PL*

5.3.3 Fractographic comparison

To compare the effect of oxidation on the S-N behavior for the three woven MI CMCs, the fracture surfaces of the three CMCs tested at the very similar applied peak stresses of 125 ± 2 MPa were investigated under SEM and EDS. This is shown in Table 22. The applied peak stress of 125 MPa selected for comparison is equivalent to 75% of the *PL* for the woven MI Syl-

iBN/BN/SiC and 81% of the *PL* for the woven MI Syl/BN/SiC, and 100% of the *PL* for the woven MI Hi-Nic-S/BN/SiC. If the thermal gradient stress of 100 MPa on the back surface is considered, the local stress state would be higher than the *PL* in all three CMCs.

In comparing the woven MI Syl-*iBN*/BN/SiC with the woven MI Hi-Nic-S/BN/SiC, the fracture surface of the latter shows significantly larger oxidized area than the other surface. Further, this larger oxidized area was attained over about half the number of cycles than that of the woven MI Syl-*iBN*/BN/SiC. The higher porosity level in the woven MI Hi-Nic-S/BN/SiC may have facilitated the oxidation deeper into the interior of the specimen. The woven MI Syl-*iBN*/BN/SiC was less affected by oxidation, as indicated by its considerably smaller oxidized area in Table 22

The longer fatigue life and smaller oxidized area exhibited by the woven MI Syl-iBN/BN/SiC could be due to its relatively high *PL* for the applied stress. The 125 MPa applied to the woven MI Syl-*iBN*/BN/SiC is 75% of the *PL* for the woven MI Syl-*iBN*/BN/SiC, while the same is equal to 105% of the *PL* for the woven Hi-Nic-S/BN/SiC. With higher stress level, the woven MI Hi-Nic-S/BN/SiC would have a larger number of matrix cracks, which could not only deteriorate the load bearing capability by coalescing into larger cracks, but also induce the oxidative degradation by facilitating the ingress of oxidants. Furthermore, the woven MI Hi-Nic-S/BN/SiC has a higher porosity in its matrix, making it susceptible to matrix cracking. Hence, the matrix cracking in the woven MI Hi-Nic-S/BN/SiC should be even more extensive, which may explain why the larger area fraction of oxidized region was observed on the woven MI Hi-Nic-S/BN/SiC.

Table 22: Fractured surfaces of the three woven MI CMCs failed under the same peak stress of 125 MPa

Peak Stress (MPa)	CMC Type	Fracture Surface	Cycles-to-failure
125 ± 2	Woven MI Sylramic-*iBN*/BN/SiC		17384
	Woven MI Sylramic /BN/SiC		3146
	Woven MI Hi-Nic-S /BN/SiC		8329

1 mm

On the comparison of the MI Syl/BN/SiC and MI Hi-Nic-S/BN/SiC, the area fraction of the oxidized region for the Hi-Nic-S MI CMC is considerably greater than the Syl MI CMC. The applied peak stress of 125 ± 2 MPa was 105 % of the *PL* for the Hi-Nic-S MI CMC, as compared with 81% of the PL for the Syl MI CMC. Thus, the Hi-Nic-S MI CMC in a greater relative stress with respect to the *PL* would presumably be at a more highly developed state of matrix cracking. The higher porosity in the Hi-Nic-S MI CMC may have also given way to oxidation such that a larger oxidized area was attained on the MI Hi-Nic-S/BN/SiC. However, the MI Hi-Nic-S/BN/SiC showed a greater fatigue life than the Syl MI CMC at the common peak stress of 125 ± 2 MPa. This observation is opposite of the one from the earlier comparison, which showed the woven MI Syl-*iBN*/BN/SiC has the higher fatigue life than the woven MI Hi-Nic-S/BN/SiC. This could be, in part, attributed to the absence of the in-situ BN coating. It may also be attributed to the scatter in the experimental data, as the fatigue life of the two were separated by relatively low
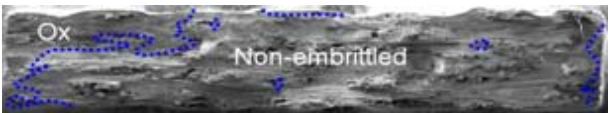
cycles of 5183, in comparison to the total number of cycles at runout of 90,000. The larger

relative oxidized area of the woven MI Hi-Nic-S/BN/SiC could be due to its high porosity level,

combined with the peak stress that exceeded its *PL* and a longer exposure in combustion.

5.3.4 Comparisons of three CMCs at 75% of *PLs*

From the S-N curves with the stress scale normalized with *PL*, it was observed that the

fatigue strength of the woven MI Syl-*iBN*/BN/SiC for runout was at the peak stress that equals to

67% of the *PL*, whereas the runouts for the other woven MI CMCs with no in-situ BN coating

were at the lower relative peak stress of $55 \pm 3\%$. The difference is attributed to the presence of

in-situ BN coating. However, there exists a probability for a wide variability in number of cycles

at which failure would have occurred, had the test not been terminated at 90,000 cycles.

Thus, the analysis was taken a step further in this direction to involve the comparisons of

the CMCs that underwent the peak stresses equal to the same fraction of their respective *PLs*.

Subjected to the same peak stress level in relation to their respective *PLs*, an initial assumption is

that the three materials would have similar level of matrix cracking, as the modulus of each fiber

making up the three CMCs are very similar and the strains corresponding to their respective *PLs*

are relatively close to one another, i.e. $0.077 \pm 0.01\%$. For this analysis, three specimens

representing each CMC underwent the peak stress of 75% of their *PLs* were selected. Because the

PL of each CMC is different, the peak stress corresponding to 75% of the *PL* is also different. The

peak stresses corresponding to 75% of *PL* are 125 MPa for the MI Syl-*iBN*/BN/SiC, 117 MPa for

the MI Syl/BN/SiC and 90 MPa for the MI Hi-Nic-S/BN/SiC, respectively. Table 23 shows the

fracture surfaces of the three CMCs fatigue loaded to the specified peak stresses.

195

Table 23: Fractured surfaces of the three woven MI CMCs failed under peak stresses equivalent to 75% of their respective *PLs*

Peak Stress (*%PL*)	CMC Type	Fracture Surface	Cycles-to-failure
75	Woven MI Sylramic-*iBN*/BN/SiC (125 MPa)		17384
	Woven MI Sylramic/BN/SiC (117 MPa)		8059
	Woven MI Hi-Nic-S/BN/SiC (90 MPa)		55664

1 mm

For the two MI CMCs using Sylramic and Syl-*iBN* fibers with similar *PLs* that underwent 75% of their *PLs*, the fatigue life of the MI Syl-*iBN*/BN/SiC was greater than that of the MI Syl/BN/SiC for the similar fractions of the oxidized area. This result reinforces the observation made earlier from the comparison between the two CMCs at the peak stress of 125 MPa that the *iBN* coating may have inhibited oxidation for the woven MI Syl-*iBN*/BN/SiC.

Between the woven MI Syl/BN/SiC and woven MI Hi-Nic-S/BN/SiC with *PLs* of 153 MPa and 121 MPa, the applied peak stresses corresponding to 75% of the *PLs* are 117 MPa and 90 MPa, respectively. From Table 23, it can be seen that MI Hi-Nic-S/BN/SiC has a substantially larger oxidized area with a longer fatigue life than the MI Syl/BN/SiC. Due to considerable difference in their *PLs*, the stress values corresponding to 75% of their *PLs* are quite different as well. With the understanding that the matrix cracking is an important consideration related with the proportional limit, it is imperative to evaluate the stress state in each CMC under the applied

load level. Evidently, the stress state of the woven MI Syl/BN/SiC under 117 MPa will be higher than that of the woven MI Hi-Nic-S/BN/SiC under 90 MPa.

If it is assumed that the strain behaviors of the two materials are similar under a given load, based on the earlier findings that the fiber volume fractions of the two materials are relatively similar and that the two fibers, the Sylramic and the Hi-Nic-S fibers, are very similar in terms of modulus of elasticity, the woven MI Hi-Nic-S/BN/SiC under 90 MPa would experience a lower strain than the woven MI Syl/BN/SiC under 117 MPa. Hence, the matrix cracking in the former with a lower strain would be less than in the latter case with a higher strain. Therefore, the woven MI Hi-Nic-S/BN/SiC under relatively low strain induced by a lower applied stress would be less prone to cracking and the damage induced by matrix cracking may have been suppressed.

As mentioned above, the optical image analysis using the Photoshop verified that the woven MI Hi-Nic-S/BN/SiC had a higher porosity in the matrix than the other two MI CMCs. The higher porosity makes the MI Hi-Nic-S/BN/SiC more susceptible to matrix cracking at a lower stress. Therefore, assuming the similar mechanical behaviors of the matrix in the three CMCs, the stress at which the matrix cracking initiates for the MI Hi-Nic-S/BN/SiC may be lower than expected from the same system with lower porosity undergoing the same load. This deleterious effect on matrix cracking incurred by the high porosity may negate the low susceptibility to cracking due to low stress on matrix.

The fatigue life exhibited by the MI Hi-Nic-S/BN/SiC under 75% of its *PL* was considerably greater than that of the MI Syl/BN/SiC at the same stress level. This could be due, to the relatively low strain associated in parallel with a relatively low applied stress of 90 MPa. With its lower strain, the material experiences less damage induced by matrix cracking. The driving force for crack growth diminishes with a lower applied stress corresponding to the low strain.

Substantially larger oxidized area shown on the MI Hi-Nic-S/BN/SiC could be attributed to significantly higher number of cycles. Cracks nucleated from the surface defect or the location of high geometric stress concentration such as a corner would propagate inward under cyclic loading to lead the path for oxidation shown on the surface. Hence, the extent of oxidation determined from the fracture surface could be as much a measure of the crack growth, when considered in relation to the number of cycles, as the parameter to evaluate the effect of oxidation on the degradation of a material.

5.3.5 Residual strength comparisons

The stress-strain data obtained from the residual strength test of the runout woven MI Hi-Nic-S/BN/SiC is plotted along with the curves for the runout woven MI Syl/BN/SiC (which survived the peak stress of 81 MPa) and the runout woven MI Syl-*iBN*/BN/SiC (which survived the peak stress of 110 MPa) in Figure 94. The runout woven MI Hi-Nic-S/BN/SiC survived the applied peak stress of 70 MPa, equivalent to 21% of the *UTS* and 58% of the *PL*.
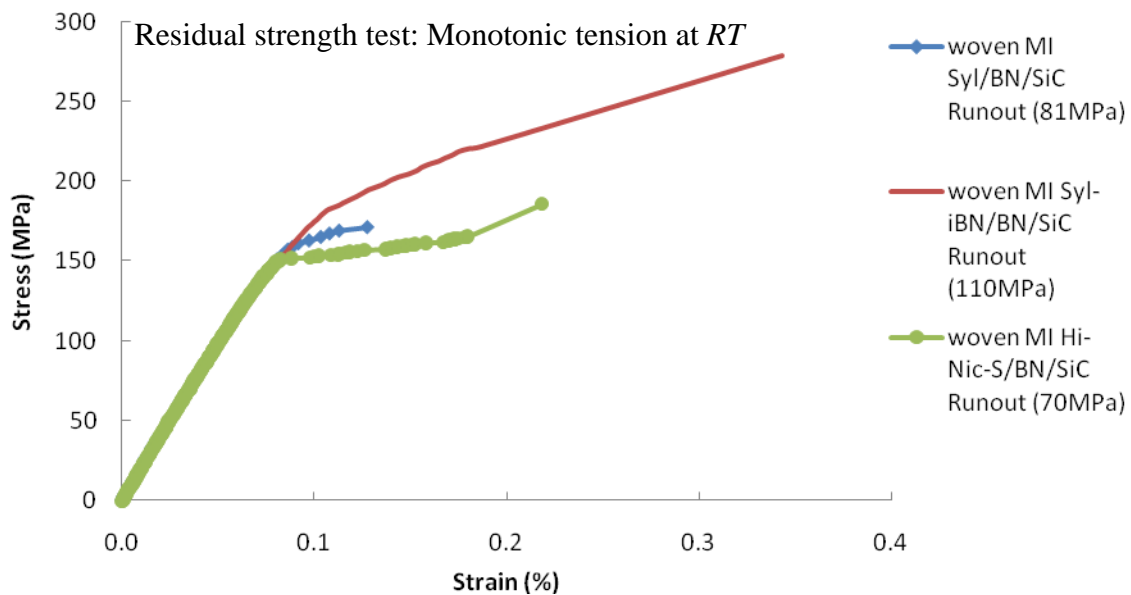
Figure 94: Stress-strain response of the three woven MI CMCs under monotonic tension after surviving 90000 cycles of fatigue loading in combustion

Figure 95 represents the residual strength and strains at failure in Figure 94 on normalized scales for both stress and strain. Normalization was done with respect to each CMC's respective *UTS* and the strain at failure measured from a room temperature monotonic tension test. The fractions of retained strength and strains with respect to the same properties of as-received materials can be measured by comparing the data point in relation to the coordinate (1, 1).
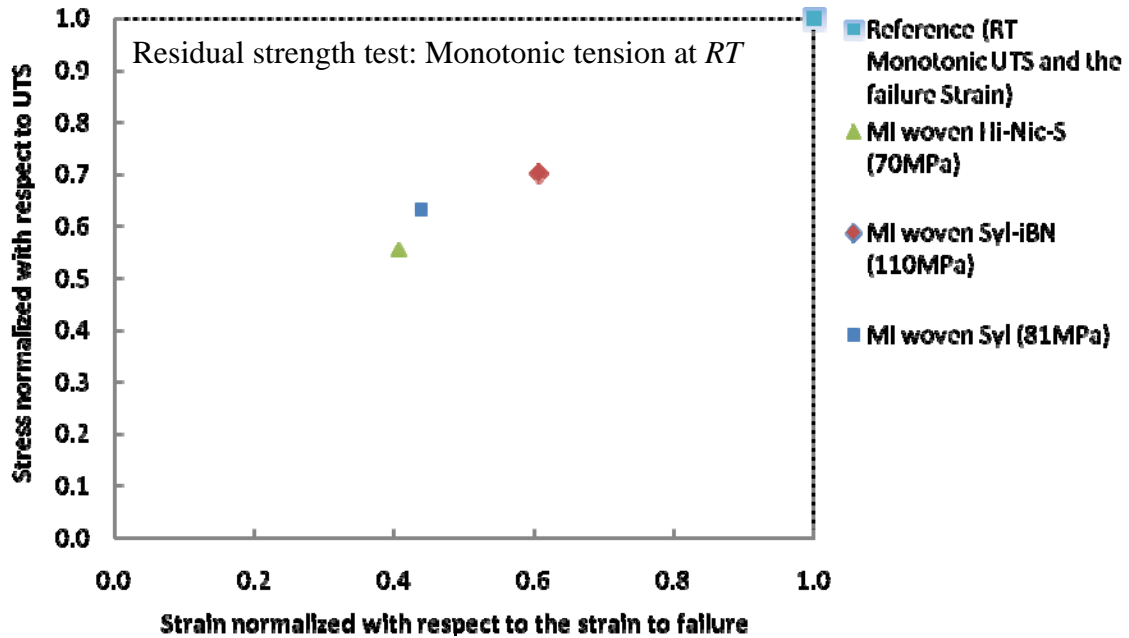
Figure 95: The stress-strain curves shown in Figure 94 with the stress and strain axes normalized against the *UTS* and the corresponding strain at *UTS*, respectively

From Figure 95, the highest stress and strain is retained by the woven Syl-*iBN*/BN/SiC, despite the fact that this CMC survived higher peak stress of 110 MPa, compared to 81 MPa and 70 MPa of the other woven MI CMCs that resulted in runout. Also evident from the plot is the runout woven MI Hi-Nic-S/BN/SiC experienced the highest strength degradation. Between the

woven MI Syl/BN/SiC and the woven Hi-Nic-S/BN/SiC that showed similar fraction of strength and strain retained, the difference is that the runout woven MI Hi-Nic-S/BN/SiC had larger inelastic strain to failure, as compared to the runout woven MI Syl/BN/SiC.
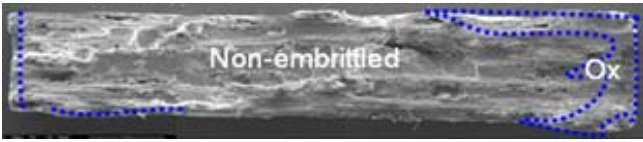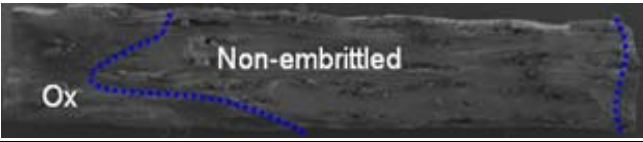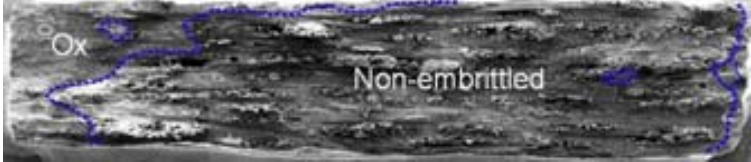
In Figure 94, the runout woven MI Syl/BN/SiC exhibited considerably less inelastic strain, compared to the runout MI Syl-*iBN*/BN/SiC. The reduction in the retained strain is, assuming no change in grain structure, is most likely caused by the change in parameters that control the crack bridging mechanism such as sliding resistance. Such change may have been brought into the system by frictional wear under cyclic loading as well as the interphase oxidation that changes the BN interphase into the liquid phase oxide. The volume expansion associated with the change in phase by the oxidation reactions [126] can accompany the change in the physical and chemical conditions on the fiber surface, and this could result in the resistance at the interphase that affects the mechanics of crack bridging mechanism during cyclic testing. In time, the liquid oxidation product solidifies adhering to the neighboring fibers and matrix and subjects the affected area to the embrittlement. The change in interphase parameter caused by wear and oxidation may be responsible for the limited non-linear stress-strain behavior observed from many of the runout specimens. More details of the failure mechanism involving the interphase oxidation will be presented in the next chapter.

5.3.5.1 Microscopic comparison of residual fracture surface

Each material tested in the prescribed combustion environment undergoes a different level and extent of oxidation depending on the level of matrix cracking induced by the mechanically applied or thermally induced stress and the level of treatment done on the material to resist oxidation such as the *iBN* coating. They are the reasons that different runout specimens of both

same and different types show different residual strengths and strains. For instance, the woven MI Syl/BN/SiC is less resistant to oxidation than the woven MI Syl-*iBN*/BN/SiC due to the absence of the *iBN* layer. This is indicated by its lower residual strength and larger oxidized area on the fracture surface of the woven MI Syl/BN/SiC shown in Table 24, despite the fact that the woven MI Syl/BN/SiC was subjected to a lower peak stress level. Similar observation applies in the comparison between the woven MI Syl-*iBN*/BN/SiC and the woven Hi-Nic-S/BN/SiC. The residual strength of the latter was 186 MPa, compared to 279 MPa for the former. The area on the fracture surface showing oxidative micrographic features is found to be larger on the runout woven MI Hi-Nic-S/BN/SiC, which survived the relatively low peak stress of 70 MPa, than on the fracture surface of the runout woven MI Syl-*iBN*/BN/SiC that endured the larger peak stress of 110 MPa.

Table 24: Fracture surfaces from residual strength tests for each of the three woven MI CMCs that survived the fatigue testing in combustion

Peak Stress (MPa)	CMC Type	Residual Fracture Surface	Residual Strength (MPa)
110	Woven MI Sylramic-*iBN* /BN/SiC		279
81	Woven MI Sylramic /BN/SiC		171
70	Woven MI Hi-Nic-S /BN/SiC		186

1 mm

In the comparison between the runout woven MI Syl/BN/SiC and the woven Hi-Nic-S/BN/SiC, the residual strength of the former that was fatigued at the peak stress of 81 MPa is

slightly greater than that of the latter with the peak stress of 70 MPa. The oxidized areas on the two fracture surfaces appear to be similar in size, which may be due to similar stress level that presumably induced similar levels of matrix cracking, as the 81 MPa is equivalent to 53% of the *PL* of an as-received woven MI Syl/BN/SiC, while the 70 MPa of the runout woven MI Hi-Nic-S/BN/SiC is 58% of its *PL.*

The fraction of the oxidized area on the fracture surface of the runout woven MI Hi-Nic-S/BN/SiC specimen was 0.3. The strength of the intact portion of 234 MPa was estimated based on this area fraction, when the runout specimen actually fractured at 186 MPa. As with the other residual strength estimation shown earlier, the overestimation may be linked to possible underestimation of the oxidized area and unaccounted failure of fibers in the intact area of the surface based on probability as well as any change in morphology of the interphase with accumulated cyclic loading. It could also be due to the carbon content on the Hi-Nic-S/BN/SiC CMC that may have undergone internal oxidation using residual oxygen in BN interphase. Usually, oxidation has to progress to a substantial level before it can be observed micrographically. More detailed analysis using Transmission Electron Microscopy (TEM) would benefit the understanding of the change in fiber and interphase surface conditions with respect to the test duration.

5.3.6 Summary of comparisons among three woven CMCs

In summary, with the peak stress of 125 MPa applied to the three woven MI CMCs under comparison, the woven MI Syl-*iBN*/BN/SiC outperformed the other two MI CMCs by surviving the highest number of cycles while showing the least oxidized region on the fracture surface. This supports the earlier observation that the insitu BN layer inhibits the damage induced by oxidation.

The woven Hi-Nic-S/BN/SiC subjected to the 125 MPa showed the most extensive oxidized area, because the applied stress exceeded the proportional limit of the material, 121 MPa, whereas the same stress was well below the proportional limits for the other two CMCs with the Sylramic-based fibers. The specimens fail at the applied stress well below or slightly exceeding the *PL* because of thermal gradient stress. The thermal gradient stress varies from compression to tension along the thickness of the specimen either adds to or subtracts from the mechanical peak stress applied.

The comparisons of the three CMCs, each subjected to a different peak stress that resolves to be equivalent to the same percentage of their respective *PLs*, i.e. 75%, were attempted to provide a qualitative understanding of the three materials in relation to matrix cracking. From this comparison, the CMCs with the insitu BN layer had the longer fatigue life and were less susceptible to oxidation. This was apparent from the smaller fraction of the oxidized area observed on the fracture surface of the woven MI Syl-*iBN*/BN/SiC for the number of cycles they survived, as compared to the other CMCs with no insitu BN tested at the same fraction of their respective *PL* that showed larger extent of oxidation and shorter fatigue life. The woven MI Hi-Nic-S/BN/SiC showed considerably larger oxidized area fraction and survived significantly longer test cycles than the other two CMCs with the Sylramic-based fibers. This is likely due to its relatively low strain corresponding to its applied stress of 90 MPa, as compared to 125 MPa and 117 MPa applied to woven MI Syl-iBN/BN/SiC and MI Syl/BN/SiC, respectively. The MI Hi-Nic-S/BN/SiC fatigue loaded by 90 MPa showed the longest fatigue life because of its relatively low applied stress. However, its low *PL* limits the applicability of the material. The high porosity facilitates the oxidation of the woven MI Hi-Nic-S/BN/SiC.

Woven MI Hi-Nic-S/BN/SiC was determined to have the lowest runout stress, followed by the woven MI Syl/BN/SiC and the woven MI Syl-*iBN*/BN/SiC. The highest residual strength of 279 MPa was obtained from the runout woven MI Syl-*iBN*/BN/SiC, followed by 186 MPa and 171 MPa from the runout woven MI Hi-Nic-S/BN/SiC and the runout woven MI Syl/BN/SiC, respectively, despite the fact that the peak stress applied during the fatigue test was highest for the woven MI Syl-*iBN*/BN/SiC at 110 MPa, followed by 81 MPa and 70 MPa for the woven MI Syl/BN/SiC and the woven MI Hi-Nic-S/BN/SiC, respectively.

5.4 Woven vs. Prepreg

In the prepreg MI Hi-Nic-S/BN/SiC, the fiber volume fraction is reduced to facilitate a uniform distribution of individual fibers. This comes at the expense of an increased stress on the fiber, which in turns reduces the overall strength of material. This negative aspect may be minimized by using a fiber type with a higher load carrying capability such as the Sylramic fiber with the ultimate strength of 3.2 GPa, as compared to the Hi-Nic-S with 2.6 GPa. In addition to the change in fiber volume fraction, the susceptibility of the matrix to cracking can be further decreased by reducing the porosity level in the matrix. Pores not only act as preferred crack initiation sites, but they also facilitate the diffusion of oxidants into the bulk interior, thereby causing oxidation-induced degradation which diminishes the fatigue life.

The prepreg MI Hi-Nic-S/BN/SiC is a type of CMC that combines the high matrix volume fraction and the low porosity in the matrix by virtue of the enhanced processing technique known as prepreg. In this section, the prepreg MI Hi-Nic-S/BN/SiC is compared with the woven MI Hi-Nic-S/BN/SiC. This comparison features two different processing techniques; slurry cast and prepreg methods. The two materials share the same fiber type, i.e. Hi-Nic-S. There also exists

close similarities in the matrix and interphase, i.e. silicon-doped BN in the interphase and SiC melt-infiltrated with Si constituting the MI matrix. However, the two CMCs have distinct differences in their fiber volume fractions, the matrix porosity level, and the chemical composition and the presence of CVI matrix; all of which are products of different processing methods used.

5.4.1 Monotonic Results

The prepreg MI Hi-Nic-S/BN/SiC has the fiber volume fraction of 20~25 *vol %*, as compared to 35.7 *vol %* of its woven MI Hi-Nic-S/BN/SiC. Generally, a larger fiber volume fraction would indicate a greater stiffness of the composite, because fibers by design usually have higher stiffness than matrix to facilitate the fiber bridging mechanism. As the two CMCs have the same fiber type as and appear to have very similar chemical ingredients in their MI matrix, the difference in the stiffness could be attributed to two major factors. First, the uniform coating provided on each fiber during the prepreg processing kept the majority of the load carrying fibers physically separated from the neighbors, such that there would be less likelihood of the failure in one fiber causing a cascading effect on the adjacent ones. Secondly, the woven MI Hi-Nic-S/BN/SiC has significantly higher porosity in the MI matrix than the prepreg MI CMC. Increased porosity reduces the stiffness of a MI matrix by making it susceptible to crack nucleation and growth.

The two CMCs have similar *UTS* despite the large difference in the fiber volume fraction. This is because the prepreg system involves the fibers more uniformly coated, which enables each fiber to act independently and thus makes better use of the strength of the fibers [76]. On the contrary, the *PL* of the woven MI Hi-Nic-S/BN/SiC was found to be significantly lower than the

average *PL* of the prepreg MI Hi-Nic-S/BN/SiC. This is believed to be due to the higher stiffness of the prepreg MI CMC that accompanies a higher stress that corresponds to the strain at which the matrix cracking occurs.

Unlike the monotonic tension data for the woven MI Hi-Nic-S/BN/SiC, which were obtained from this study, the monotonic tension test data for the prepreg MI Hi-Nic-S/BN/SiC were supplied by the manufacturer. To ensure the validity of direct comparison with the data collected in-house of the other CMCs, the methods of determining the mechanical properties for all the CMCs in this study were standardized to the methods used to determine the supplied data for the prepreg MI Hi-Nic-S/BN/SiC by the manufacturer. The data presented in Table 25 are very similar to those previously reported [76].

Table 25: Comparisons of mechanical strengths and strains between the prepreg MI and the woven MI Hi-Nic-S/BN/SiC from room temperature monotonic testing

	Young's Modulus (GPa)	Ultimate Tensile Strength (MPa)	Strain at failure (%)	Proportional Limit (MPa)
Prepreg MI Hi-Nic-S/BN/SiC	264 ± 13	340 ± 19	0.71 ± 0.12	197 ± 23
Woven MI Hi-Nic-S/BN/SiC	195	334	0.54	121

5.4.2 S-N curve comparison

The life data obtained from the fatigue tests of the prepreg MI Hi-Nic-S/BN/SiC and the woven MI Hi-Nic-S/BN/SiC in combustion environment are plotted in Figure 96. The test runout was attained at the peak stress of 105 MPa for the prepreg MI Hi-Nic-S/BN/SiC, which is an improvement from the woven MI Hi-Nic-S/BN/SiC with the runout strength of 70 MPa. The dense matrix of the prepreg MI CMC along with low porosity, which inhibits the degradation of the enclosed fibers, is a likely reason for the increased fatigue strength. The S-N curve for the prepreg MI CMC is less steep than the woven MI CMCs, as shown in Figure 96.
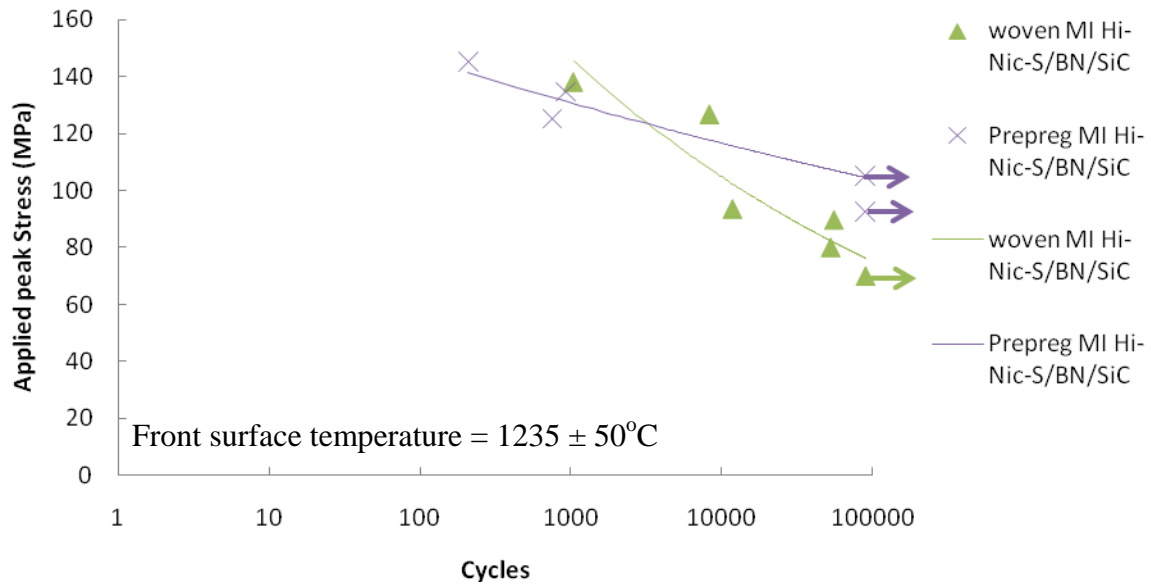
Figure 96: S-N data of the prepreg MI and the woven MI Hi-Nic-S/BN/SiC
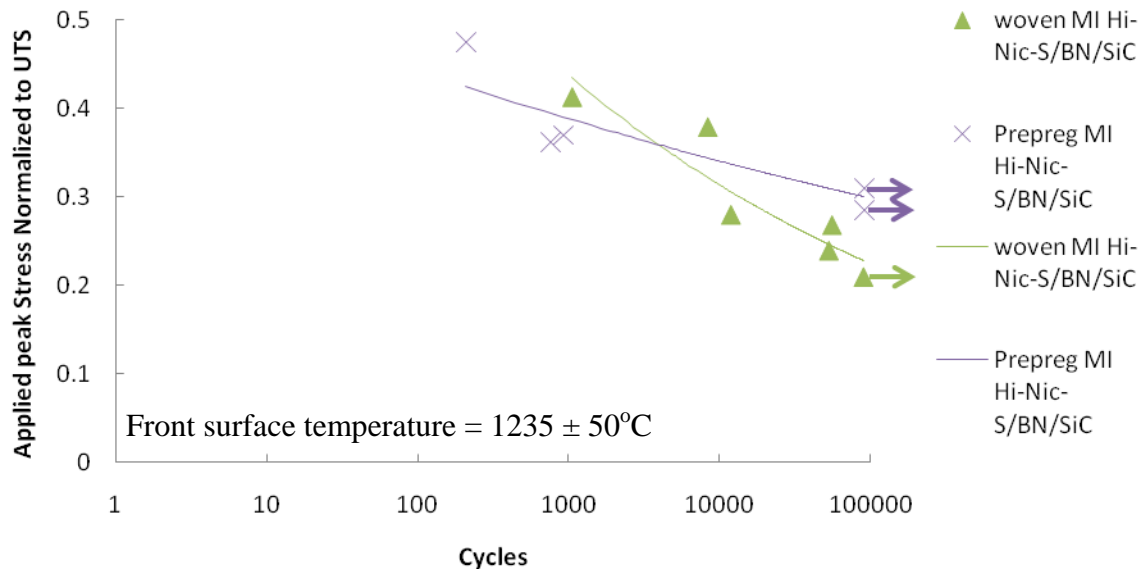
Figure 97: S-N data of the two MI Hi-Nic-S/BN/SiC CMCs with peak stress normalized against *UTS*

Figure 97 displays the applied peak stresses in terms of the fraction of the *UTS* plotted

against the cycles-to-failure. Because the *UTS* of the prepreg MI Hi-Nic-S/BN/SiC and the woven

MI Hi-Nic-S/BN/SiC are similar, the S-N curves take on similar shapes and trends as in on Figure

96. The prepreg MI Hi-Nic-S/BN/SiC suffered a smaller knockdown in strength from the room temperature *UTS* than the woven MI Hi-Nic-S/BN/SiC.

The peak stresses normalized to the proportional limit were plotted against the cycles-to-failure in Figure 98. Though the rate of degradation with time appears to be higher for the woven MI Hi-Nic-S/BN/SiC, the fatigue strengths at runout of 105 MPa for the prepreg MI Hi-Nic-S/BN/SiC and 70 MPa for the woven MI Hi-Nic-S/BN/SiC were quite similar, when expressed as fractions of their respective *PLs*, at 58% and 53%, respectively. A continued testing beyond the prescribed test condition of 90000 cycles for 25 hours would have perhaps resulted in different runout strengths.
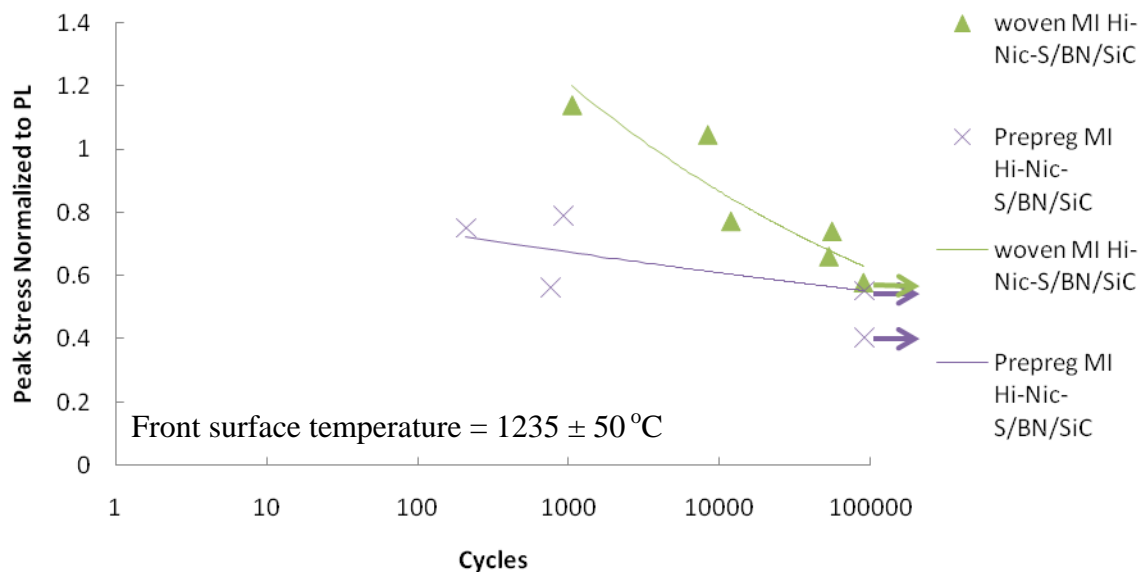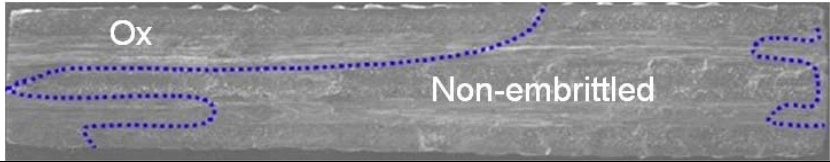
Figure 98: S-N data of the two MI Hi-Nic-S/BN/SiC CMCs with peak stress normalized against *PL*

5.4.3 Fractographic comparison

The fractography using SEM and EDS was used to link the effects of oxidation to the strength degradation for the prepreg MI Hi-Nic-S/BN/SiC and the woven MI Hi-Nic-S/BN/SiC.

The fracture surfaces of the two specimens, subjected to the applied peak stress of 125 ± 2 MPa, were compared to determine the extent of oxidation from the fracture surface, which are shown in Table 26. The applied peak stress of 125 MPa is equal to 66% of the *PL* for the prepreg MI Hi-Nic-S/BN/SiC and 103% of the *PL* for the woven Hi-Nic-S/BN/SiC.

Table 26: Fracture surfaces for the woven MI and prepreg MI Hi-Nic-S/BN/SiC both fatigue loaded at the same peak stress of 125 MPa

Peak Stress (MPa)	CMC Type	Fracture Surface	Cycles-to-failure
125 ± 2	Woven MI Hi-Nic-S /BN/SiC		8329
	prepreg MI Hi-Nic-S /BN/SiC		758

1 mm

The comparison in Table 26 demonstrates that the woven MI Hi-Nic-S/BN/SiC survived much higher number of cycles while showing less oxidized area than the prepreg MI Hi-Nic-S/BN/SiC. Taking into consideration that the applied peak stress of 125 MPa was a higher stress level for the woven MI Hi-Nic-S/BN/SiC with the proportional limit of 121 MPa than for the prepreg MI Hi-Nic-S/BN/SiC with the proportional limit of 197 MPa, the woven MI Hi-Nic-S/BN/SiC is expected to have undergone a greater degree of matrix cracking that would translate to a larger oxidized area and generally reduced number of cycles-to-failure. The seemingly inexplicable outcome for the prepreg MI Hi-Nic-S/BN/SiC that involved a large oxidized area for a relatively short time of testing may be attributed to a multiple of causes, all of which trace back to the fundamental difference that exists between the two systems; they are different systems built

on different manufacturing concepts that demonstrate different mechanical behaviors. Among the most overarching one is the difference in the failure kinetics under a given fatigue condition. The prepreg MI Hi-Nic-S/BN/SiC is built on each individual fiber uniformly coated and surrounded by dense matrix that separates the fibers, while the woven MI Hi-Nic-S/BN/SiC is constructed with the bundled fiber tows enclosing approximately 500 densely populated fibers, which limits the wettability around the individual fibers during melt-infiltration resulting in relatively low matrix density and high void concentration, undermining the overall material's capability to carry load. The parameters that affect the damage including crack propagation are likely different for the two material systems.

For the prepreg MI CMC with low fiber volume fraction, the surface area over which the load transfer occurs between the fibers and matrix is less than in the woven MI CMC with high fiber volume fraction. As a result, relatively higher shear stress would be acting upon any given fiber in the prepreg MI CMC, which accompanies the increase in the debonding stress. There are two microscopic observations that may relate to this phenomenon. One is the spallation of the MI matrix seen surrounding the fibers. The weaker *Si* in the MI matrix may have degraded at the high temperature during the load transfer from the matrix to the fibers. The other observation is the relatively short fiber pullout exhibited throughout the non-embrittled area. Both of these observations were documented in Chapter IV, and will be revisited for more in-depth coverage in the next chapter. The sliding distance would decrease with the increased shear stress that needs to be overcome for debonding to occur. With this, the probability of fiber fracture as well as the energy that becomes released upon failure of a load carrying fiber increases. The higher energy released from the fracture of each bridging fiber increases the rate of crack propagation. The oxidation would follow the advancing crack tip under cyclic load. This is one possible scenario

that provides an explanation for the prepreg MI Hi-Nic-S/BN/SiC showing a large oxidized area over relatively short test duration.

The mechanism assumed in development of the above scenario is the debonding and sliding, which slows the crack growth by dissipating the energy by frictional shear at the interface between the bridging fibers and the matrix. The failure of one of the bridging fibers releases the energy, which avails itself to crack tip advancement. If, however, the applied stress combined with the thermal gradient stress at its peak were below a threshold stress corresponding to a minimum level of matrix cracking, in a probabilistic sense, conducive to the development of an edge crack at a rate low enough not to cause failure during the 25-hour test duration, then the failure mechanism described above would not be triggered. While the exact value of the threshold could not be resolved, its existence is confirmed with the determination of the peak stress level below which a specimen did not experience an extensive penetration of cracks which lead to the oxidation. For example, it is evident that the runout stress for the prepreg MI Hi-Nic-S/BN/SiC in a given condition exists between 125 MPa and 105 MPa. In the case of the woven MI Hi-Nic-S/BN/SiC, the runout stress would be between 80 MPa and 70 MPa. This stress level exists for every material system.

It is shown from the preceding discussion that the different material systems can be governed by different damage mechanisms, which have implications on the rate of crack propagation and the oxidation. In addition, the stress level was identified below which failure does not occur for a given system and condition.

5.4.4 Fractographic comparison: Fiber pullout behaviors

A 100 μm

B 50 μm
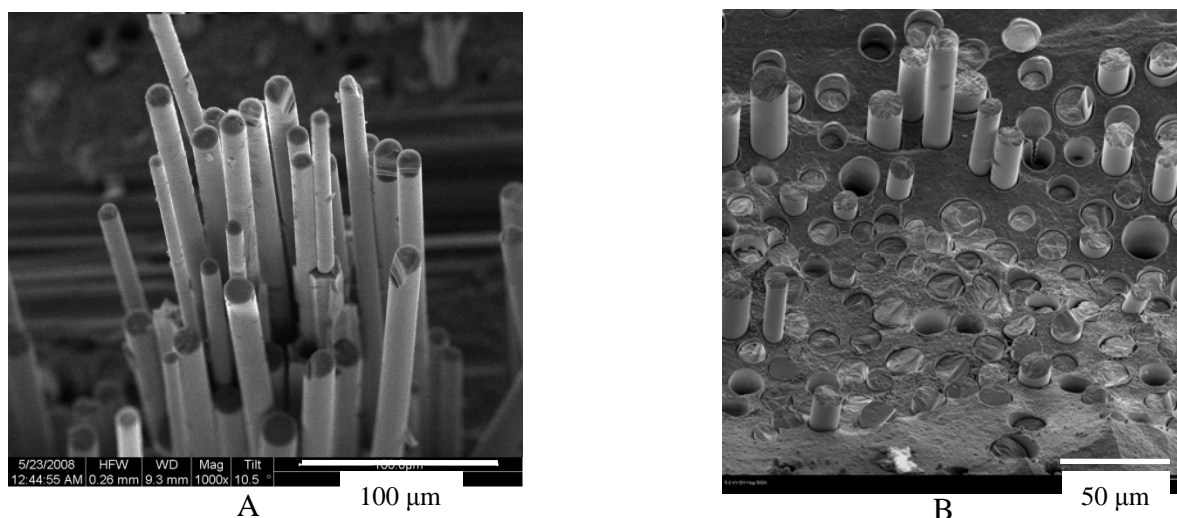
Figure 99: Fiber pullout in the non-embrittled regions of the two CMCs; (A) Long fiber pullout typical of the woven MI Hi-Nic-S/BN/SiC fractured after 53034 cycles under the peak stress of 80 MPa, (B) short pullout typical of the prepreg MI Hi-Nic-S/BN/SiC failed after 758 cycles under 125 MPa

Figure 99 depicts the fiber pullout in the non-embrittled region of the two CMCs that survived the test condition without failure. It is evident from the comparison of the fiber pullout lengths that the woven MI has much longer pullout. The woven MI and the prepreg MI Hi-Nic-S/BN/SiC specimens depicted in the figure were subjected to 80 MPa and 125 MPa during the fatigue test, respectively. The pullout length observed from the woven MI specimen that underwent 127 MPa was too long to be captured in the shown magnification, so instead the 80 MPa specimen with shorter pullout was shown to demonstrate the difference in the pullout length between the two CMCs. In addition, the fracture surface can be multi-faceted in the prepreg MI, as shown in Figure 100. The uniform coating in the prepreg MI processing resulted in the finely dispersed fibers that are distributed evenly throughout the area at the expense of a relatively low fiber volume fraction. Shorter fiber pullout can be due to the relatively greater shear stress on an average individual fiber transferred through the interphase for a given stress with lower fiber volume fraction of the prepreg MI CMC. The difference in the distribution and volume fraction of

212

the fiber would affect the failure mode, as evident from the different fractographic observations as shown in Figure 99.
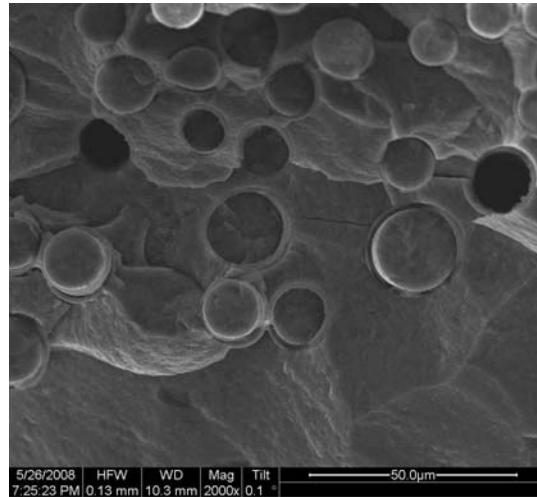
Figure 100: Multifaceted fracture on prepreg MI Hi-Nic-S/BN/SiC at 105 MPa

In Ref [117], it was shown that the fiber pullout length of the woven MI Hi-Nic-S/BN/SiC was inversely related to the number of fatigue cycles or the time exposed to the combustion. The sample under lower applied stress level that survived a larger number of cycles showed significantly shorter fiber pullout. The prepreg MI Hi-Nic-S/BN/SiC, however, did not show such trend. In fact, the pullout length did not vary with either the applied stress or the number of cycles.

5.4.5 Residual strength comparisons

The specimens of the prepreg MI Hi-Nic-S/BN/SiC and the woven MI Hi-Nic-S/BN/SiC that survived the test condition without fracture were subsequently tested for the residual strength at room temperature. The stress-strain data from the monotonic tension testing of the runout specimens are plotted in Figure 101.
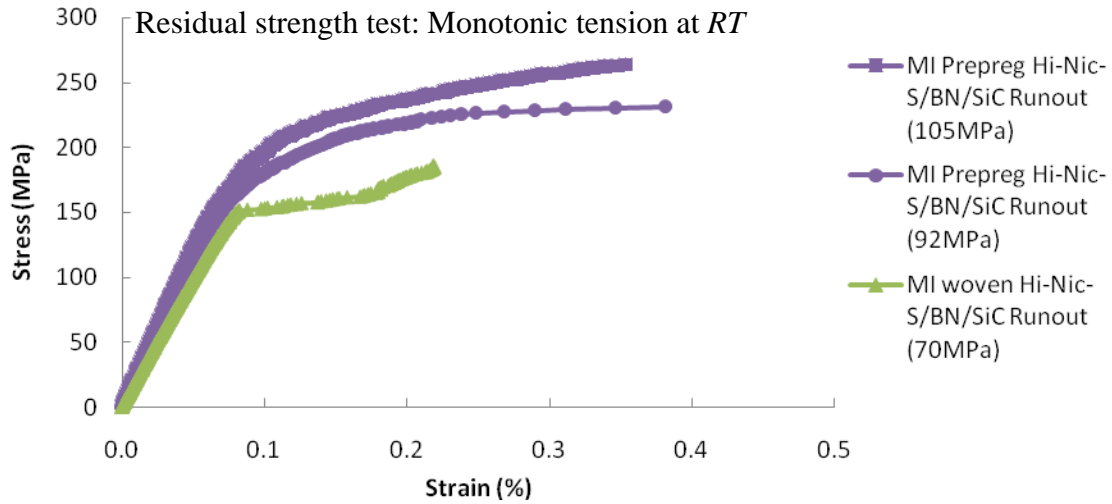
Figure 101: Stress-strain response of two prepreg MI and one woven MI Hi-Nic-S/BN/SiC under monotonic tension after surviving 90,000 cycles of fatigue loading in combustion

There are two prepreg MI Hi-Nic-S/BN/SiC specimens that survived the test condition without fracture; one at the peak stress of 105 MPa and the other at 92 MPa. The strengths retained by the two prepreg MI Hi-Nic-S/BN/SiC runout specimens were 225 MPa and 263 MPa. One notable observation is that the specimen subjected to 92 MPa had the lower retained strength than the one loaded with the peak stress of 105 MPa. This could be in part due to scatter in the data, which stems probably from the relatively large scatter in fiber volume fractions, i.e. 20~25 vol %. The variations in material properties between different panels were relatively large for the prepreg MI Hi-Nic-S/BN/SiC tested in this study. A specimen from the same panel that produced the one that survived at the peak stress of 105 MPa showed the room temperature UTS of 339 MPa, as compared to the *UTS* of 324 MPa for the specimen from the same panel as tested with the peak stress of 92 MPa. It may also be attributed to the scatter that exists with the rate of degradation by varying rates of oxidative degradation [127]. The variations in material properties between different panels were relatively large for the prepreg MI Hi-Nic-S/BN/SiC. The variability is inherent to the prepreg processing which involves the relatively wide range of the

214

fiber volume from 20% to 25% by volume, as compared to the smaller uncertainties in the fiber

volume fractions of the woven CMCs.
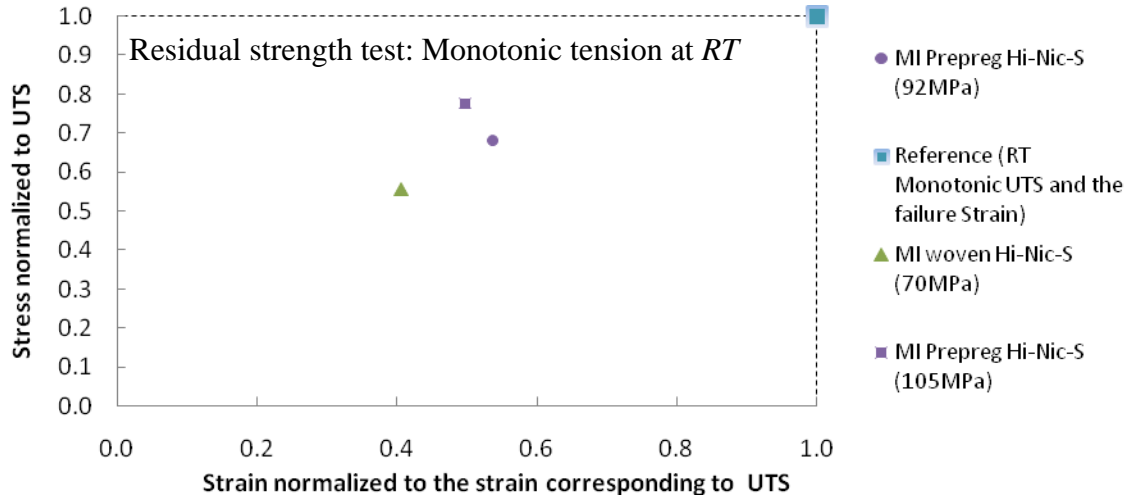
Figure 102: The stress-strain curves shown in Figure 101 with the stress and strain axes normalized against the *UTS* and the corresponding strain at *UTS*, respectively

Figure 102 is plotted to facilitate the investigation of the knockdown in stress and strain

due to the applied test condition. The figure depicts the strength and strain retained by each runout

specimen of both types normalized with respect to the room temperature *UTS* and the strain at

failure, respectively. The prepreg MI Hi-Nic-S/BN/SiC loaded with the peak stress of 105 MPa,

equivalent to 55% of its *PL* retained 78% of its *UTS* at room temperature, while the woven MI Hi-

Nic-S/BN/SiC subjected to 70 MPa or 58% of the *PL* retained less than 50% of its original

strength. These two runout specimens underwent the peak stress level similar in terms of the

fractions of their respective *PLs*. The comparison between these two CMCs that showed higher

stress and strain retained by the prepreg MI Hi-Nic-S/BN/SiC adds to the suggestion that the

prepreg MI CMC has a higher potential than the woven MI CMCs for structural applications

subjected to a fatigue loading in combustion environment.
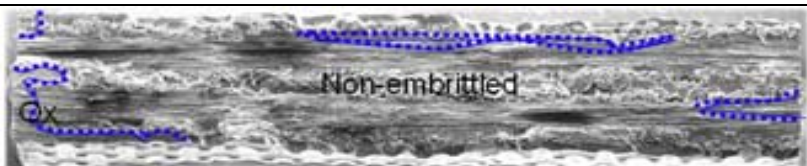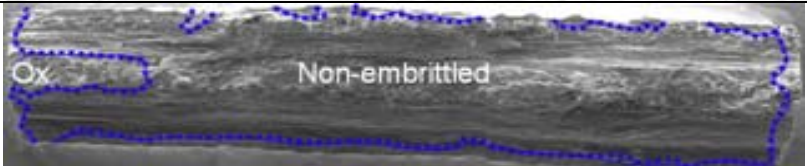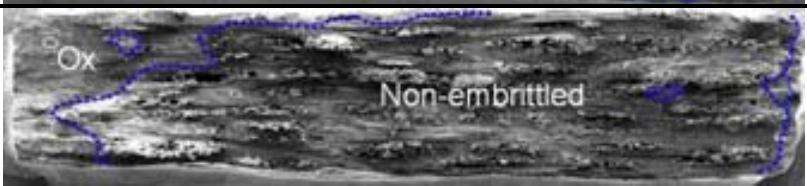
5.4.5.1 Fractographic comparison: Residual fracture surfaces

The fractographic investigation of the fracture cross-section obtained from the residual strength tests of the two runout prepreg MI Hi-Nic-S/BN/SiC reveals the mixed modes of oxidation including the pervasive oxidation along the edges by diffusion and the oxidation that occurs behind the crack tip which develops under fatigue. The fracture of the runout specimen fatigued to the peak stress of 92 MPa occurred at the geometric center of the specimen, with which the center of the applied combustion flame aligned. The surface temperature measured using the calibrated IR system showed the surface during the test was $1280 \pm 25^{o}C$ along the fracture cross-section. This fracture surface shows primarily a pervasive mode of oxidation that developed from surface, as evident from the picture-frame shape of the oxidation profile in Table 27. The fracture of the other runout prepreg MI Hi-Nic-S/BN/SiC specimen fatigue-loaded to the peak stress of 105 MPa occurred at a cross-section 25 *mm* distant from the geometric center, at which the surface temperature was estimated to be $1025 \pm 25^{o}C$ on the front (and $845 \pm 5^{o}C$ on the back). This suggests that the degradation at this cross-section could be driven by the intermediate temperature phenomenon, also referred to as the embrittlement. There were no signs of pervasive oxidation on this fracture surface. The regions on this surface microscopically determined to contain the features suggesting oxidation include side edges and corners. Deeper permeation of oxidation was observed on select 90° tows.

The woven MI Hi-Nic-S/BN/SiC that survived the test with the peak stress of 70 MPa fractured under the subsequent residual strength test at 25 *mm* from the geometric center, where the temperature during test was approximately $1185 \pm 35^{o}C$ on the front surface (and $910 \pm 25^{o}C$ on the back). The failure outside the heated gauge length, together with the micrographic features indicating oxidation as illustrated in Table 27, suggests that the failure may have been driven by

the intermediate temperature embrittlement. The resulting fracture surface shows oxidation extending from the left edge which appears to have taken place behind the cracks emanating from the rear left corner. The extent of oxidation on this surface is significantly larger than the oxidized region on the fracture cross-section of either runout prepreg MI Hi-Nic-S/BN/SiC specimen. The observation that less oxidation observed from the runout prepreg MI Hi-Nic-S/BN/SiC that underwent higher peak stress than the runout woven MI Hi-Nic-S/BN/SiC showing larger oxidized area suggests that the prepreg MI CMC with dense matrix was less prone to oxidation.

Table 27: Fracture surfaces from residual strength tests for two prepreg MI and one woven MI CMCs that survived the fatigue testing in combustion

Peak Stress (MPa)	CMC Type	Residual Fracture Surface	Residual Strength (MPa)
105	prepreg MI Hi-Nic-S /BN/SiC		263
92	prepreg MI Hi-Nic-S /BN/SiC		232
70	Woven MI Hi-Nic-S /BN/SiC		186

1 mm

5.4.5 Section Summary

The advantages of the prepreg MI CMC are the dense matrix that protects the enclosed fibers from oxidation and the processing that provides the uniform coating of individual fibers,

which effectively separate the fibers preventing any grouped damage. As a result, the prepreg MI Hi-Nic-S/BN/SiC retained the high fraction of its original strength and strain after 90,000 cycles of the fatigue loading involving the peak stress of 105 MPa. The downside of the prepreg MI CMC is that the dense matrix and the uniform coating were at the expense of the fiber volume fraction. The relatively low fiber volume fraction limits the material strength. With smaller number of fibers, for a given load, the shear stress between fiber and interphase may be more significant than in the woven MI CMC with higher fiber volume fraction. A higher stress state due the increased shear stress at the interphase may have led to the fracture of the weaker, possibly oxidized matrix in contact during the load transfer. The resulting porosity in the MI matrix surrounding the fibers leaves behind voids which can not only facilitate the transport of oxidants, but serve as potential crack initiation sites under cyclic stress. The porosity was found to be more pronounced on the plies close to the flame-impinged surface, suggesting that the temperature may have an effect on the phenomenon.

5.6 Chapter Summary

In summary, the highest runout fatigue strength was obtained by the woven MI Syl-*iBN*/BN/SiC with the peak stress of 110 MPa, followed by 105 MPa for the prepreg MI Hi-Nic-S/BN/SiC, 81 MPa for the woven MI Syl/BN/SiC and 70 MPa for the woven Hi-Nic-S/BN/SiC. This result is highlighted in Table 28 showing the fatigue strength with respect to the proportional limit (*PL*) and ultimate tensile strength (*UTS*) of an as-received material of the same kind. Comparing the S-N curves for all four MI CMCs tested, it was clear that the woven MI Syl-*iBN*/BN/SiC had the longest fatigue life for a given stress. This is most likely due to the presence of *iBN* layer, which appears to have inhibited the oxidative degradation and increases the creep

resistance, etc. The other three MI CMCs use the fibers whose surface consists of excess carbon, instead of the in-situ *BN* [22].

Table 28: Fatigue strength of the four CMCs at the test runout condition

	Woven MI Syl-iBN/BN/SiC	Woven MI Syl/BN/SiC	Woven MI Hi-Nic-S/BN/SiC	Prepreg MI Hi-Nic-S/BN/SiC
Runout strength	110 MPa	81 MPa	70 MPa	105 MPa
	26% *UTS*	30% *UTS*	21% *UTS*	31% *UTS*
	67% *PL*	53% *PL*	58% *PL*	55% *PL*

In an attempt to interpret the experimental stress data in terms of physical phenomena such as microcracking, the peak stresses were normalized to the characteristic strengths of each material such as the *PL* and *UTS*, and the comparisons between the materials were extended to include those of the normalized stresses. Comparing the normalized stresses between different CMCs resulted in some salient observations that led to the increased understandings of the phenomena and trends observed from the comparisons of peak stresses in the absolute unit. It was determined from the series of comparisons among the three woven MI CMCs that the woven MI Syl-*iBN*/BN/SiC with the *in-situ BN* protective fiber coating possesses the highest fatigue strength and retains the highest fraction of the material's original strength. The outcome was reinforced by the fractographic investigation of the surfaces that showed the least amount of oxidation accrued on the woven MI Syl-*iBN*/BN/SiC for a given fatigue life.

Similar comparisons were carried out between the prepreg MI Hi-Nic-S/BN/SiC and the woven MI Hi-Nic-S/BN/SiC. The prepreg MI Hi-Nic-S/BN/SiC was built on a different processing concept that increases the density of the matrix and the protection against oxidation. The low porosity level unique to the prepreg MI processing increases the stiffness such that its PL is significantly higher than the woven MI CMC made by the slurry cast processing. With the increased volume fraction of the dense matrix and low porosity inherited from the prepreg

processing, the enclosed fibers are better protected, increasing fatigue life over that exhibited by the woven MI Hi-Nic-S/BN/SiC. The prepreg MI CMC experienced the lower fraction of the knockdown in strength from its *UTS*, compared to the three woven CMCs. The fatigue strength of the prepreg MI Hi-Nic-S/BN/SiC is close to that of the woven Syl-*iBN*/BN/SiC, the best of the three woven CMCs.

The investigation by fractography of oxidation suggested that there might have been two modes of oxidation; the pervasive oxidation that occurred by diffusion through bulk SiC matrix and the other oxidation led by the crack front. But this is a very slow process that is not believed to occur in the relatively short test duration. Most specimens that failed during the combustion test fractured inside the heated zone and showed the microscopic features such as the silica overlayer that suggested the oxidation occurred behind the propagating cracks, or by the second mode of oxidation. Hence, the failure mechanism would probably involve the edge cracks that propagate inward under cyclic stress, oxidizing the BN interphases that become exposed in the crack path. The presence of the *iBN* layer as fiber coating in the woven MI Syl-*iBN*/BN/SiC made the BN interphase less susceptible to oxidation, as evident from the microscopic observation that showed the smallest extent of oxidation for a given number of cycles and time of combustion exposure. A thin carbon layer present on the surface of the other types of fiber used in this study triggers another type of BN oxidation that is much faster and deeper penetrating, which explains relatively larger extents of oxidation observed on their fracture surfaces. Lastly, there were those fracture surfaces that showed "picture-frame" type oxidation profile, suggesting a pervasive oxidation. The ones that showed this type of oxidation are those exposed to the combustion flame for extended period of time such as the woven MI Syl-*iBN*/BN/SiC and the prepreg MI Hi-Nic-S/BN/SiC that survived the 25 hour test duration without fracture.

In the next chapter, the thermal gradient stress that changed the stress field on the specimen is discussed in detail. The thermal gradient stress elevates the stress state, explaining the generally low peak stresses in relation to the proportional limit that caused failure. Then, failure mechanisms are discussed in details, based on the thermal gradient stress consideration as well as from the experimental and microscopic observations elaborated in the preceding chapters. Part of what makes this study unique and realistic to the proposed application is the use of combustion flame as the method of heating the specimen. For a comprehensive analysis of the failure mechanisms, it is necessary to identify and explore the physical and chemical conditions rendered by the combustion environment and the way it was introduced to the material system. Then, the physical implications of such conditions are made in terms of thermal and chemical fields around the specimen. Considerations of the synergistic effects of the thermal and chemical conditions as well as fatigue loading subjected to a dog-bone test coupon lead to the identification for a few probable causes that may have led to the failure of specimen.

VI. Analysis

One of the objectives of this study is to investigate failure mechanisms in relation to oxidation and thermal gradient. Two important aspects to consider that help determine failure mechanisms are how the failure occurs and what caused it. This chapter attempts to answer these questions in pursuit of failure mechanisms. Firstly to answer what caused the failure, the thermal gradient stress that puts a specimen at an elevated local stress level than what was applied mechanically is discussed in detail using finite element analysis. Combined mechanical fatigue and thermally induced stresses create a critical stress state even when the mechanically applied stress is well below the proportional limit. This was evident from the fatigue runout stresses of the four CMCs after 25 hours or 90,000 cycles ranging from 70 to 110 MPa, which are well below the stress level that are known to cause matrix cracking. Secondly to answer how the failure occurred, a fracture mechanics based model was developed to how much of the failure was dominated by either average stress or crack development. A finite element model was used in conjunction with the characteristic microscopic features that apply commonly to all four CMCs, in order to demonstrate the thermal gradient stress effect as well as to develop a failure mechanism in oxidative environment.

6.1 Fatigue strength: Comparison with other literature data

The fatigue runout stresses of the four CMCs after 25 hours or 90,000 cycles ranged from 70 to 110 MPa, which are well below the proportional limit (*PL*) of a pristine form of each CMC. It is generally understood that matrix cracking, while starts occurring at well below the *PL*, does not become appreciably dense until the stress level reaches beyond 85% of the *PL* [76]. It is

feasible that thermally induced stress elevated the stress state locally such that the level of matrix cracking is extensive enough for oxidation to ensue and lead the specimen to failure.

Morscher et al [50] carried out fatigue testing of the CMC system very similar to the woven MI Syl-*iBN*/BN/SiC, known as N24A [22] in a furnace environment heated to the similar temperature of 1204°C. The N24A is similar to the woven MI Syl-iBN/BN/SiC of this study in terms of chemical constituents, architecture, and processing steps, but it consists of eight plies, instead of six plies as in the material of this study. Table 29 lists the material data of the N24A and the woven MI Syl-*iBN*/BN/SiC of this study. Morscher et al applied the same stress ratio and frequency used in this study (i.e. $R = 0.05$ and 1 *Hz)*, and found that two of the N24A specimens failed under the peak stress of 220 MPa after approximately seven hours. Considering scatter, this failure in furnace environment can be compared with the failure of a woven MI Syl-*iBN*/BN/SiC specimen of the present study tested at 125 MPa, which ended with fracture after approximately five hours in a more oxidative, combustion environment.

Table 29: Comparison between the two MI woven Syl-*iBN*/BN/SiC [22,50]

		This study	N24A
Constituents	Fiber	Sylramic-iBN	Sylramic-iBN
	Matrix	CVI + MI SiC	CVI + MI SiC
	Interphase	Silicon doped BN	Silicon doped BN
Architecture	Type	5 harness satin weave	5 harness satin weave
	# of Plies	6	8
	Layup	Warp Aligned	Warp Aligned
	Ends per inch	20	20
Fiber vol% (%)		38~40	38~39

While the two CMCs are similar in many ways, there are slight differences in properties. Table 30 summarizes the properties of two systems. The elastic modulus (*E*) and the *UTS* of the as-produced N24A monotonically tested under tension at room temperature were 259 GPa and

470 MPa, respectively [50]. Compared to the properties of the material of this study shown in Table 11 of Chapter III, the modulus and *UTS* of the N24A are greater by $21 \pm 4\%$ and $9 \pm 6\%$, respectively. A considerable difference in modulus may be due to the difference in porosity level in the two materials.

If the identical fatigue parameters including the frequency, stress ratio and peak stresses are applied to two materials with different moduli while other properties are relatively similar, then the material with a larger elastic modulus would experience a relatively smaller strain and thus will likely survive more cycles to failure. The higher elastic modulus of the N24A is probably due to its denser MI matrix with 2 *vol %* of porosity [50], compared to ~4.0 vol % porosity of the woven MI Syl-iBN/BN/SiC of this study. The difference in elastic modulus between 259 GPa of N24A and 207 ± 9 GPa of the woven MI Syl-*iBN*/BN/SiC cannot account entirely for such a large difference in stress required to cause fatigue failure between 25 and 7 hours, the peak stresses applied to two CMCs which resulted in a similar cycles-to-failure, because the applied stress is outside the elastic range. In addition, the differences in the room temperature properties such as the ultimate tensile strength and the proportional limit between the two materials are too small to justify such a large difference in stress that resulted in failure after 5~7 hours. Thus, it is concluded that the difference in the material properties between the N24A and the woven MI Syl-*iBN*/BN/SiC is a minor factor, compared to the difference in the test conditions, to the difference in the peak stresses that resulted in similar cycles-to-failure between the two tests.

The major difference in measured or apparent fatigue strengths is due to the difference in the method of heating. Unlike in the furnace heating used in the study by Morscher et al, the

heating by the atmospheric combustion burner rig involves the impingement of a directional flame over the width of a specimen such that the flame deflected off the impingement zone on the front surface splits and travels along the planar directions providing convective heating to the specimen outside the zone of direct flame impingement. In the meantime, the temperature increases on the unheated reverse surface of the specimen as the conduction carries the heat flux across the bulk of the specimen. Thus, a rather large temperature gradient is generated over the dimensions of the specimen. The thermal gradient subsequently induces the thermal gradient stresses, which is superposed on the mechanically applied cyclic stress, likely resulting in more matrix cracking and more oxidation. This is believed to be the main reason for the significantly reduced fatigue strength of the material of the current study.

Table 30: Test parameters and Properties of the two woven MI Syl-*iBN*/BN/SiCs [22,38,50]

Test Type		This Study	N24A
Room Temperature Tension	Elastic modulus (GPa)	207	259
	PL (MPa)	167 ± 7	~180
	UTS (MPa)	431	470 (est.)
High Temperature	Stain at failure (%)	0.57	0.48 (est.)
	Temperature (^{o}C)	1235±50 (Front)	1204
		850±50 (Back)	
	Stress Ratio, *R*	0.05	0.05
	Applied Stress (MPa)	125 @ 1Hz	220 @ 1Hz
	Applies Stress Normalized to RT *UTS*	0.29	0.47
	Time (Cycles)-to-failure	apprx. 5 hours	apprx. 7 hours

In addition, there is a non-uniform gas chemistry field surrounding the specimen due to the single-sided heating by combustion. Further, the combustion products contain up to 50% moisture by volume or 30% by weight, compared to the furnace environment containing much lower level of moisture. The gas chemistry interfacing with the front surface under direct

impingement of combustion flame has the highest moisture content, while the unheated reverse surface interfaces with the lowest moisture content at lower temperature. As the moisture accelerates oxidative degradation, the damage evolution process in which oxidation adds to detrimental effects will occur faster and easier, reducing the fatigue life.

Finally, the gas pressure load associated with combustion flame is unique in the test setup used in this study. However, the load is estimated to be only 10N, roughly 100 kPa over the gauge section of the specimen, and there are no solid particles in the combustion that would impinge and apply impact loading on the specimen. Hence, the erosion by gas flow is considered to be of a secondary importance, and is left out in the current analysis. There are other subtle differences between the two test environments including equipment, testing protocols, methods of thermal protection of the apparatus, etc. However, these are also considered either relatively insignificant or as a subset of the three key differences identified above. Although the ensuing discussions of the three key features are developed with the illustration using the woven MI Syl-*iBN*/BN/SiC specimen, the understandings obtained from the illustration apply not just to the woven MI Syl-*iBN*/BN/SiC, but to all four CMCs tested in the present study.

6.2 Thermal gradient stress

The thermal gradient stress arises due to the non-uniform temperature field created by the combustion heating applied from one side of specimen. Figure 103 and Figure 104 depict the thermal images and compare measured and modeled temperature profiles along the longitudinal axis of a specimen on the flame-impinged surface and unheated back on the opposite surface, respectively. Thermal gradient is due to the underdeveloped turbulent flame, which involves high temperature premixed flame of the inviscid core mixing with cooler secondary combustion in the

outer ring of the flame, resulting in a parabolic flame temperature profile with large gradients in the radial direction. Details of the flame were discussed in Chapter III. This flame is approximately 20 *mm* in diameter, and the heat flux delivered by the impingement of this flame on the central gauge section of the specimen from one side will preferentially heat the zone of direct flame impingement. The specimen outside this zone is heated by forced convection of the deflected flame of reduced intensity. Due to this secondary heating outside the zone of direct flame impingement, the resulting temperature gradient on the in-plane directions is less severe. The specimen may be expected to fail where the largest thermal gradient stress is experienced in the loading direction. This is the reason that the fracture cannot directly be attributed to the parameters associated with the prescribed combustion condition. The heat flux received at the front surface is simultaneously conducted across the thickness of the specimen. But due to the preferential heating on a concentrated zone that results in thermal gradient on the surface, a lateral spreading of heat is experienced, referred to as the thermal spreading effect [128]. The thermal spreading effect involves reduced heat flux in any one direction due to the lateral spreading [128] of the heat flux as the heat conducts across the specimen thickness. This causes the specimen to experience a large temperature drop across the thickness during heating, which was observed experimentally to be as much as 450$^{\text{o}}$C. The lateral spreading involves mixing of the heat of varying intensities from the gradient of heat flux interfacing with the front surface. The mixing produces a more uniform temperature on the reverse surface, as seen from the measurement by the IR system.

The thermal gradient stresses generated in the specimen due to the temperature gradients can be quite significant. A simple one dimensional thermal stress analysis across two surfaces at the temperatures of 1250$^{\text{o}}$C and 900$^{\text{o}}$C indicates a thermally induced stress of approximately 330

227

MPa between the two surfaces, assuming that the sample cannot warp or bend and that the material properties are those of the woven MI Syl-iBN/BN/SiC, i.e. *CTE* of 4.5 X 10^{-6} /^{o}C and *E* of 207 GPa. In this one-dimensional scenario, the heated surface at 1250°C would be under compressive stress of -165 MPa, while the opposite surface at 900°C is under tensile stress of +165 MPa in addition to the applied load. The thermally induced stress estimated from this one-dimensional consideration is close to or exceeding the room temperature proportional limit of 167 ± 7 MPa, and thus may approach or exceed the level that initiates matrix cracking. This thermal stress coupled with mechanically applied stress could easily elevate a stress well above the material's proportional limit. With the thermal gradient stress identified as a potentially major contributor to failure, a more in-depth investigation of the stress state was warranted for the specimen, in which the temperature field with large gradients exists in all directions.

6.2.1 Finite Element Modeling

A sequentially coupled thermal-stress analysis was used, which takes a two-step approach involving, first, the development of a three-dimensional finite element model that simulates the temperature field of a specimen that matches the experimental observation using the commercial code, ABAQUS [129]. The second step involves the determination of the thermal gradient stresses based on the temperature field from the first step. For this, the temperature field obtained from the first step along with the thermal and mechanical properties intrinsic to the material for the given condition is input into the finite element model of the specimen created in ABAQUS.

The physical dimension of the specimen modeled in ABAQUS does not include the grip portions, whose surfaces were engaged with the upper and lower MTS grips, and thus the model specimen length is approximated at 100 *mm*, not the whole specimen length of 150.4 *mm*. The

assumption is that the MTS grips are rigid bodies and therefore the gripped portion of the specimen does not deform. The rest of the specimen dimension was input according to the measured physical dimension of the woven MI Syl-iBN/BN/SiC specimen. After that, its surface was partitioned into several regions before they were meshed. In particular, the heated gauge section was partitioned into several finer regions. Finer mesh was created on those smaller partitioned areas encompassed by the heated gauge section, as they were considered of a higher importance.

6.2.1.1 Temperature Gradient

This stage of the model captures only the temperature profile surrounding the specimen with no consideration of any applied stress. On the modeled specimen, the temperature field was created such that it closely matches the experimental observation made by the IR system. Each partitioned surfaces of the modeled specimen was assigned gas temperature and convection heat transfer coefficient. Gas temperature input was either measured or estimated to have interfaced with each specific surface, and the convective coefficient was estimated based on the understanding of its convective environment, i.e. the degree of forced convection. For instance, the flame impinged area was given the gas temperature of $1800^{o}C$, while $450^{o}C$ were assigned on the opposite surface. In addition, the directional thermal conductivities, i.e. k_{11}, k_{22} and k_{33} were provided as input. These properties, shown in Table 31, were temperature-dependent and thus were put in a tabular format with respect to temperature based on the data available from DiCarlo et al [22]. For these inputs, a steady state analysis was performed to result in the temperature fields represented in Figure 103B and Figure 104B.

Table 31: Thermal and Mechanical Properties of woven MI Syl-*iBN*/BN/SiC as Input to FEM

Temp-erature (^{o}C)	Thermal conductivity ($W/m^2 \cdot {}^o C$)			CTE ($/^o C$)	Density (g/cm^3)	E_e (GPa)	E_p (GPa)	PL (MPa)	UTS (MPa)
	k_{11}	k_{22}	k_{33}						
204	45	45	25	2.0E-6	2.7	207	50	167	410
1200	45	45	10	4.6E-6	2.7	207	50	167	410

Figure 103C and Figure 104C compare the temperature profile collected from the post-processing of a set of IR images of the specimen taken during testing and the ABAQUS rendition of the temperature profile. Jitters in the model temperature curves, found more pronounced away from the center of each curve, are the noise due to the edge effect associated with relatively large mesh size away from the gauge section.
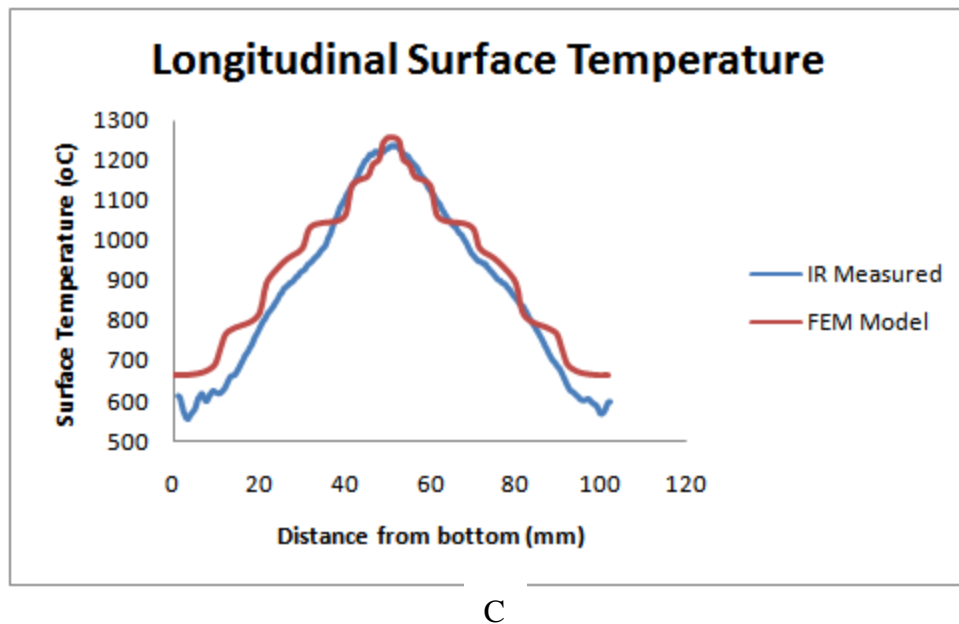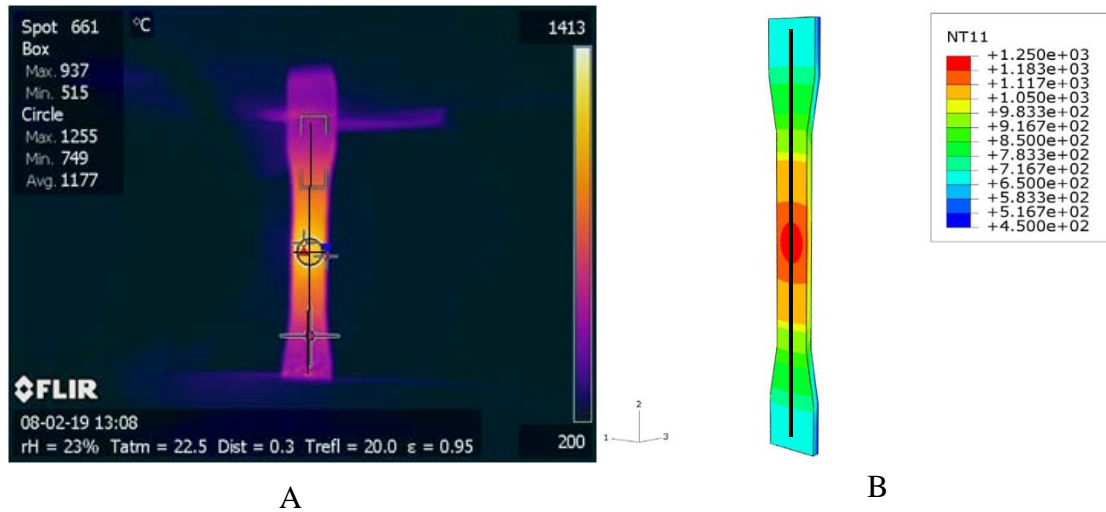
Figure 103: Surface temperature profile on the front surface; (A) measured along the longitudinal axis as shown using IR, (B) modeled in ABAQUS; (C) comparison between measured and modeled along the longitudinally drawn line in (A) and (B).

A   B

C
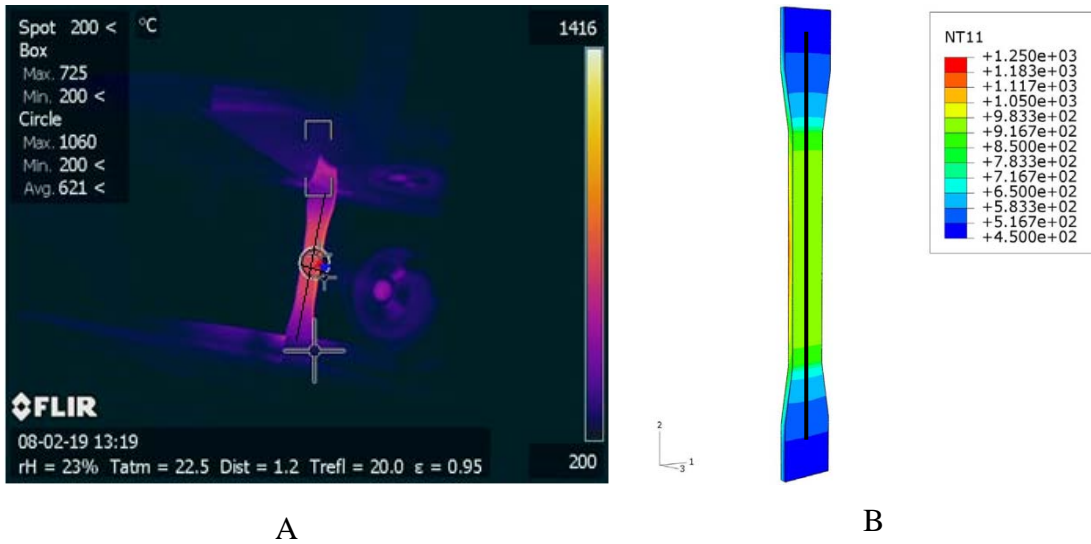
Figure 104: Surface temperature profile on the back surface; (A) measured along the longitudinal axis as shown using IR, (B) modeled in ABAQUS; (C) comparison between measured and modeled along the longitudinally drawn line in (A) and (B).

6.2.1.2 Thermally Induced Stress

Based on the temperature profile, the thermally induced stress field was subsequently computed using another model in ABAQUS. With the temperature field from the earlier analysis put in as the predefined field, the thermal properties such as coefficient of thermal expansion

(*CTE*) as well as mechanical data such as the stress-strain data were inserted into the stress model that assumed orthotropic mechanical and thermal properties. In order to reflect the temperature-dependence of these properties, they were put in as a function of temperature based on the data available from DiCarlo et al [22], as shown in Table 31. A bilinear representation of the stress-strain data reported for this material in this study was inserted into the model using the notation and method prescribed by John et al [130]. Figure 105 describes the bilinear stress-strain used to simulate the data. The thermal and mechanical properties used in this model are represented in Table 31.
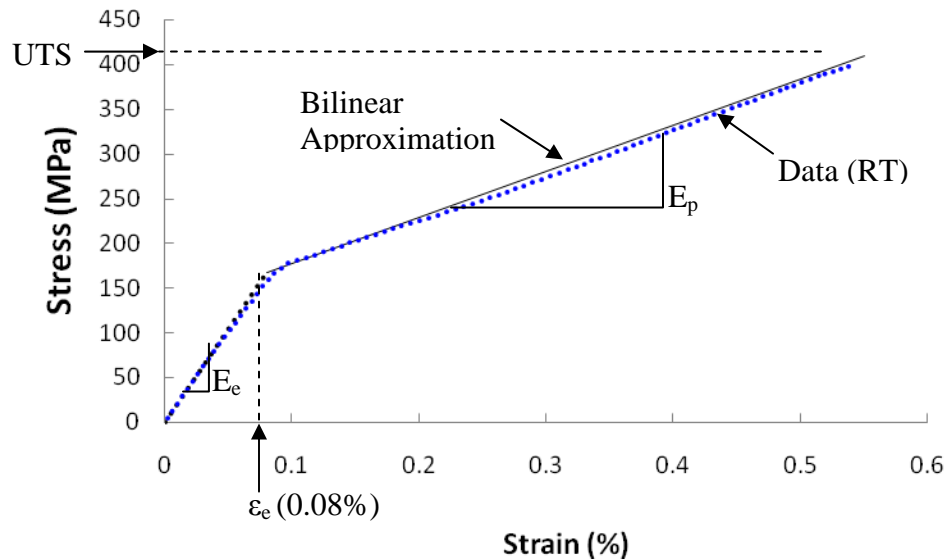
Figure 105: Bilinear stress-strain response simulating the data

In addition, boundary conditions were applied based on the assumption that the MTS grips behave like rigid bodies. This corresponds to making the upper and lower surface of the modeled specimen to be kept from any displacements other than that in the direction of loading, (22 direction). A steady state analysis using these boundary conditions and the properties specified in Table 31 was carried out to result in the stress field induced purely by the temperature profile

233

modeled earlier. This is represented in Figure 106, which displays the stress in 22 direction in terms of color contour. The stress field was shown in the 22 direction, because some of the largest thermal gradients were experienced in the shown direction, resulting in large stress in that direction. Further, the mechanical load will be applied in the 22 direction, adding to the shown stress field. From the figure, it can be observed that the front surface is under compression and the back surface under tension. This is because the expansion of the specimen due to temperature rise is greater on the front surface at higher temperature than on the back surface at lower temperature. The average stress on any cross-section is zero because there is no applied load. Note also that the end concentration near the gripped portion of the modeled specimen is to be ignored as it is due to boundary condition being infinitely stiff.

(Front)   (Back)
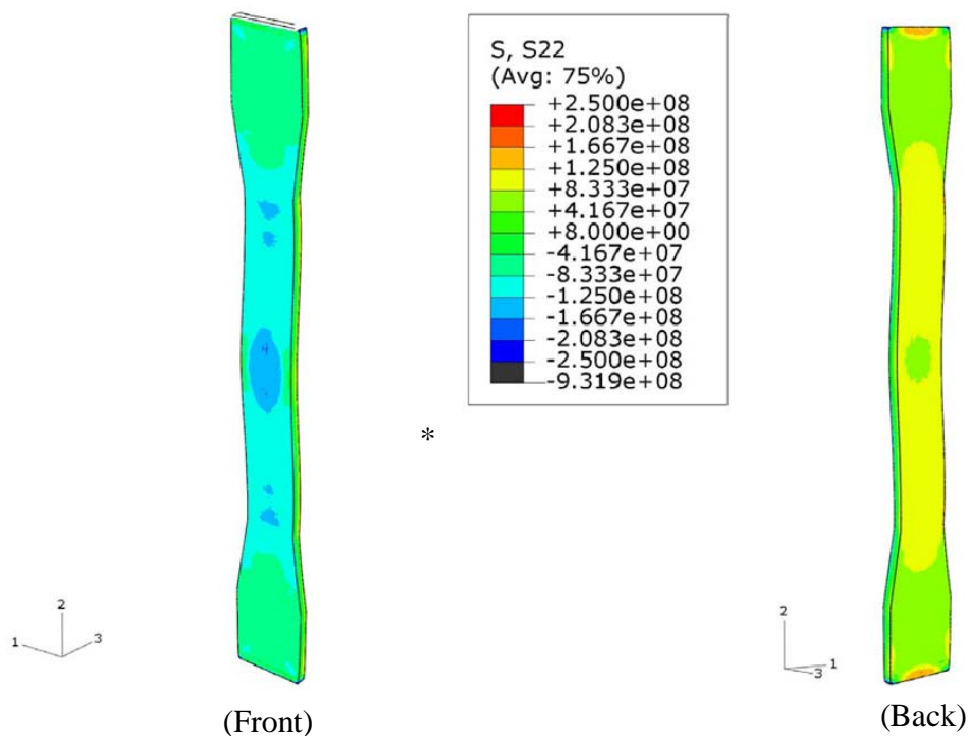
Figure 106: Stress induced by thermal gradient represented in color contour: Stress in the longitudinal direction (S22) Deformation is magnified for illustration by 33.5 times

The highest compressive stress is experienced on the front surface at the geometric center of the specimen is approximately -160 MPa. On the unheated back surface undergoing tensile stress, however, the peak tensile stress up to +110 MPa is induced on the back surface at the cross-sections approximately 12~25 *mm* above and below the geometric center of specimen. This is indicated by the hump depicted by arrows on the stress curve in Figure 107. This is where the largest curvature is experienced during the thermally induced bending of specimen in the presence of the mechanical constraint boundary conditions imposed by the MTS grips. The stress profile along the longitudinal axis for the front and back surfaces is shown in Figure 107 to illustrate the locations of the peak compressive and tensile stresses. Smaller oscillations in the stress curves are due to the change in boundary conditions along with the effects associated with relatively coarse mesh.

Figure 108 shows the thru-thickness profiles at the mid plane. Across the thickness less than 1.6 *mm*, a drop in temperature of $450^{o}C$ is observed both experimentally and by the model, as evident from the comparison of the temperature profiles demonstrated in Figure 103 and Figure 104. The thermal stresses were plotted across the specimen thickness at the center of the specimen, as indicated by a dotted line on the model specimen in Figure 108, and also along the side edge surface of a specimen at the same cross-section.
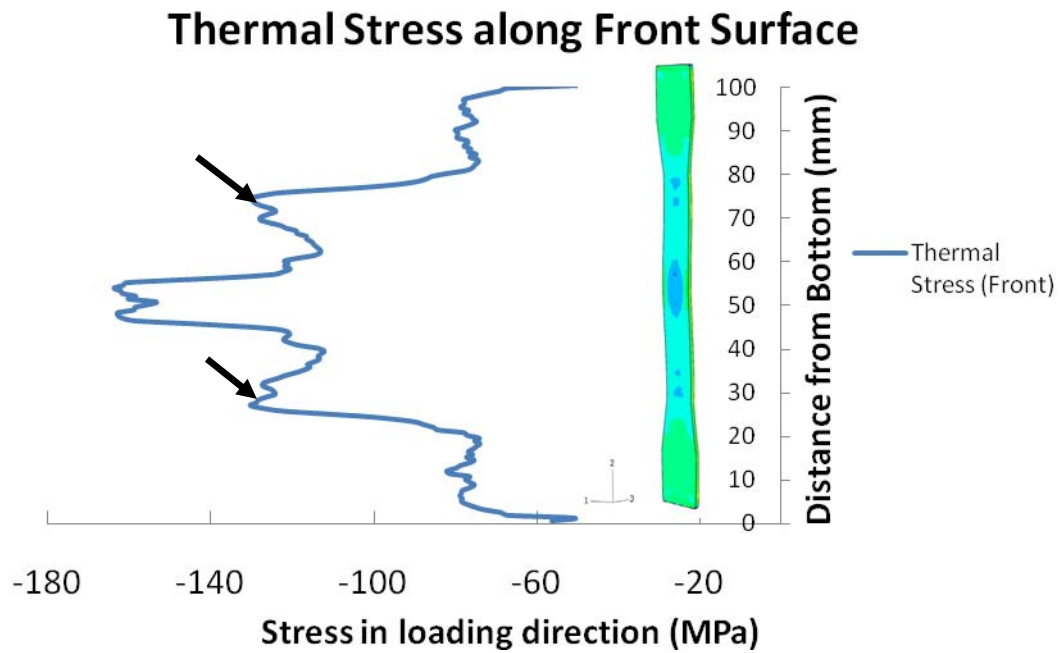
A
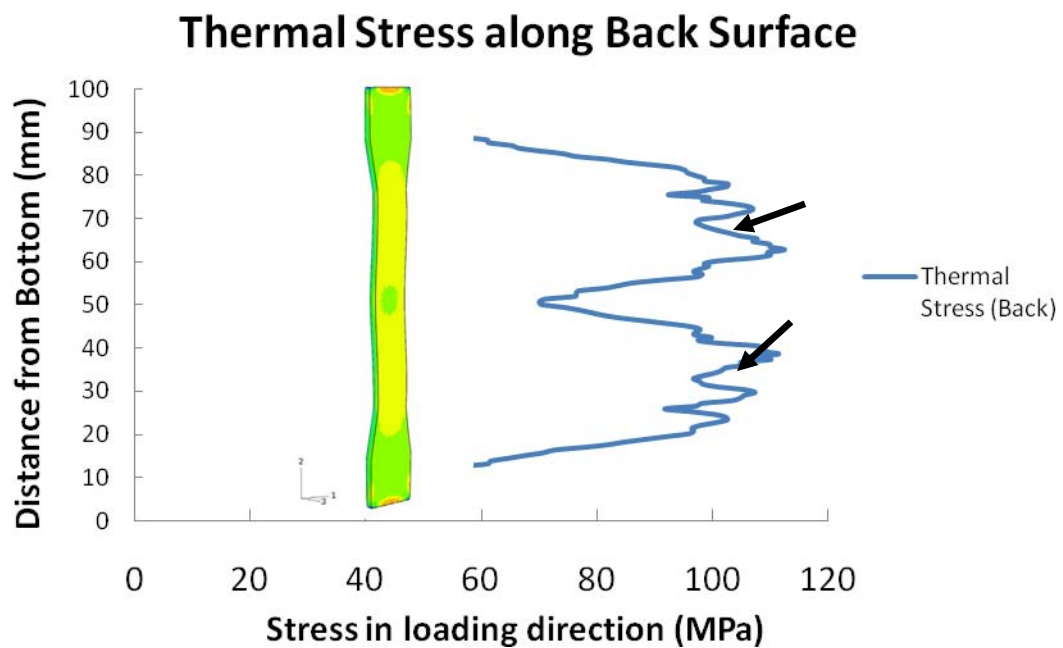
B

Figure 107: S22 induced by thermal gradient; (A) on the front surface and (B) on the back surface: Arrows indicate the locations of the stress induced by the bending moment
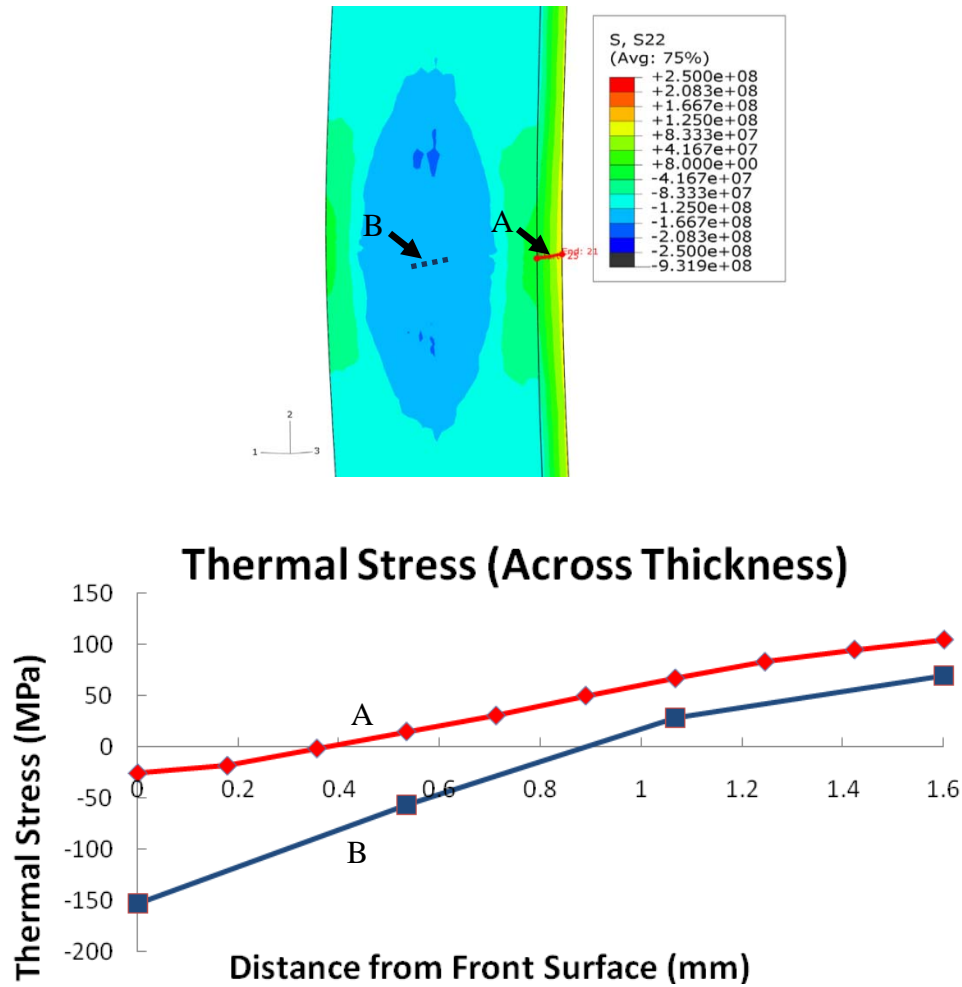
Figure 108: Thermally Induced S22 across the thickness

Along the side edge surface, the thermal stress varies gradually from -30 MPa at the front

corner to +105 MPa at the rear corner. Through the specimen centerline, the front surface is under

a compressive stress with a greater magnitude, i.e. -155 MPa, than along the side edge surface,

while smaller tensile stress is experienced on the opposite surface. For comparison, the initial

simple estimate predicted ±165 MPa. There are two clear observations from this analysis. First,

the plies near the front surface experience compressive stress, while the plies adjacent to the back

surface experience tensile stress. Both compressive and tensile stresses are induced by

temperature gradients across the specimen, independent of any applied load. Secondly, the magnitudes of the compressive and tensile stresses are position-dependent, resulting in a non-uniform stress field. The same ply undergoes both tension and compression depending on the specific location on the ply. The 3rd ply from the front surface, which is spanned by the distance between 0.5 *mm* to 0.75 *mm* from the front surface, for example, is under tension near the side edge and under compression close to the center of the specimen width, as evident from the comparison of the two curves in Figure 108 in the specified span. The non-uniform stress field on a transverse plane defined by the width and thickness considered here is further complicated by the non-uniformity in the longitudinal thermal stress gradients described earlier. The complexity causes a unique stress state on all points in the specimen. The non-uniformity is maintained as the stress level shifts up in the event that a mechanical load is added.

Combined with the thermally-induced non-uniform stress field, the mechanical fatigue loading with the peak stress of 125 and R =0.05, for instance, elevates the stress level globally in a cyclic manner as shown for a through-thickness line at the center of the specimen in Figure 109C and a line along on the side edge surface as shown in Figure 109D. In each of Figure 109C and D, the stress profiles corresponding to the stress excursion between 125 MPa and 6.25 MPa are nearly parallel. The changes in slopes in both figures are due to the bilinear characteristics of the model, which, upon reaching the proportional limit of 167 MPa, takes on the characteristics of plastic region of the stress-strain curve. The change in stress between the maximum and minimum stress case in either figure does not correspond to the amount applied mechanically, because the stress profile plotted here is a section cut along the through-the-thickness direction from continuum of thermal stress contour, whose integral over the entire cross-section of specimen equals the applied mechanical stress.
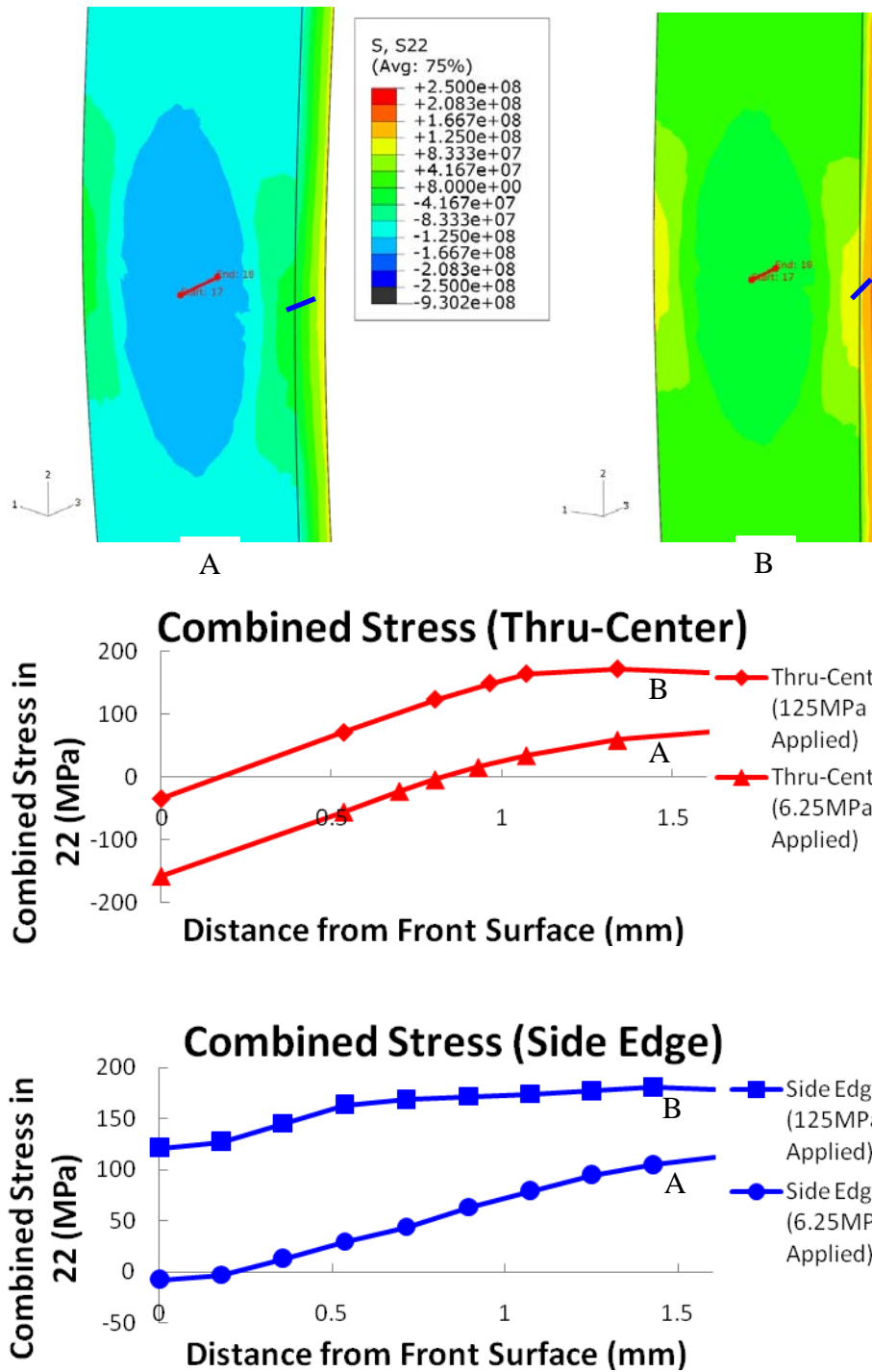
Figure 109: Combined Thermal and mechanical stress across thickness in the 22 direction under (A) 6.25 MPa and (B) 125 MPa: (C) Stress (S22) profile through the center and (D) stress (S22) profile along the side edge.
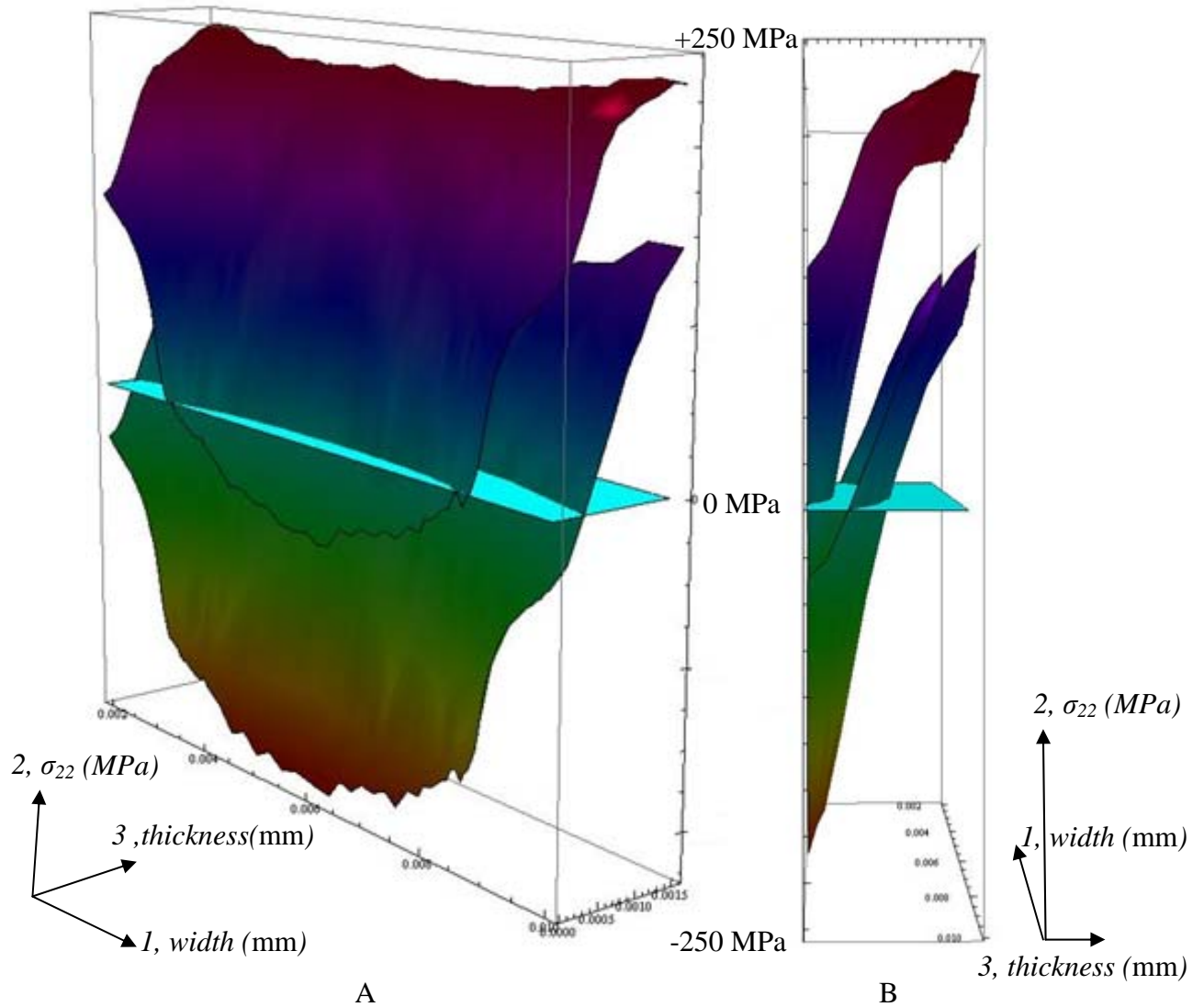
Figure 110: Surface contours representing upper and lower limits of stress acting on a cross-section undergoing the applied fatigue between 125 MPa and 6.25 MPa

Figure 110A illustrates two stress contours plotted using Mathematica based on the combined stress resulting from the ABAQUS finite element model. The contours represent the stresses on a cross-section in the heated zone of the maximum of 125 MPa and minimum applied axial stress of 6.25 MPa. Figure 110B shows the same surface contours from a different viewpoint (i.e. parallel to the vector normal to the specimen's side surface). In both figures, the vertical axis

represents the stress (in MPa) in the loading direction on the cross-section, and the two axes defining the plane normal to the vertical axis represent the width and thickness of the cross-section. With respect to the zero stress plane shown in cyan color, the volume integral of each contour should equal 125 MPa and 6.25 MPa, respectively. It is easily confirmed qualitatively from a visual examination of the position of each contour relative to the zero stress; the upper contour representing the 125 MPa case has most of its surface area above the zero plane, while the lower contour that represents 6.25 MPa case has about an equal volume above and below the zero stress plane, canceling each other out to leave a small difference amounts to 6.25 MPa. The stress profile along the through-the-thickness direction plotted in Figure 109 is a cross-section of the upper and lower contours.

A cyclic loading between the maximum and minimum stress represented by the curves in Figure 109 can therefore constitute, for this particular cross-section, a compression-compression (C-C) fatigue in the region from 0.0 to 0.1 *mm*, a tension-compression (T-C) fatigue from 0.1 to 0.9 *mm*, and a tension-tension (T-T) fatigue from 0.9 to 1.6 *mm* relative to the front surface. As the combined peak stress changes from -23 MPa on one end to +168 MPa on the other, the effective local *R*-ratio changes as well. From the analysis, the C-C fatigue is predicted in the part of the specimen adjacent to the zone undergoing the direct flame impingement, while T-T fatigue is experienced in the region close to the back surface. The T-C fatigue occurs in the transitional region. This is schematically illustrated in Figure 111 for a representative plane cut in perpendicular to the loading direction across the center of specimen. The mechanical loading is applied in the out-of-plane direction.
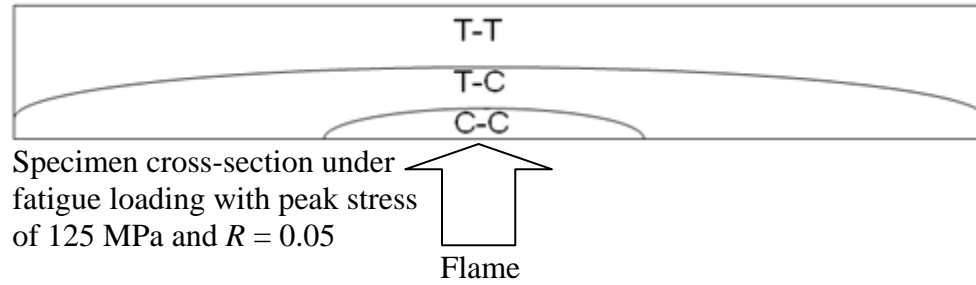
Figure 111: Illustration of varying stress states on a cross-section due to thermal gradient stress

The use of the maximum and minimum stresses to describe the applied fatigue loading is approximate because it ignores the progressive change in conditions under cycles and the time-dependent change in properties with, for example, frictional heat generation. However, the approach provides a good indication of the stress state in a specimen. Detailed fatigue modeling that builds upon the current model and takes into account the progressive and time-dependent effects of CMCs would further benefit the understanding of the failure mechanisms under fatigue.

6.2.2 Assessment of the finite element model

A qualitative assessment was made using optical and scanning electron microscopy (SEM) in an attempt to substantiate the numerical analysis results involving the thermal gradient stress discussed above. For this, the number of cracks was counted from a set of the woven MI Syl-*iBN*/BN/SiC, each sliced by 2 *mm* length along the loading direction from the specimen that resulted in runout under the peak stress of 125 MPa. The surface of each sliced section was then polished and examined under the optical microscope. The number of cracks was recorded over a group of two adjacent plies. Total crack count from all the sectioned surfaces of the runout specimen is summarized on Table 32 with respect to the plies. Figure 112 captures one of the sectioned surfaces examined under optical microscope.

Table 32: Crack distribution across the thickness of the runout woven MI-Syl-*iBN*/BN/SiC

Ply	Number of cracks in thru-thickness direction
5th & 6th plies	31
3rd and 4th plies	19
1st & 2nd plies	5
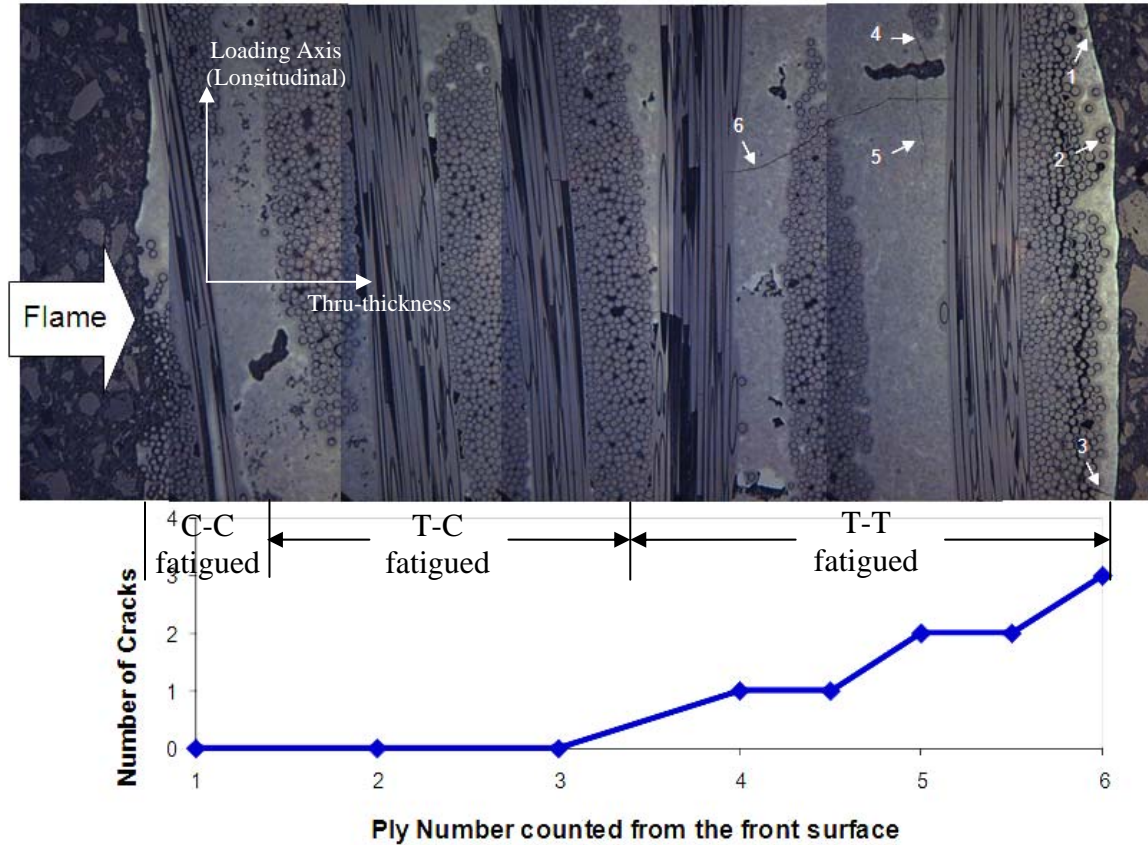
Figure 112: Representative crack distribution across the thickness of the runout woven MI Syl-*iBN*/BN/SiC. The combustion flame was applied onto the first ply on the left.

In Figure 112, there were no visible cracks near the front surface of the specimen which the model predicts to have undergone T-C and C-C fatigue, while four cracks aligned in thru-thickness direction were found on the part that underwent T-T fatigue. A similar trend is observed from Table 32 that shows relatively small number of cracks found aligned along the thru-

243

thickness direction on the plies near the flame impinged surface, at which the T-C fatigue presumably occurred during the fatigue test. The trend in crack distribution was common in most sections optically examined and thus resulted in a similar trend when all the cracks aligned along the thru-thickness direction are collected from all four sectioned samples. This microscopic observation supports the finite element analysis that showed the plies near the unheated back surface were under tension-tension (T-T) fatigue loading with peak stress ranging from +168 MPa to +210 MPa. This implies that the region underwent a fatigue loading with the peak stress exceeding the proportional limit of the material, causing matrix cracks to nucleate and develop in a perpendicular direction to the loading.

With the increased understanding of thermal gradient stress, the difference in the peak stress applied in this and Morscher's tests can be accessed. The peak stress of 125 MPa applied to woven MI Syl-*iBN*/BN/SiC caused failure after approximately 5 hours in the combustion environment of this study, and the peak stress of 220 MPa specimen caused failure to the N24A after about 7~8 hours in furnace air environment of the tests reported by Morscher et al [50]. The single-sided combustion heating of this study induced thermal gradient stresses along with the fatigue loading with peak stress of 125 MPa put the plies near the front surface under compression-compression or tension-compression fatigue and the other plies under tension-tension fatigue with larger peak stresses up to +180 MPa with increased R-ratio. An elevated stress states caused by the thermally-induced stress combined with the mechanical fatigue may be the key explanation that the specimen exposed to the single-sided combustion loading showed lower fatigue life at 125 MPa, as compared to 220 MPa in a furnace with no thermal stress.

Above all, it is clear that the non-uniform thermal gradient stresses changed a well-defined mechanical fatigue loading with the uniformly applied peak stress of 125 MPa and a specific *R*-

ratio of 0.05 into a non-uniform peak stress field with each point in the specimen undergoing a different temperature as well as a different type of fatigue cycle, i.e. C-C, T-C and T-T fatigue, along with a non-uniform stress field and *R*-ratios. This makes a direct comparison between the test results from Morscher's study and the current one impossible. However, the finite element analysis was used to demonstrate that the difference in fatigue strength could in part be attributed to thermal gradient stress. This is an important consideration in the airfoil applications of gas turbine engines, because all real service conditions will also be complicated with thermal gradient stress.

6.2.2.1 Experimental validation of the finite element model

As discussed in Chapter IV, fatigue testing similar to those performed in burner rig environment was carried out on woven MI Hi-Nic-S/BN/SiC in laboratory air furnace environment. As evident from Figure 60, fatigue strengths obtained from the furnace tests were greater than those from the burner rig tests by relatively constant amount, i.e. 45 MPa. This clearly suggests that thermally induced stress added to the combined stress that resulted in lower fatigue strengths. If a transient degradation mechanism such as oxidation were the main cause of the observed difference in strength, the two S-N curves would not be as parallel as shown, because oxidation would have had greater effects on specimens with greater time of exposure to oxidative environment.

Still, there may be a question as to relatively small difference in fatigue strength between the two tests, i.e. 45 MPa as compared to 100+ MPa predicted by the finite element model (FEM) results. There may be a couple of explanations for this observation. First, the cross-sections at which all three woven MI Hi-Nic-S/BN/SiC failed from the furnace tests were well outside the

gauge section (Table 16), where the specimen temperature was somewhat lower than 1235 ± 5°C. In fact, the cross-section at which the runout specimen fractured was slightly outside the reduced section of the specimen, close to the outside of the furnace. Much of the furnace heating was diluted by room air and the specimen temperature was believed to be below 1000°C, or inside the intermediate temperature regime where the SiC/SiC CMC materials are known to degrade at higher rates by oxidation due to the relatively low growth rate of protective silica. Thus, the failure at the proximity of this location could occur at lower stress, accounting for the relatively small difference in fatigue strength. Secondly, the temperature drop across the thickness of a woven MI Hi-Nic-S/BN/SiC specimen in burner rig exposure was similar to that observed from the woven MI Syl-iBN/BN/SiC used in the finite element analysis demonstrated in the preceding section. However, the thickness of woven MI Hi-Nic-S/BN/SiC is 2.2 mm, as compared to 1.6 mm of the woven MI Syl-iBN/SiC. Thus, the temperature gradient is not as stiff as in the modeled case and the resulting thermal gradient stress would be less than those demonstrated in the preceding section, i.e. 100+ MPa. Thirdly, the furnace tested runout specimens failed near the grip whereas the burner rig tested specimens failed within the reduced section. In general, the failure outside the reduced cross-section occurs at a lower stress. Lastly, as apparent from the gradient of stress across the specimen dimension demonstarted in the preceding discussion, the local stress at which a crack initiates varies by location on the specimen. Once the crack develops under cyclic load, it would preferentially grow along the morphologically rough machined edge and reduce fracture toughness. This is likely followed by the crack propagating inwardly as observed from micrographic analysis. Thus, it is the stress accountable for the initial crack formation that affects the failure strength, and this stress can vary probablisically depending on the location on the edge that the crack initiates.

6.3 Gas Chemistry

In addition to thermal gradient stress, the disparity in the distribution of the microscopic features between the front and rear part observed on the sectioned runout specimen could be in part attributed to the difference in the gas chemistry that interfaces with the front surface from the gas chemistry on the back surface. The front, flame-impinged surface interfaces with high moisture content from the direct impingement of the primary combustion of the premixed gas in the core of the flame, which contains about 32 *vol %* of H_2O. The combustion that takes place outside the flame core is referred to as the secondary combustion, which is the physical mixing of the flame core with compressed air on the periphery. Any fuel left unreacted from the primary combustion reacts with the compressed air to combust and produce moisture content up to 23 *vol %* of H_2O. It is the primary combustion that contains 32 *vol %* of H_2O that interfaces with the area on the front surface under direct flame impingement.

The machined edge surface on the side of a specimen is primarily under the effect of the secondary combustion, as the side surface is roughly aligned with periphery of the combustion core. In addition, the products from the primary combustion get deflected and merge onto the stream that carries the secondary combustion products. Thus, the moisture level that interfaces with the side surface will likely fall between 23 and 32 *vol %* of H_2O. If a simplifying assumption is made that the ratio of the flow rate of reactant oxygen to that of the compressed co-flow air is used to determine the weighted contribution of the primary and secondary combustions, then 220 *standard cubic feet per hour (scfh)* of O_2 is nearly three times as much as the 77 *scfh* of O_2 in 368 *scfh* of the air. Thus, the moisture level estimated based on the weighted average between the two combustions determined with the simplifying assumption stated above is approximately 30 *vol %* of H_2O.

High-velocity combustion flow accompanies the formation of turbulent vortices curling behind the specimen that mix continuously with the ambient air residual near the unheated back surface. Consequently, the temperature and chemistry immediately behind the specimen is diluted. This was validated experimentally by the oxygen and nitrogen contents that were measured to be larger, and the moisture content that was lower than on the front or the side surfaces. With the gas temperature behind the specimen measured to be approximately 450~550°C, considerably lower than the combustion flame interfacing with the front surface, the rate of oxidation by gaseous diffusion through a crack developing from the back surface would be slower. Also with low moisture level interfacing with the back surface, the time it takes for boron content in the oxide to be leached out and for the subsequent boron-free oxide to solidify and adhere to adjacent constituents would be relatively long if a crack developed from the back surface.

Higher moisture content with lower O_2 and N_2 concentrations measured in the flame in front of the specimen, as compared to the lower moisture and higher O_2 and N_2 contents measured behind the specimen proves that the gas chemistry surrounding each specimen surface is non-uniform. The front and the side surfaces were interfacing with the combustion products with minimum air entrainment, while the gas chemistry interfacing the back surface is diluted by mixing of ambient air, explaining reduced level of moisture. High gas temperature and moisture contents make the front and side surfaces subject to increased rate of oxidation, compared to relatively slow oxidation on the back surface due to low temperature and moisture level.

Reduced fatigue strength life can also be attributed in part to the moisture in the combustion environment. The presence of H_2O accelerates the oxidative degradation by leaching out boron from the oxide. High moisture level increases the rate of boron removal from oxides, thus assisting the solidification process of the boron-free oxide that leads to rigid silica

interphases that in turn cause the grouped failure of fibers. There are no available data that can be put to direct comparison with the outcome of this study due to unique features of this test such as non-uniform gas chemistry and the thermal gradient stress. Still, degradation mechanism involving moisture has been validated through many studies of similar and same kind of SiC/SiC CMCs at intermediate and high temperature [13,25,28,42,44,124]. From these studies, it was confirmed that degradation by oxidation is accelerated at increased moisture level. Based on this, moisture is regarded in this study as an additive factor of consideration in explaining the reduction in the apparent fatigue strength. For more in-depth study of the moisture effect on fatigue life, a comparative study of similar tests with multiple different levels of moisture should be pursued to highlight the effect of moisture on fatigue in combustion environment.

6.4 Synergistic effects of thermal gradient stress and gas chemistry

In the attempt to put both the thermal gradient stresses and the non-uniform gas chemistry into a single context and formulate a comprehensive mechanism, multiple plausible scenarios that may have led a specimen to failure were considered. First, the thermal gradient stress puts the plies near the relatively cool back surface under elevated stress state with increased tensile peak stresses. The detrimental effect of an elevated tensile stress level is somewhat reduced by the increased stress ratio. Oxidation will ensue at relatively low rate due to relatively low temperature and moisture level. This is the mechanism in which a crack propagating from the back surface would lead a specimen to failure. Recalling from Figure 107 that showed that the peak tensile stress is experienced at approximately 12~25 *mm* above or below the center of the specimen, where curvature induces high bending stress, the failure may have been initiated at such cross-section experiencing the curvature. The experimental results show that four out of five runout

249

specimens tested for residual strength under monotonic tension fractured at the cross-sections that fall between 12 *mm* and 25 *mm* from the center of the specimen. All specimens that fractured during fatigue test in combustion failed within the gauge section (i.e. ± 6.4 *mm* from the specimen center) in which the peak compressive stresses occur on the front surface according to the finite element analysis.

As the positions between 12 *mm* and 25 *mm* above and below the specimen center, according to the model, are critical due to high tensile stress on the rear surface, the cracks must be open to the chemistry that interfaces with the back surface. The oxidative degradation can be severe, even with low moisture content, due to its intermediate temperature (i.e. $750 \pm 50^{\circ}$C), in which the rate of silica formation is not high enough to seal the cracks propagating under fatigue. Microscopic study of the fracture surface from residual strength tests of the runout specimens shown in Table 24 show the planar fracture surface with oxidative features, suggesting that the intermediate temperature oxidative degradation phenomenon may in fact have played a role in permanently reducing the residual strength.

Secondly, the plies adjacent to the flame impinged surface have higher propensity towards oxidation with 32 *vol %* of H_2O in higher temperature environment. Compressive thermal gradient stresses are acting on these plies, lowering the mean stress of the applied mechanical fatigue cycle such that either compression-compression or tension-compression fatigue is in effect. The SEM analysis of the region that underwent the tension-compression (T-C) and compression-compression (C-C) fatigue showed that they have more cracks that developed in parallel to the loading direction than the plies that experienced tension-tension fatigue, as shown in Figure 69 for the woven MI Hi-Nic-S/BN/SiC and Figure 80A for the prepreg MI Hi-Nic-S/BN/SiC in Chapter

IV. With peak stress of 125 MPa, the fracture surface showed glassy appearing oxides formed on the first two plies from the front surface. The oxidation reactions that produce such oxides occur almost instantaneously according to the estimation made using simplistic analysis of the chemical kinetics of the liquid boria evaporation [93] illustrated in Appendix E. This estimation is based on the assumption that the glassy appearing oxides are silica that solidified after leaching of boron content by evaporation. The estimated reaction time suggests that the region containing the oxides must have been exposed to the combustion environment for tens to hundreds of seconds prior to ultimate failure for a crack developing from the side edge of a specimen. Recalling that the finite element analysis which suggested that the first two plies relative to the front surface showing oxide layers formed on the surface underwent either T-C or C-C fatigue, these regions must have failed and been exposed to the combustion environment for at least hundreds of seconds before intact portion of the cross-section, which shrink with the cyclic load, finally failed by overload. This suggests that part of the specimen under either T-C or C-C fatigue degraded prior to the ultimate failure.

Data on SiC/BN/SiC CMCs under tension-compression is not available in open literature. For other types of CMCs tested under tension-compression, the failure was reported in relation to such micrographic features as ply-splitting [131,132] and matrix shear [133], both of which were observed from the current CMC material, as shown in Figure 43A, C, D and E in Chapter IV. Zawada and Pernot [132,134] investigated the tension-compression fatigue behavior of SiC/1723 CMC at room temperature. 1723 is the code name for aluminosilicate amorphous glass manufactured by Corning Glass Works that consists chemically of 57% SiO_2, 16% Al_2O_3, 7% MgO, 6% BaO and 4% B_2O_3 [135]. They reported that the tension-compression cycling resulted in cracks growing parallel to the loading direction and this reduced the overall fatigue life. Similar

longitudinal cracks were observed in Figure 43A, C and E from the area loaded with tension-compression fatigue of the MI Syl-*iBN*/BN/SiC. Most of the longitudinal cracks were found near the cross-section of residual fracture, approximately 19 *mm* from the geometric center of the runout specimen. 0° tows near the front surface showed ply-splitting and interply delaminations. The observation of these micrographic features in this study appears to be consistent with those documented by previous research on tension-compression fatigue of other types of CMC materials [131,133,134]. While no conclusive statement can be made about the correlation between the observed micrographs and the stress condition for the small test data collected from this study, the potential correlation may be validated through experimental study using the materials of this research under the T-C fatigue in uniform temperature environment.

From the microscopic examination of polished surfaces sectioned in parallel to the loading direction after the residual strength test that resulted into two fractured pieces, it was apparent that the 90° tows next to the front surface cracked preferentially in the plane of the plies. Figure 69 for the woven MI Hi-Nic-S/BN/SiC shows such splitting of the fiber bundles near the front surface, in comparison to the plies situated close to the opposite surface, which show no splitting. Matrix shear, ply splitting and interlayer delamination apparent from the tension-compression fatigued area of the sectioned surface were consistent with those reported on other types of CMC specimens that underwent tension-compression fatigue of other types of CMCs in previous studies, which documented reduced fatigue life under tension-compression fatigue. This is the second possible mechanism that may account for the failure initiated or developed under the tension-compression or compression-compression fatigue loading.

Continuous fiber reinforced SiC/SiC CMCs are usually much stronger under compression [40]. Tension-compression (T-C) fatigue, however, can be detrimental to the life of fiber

252

reinforced ceramic matrix composites, if the tensile peak stress is high enough to cause matrix cracking. From the model discussed earlier, it was shown that the tensile peak stress experienced at the front corner undergoing T-C fatigue could be 120 MPa for the specimen fatigued at 125 MPa applied peak stress. While the rear corner undergoing a higher combined stress of 180 MPa likely cracked first, the presumable initial failure at this site changes the stiffness of the material and makes the front more tensile to greater than 120 MPa during the progressive failure under cyclic loading. The higher tensile stress leads to matrix cracking on the front, and the cracks along the width may have propagated towards the center of the specimen providing the path of oxidation, as suggested by the shape of the oxidized region on the fracture surface shown on the bottom of Figure 37.

Even with the micrographic observations suggesting that the SiC/BN/SiC CMC of this study appeared to have degraded in tension-compression fatigued area, the presence of different stress states nearby this area that simultaneously experiences different modes of fatigue, e.g. T-T fatigue with varying R ratios, makes it uncertain whether the ply-splitting and matrix shears are direct results of the T-C fatigue or secondary ones that ultimately trace back the T-T fatigue with high peak stress on plies near the back surface.

The third possible scenario that may explain the failure involves the failure initiating from a spot close to the rear corner. The surface morphology of side edges is rough with fiber endings of irregular heights. This is the case especially for the woven MI CMCs. The corners as well as defects found on the edges are associated with high stress concentration, which makes them susceptible for cracks to initiate from. They are exposed to the high temperature combustion with moisture content up to 30 *vol %.H$_2$O.* Thus, a faster oxidation is anticipated than a crack developed from a back corner. In fact, the SEM analysis of most fracture surfaces revealed that

the corners and edges are severely oxidized. Unlike the failure in the intermediate range considered the first scenario, the oxidation in the high-temperature moisturous environment occurs at higher rate and produces the less viscous silica that flows and facilitates diffusion across to undermine its effectiveness as a protective layer against oxidation. Further, the finite element analysis presented earlier revealed that the vicinity area of rear corners experiences relatively high local tensile stress under tension-tension fatigue with the overall stress level increased by tensile thermal gradient stress on the plies adjacent to the unheated surface.

For each of the three possible failure scenarios described above, there are fractographic data that complement experimental observations and the finite element model that supports each mechanism. Microscopic evidence that the edges and corners are among the most severely oxidized area on the specimen fracture surface lead to the suggestion that the failure may likely have initiated from an edge or a corner on the fracture surface obtained from the gauge section, which supports the third hypothesis. This, however, does not exclude the other two scenarios to take effect, as there were, for instance, some fracture surfaces that showed the edge oxidation and at the same time fractured at the cross-section located at 19 *mm* above the specimen center like the MI Syl-*iBN*/BN/SiC runout specimen tested under monotonic tension for residual strength. Similarly, the MI Syl-*iBN*/BN/SiC that underwent the peak stress of 125 MPa, which was used to demonstrate the failure under compressive stress, showed edge oxidation as well.

The failure initiated at defective edge or corner may be linked to the region undergoing either tension-tension near the back surface or tension-compression near the front surface. From the comparison of the oxidation developed on each fracture surface obtained with the application of different peak stress, it is conceivable that there may be a stress condition more intrinsic to a particular mode of failure. For instance, the stress state generated in the specimen by the peak

254

stress of 110 MPa was evidently below the level that is conducive to failure during the fatigue test. Subsequent residual strength test revealed that the fracture occurred at 19 *mm* above the specimen center, which coincided with the location of high tensile stress near the back surface. The FEM model estimated approximately 180 MPa to be the total stress applied to this location of fracture during the fatigue test at 125 MPa applied. This suggests that the degradation was probably initiated and developed by the tensile stress exceeding the proportional limit, as described in the first possible mode of failure. Microscopic analysis of the fracture surface show that the oxidation developed primarily from the edges with no apparent preferential linking to the tension-tension fatigued area. The microscopic observation reinforces the assumption that the edge and possibly corners served as the failure initiation.

For the peak applied stress above 110 MPa, the failure occurred during the fatigue test in combustion within ± 3 *mm* of the specimen center, suggesting that the failure might in part be affected by the tension-compression fatigue. The fracture surface on the microscopic scale showed the glassy appearing oxides on the plies adjacent to the flame impinged surface, alluding to the possibility that the area under tension-compression fatigue may have failed during cycling and be exposed to the highly oxidizing environment before the ultimate failure. Hence, above the runout peak stress, the failure may be affected by the tension-compression fatigue, resulting in the fracture at the cross-section of the highest compressive stress. With the peak stress below the stress, the runout specimen, under the subsequent tension test at room temperature, failed at the cross-sections that underwent tension-tension fatigue with higher peak stress during the fatigue test.

The observation that the failure occurred in the intermediate temperature locations for the runout specimen under residual tension test, contrasted by the failures that occurred in higher

temperature zone of the gauge length of the third scenario, could also lead to the notion that the intermediate temperature interphase degradation phenomenon can be dominant mechanism of failure when the stress level is locally beyond that which causes enough matrix cracking, such as at 12~25 *mm* from the specimen center. If not, the interphase degradation in the limited exposed area would not be a dominant mechanism, as suggested by the different fracture location. The inviscid flame core that interfaces with the gauge section of the specimen is approximately $1800^{o}C$ in temperature and may contain very high moisture content up to 32 *vol % H_2O* along with higher concentrations of such species as CO_2 and O_2. These species are known to react with silica to form the volatile gaseous silicon oxyhydroxide (Si-O-H) molecules [84] by Equations (6-10) described in Chapter II. At such high temperature and high moisture content, the viscosity of SiO_2 is low enough to allow diffusion across, consuming the underlying SiC material continuously through its oxidation by H_2O, CO_2 and O_2. The rates of these volatilizing reactions increase in the turbulent flow condition [85] such as in the burner rig environment. If the 90° tows of the woven MI CMC were to fracture under cyclic load in such environment, then they could serve as the ingress route for oxidation that link up with loading carrying fibers on 0° tows. This is one way in which the third scenario could cause degradation to the load bearing capability, and will be illustrated with the aid of micrographs in the ensuing section.

In summary, two or more modes of failure are in effect simultaneously on a single specimen in which peak stresses and R-ratios change depending on the location. The temperature gradient generates a non-uniform stress field such that compression-compression, tension-compression and tension-tension fatigues with various R-ratios are experienced at different locations in the specimen for a nominal tension-tension fatigue loading applied. From the finite element analysis, the highest compressive stress occurs inside the geometric center of the

specimen, where all of the specimens failed that did not run out. The highest tensile stress is at a cross-section approximately 20 *mm* from the specimen center, where the highest curvature is experienced. This is the cross-section where all but one runout specimen fractured during the residual strength test carried out at room temperature. There appears to be a range of peak stress for a given condition that favors a certain mode of failure over another.

6.5 Microstructure characteristic of the combustion heating

The mechanistic approach using the finite element model above suggested the modes of failure stem from the non-uniform thermal and chemical conditions surrounding the specimen. This assessment may be reinforced by the fractographic study of oxidation, as the reactions that lead to oxidation occur upon chemical contact with oxidants from the environment that reached through diffusion process, which is affected by environmental parameters such as temperature and gas chemistry. Therefore, understanding the path of oxidation, which can be enhanced by micrographic study, is an important consideration in determining the failure mechanisms. In the following, two microscopic trends that apply to each of the four types of SiC/BN/SiC CMCs are highlighted in light of their roles on failure mechanism.

6.5.1 Porosity in Matrix

The intact MI matrix consisted of two different phases of *SiC* and *Si* metal as main constituents with Boron (*B*) and Aluminum (*Al*) impurities found in the dark spots indicated on Figure 113, which was taken from an intact region of the runout woven MI Syl-*iBN*/BN/SiC specimen. *B* and *Al* contents are confirmed through EDS (Figure 114). *Al* could have been either an unintended impurity species or a designed addition that could have been put in to keep the melting temperature of Si low for processing. Boron content probably stems from the boron filler

material in the matrix. As documented in Chapter IV, there can be also iron (*Fe*) found in the slurry cast CMCs as the inexpensive SiC used for the processing is known to contain impurities such as *Fe* [121]. From Figure 113, molten *Si* evidently did not wet on the entire surface area inside the void during the infiltration process, and thus did not densify completely, which may have reduced material's resistance to fracture. These pores appear to be random in their distributions throughout the matrix in all four CMCs.

The microscopy of the specimens of the four CMCs that were exposed to the fatigue tests in combustion indicated a graded distribution of porosity in the matrix. The post-test observed pores depicted in Figure 115. The SEM analysis showed that the pores appeared in the MI matrix along the outer surface of fiber tows for woven MI CMCs and in the area encircling each individual fiber for prepreg MI CMC. The EDS of an MI matrix rich in porosity showed oxygen content, as shown in Figure 116.
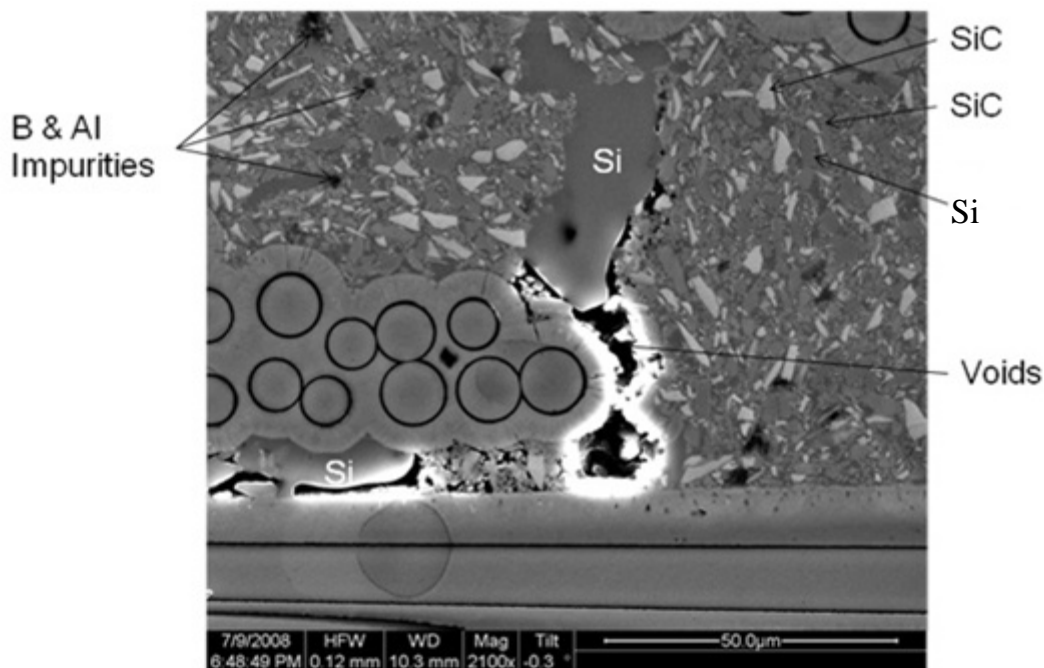
Figure 113: Chemical composition of the MI woven Syl-*iBN*/BN/SiC
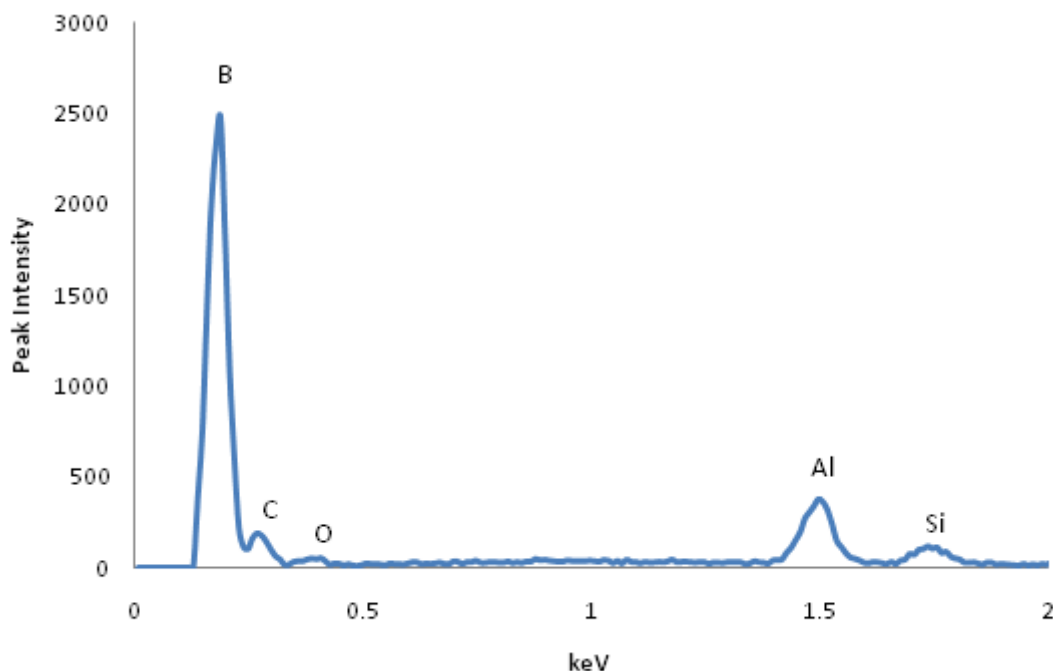
Figure 114: Chemical species in the dark spots in the MI matrix of the woven Syl-*iBN*/BN/SiC detected using EDS

The porosity decreased with the distance from the flame-impinged surface. This suggests that the phenomena may be enhanced at high temperature. High temperature can accelerate the physical and chemical changes by increasing the rates of diffusion and chemical kinetics. Based on this, there can be a few potential explanations for the observed porosity and its graded distribution. Carbon and silicon are two species of main interest for this discussion, because the pores were observed in the vicinity of regions in which residual carbon was expected from processing (e.g. fiber or tow surface) and in which molten silicon along with impurity species such as boron appeared to be rich (e.g. MI matrix surrounding fiber or fiber tow).
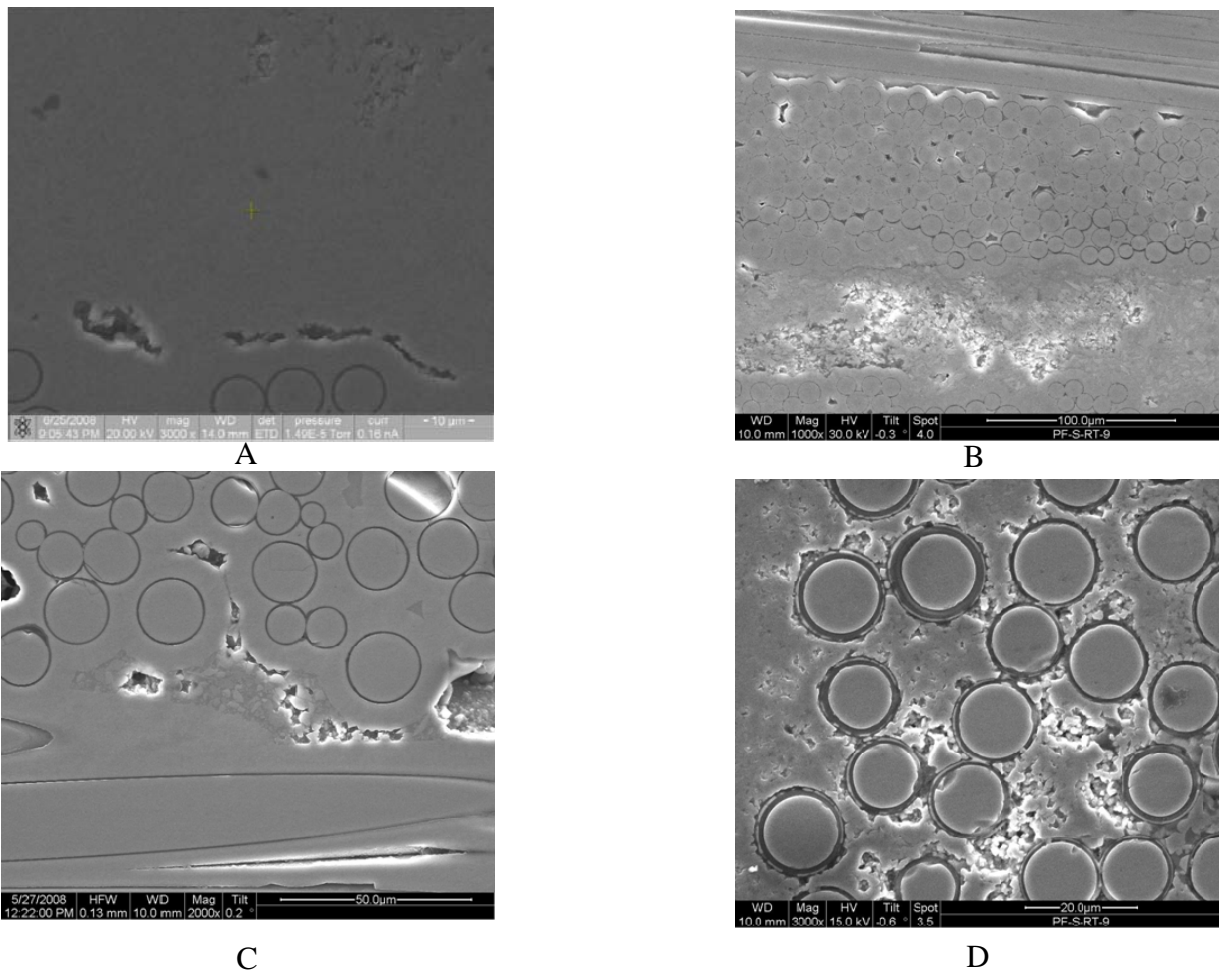
Figure 115: Matrix recession in all four CMCs: (A) woven MI Syl-*iBN*/BN/SiC, (B) woven MI Syl/BN/SiC, (C) woven MI Hi-Nic-S/BN/SiC and (D) prepreg MI Hi-Nic-S/BN/SiC
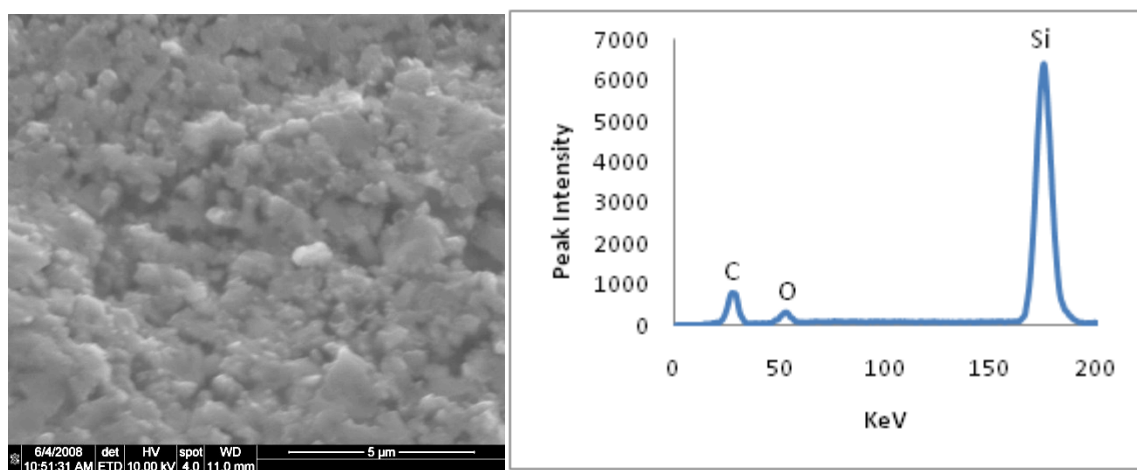
Figure 116: Chemical contents in the porous MI matrix according to EDS

First, the porosity could be a by-product of degraded regions in the MI matrix due to carbon diffusion. A previous study by DiCarlo et al [22] reported that silicon (Si) in the MI matrix diffused through CVI SiC matrix at high temperature to attack and degrade the SiC fiber and BN interphase coating. This is due to low density of the CVI matrix [121]. Carbon is a reactive species that exists on the surfaces of some fibers and tows. It has a lower molecular weight than Si, which facilitates the diffusion through the CVI matrix. Diffusion of carbon through low density constituents such as BN interphase and CVI SiC matrix would change the carbon contents in the nearby constituents. At high temperature, the carbon can react with Si and other impurity species such as *B*, *Al* and *Fe* existing in the matrix to form SiC and other product species containing impurity. It is possible that the porosity originates from degradation of the carbon-diffused regions of matrices and interphases under fatigue loading. More detailed micrographic study is needed to assess the fidelity of this conjecture.

Secondly, BN interphase, CVI SiC matrix or CVI S_3N_4 in the protective layer can crystallize, which causes shrinkage in its dimension at high temperature. The resulting shrinkage in dimension could lead to debonding. This is apparent from the Si_3N_4 protective layer in Figure 115D, considerably thinner in comparison to as-received shown in Figure 15B of Chapter II. The porosity may be a by-product of the degradation that follows from the debonding. The graded distribution is attributed to the rate of crystallization that increases with temperature. The three woven MI CMCs did not show the similar thinning of CVI matrix, however.

Thirdly, based on the graded pore distribution and its chemical contents, it can also be conjectured that the porosity in the MI matrix may evolve due to reducing chemical reactions that produce gaseous species, which could then outgas into the atmosphere. Oxidation can occur through matrix cracks evolving under cyclic load. The outgassing was indicated in the form of

bubbles observed in Chapter IV. The bubbles were found predominantly on the plies close to the flame-impinged zone. Along with carbon that readily reacts to form *CO* and *CO₂*, Opila et al [92] reported that the volatilization reactions occurred by producing silicon oxyhydroxide such as $Si(OH)_2$, $Si(OH)_4$ and $Si_2O(OH)_6$ under atmospheric pressures in the presence of water vapor. In addition, the regions on the MI matrix surrounding fiber tows were also where many of the dark spots containing boron were spotted, as shown in Figure 59 of Chapter IV. With moisture contents in the environment, the reactions described by Equations (16-18) could occur to produce gaseous forms of boric acids such as H_3BO_3, $H_3B_3O_6$ and HBO_2. Bubbles could be the liquid oxide surface bloated off the fracture surface as a result of the localized pressure buildup underneath the oxide due to the formation these gaseous products. Extensive outgassing could have caused the volume loss in the MI matrix in the form of the pores.

Finally, the matrix porosity could also be a byproduct of frictional wear of the matrix due to local residual stress that arises between *Si* and *SiC* with different CTEs at high temperature. Cyclic loading in the local region, at which residual compressive stress resulting from the CTE mismatch between SiC and the Si metal is experienced in the MI matrix, could induce erosion of the weaker of the two species. The micrographic observation that higher Si occurrence, as compared to the rest of the MI matrix, in the regions surrounding fiber tows and fibers in the woven and prepreg MI CMC, respectively supports this assessment. The porous matrix could, in turns, facilitate the diffusion of oxidants, exposing the inner part of the specimen that otherwise would have been isolated from the oxidizing environment.

6.5.2 Deeper oxidation penetration along 90° ply

Another common microscopic observation that may have an importance in the failure mechanism is the longer depth of oxidation exhibited along the 90° tow, in comparison to that along the 0° ply. This was indicated by the oxidation profile illustrated on Figure 42 in Chapter IV, which showed the depth of edge-on oxidation on the 0° tows was on the average 70 to 100 μm from either side surface, while oxidation was evident to the depth of 2700 μm along the 90° ply near the front surface on the right edge of the cross-section in Figure 42. The oxidation on 90° ply was observed both along the BN interphase and through the voids in the CVI SiC matrix on the 90° tows. The oxidation by diffusion may be limited by the oxides formed that could impede with the diffusion down the BN interphase.

The deeper oxidation exhibited by the 90° ply can sometimes extend over to the fibers in the adjacent 0° tows, causing the oxidation damage of the load carrying fibers at some depth from the surfaces. The phenomenon is depicted in Figure 117, which was taken at approximately 150 μm from the left side edge of the cross-section shown on Figure 42. The interphase along the 90° ply appeared to have served as conduit for oxidants to permeate into a neighboring 0° ply through contacting interphases. This suggests a way in which the oxidation of 90° ply can cause a detrimental effect to the durability of the fibers in the loading direction.
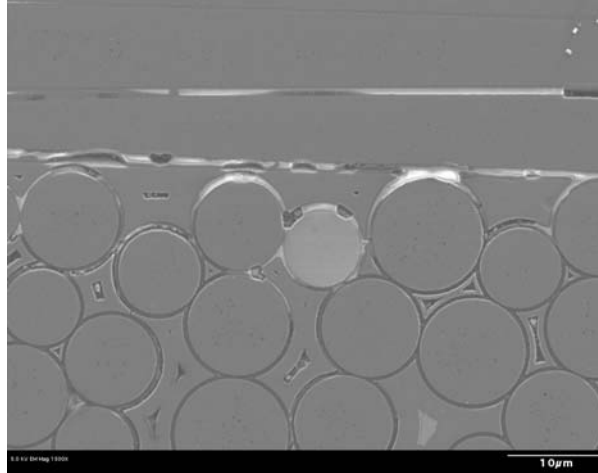
Figure 117: Oxidation penetration between two adjacent tows: interphase oxidation on 90° ply carried over to the adjacent 0° fibers and interphase.

The oxidation along the 90° ply is also affected by the diffusion of oxidants through the oxide layer formed on the surface of the specimen. Diffusivity differs by the phase of the oxide. On the side edge surface, the formation of solid phase oxides is questionable due to the local condition that involves the presence of moisture which significantly lowers the glass transition temperature, T_g below which the solid behaves in a brittle manner [88]. T_g of pure silica is approximately 1200°C in air. With the water content locally approaching of 30 *vol %* in the combustion gas flow, T_g is likely below the local operating temperature. There is some uncertainty in this assessment because of the boundary layer that develops from the corner of the front surface that serves as the leading edge. The boundary layer arises due to the redirection of gas flow around the corner and creates concentration gradients of chemical species. Moisture or hydroxyl concentrations would be lower at the surface level than in the main flow. This implies that T_g may not be as low as that predicted based on 30 *vol %* moisture content in the stream. Diffusion of the moisture and hydroxyl contents through the layer can be further complicated by the eddies that form inside the boundary layer behind the leading edge of a turbulent flow. Detailed characterization of the gas flow is needed to predict the concentration of the moisture at

the surface level, from which the glass transition temperature could be estimated and the phase of the oxide formed on the surface could be accessed. The phase of the oxides has an important implication in the failure mechanism, as the brittle oxide with relatively low fracture toughness can serve as crack initiation sites. Then the crack in the oxide can link up with the underlying SiC fibers causing failure [51]. Further study is required to increase the understanding in this direction.

6.6 Failure mechanisms

In Chapter IV, microscopic evidence was demonstrated suggesting that the failure may have initiated from the edge or corner. This observation was reinforced by the finite element analysis presented in this chapter that showed higher stress concentrated in the corners and edges than elsewhere in a specimen. The modes of failure appear to be different depending on the local condition on a specimen. Regardless of the modes, however, the microscopy of the four CMCs clearly supports the notions that the edges and corners are among the most heavily oxidized regions and that cracks appeared to have developed from there. Other common observations included the spalled matrix and the deeper permeation of oxidation on 90° tows. These common microscopic features and trends including the edge-on oxidation are incorporated into a failure model that may describe the steps that led to the failure of a specimen during fatigue test. In the following section, the failure model is illustrated in two steps. First, a mechanism is demonstrated that may have led to the oxidation of load carrying fibers in the specimen interior. Next, the attention is focused into a representative fiber that is undergoing oxidation brought upon by the mechanism illustrated in the first step. The degradation of fiber by oxidation is demonstrated here using the oxidation kinetics.

6.6.1 Failure Mechanisms

Microcracks nucleate and coalesce into matrix cracks under fatigue loading and thermal gradient stress that collectively causes the local stress state to approach and exceed the proportional limit. Concurrently, the oxidants in the combustion environment react with Si, SiC and BN on the 90° tows exposed to the environment at the machined edge surface. The oxidation reactions produce the silica (SiO_2) layer on the machined edge with rough surface morphology. Aside from the high water vapor content in the combustion gas applied to the specimen, the gas chemistry that interacts with the machined edge has relatively high hydroxyl concentration, which along with water vapor has an effect of reducing the viscosity of silica. The estimated hydroxyl contents of 0.65~0.91 *wt %* decreases the viscosity of silica such that the glass transition temperature is below 1000^oC [88]. The decomposition of water vapor that exists in relative abundance in the combustion environment with temperature approaching 2500^oC should also add to the overall hydroxyl content substantially. This implies that the silica layer may have been low in viscosity, as the local condition of the gas that interfaces with this edge consists of the temperature well above the presumed glass transition temperature. As a result, the silica layer does not inhibit oxidation of the underlying substrate, as a dense solid phase layer would do. The viscous flow layer facilitates the diffusion of oxidants across and enables the continuous oxidation of the underlying CMC surface. In addition, the outgassing of silicon hydroxide and hydroboric gaseous products of oxidation would open up the silica layer as well.
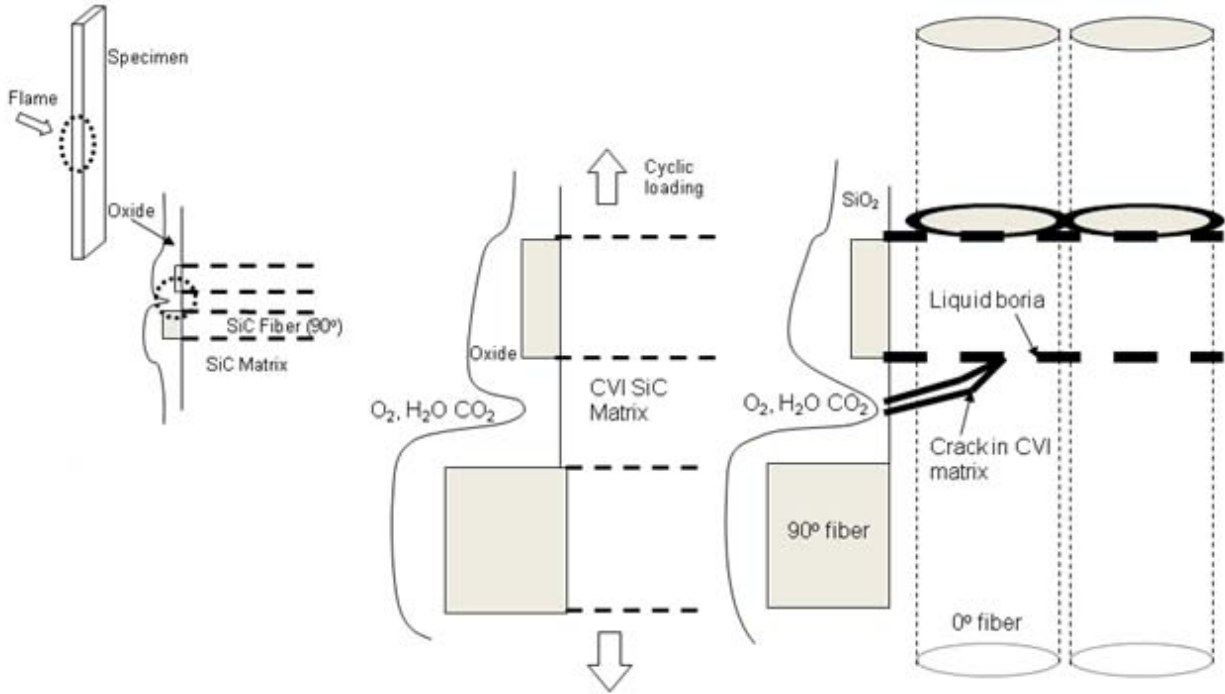
Figure 118: Viscous Oxide Layer Mechanism

The CMC surface exposed to the oxidizing environment either directly or indirectly through the silica layer with the viscosity less than that of a dense solid phase is depicted in Figure 118. The BN interphase acts as a conduit for rapid transport of oxidation within the fiber tow [136]. Gaseous diffusion of oxidants is facilitated on 90° fiber tows through the voids and cracks in the CVI matrix. The BN interphase is oxidized to form low viscosity borosilicate phase that simultaneously receded by the outgassing. The 90° fiber tows are weaker for the load applied in the specimen axis and will introduce cracks in the matrix first. This observation has been validated by several previous studies [95,137-140] that showed the 90° tows developed cracks early in the fatigue life of CMCs with the layup sequence that included 90° orientation. The CVI matrix surrounding the fibers aligned in 90° are also susceptible to cracking due to the high stress concentration at the sharp apexes. These cracks in conjunction with the process-induced voids and the BN interphase provide the ingress route for oxidants to penetrate into the deeper interior of

specimen. The oxidation damage on the 90° fibers does not contribute much to the mechanical degradation. However, as the extent of the oxidation expands along the 90° tows further into the deeper bulk region of the specimen, the oxidation would branch into the 0° tows in the vicinity of its path through cracks in the matrix and oxidize the load-carrying fibers.

In the woven MI CMCs, the crossover points exist where two fiber tows of different orientations come in physical contact. In the case of the CMCs with [0/90] fiber alignment, some crossover points are such that fibers from 0° and 90° tows are in very close proximity to one another. Oxidants carried in through the trapped voids, cracks and interphases along 90° tows can then be transferred to the load carrying 0° fibers, as illustrated in Figure 118. The transfer of oxidation from one ply or fiber bundle to another was previously reported by Ogbuji [77].
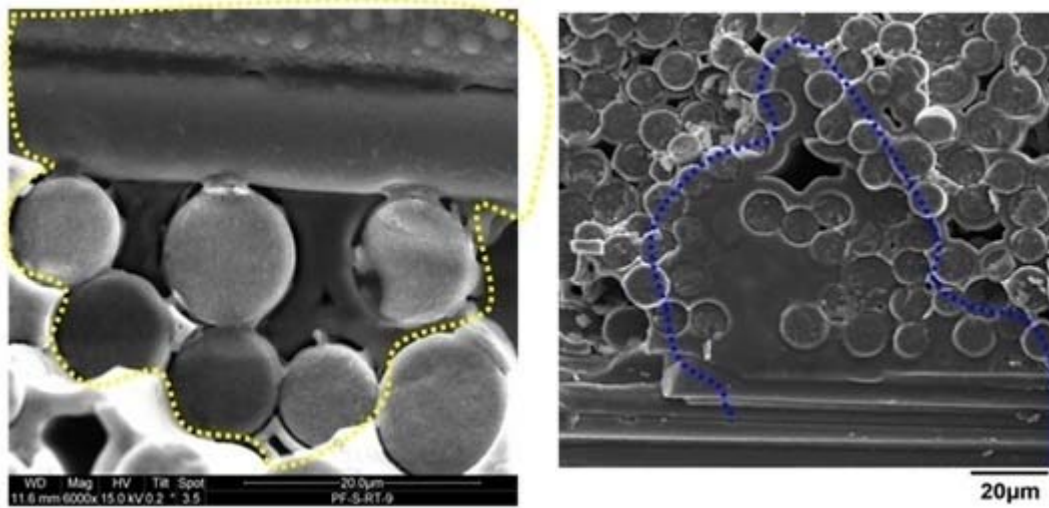
Figure 119: Oxidation transferred from 90° to 0° tows; 100 *μm* from machined edge (Left) and 300 μm from machined edge (Right)

Figure 119 depicts the linking of oxidation from a machined edge surface of a woven MI Syl/BN/SiC that failed during fatigue loading in combustion. The zone outlined by the dotted line on each image confines the area that underwent oxidation due to the oxidizing agents carried in through 90° tows. This was evident from the oxidized 90° tows determined using EDS as well as

other micrographic features such as the rigid interphase by oxidation and silica overlayer flown on the fracture surface observed using SEM, as shown in Figure 119. The oxidation of the 0° fibers directly impacts the mechanical load bearing capability of a specimen.

In Chapter IV, it was mentioned that the specimen that underwent the combined mechanical fatigue and combustion loadings was found to be spalled in the MI matrix around the fiber tows. One of the observations that led to the identification of this phenomenon is the voids nucleated along the surface of 0° fiber tows. If the oxidants transfer onto a 0° fiber tow surrounded by such voids, the diffusion becomes facilitated along the path created by a series of successive voids, as depicted in schematic way in Figure 120. This, in turns, reduces the time to oxidize the enclosed fibers by allowing oxidants to diffuse and attack the enclosed fibers from all angles.

Prepreg MI CMCs may not undergo the transfer of oxidation in the manner described above due to the systematic segregation of the unidirectional prepreg tapes of different orientations during processing. The 90° tows still likely serve as the conduit for the transport of oxidants due to their relatively lower fracture toughness. This allows the access of oxidants into the close proximity of the 0° fibers in the interior, as is the case in the mechanism for the woven MI CMCs illustrated above. The difference is that each fiber is attacked individually in the prepreg MI CMC, as opposed to the cases with the woven MI CMCs which tend to subject the entire fiber tow to the path of oxidation with the aid of the MI matrix spallation surrounding the tow. From this point of view, the prepreg MI CMC should demonstrate a smaller extent of oxidation for a given fatigue life. However, the microscopic analysis revealed that the extent of oxidation comparable to those demonstrated on the woven MI CMCs is observed in the 0° fibers deep in the interior, which is apparent from the comparison of Figure 51 and Figure 62 of Chapter

IV. This may, as described in Chapter V, be attributed to the difference in the crack growth rates of the two systems. It is conceivable that cracks propagate faster due to the larger increment of stress on fiber transferred to the surrounding intact fibers after the fracture of fibers in the prepreg MI CMC with lower fiber volume fraction.
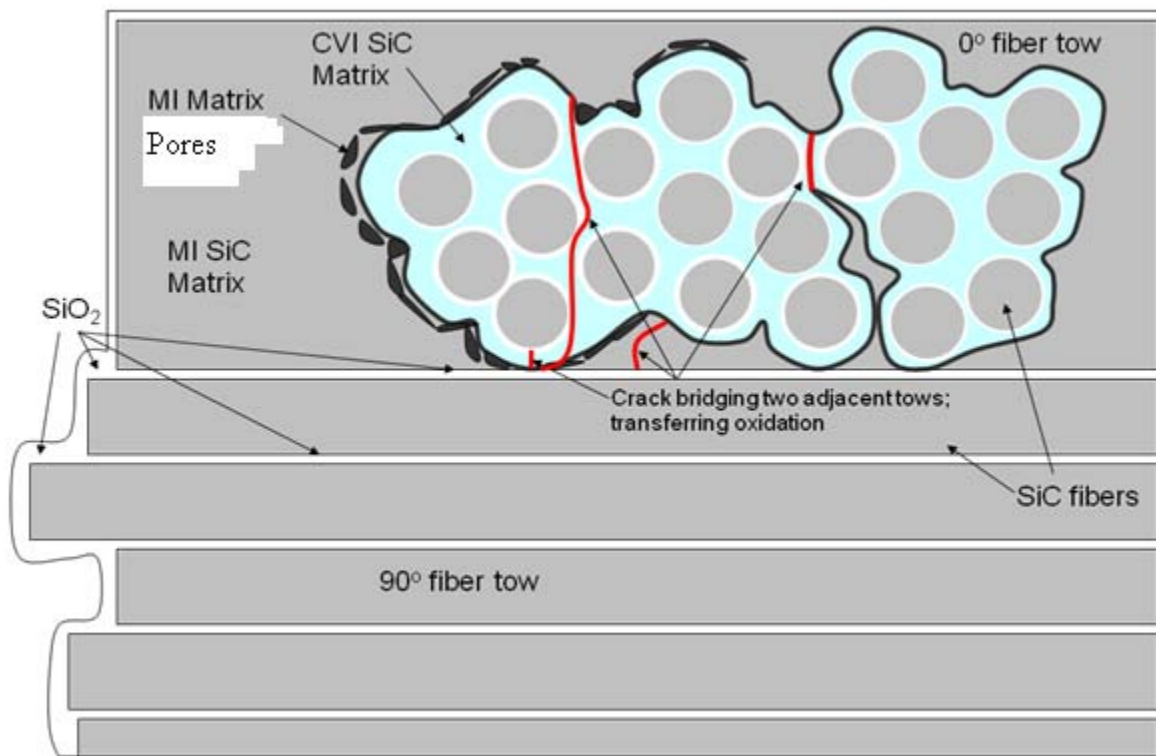
Figure 120: Illustration of how the load carrying fibers (whose cross-section is shown) in the bulk interior are reached in by the oxidants of the environment

6.6.2 Degradation mechanism for the fibers undergoing oxidation:

Once the matrix protecting the load carrying fibers in the bulk interior are breached as illustrated in the preceding discussion, the exposed 0° fibers and the BN interphases surrounding them readily undergo oxidation. Depending on the surface composition of fibers used, the type of oxidation that the BN interphase undergoes may differ as discussed in Chapters IV and V. For simplicity, the BN oxidation is assumed for the *iBN* extra layer and the BN interphase of the

270

woven MI Syl-*iBN*/BN/SiC in the illustration shown in Figure 120. The illustrated mechanism applies to all woven MI CMCs.

Upon exposure of the interphase to an oxidizing environment at the ambient temperature greater than 1000°C, BN in the interphase reacts readily with oxidants to produce liquid boria, B_2O_3 (*l*). This reaction occurs at lower temperature as well, although the rate of reaction is not as high and concerning as at temperature greater than 1000°C. The liquid boria dissolves SiC in the fiber and matrix and forms viscous borosilicate liquid in the reaction described in Equation (14). This is depicted in the illustration in Figure 121.
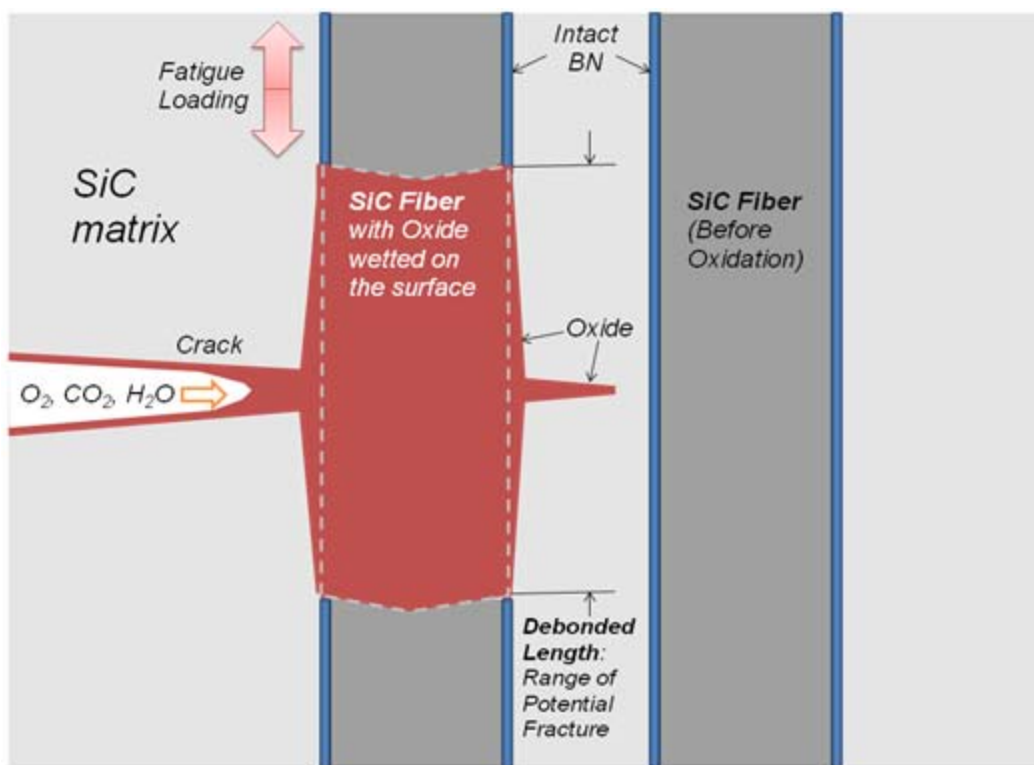
Figure 121: Schematic illustrating the crack growth followed by the oxidation of BN interphase

Simultaneously as the liquid borosilicate product forms and fills any nearby opening space, as illustrated in Figure 121, a transient process occurs which leaches boron out of the borosilicate

liquid by equations (15-18), increasing the viscosity of the liquid product until it is transformed to a dense solid phase SiO_2. [46,45,48,73]. From Appendix E, it was shown that the volatilizing process can take up to hundreds of seconds. The rate of this gradual cementing process that follows is determined by the physical and chemical conditions in the environment including pressure, temperature and moisture content. Fracture of the fiber enclosed by the oxidized interphase may originate from the solidification of the liquid oxidation product. Under fatigue loading, the fiber slides against the interphase at a given frequency. This makes the fracture mechanics for fatigue-loaded fiber more sensitive to the change in fiber surface condition than it is for a static loading scenario. As the cementing of the liquid phase oxide begins after tens to hundreds of seconds from the initial BN oxidation, the leaching of boria would occur from the oxide closest to the outside environment and then inwardly. This is because the concentration of the water vapor to react and form gaseous boria or hydroboric species is the highest in the environment and decays with increasing diffusion length. As the solidification process continues, and the boria in contact with the fiber under load reacts away to produce the silica that adheres to the fiber by Equation (14) [93]. It is a matter of probability to predict the cross-section of failure within the debonded length. This is in agreement with the micrographic observation that found very short fiber pullouts along with the oxidized planar fracture surface. Figure 122 captures one of the pulled-out fibers that fractured out of the crack plane. The interphase and matrix surrounding the fiber were determined to have oxidized, making the unexposed top surface of the pulled-out fiber the only place in the image that did not demonstrate oxidation.
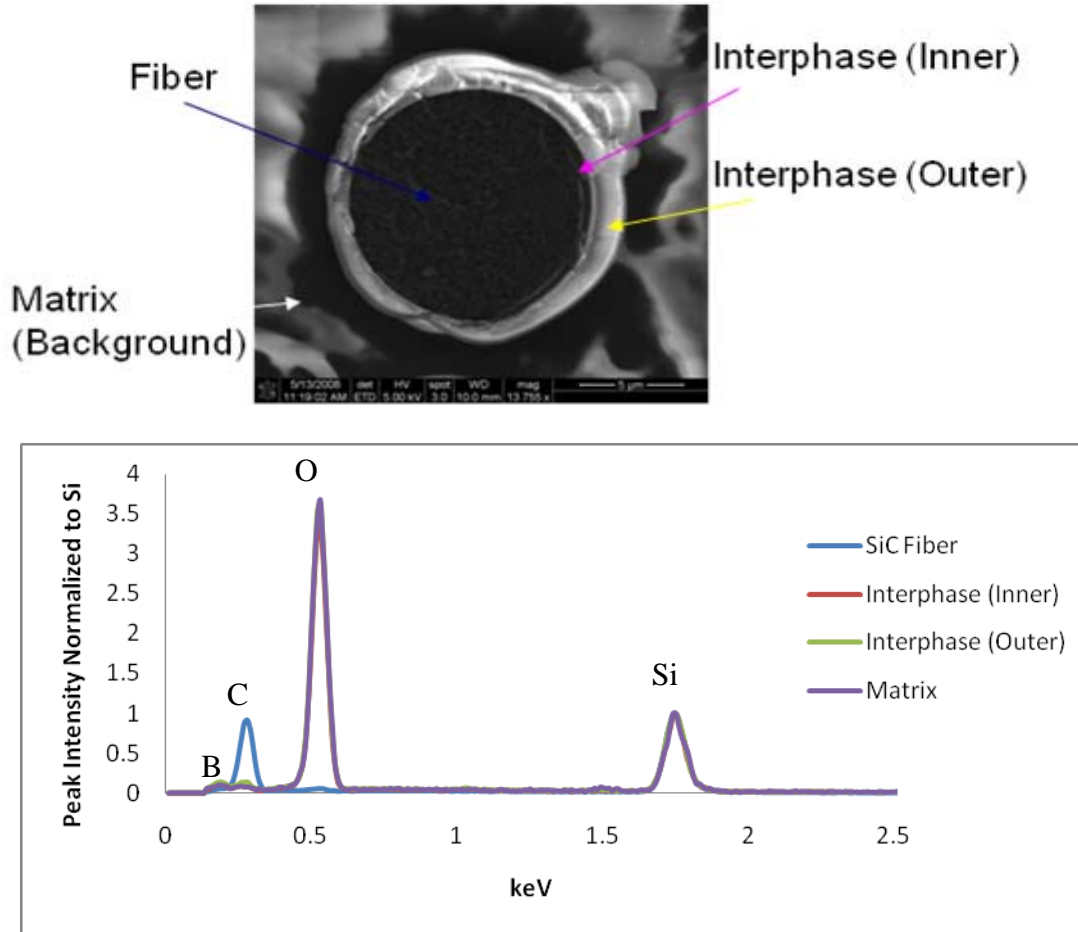
Figure 122: EDS of chemical species around a representative fiber in the oxidized region (woven MI Syl/BN/SiC shown)

Along with the failure mechanism involving the transient process that leads to the fiber fracture via solidification, the fiber may degrade or even fracture due to the secondary effects of oxidation such as the change in the fiber-interphase mechanics. As a crack propagates past a bridging fiber, the fiber debonds from the matrix over the debonded length. Oxidation takes place by the pipeline diffusion along the interphase, which transforms the BN interphase in the debonded region into viscous borosilicate liquid. This reaction involves volumetric expansion of the liquid product that amounts to approximately 100% [126], causing it to flow out of the interphase zone, leaving behind liquid oxide product with low viscosity. The overflow of the

liquid product will flood over the open crack surface and fill any voids nearby, which is believed to be the precursor to the silica overlayer observed on the fracture surfaces of all CMC types. With the discharge of the liquid boria or borosilicate out of the interphase, the parameters that control the mechanics of the fiber-interphase interaction under fatigue will change. Considerable changes in surface roughness and sliding resistance in the affected area are a few examples of the interphase parameters affected by the BN oxidation [32]. Loss of friction can be viewed in two ways, both of which capture its deleterious effects. First, it results in a reduced frictional dissipation of the energy associated with crack growth. Hence, cracks, which drive the oxidation, will propagate faster. Secondly, the reduced friction translates to the ineffectiveness in transferring load from matrix to the fiber in the affected area. Any pre-existing defect that increases the stress concentration on the fiber may lead to its failure due to the increased stress state inside the debonded length under cyclic loading that opens and closes the crack repeatedly. In addition, the intact portion of the BN interphase distant from the crack will have to transfer an increased amount of load. From a probabilistic standpoint, there is a distinct possibility that the fiber is open to multiple cracks simultaneously. With more cracks, the shear stress on the intact BN interphase increases further, which may contribute to premature failure of the fiber.

For the fiber with a thin carbon finish, the mechanism described here remains applicable, although the oxidation would occur at an accelerated rate due to the undermining of the interphase by the carbon oxidation that leads to a faster and more severe BN oxidation.

6.7 Fracture Mechanics

Two approximate analyses were carried out by merging the understanding gained from micrographic analysis presented in Chapter IV with the mechanical data corresponding to each

fracture surface. In this, each fracture surface obtained from fatigue testing in combustion was micrographically analyzed. Based on the oxidation profile resulting from this analysis, the crack profile including its geometry and dimensions was estimated, as a crack open to oxidative environment must have undergone oxidation and left the micrographic signs suggesting it. With three simplifying assumptions that failure occurs at the peak stress and that no fiber in the oxidized area carries an applied load and that thermal stress is neglected, two analyses were performed that examined the roles of net section stress and fracture mechanics in explaining the observed failure. As these analyses capture the moment of failure, cracks by then should have altered the temperature field surrouond the specimen to reduce the thermal stress effect substantially. A complete coverage of the fracture mechanics would require an additional finite element analysis representing the final stage of the failure that factors in an updated physical boundary condition by the crack growth. This is beyond the scope of the current study and is left for a future research.

6.7.1 Net section stress analysis

First, the net section stress, σ_{Net} was estimated based on the micrographic observation that led to the determination of the oxidized and non-embrittled regions. It is the stress carried by the intact portion of a failure cross-section, assuming fibers in the non-embrittled region carry no load, and was computued by dividing the applied mechanical load, P_{max} by the area of non-embrittled, intact-appearing regions on the corresponding fracture surface or $(1 - A_{ox})$. Figure 123 demonstrates the net section stress (σ_{Net}) estimated for three woven MI Hi-Nic-S/BN/SiC specimens that failed during fatigue testing in combustion, each tested at a different stress level. The net section stress corresponding to the specimen that failed under the peak applied stress of

127 MPa was 212 ± 15 MPa, whereas that of the other specimen which failed under 80 MPa was 162 ± 10 MPa. The range in both σ_{Net} came from the uncertainty associated with determining the intact area through micrographic analysis. One observation is that σ_{Net}'s are significantly less than the ultimate tensile strength (*UTS*) of an as-received sample of this material at room temperature, i.e. 334 MPa. The large $\Delta\sigma$, difference between *UTS* and σ_{Net}, may be due in part to the sharp edge effect existing at a crack tip that was not taken into consideration in this estimation. In addition, thermal gradient stress and possible reduction in overall strength due to high temperature unaccounted for here could make up some portion of the observed discrepancy in stress.
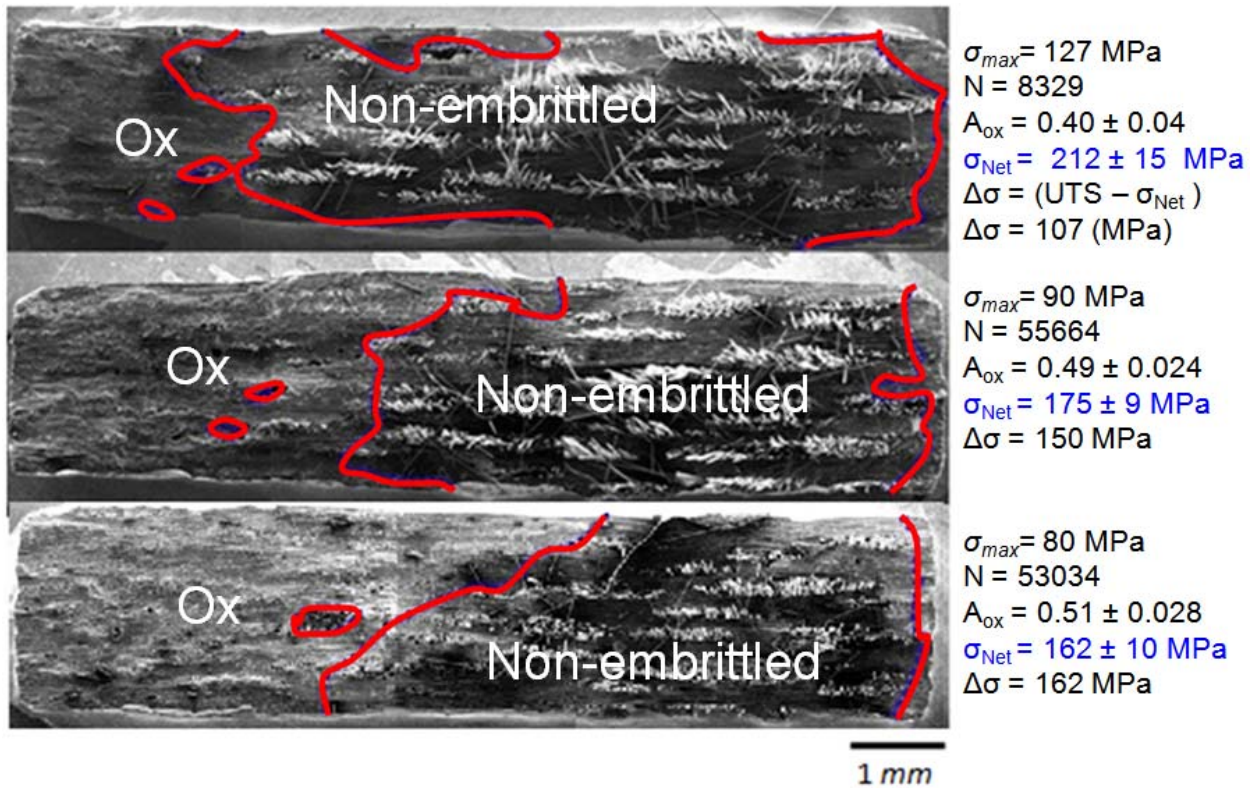
Figure 123: Net Section Stress of three woven Hi-Nic-S/BN/SiC fatigue tested at different peak stresses estimated from micrographic analysis of fracture surface

Another observation evident from the comparison of σ_{Net}'s among specimens with different fatigue cycles at failure involves a trend in σ_{Net} that it appears to be decreasing with

increasing number of cycles, *N*. In fact, this trend appears to hold for the other CMCs as well, as evident from Table 33. For prepreg MI Hi-Nic-S/BN/SiC, the room temperature *UTS* from the same panel was used to take the difference with σ_{Net} to obtain $\Delta\sigma$, whereas an average *UTS* was used for the other three CMCs. Note that prepreg MI Hi-Nic-S/BN/SiC specimens, which showed seemingly an opposite trend, may not be a good sample to draw any comparison, because they are within experimental uncertainty with numbers of cycles at failure separated only by about 700. For the other three CMCs, the net section stress was lower for a specimen that survived a higher number of cycles, as shown in Figure 124. The errors shown on each data point are derived from uncertainty associated with determining the intact region using micrographic analysis. This observation could be attributed to the damage accumulated at the interphase, probably in the form of frictional wear, as fibers slide up and down against matrix under cyclic loading. This suggests that the load bearing capability of intact portion of a material diminishes with increasing number of fatigue cycles, which, along with oxidative degradation, reduces the overall material's load carrying capability. The pullout lengths of the "intact" fibers that were different with number of cycles at failure, as shown in Figure 63 of Chapter IV, are micrographic observations that support this view.

Table 33: Net Section Stress, σ_{Net} for all the test specimens failed during fatigue tests

Woven MI Syl-iBN						Woven MI Syl-CVIBN					
σ_{max} (MPa)	A_{ox}	UTS (MPa)	$\Delta\sigma$ (MPa)	σ_{net}(MPa)	N	σ_{max} (MPa)	A_{ox}	UTS (MPa)	$\Delta\sigma$ (MPa)	σ_{net}(MPa)	N
187	0.32±0.03	431	145	273±12	1014	172	0.27±0.03	271	25	235±11	1979
169	0.34±0.03	431	166	255±10	7637	162	0.26±0.03	271	43	220±8	2655
125	0.44±0.03	431	195	224±11	17385	124	0.23±0.02	271	106	160±5	3146
						117	0.29±0.03	271	99	164±8	8059

Woven MI Hi-Nic-S						Prepreg MI Hi-Nic-S					
σ_{max} (MPa)	A_{ox}	UTS (MPa)	$\Delta\sigma$ (MPa)	σ_{net}(MPa)	N	σ_{max} (MPa)	A_{ox}	UTS (MPa)	$\Delta\sigma$ (MPa)	σ_{net} (MPa)	N
127	0.4±0.04	334	107	212±15	8329	145	0.21	305	121	184	209
90	0.49±0.02	334	150	175±9	55664	133	0.30	363	173	190	926
80	0.51±0.03	334	162	162±10	53034	125	0.38	346	146	200	758
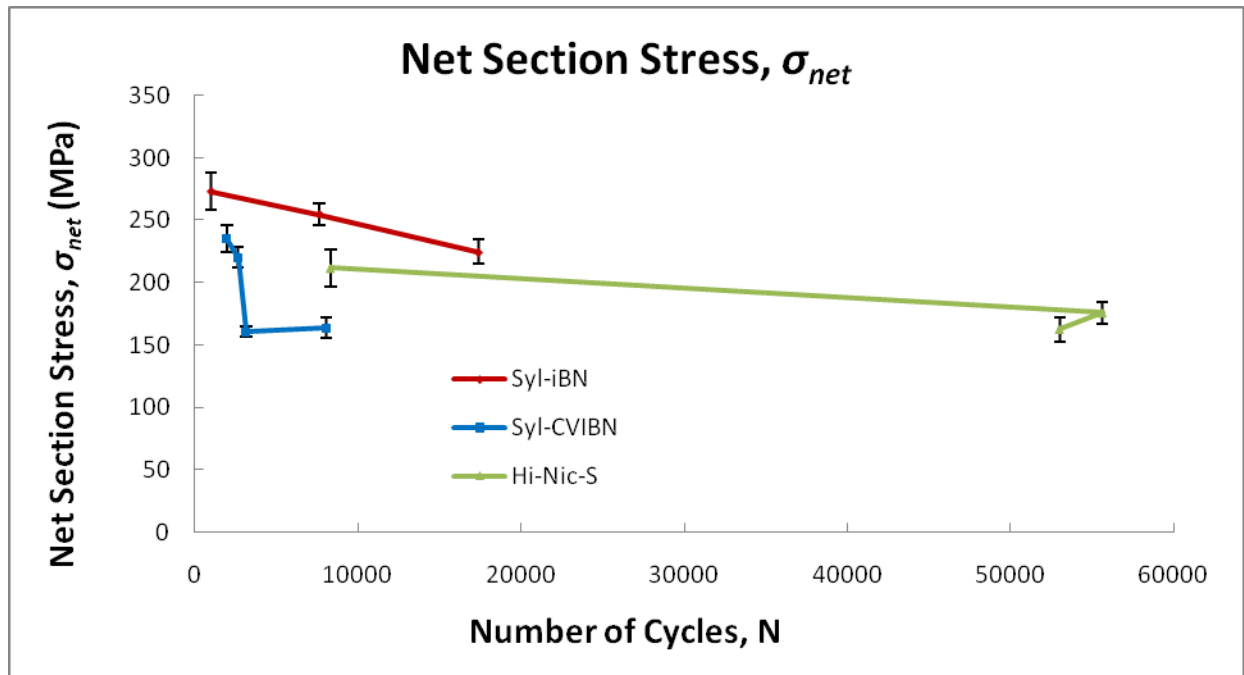
Figure 124: Net Section Stress vs. number of cycles for three woven MI CMCs

6.7.2 Stress intensity analysis

The critical stress intensity, K_{IC} was calculated for three of the four CMCs that showed predominantly a single edge-crack profile based on their micrographically-determined trace of

oxidation. In addition to the fact that the fatigue life of the three tested specimens were separated only by about 700 cycles, prepreg MI Hi-Nic-S/BN/SiC did not show a crack profile consistent with a single-edge crack estimation. For these reasons, prepreg MI Hi-Nic-S/BN/SiC was not considered for this discussion. The equation, $K = F \sigma_{max}.\sqrt{\pi a}$ is used to calculate the stress intensity with 'a' representing the length of the single predominant crack estimated by taking the area ratio of the oxidized surface to the entire fracture surface. σ_{max}. is the peak applied stress at the time of fracture (failure was assumed to have occurred at the peak stress.) F is a factor that changes with geometries and dimensions of both the specimen and crack, and it was determined by R. John of AFRL using the method involving the use of finite element analysis as prescribed by R. John's work published in Ref [141]. The K from the finite element analysis in Ref [141] was verified to be less than ±1% of the handbook solutions [142].

The stress intensity calculated as described are represented on Figure 125 for three woven MI CMCs. Error bar shown on each data point is derived from uncertainty associated with determining the intact region using micrographic analysis. From the comparison between the three materials, woven MI CMC reinforced by the Syl-*iBN* fiber, on the average, has the highest K values, followed closely by woven MI CMC reinforced by the Hi-Nic-S. Sylramic fiber reinforced woven MI CMC has the lowest K among the three. The order in which the three CMCs stand in terms of K values agrees with their relative orders in strain energy (the area under each of the stress-strain curve) obtained from both the monotonic tension tests of as received specimens (Figure 34 of Chapter IV) and the residual strength tests of runout specimens (Figure 94 of Chapter V). The MI CMCs reinforced by Syl-*iBN* and Hi-Nic-S fibers with larger strain energy values showed higher K, whereas the Sylramic fiber-reinforced CMC with relatively low strain energy showed a lower K. The stress intensity values for the three CMCs would have been greater

279

with thermally induced stress factored in. In addition, the stress intensity, K calculated here agrees reasonably well with the published fracture toughness on similar other SiC/SiC CMCs [143].
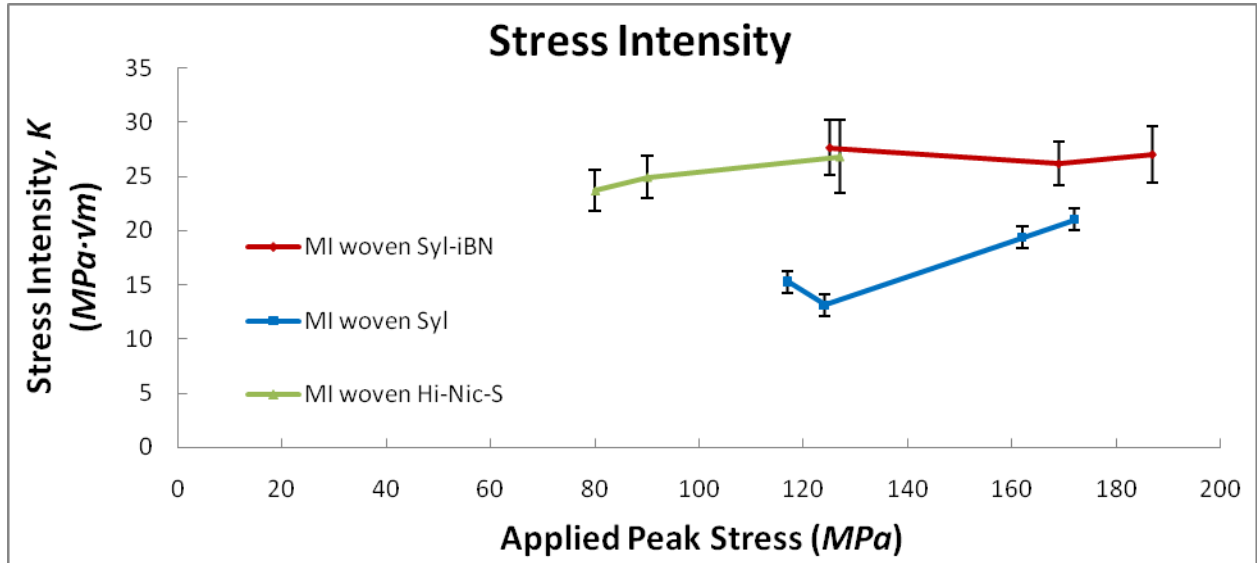
(A)
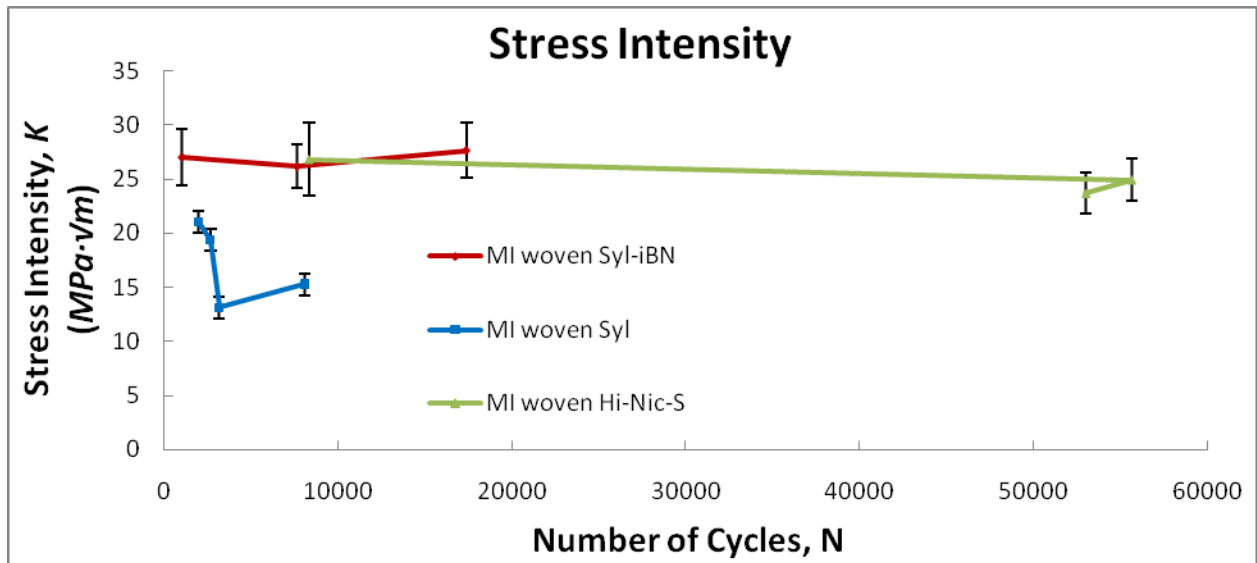
(B)

Figure 125: Stress Intensity plotted with respect to.(A) applied peak stress and (B) number of cycles

In considering the trend of stress intensity, K with respect to applied stress and number of cycles, it appears for woven MI CMCs reinforced by the Sylramic and Hi-Nic-S fibers that K decreases with applied peak stress, which is in turn inversely related to the number of fatigue

cycles, as shown in Figure 125. The trend could also be driven by an underestimation of crack length, which was based on the outline of the oxidation front. An actual crack length may have been smaller with some fibers in the oxidized region bridging the crack, which is a more likely event at a lower applied peak stress with smaller span of sliding. Another possible explanation for this trend would be the damage accumulated in "intact" fibers with increasing fatigue cycles, which was supported by the micrographic observation that the fiber pullout length decreased with increasing fatigue life, as shown in Figure 63 of Chapter IV. This suggests that the degradation in strength properties of a CMC is driven not just by oxidation, but also by the incremental frictional wear experienced at the interphase of load carrying fibers in the intact part of a material.

While these explanations are provided to reason the observed decreasing trend of K with increasing number of cycles, it may be argued that fracture toughness, K should be considered constant with either the applied stress or number of cycles, considering the uncertainty associated with each data point. This view is supported by the case of woven MI Syl-*iBN*/BN/SiC that showed no apparent trend with applied stress or number of cycles. More in-depth study that employs more sophisticated methods of measuring fracture toughness to test a large number of samples would be needed to validate the trend discussed above.

6.8 Chapter Summary

The micrographic observations were used in conjunction with the finite element model constructed based on the thermal properties and measured surface temperature profile to develop the failure mechanism for the test specimen. From the model, it was determined that the specimen was in a non-uniform stress state due to the thermal gradient introduced by the directional combustion heating. Under mechanically applied tension-tension fatigue loading, the specimen

underwent tension-tension, tension-compression and compression-compression fatigue of varying R-ratios at different locations in the specimen. Possibilities for different failure modes accounting for different modes of the fatigue loading were diagnosed, from which it was determined that cracks may have initiated from less fracture-resistant 90° tows on the machined edges, then they propagate into the bulk interior, leading the way for oxidation in the wake of the advancing crack tip. The resulting oxidation of the BN interphase assisted in causing failure of the bridging fibers and resulted in reduced load carrying capability. It was also noted that the change in the fiber-interphase mechanics brought upon by the interphase oxidation may have increased the shear stress in the intact interphase, which in turn may have caused the fiber failure. Finally, two approximate analyses of the fracture mechanics were performed on the CMC specimens that failed under the applied fatigue loading in combustion. Both the net section stress and stress intensity appeared to decrease with increasing number of cycles. This suggested that the fibers that appeared intact may have undergone degradation in load carrying capability with cycles. This view was supported by the micrographic observation that the fiber pullout length appeared to be decreasing with increasing number of cycles.

VII Summary and Conclusions

This study set out to investigate and characterize the failure of the four different types of SiC/BN/SiC CMCs under fatigue loading in oxidative combustion environment. The four CMCs selected for this study are woven MI Syl/BN/SiC, woven MI Syl-*iBN*/BN/SiC, woven MI Hi-Nic-S/BN/SiC and prepreg MI Hi-Nic-S/BN/SiC, and they are candidate materials for structural applications in next generation gas turbine engines such as turbine vanes and blades. A versatile burner rig facility was developed to enable a realistic simulation of a variety of realistic service environments by providing the capability to apply mechanical loading and combustion environment simultaneously, as the projected applications involve mechanical loading from operational maneuvering or angular momentum applied by the airfoils rotating at high speed in high temperature, harsh chemical combustion environment. The focus of previous studies on this class of material has been primarily the creep-rupture behavior in high temperature environment with controlled moisture level. However, relatively little work has been reported on their fatigue behavior.

Previous studies investigated the oxidative degradation of the SiC/BN/SiC CMCs under sustained loading in humid conditions. They reported that the degradation occurred by adhering of neighboring fibers, initiated by oxidation of the BN interphase and that it causes the solidification of the fibers to matrix removing fracture toughness from the CMC. The moisture level and temperature was shown experimentally to be factors of important consideration in causing embrittlement. These studies elevated the basic understanding of the effect of moisture in terms of the change in creep strength and life. However, the SiC/BN/SiC CMCs in gas turbine engine would be subjected to a number of other chemical species that could synergistically

improve or worsen the effect of moisture. In order to take this concern into consideration and to meet the needs for a test stand that provides a link to a representative service environment, the AFIT/AFRL Burner Rig that combines the real combustion environment with mechanical loading capabilities was developed. This study using the burner rig facility would build on the previous studies conducted on the SiC/BN/SiC CMCs.

7.1 AFIT/AFRL Burner Rig

The AFIT/AFRL Burner Rig developed as a part of this study is a one-of-a-kind mechanical testing facility that provides a unique capability of testing a coupon-size specimen under various simulated combustion and mechanical loading conditions of gas turbine engine components. The uniqueness of this facility lies in the integration of a combustion environment to a mechanical test stand. An atmospheric pressure burner rig system mixes fuel and oxidizers to generate high temperature, high speed combustion flame, which is guided into the direction of a test specimen with the capability to vary the impingement angle to simulate an angled impingement for future studies. The specimen under the flame impingement simultaneously undergoes a controlled mechanical loading by an MTS servo-hydraulic material testing system. The burner rig system is capable of producing hot combustion gas which travels into the downstream at the speed exceeding *Mach 1.0*, providing extra usefulness to simulate even a high-end thermal cycling condition of even the most advanced gas turbine engines. Thermal cycling is facilitated by a programmable mechanical actuation of the combustion rig in and out of the alignment with test specimen. The mechanical loading of 25 *kN* can be applied in either a static form to study a creep scenario or a cyclic configuration to investigate fatigue behavior. With its programmed thermal cycling capability as well as mechanical loading facilitated in both static and

cyclic forms, virtually any combinations of thermal cycling and mechanical loading experienced by a component in gas turbine engine can be accommodated with the AFIT/AFRL Burner Rig.

The current configuration of this facility was used to explore the potentials of four SiC/BN/SiC CMCs for gas turbine engine airfoils by investigating their fatigue behaviors in a realistic combustion condition. It was of particular interest to investigate the effect of thermal stress. Hence, the AFIT/AFRL Burner Rig was configured such that a non-symmetric thermal field was rendered on the test specimens by imposing the combustion condition on only one side of the specimen, while the other side was allowed to undergo natural convection with the ambient.

7.2 Fatigue behavior of CMC in combustion environment

Using the Burner Rig, the fatigue behavior of the four CMCs in high temperature, oxidative combustion environment was investigated. The combustion environment, applied throughout this study, was prescribed to a realistic service condition including the surface temperature of $1235 \pm 50^{\circ}$C and the gas chemistry containing oxidizers such as CO_2, CO, O_2 and H_2O from combustion of hydrocarbon gas. For each CMC, a specimen was subjected to this combustion environment, simultaneously while undergoing fatigue loading with the peak load varied between each test such that the S-N behavior of the CMC was obtained. Other fatigue parameters such as frequency and stress ratio (R) remained constant throughout the tests at 1 Hz and 0.05, respectively. Each fracture surface was investigated for microscopic evidence of oxidation using SEM and EDS in the effort to correlate the fatigue behavior to the extent of oxidation. It was determined that, for all four CMCs, the extent of oxidation was inversely directly to the fatigue life, which was inversely related to the applied peak stress. Those specimens that survived the prescribed 25 hours (90,000 cycles) of test duration without failure

285

were subsequently tested at room temperature under monotonic tension to determine the residual strengths. The resulting fracture surfaces were investigated for microscopic details such as oxidative degradation and pull-out. The area fraction of the non-embrittled region approximately corresponded to the residual strength of the CMC. It was consistently observed that the specimens failed under fatigue showed fracture at the cross-section inside the zone of direct heat impingement, whereas the runout specimens tested for residual strength failed outside the zone. Some of the fractured specimens including the fractured runout specimens were sectioned in perpendicular as well as parallel to the loading direction. The surface sectioned perpendicularly to the loading direction beneath the fracture surface provided insights into the understanding of the state of oxidation on the section exposed to the combustion. The sections sliced in parallel to the loading direction provided the information on the secondary cracks as well as the understanding of the oxidation of vulnerable machined edges and the progression of such oxidation with respect to the depth from the surface. The understanding of failure mechanism was supplemented and enhanced through the micrographic observations of the sectioned surfaces.

In comparing the four CMCs tested in this study, three of the four are manufactured by the same method that involves slurry casting warp aligned laminates woven in 5 harness satin pattern. The other involves the laying up of unidirectional prepreg tape in [0/90/90/0]$_s$. Both methods used a densification process of melt-infiltration (MI) of molten silicon to fill pores in the matrix. The prepreg MI CMC Hi-Nic-S/BN/SiC exhibited the fatigue strength at runout of 105 MPa and the residual strength of 264 MPa, both of which are second highest of the four CMCs by small margins. The reason for the prepreg MI CMC with low 20~25 *vol %* of fibers survived relatively high peak stress was believed to be the dense matrix, which is a result of the prepreg processing that, unlike the slurry casting of woven cloths, facilitates uniform coating of individual fibers by

spreading fiber tow during fiber coating process. Unlike the woven MI CMCs, the prepreg MI showed a relatively even distribution of fibers, minimizing the number of fibers touching each other, systematically creating a discontinuity in the path for oxidation. Of the three woven MI tested under fatigue in the prescribed combustion environment, the one with Sylramic fiber coated with in-situ BN (*iBN*) layer showed the highest applied stress of 110 MPa at runout and the highest residual strength of 279 MPa. From the comparison with the woven MI Syl/BN/SiC, it was concluded that its longer fatigue life and higher fatigue strength are attributed to the *iBN* layer that keeps neighboring fibers from being in direct contact. This was evident from the microscopic analysis that revealed relatively smaller size of oxidized area exhibited by a specimen fatigued at a given peak stress, as compared to the CMC without *iBN* at the same peak stress. The woven MI CMC with Hi-Nic-S fiber showed the lowest applied peak stress of 70 MPa at runout and the second lowest residual strength of 186 MPa. The poor fatigue behavior of the woven MI Hi-Nic-S/BN/SiC was attributed to its relatively high porosity level. The fatigue strengths of the three woven MI CMCs were ranked in the same order as their proportional limits (*PL*), which suggested possible correlations with the microcracking phenomenon, often associated with *PL*. Besides, comparison of two different materials with different properties called for normalization of the peak stress against a parameter associable with a common physical phenomenon such as *PL*. From the comparison of the runout strengths normalized with their respective *PLs*, the CMC with *iBN* had the highest fraction its *PL* as peak stress that resulted in runout at 66 *%PL*, compared to 53 *%PL* and 58 *%PL* for the CMCs with Sylramic and Hi-Nic-S fiber, respectively. In conclusion of the comparison, it was determined that prepreg MI CMC with denser matrix showed significantly higher fatigue strength and retention strength than the woven MI CMC made with the same Hi-Nic-S fiber using twice as number. It was also determined that,

among the woven CMCs, the one with Sylramic fiber showed better fatigue and retention strength than the one with Hi-Nic-S fiber, and that the one with Sylramic with *iBN* was better than the one without it.

The apparent fatigue strengths at runout for the four CMCs were from 70 MPa to 110 MPa, which are from 50 to 60 *%PL*. This stress level is significantly below the matrix cracking stress. In fact, the apparent fatigue strength of the woven MI Syl-*iBN*/BN/SiC determined from this study was lower by more than 100 MPa than that of the similar N24A tested by Morscher et al using the same fatigue parameters at similar temperature. Thermal gradient stress, moisture and gas flow pressure were identified and diagnosed for their roles in degrading the strength of the CMC. Thermal gradient stress was the key factor accounting for the large difference. The finite element analysis (FEA) was carried out to quantify the contribution by thermal gradient stress. It was shown that the thermal gradient stress as great as 115 MPa and as low as -160 MPa were induced by the directional heating on different locations in the specimen. Under the nominally applied tension-tension fatigue loading with fixed *R*-ratio, different parts of the specimen undergo different modes of fatigue depending on the local thermal stress condition. In general, the tension-compression (T-C) and compression-compression (C-C) fatigue with negative R-ratios of varying magnitudes are experienced near the flame impinged front side of the specimen, whereas the tension-tension (T-T) fatigue with positive *R*-ratios of different amounts are imposed near the back surface. The finite element analysis and the gas chemistry analysis were used in conjunction with microscopic observations to determine the failure mechanism of the test specimens. The finite element analysis showed that the compressive stress peaks in the gauge section, which coincided with the cross-sections of fracture by most specimens that failed during the fatigue tests. The tensile stress peaked at approximately 12~ 25 *mm* from the center of the gauge section, which

agreed with the fracture locations of fracture by most runout specimens that failed under residual strength tests. The temperatures experienced at the two fracture locations were different. The front surface temperatures were both well above 1000^oC at both cross-sections. The temperatures of on the opposite surface were approximately 930 ± 100 ^oC directly behind the gauge section and approximately 750 ± 100^oC at the cross-section of the residual fractures. Considering the moisture content in the environment, the failure under the residual strength tests could be attributed to the combined effect of the relatively high local tensile stress and the oxidative degradation, which was documented to be more significant at the intermediate temperature of 750^oC than 950^oC in humid environment [28]. The failure during the fatigue tests could be attributed also to combined effect of the tensile stress and the oxidative degradation. However, the failure appeared to be more to do with oxidative degradation than the tensile stress, as the temperature exposed in the gauge section was greater and the local tensile stress was lower than at the location of residual fracture. From the microscopic observations that every oxidized region was connected to either edge or corner of specimen and that the penetration of oxidation was deeper along 90° tows, a failure mechanism was developed that involves the failure initiating along the more fracture-prone 90° tows. Then oxidants, across the silica formed due to edge oxidation, diffuse deep into the interior either along the BN depleted interphase or through voids in the CVI and MI matrix on 90° fiber tow. With repeated loading and unloading, the cracks along the 90° tow propagate into the adjacent 0° tow and open the path for oxidation on the load carrying fibers. From there, the oxidation of the BN interphase results in the formation of liquid boria, which evaporates as itself or react with moisture to form gaseous species. The remaining silica adheres to neighboring fibers and matrix, preventing each fiber to react independently under load. The porous MI matrix in the

289

surrounding regions of the fiber tows for woven CMCs and the individual fibers for prepreg MI CMC could facilitate the diffusion of oxidants.

Finally, fracture mechanics aspects of the observed failure by four CMCs were accessed by carrying out the net section stress analysis and the fracture toughness anlaysis. An outcome of the two analyses suggested that the degradation of a specimen under fatigue loading in comobustion was not solely driven by oxidation, but rather was accompanied by diminishing load carrying capability of fibers with increasing cycles in the intact portion of a material through such mechanisms as frictional wear of BN interphase.

7.3 Future Research

From this research, it was shown that the prepreg MI CMC performed better than the woven MI CMCs of the same constituents under the combined fatigue and combustion environment. This was attributed to the dense matrix from a uniform coating applied to individual fibers during the prepreg processing. It was also determined that the Sylramic-*iBN* fiber was the best of the three fiber types tested. The *iBN* fiber coating minimized the oxidative degradation, which was evident from the comparison in the extent of oxidation between the two CMCs with and without the *iBN* coating. Based on these findings, it is recommend to pursue a new CMC that combines the prepreg MI processing and the Sylramic-*iBN* fiber to attain high oxidation resistance at a minimum reduction in mechanical strength.

CMCs in this study were characterized with the surface temperature of $1235 \pm 50^{o}C$ on the flame-impinged side, which is approximately at an upper bound of the temperature excursion during the operation of advanced gas turbine engines. The airfoils undergo the thermal gradient stress, as the CMC specimens of this study were subjected to. Materials with even higher

temperature capability will allow engine designers to develop more efficient engines for future applications. There are other areas that such materials would benefit, which include the leading edge in hypersonic vehicle application. Such application would require material to sustain the temperature up to and exceeding 1500°C. The prepreg MI Syl-*iBN*/BN/SiC CMC, while concluded from this study as an optimal combination of the processing method and the choice of fiber, would not be able to keep its structural integrity at temperature beyond 1414°C, because the current MI processing involves densification of the matrix by the infiltration of molten silicon, which melts at a higher temperature. Not all the silicon reacts with carbon to form SiC, leaving some pores filled with silicon. This was evident from the EDS analysis of the matrix that showed considerable amount of silicon phase. To increase the temperature capability of the prepreg MI CMC, it is crucial that more research is done to find a way to eliminate the silicon phase in the matrix.

As for the AFIT/AFRL Burner Rig and its future use in research, it would be of great use to install the second combustion system that impinges on the reverse side of test specimen. While the system was purchased and available for installation, the second system was not installed for the current study due to concerns over fire safety and the shortcoming in the capacity of the current ventilation system. With two independently controlled combustion systems impinging from both sides of test specimen, it is possible to control the thermal gradient stress and to capture more realistic gas chemistry surrounding the specimen.

On a near term, it would be of immediate use to inject another species such as Na or Cl into the combustion and compare the results from otherwise the same test as done in this study, as such species has been known to increase the oxidation potential of CMCs. The burner rig is equipped with the gas passage that readily enables the injection of such species. Instead of the Na

or Cl, it is also possible to introduce additional moisture into the combustion by injecting water vapor through the passage. This provides the ability to control the moisture content without changing other aspects of the combustion. With the moisture content as input variable, the pending study can be compared with the results from the current study to provide an effect of moisture on oxidation-induced degradation phenomenon in combustion environment.

Lastly, the finite element modeling (FEM) work presented in this study is a simplistic representation of the complicated thermal and mechanical conditions applied to the test specimens. However, the current work successfully demonstrated the critical stress state for the given condition and laid a ground work for further enhancement of the model. Two key areas of future studies for modeling are the incorporation of the progressive damage evolution in the stress analysis and the improved method for specification of the thermal boundary conditions based on combustion conditions.

Appendix A: Surface Recession on CMC

When a crack is formed in the ceramic matrix, it provides a path for ingress of oxidants. The slow growth rates of silica means the crack cannot be sealed by oxidation [83,144]. The growth kinetics of protective SiO_2 scales is paralinear, i.e. parabolic growth moderated simultaneously by linear volatilization [47,83-85,92]. The parabolic growth is consistent with Equations (1-5) of the previous section. The reduction step, which exhibits linear kinetics, occurs according to Equations (6-10). As shown in Figure 126, the paralinear oxide growth curves show a period of oxide growth, followed by a linear volatilization region in which the scale thickness remains constant but net material consumption is occurring. Figure 127 [84] illustrates the physical SiO_2 scale volatility process and corresponding SiC recession.

The rate of the SiC recession depends on multiple parameters including temperature, moisture content, system pressure, and gas velocity. Robinson and Smialek [56] studied the parametric dependency of material recession by performing a series of tests using the NASA High Pressure Burner Rig (HPBR) over a range of temperature, moisture content, system pressure, and gas velocity. The parabolic dependencies of pressure and velocity as well as an Arrhenius dependency of temperature were confirmed, which led to the prediction that the material recession followed the form: $\exp(-Q/RT) \cdot P^x \cdot v^y$ [83,56]. Multiple linear regression analysis of lean and rich data sets yielded the following fits to the data [56]:
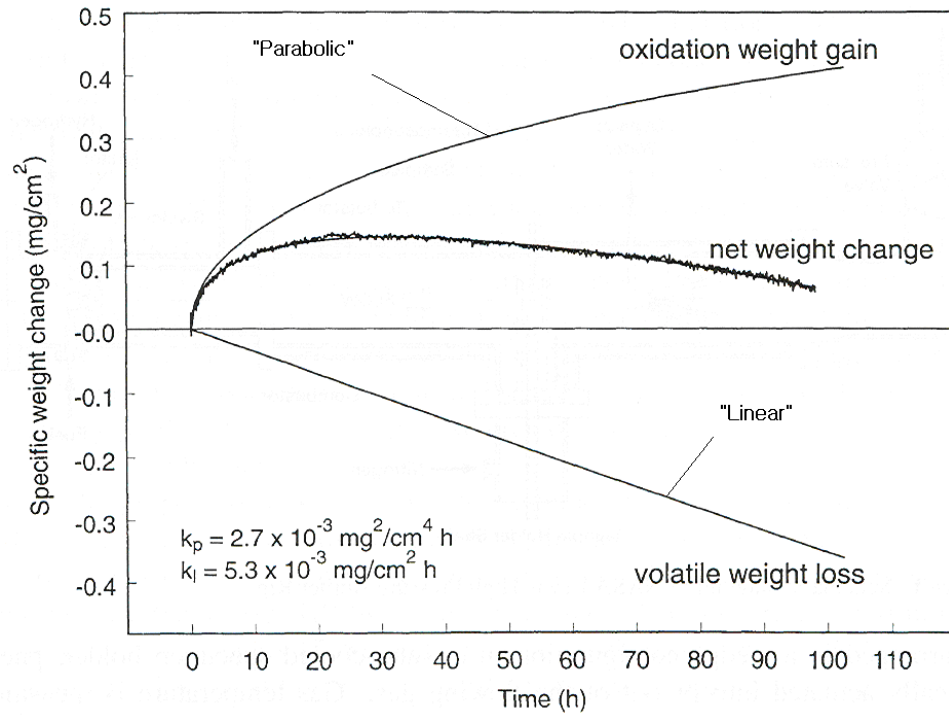
Figure 126: Paralinear weight change curves for CVD SiC [84]
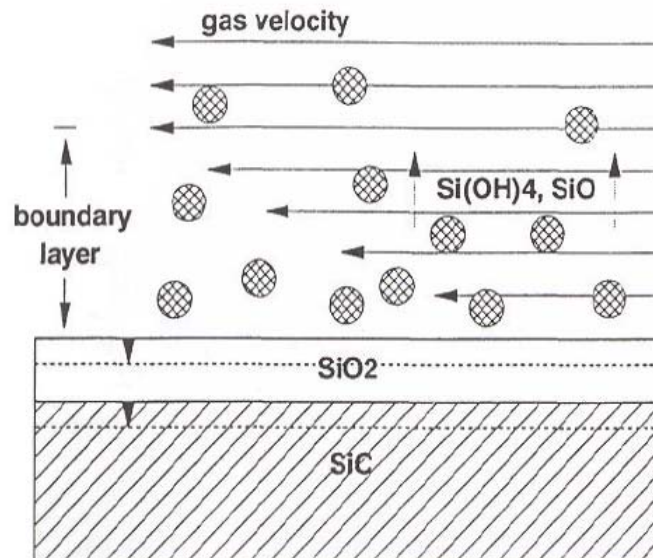
Figure 127: Physical silica scale volatility and SiC recession [84]

$$\text{Lean: } k_1 \ (mg/cm^2 \cdot h) = 2.04 \exp(-108kJ/mol/RT) P^{1.50} v^{0.50} \qquad \text{(A1)}$$

$$\text{Rich: } k_1 (mg/cm^2 \cdot h) = 82.5 \exp(-159kJ/mol/RT) P^{1.74} v^{0.69} \qquad \text{(A2)}$$

,where pressure is in atmospheres, velocity in meters/second and temperature in Kelvin. These two equations apply only when the flow is laminar. If universal gas constant R is assumed, for a representative lean burn condition with $P = 1$ *atm*, $v = 300$ *m/s*, and $T = 1400$ *K*, k_1 is 3.3×10^{-3} *mg/cm^2 h*. Assuming the density of SiC is equal to 3.0 *g/cm^3*, this k_1 extrapolates to be a recession rate of 1.10×10^{-6} *cm/h or* 0.010 *μm/h.* During the 25-hours of operation in this condition, 0.25 *μm* of material recession occurs, and this does not figure to be a major concern for the degradation in the load bearing capability. The preceding analysis of the representative case features a laminar flow of $Re \approx 1850$. For a turbulent flow ($Re > 4000$), the volatility is expected to occur at a higher rate due to free evaporation of gaseous species [47]. Hence, the estimated recession using Equations (A1) developed for a laminar flow serves as a lower bound. Still, the surface recession that occurs during the test duration of 25 hours or less should be insignificant, as this preliminary analysis suggests.

Appendix B: HVOF Combustion

Primary combustion: Inviscid core

Secondary combustion: Bright luminescent blue
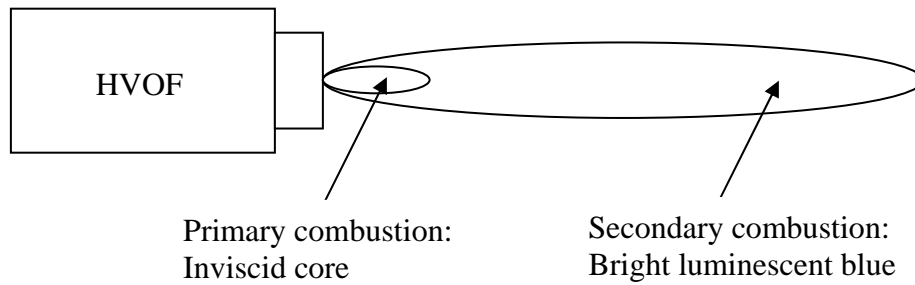
Figure 128: HVOF flame illustration

The HVOF uses a gaseous hydrocarbon such as propane as fuel, oxygen as oxidizer and the air to cool the surrounding metal-based housing. The air has a secondary role as oxidant in the secondary combustion. The primary combustion, which usually takes place within the first 10 *mm* outside the nozzle, occurs by combusting the premixed fuel and oxygen and can be described by Equation (B1). The primary combustion usually takes place in the inviscid core encompassing the first 10 *mm* outside the nozzle, as illustrated in Figure 128. For being the region where 70% of the total energy is released, the primary combustion involves very high temperature, causing chemical dissociation of stable chemical CO_2 and H_2O into CO and OH, etc.

$$C_3H_8 + 5O_2 \rightarrow 3CO_2 + 4H_2O \qquad \text{(B1)}$$
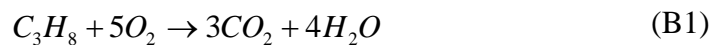
If the equivalence ratio diverges from 1, then there could be excess oxygen that may decomposes due to heat energy or excess hydrocarbon fuel left unreacted in the product, which subsequently undergoes combustion in the secondary region. A bright luminescent blue flame, outside and downstream of the inviscid core is indicative of the secondary combustion flame. In this region, chemical reactions as well as physical mixing occurs between the gas products from the primary combustion and the room temperature air. There are two sources of this room temperature air. One is the compressed air that merged onto the primary combustion products at

the nozzle exit. Inside the nozzle cap, the high-temperature flame is concentrated in an annular region between the cooling air streams where the cooling along the nozzle cap surface remains attached and effective up to the exit, thus protecting the hardware from the high temperature gas. The hot region corresponds to the annular glowing cone, which has been observed visually. Along with this cooling air, the ambient air gets entrained by the jet flame to form a shear layer. It is the products of the secondary combustion that interfaced with the CMC specimen positioned 60 ± 5 *mm* downstream. In fuel-lean region, whereby the equivalence ratio (φ) is smaller than 1, the following stoichiometric combustion reaction occurs to produce CO_2, O_2, H_2O and N_2 in the case of propane, C_3H_8 as fuel under the assumption that the combustion is a fully-mixed and chemically equilibrated reaction described by the following global reaction.

$$C_3H_8 + \frac{5}{\varphi}O_2 + n(O_2 + 3.76N_2)$$

$$\rightarrow 3CO_2 + 4H_2O + 3.76nN_2 + \left(\frac{5}{\varphi} + n - 5\right)O_2 \qquad \text{(B2)}$$

In fuel-rich scenario ($\varphi > 1$),

$$C_3H_8 + \frac{5}{\varphi}O_2 + n(O_2 + 3.76N_2)$$

$$\rightarrow \left(\frac{10}{\varphi} - 7 - 2n\right)CO_2 + \left(10 - \frac{10}{\varphi} - 2n\right)CO + 4H_2O + 3.76nN_2 \qquad \text{(B3)}$$
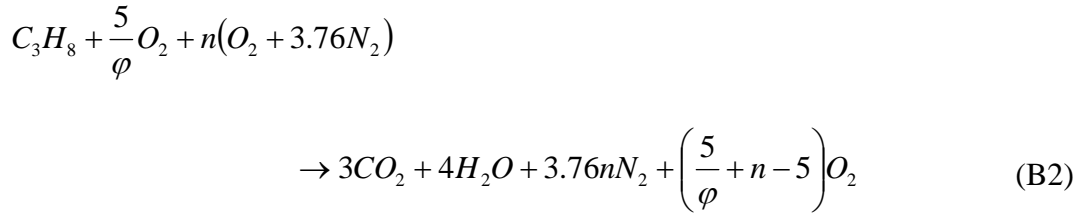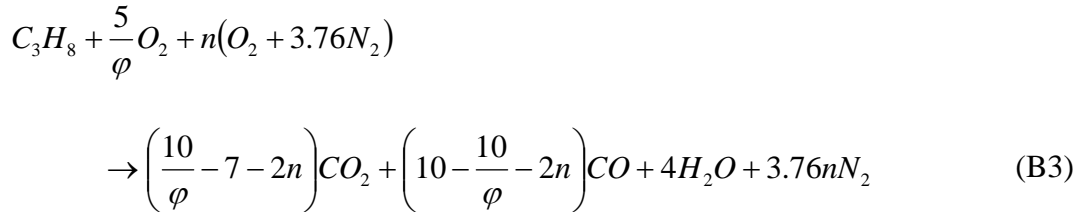
,where *n* is the ratio of air to fuel flow rates.

The products of each of the two equations above (e.g. CO_2, CO, O_2, H_2O and N_2) are similar to those produced from the combustion reactions inside gas turbine engines. The mole fraction of the chemicals in products depends on Φ and *n*, which vary with the flow rates of the reactants. Figure 129 and Figure 130 show the ranges of the temperature and gas velocity

attainable through the use of the HVOF with respect to the equivalence ratio, or richness of fuel. Each data point on the figures indicates potential operating conditions. Figure 129 and Figure 130 are temperature and gas velocity with respect to equivalence ratio at constant air flow rate of 200 *scfh* and at 800 *scfh*, respectively. From Figure 129 (a) and (b), peak temperature of 2300 K is reached at the equivalence ratio of 1. Peak gas velocity of 860 *m/s* (*Mach* 0.95) occurs at the equivalence ratio of about 0.5. Comparing between Figure 129 and Figure 130, it is obvious that the temperature and gas velocity are higher at the air flow rate of 200 *scfh* than at 800 *scfh*. The air will play a role of a cooling agent, reducing both temperature and gas velocity. Figure 131 represents the gas temperature envelop showing the highest temperature attainable for various combinations of equivalence ratio and gas velocity at the two flow rates.

(a)   (b)
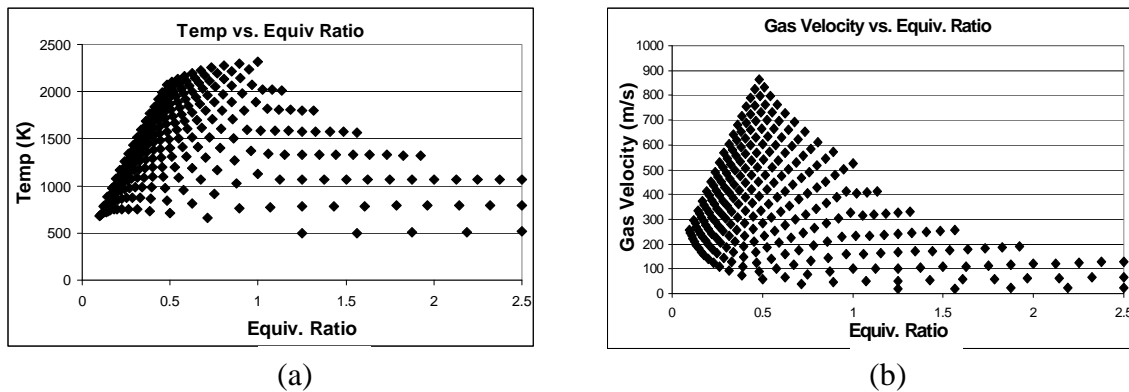
Figure 129: (a) Temperature vs. Equivalence ratio and (b) Gas Velocity vs. Equivalence ratio at air flow rate of 200 *scfh*
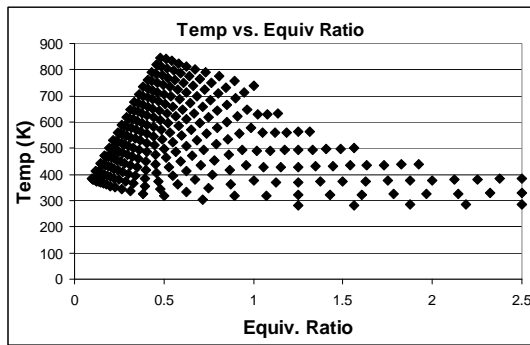
(a)
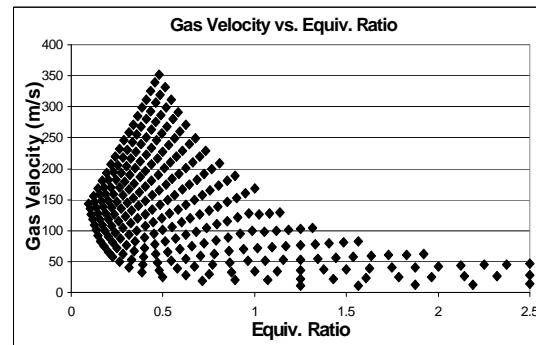
(b)

Figure 130: (a) Temperature vs. Equivalence ratio (b) Gas Velocity vs. Equivalence ratio at air flow rate of 800 *scfh*
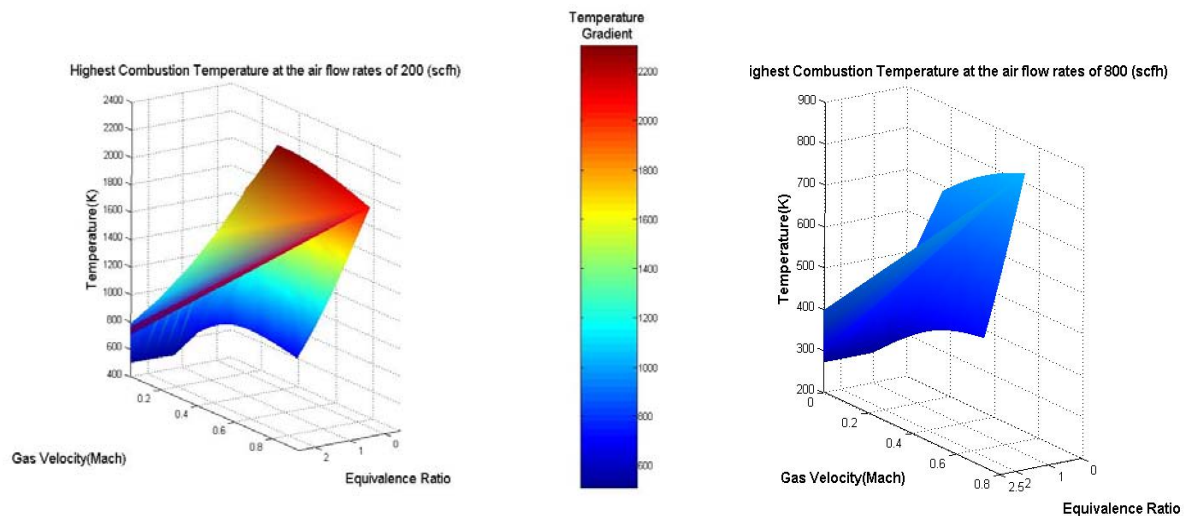
(a) Surface plot taken at air flow rate of 200 *scfh*.

(b) At air flow rate of 800 *scfh*. Lower overall temperature is caused by high air flow rate.

Figure 131: Surface plots of the highest achievable temperature for a given equivalence ratio and gas velocity: Wide range of gas temperature is attainable at a variable equivalence ratio.

Appendix C: Assessment of Gas Chemistry

In Chapter III, a fully-mixed, instantaneous equilibrium local flame condition was assumed to estimate the local chemical condition using Chemical Equilibrium with Applications (CEA) based on a global chemical reaction. In reality, many intermediate steps occur between the initial and final steps with many intermediate species produced and consumed in the process. In addition, each of the reactions takes time to complete. An evidence for this would be the fact that as much as 0.75 *vol %* or 7500 *ppm* of unburned hydrocarbon was detected at 163 *mm* downstream of the nozzle exit for a slightly fuel-rich premixed combustion, i.e. φ of 1.2. The temperature at this location was 850$^{\text{o}}$C. Considering the air entrainment from both cooling and room, to observe the hydrocarbon of such quantity at relatively far in the downstream suggests that some of the intermediate chemical reactions that were described as occurring in chain or simultaneously may not have fully occurred. It is evident that either some hydrocarbon molecules have escaped from reacting with oxidizer in the primary combustion, which occurs in the inviscid core that encompasses about the first 10 *mm* outside the nozzle exit, or the radial mixing of the combustion gas with the entrained air was minimal, possibly due to the momentum of the flow. The latter is less likely as the gas temperature was observed to drop very rapidly, which is an indication for the physical mixing of the combustion gas with the surrounding air.

As with any chemical species, the reaction potential of the hydrocarbon decreases at lower temperature. The consequent reduction in the rate of chemical reactions makes the oxidation of the unburned hydrocarbon slower. In the context of a fast moving combustion jet stream approaching *Mach 1.0*, this implies that the complete oxidation of the hydrocarbon will be delayed until the molecules reach farther in the downstream.

At 150 *mm* downstream of the nozzle exit, where the gas temperature was about 929°C, 0.21 *vol % CO* was detected experimentally, whereas the corresponding *CO* content from CEA was negligibly small. From the input reactants, the amount of air entrained was adjusted in the CEA with the input reactant gas ratios such that the measured temperature was attained. Larger detected *CO* content is an indication that the combustion of hydrocarbon may have been delayed. This is in agreement with the observation that relatively large hydrocarbon was detected at 163 *mm* downstream.

The nozzle is cooled by the compressed air passing along its outside surface, which entered through the inlet of the HVOF system. Some of the air enters the secondary combustion, while others accelerate out of the nozzle unreacted by forming a thin layer that thermally isolates the inner surface of the nozzle. Therefore, the primary combustion occurs between the premixed fuel and oxygen along with only some of the compressed air. Hence, the combustion at this stage is very rich, leaving many fuel molecules unreacted. The rich primary combustion produces much more *CO* than anticipated in the calculations, thus accounting in part for a higher measured *CO* *vol %*.

The condition of equilibrium imposed in the calculation using CEA assumes the oxidation of *CO* occurring instantaneously. However, as the large discrepancy between the estimated and measured content shows, *CO* does not oxidize quickly enough to validate the assumption of equilibrium unless radicals like *OH* and *O*, with which it readily recombine to form CO_2 are present. The reactions that produce these radicals involve high activation energy, and thus usually occur at very high temperature. The recombination of *CO* would be very slow at a lower temperature such as 929°C. Slow recombination, together with the relatively larger *CO* content produced from the fuel-rich primary combustion, could explain the higher measured *CO* content.

The CO_2 and O_2 contents, on the other hand, show good agreement between the measured and the computed at the same location in the downstream. For the measured CO_2 and O_2 contents of 6.50 *vol %* and 18.4 *vol %*, the corresponding values computed using CEA were 4.34 *vol %* and 18.2 *vol %*, respectively. The relatively close agreement between measured and calculated contents stems from the high stability of CO_2 and O_2, as compared to CO. Stable species have low propensity towards chemical reactions, making them relatively inert with other species in the environment. This can be shown in Figure 132, which represents relatively steady slopes for the O_2 and CO_2 *vol %* contents with respect to temperature. As the temperature becomes lower, the O_2 and CO_2 contents tend to the ambient condition.
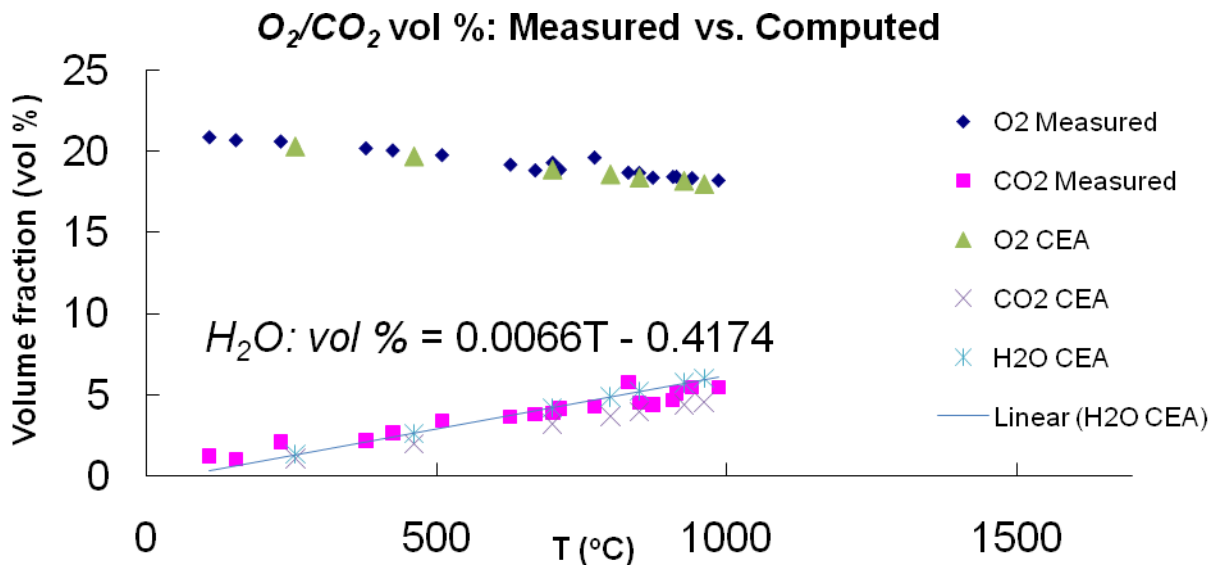
Figure 132: CO_2 **and** O_2 **concentrations in the flame with temperature**

H_2O is another stable species with strong covalent bonding that seldom react into another species. Based on the observations of the other stable species, a reasonable agreement with the measured may be assumed. Testo 350 Gas Analyzer does not have the capability to directly measure the moisture and nitrogen contents. As nitrogen is inert, relatively small fraction of it

reacts to form *NO* or *NO₂*. Thus, the amount of nitrogen was calculated from the compressed air input into the HVOF in addition to the nitrogen from the estimated entrained air. After that, it was assumed that the moisture was the remainder of the nitrogen content as well as all the measurable gases such as CO_2, O_2, NO_2, etc. The moisture content calculated by CEA is represented by the line in Figure 132. Assuming good agreement with the measured, the extrapolation of the line to estimate the moisture content at the cross-section of specimen was attempted at first, which showed the moisture content of 11.5 *vol %* for the gas temperature of 1800°C. At first, it was believed that the extrapolated moisture content was an underestimation because of exponential nature of the amount of air entrainment with respect to the distance from nozzle and the physical translation of H_2O along the distance of flame propagation without decomposition or recombination reactions. However, it was realized that the moisture content remains unchanged whereas the entrained air increases in volume. As a result, the mole fraction of H_2O would likely be smaller as more air becomes entrained into the flame. The closer it is from the nozzle, less of the entrained air enters the combustion. For this reason, the method described in Chapter VI, which considers the primary and secondary combustions separately, was used to estimate the moisture content instead. Nevertheless, the fact remains that the measured concentrations agree reasonably well with those calculated using CEA within the temperature range of measurement for the stable species, e.g. CO_2 and O_2. Less stable species such as *CO* showed considerable discrepancy, which can be attributed to possible delayed combustion of unburned hydrocarbon. Thus, it was validated that the codes assuming a fully-mixed, equilibrium reactions can reasonably estimate the true concentrations of stable species for the temperature range used in the calibration process. For a complete validation of the code results, it would be necessary to perform the similar analysis at higher temperature, which, due to extreme temperature, may

require a non-contact method of measuring the gas temperature and chemical species such as the

laser spectroscopy facility [145] at Air Force Institute of Technology (AFIT).

Appendix D: Directional Fracture

All fracture surfaces demonstrated the oxidation near the corners and along the machined edges and it appears that the oxidation front has advanced from the edge or corners on the left in each of the three cases shown in Figure 62 of Chapter IV.

For most of the fracture surface of all three woven CMCs, it is apparent that the cracks have developed preferentially from the left edge over the right one. This could be due to multiple reasons including possible mis-alignment of the grips and a non-symmetric method of introducing the heat to the specimen, albeit at lower temperature.

First, the alignment of the MTS grips was done at room temperature to the highest precision available with the alignment specimen, as described in the procedure of Chapter III. At high temperature, however, the scale of the error in axial alignment that was considered within the acceptable range at room temperature could be magnified with the thermal expansion of the specimen. This is one possible reason for which failure was consistently demonstrated from one side of the specimen.

Secondly, the combustion gas was brought to the specimen by swinging in the burner rig from the left side at a distance. As described in the procedure of Chapter III, the change in surface temperature associated with this directional introduction of the flame was $700 \pm 50^{o}C$ from the room temperature. Change in temperature by as much as $750^{o}C$ in less than one second could induce compressive stress as large as -600 MPa, if the specimen was not allowed to expand. The MTS grips were controlled to remain at zero force during the flame introduction, which was done by use of the built-in feedback system that reacts to the change in conditions such as a specimen expanding upon higher temperature exposure. There were also differential in temperature on the surface upon the initial introduction of the flame from the left. This could have momentarily

applied gradient of stress along the width of the specimen. If even a small fraction of the large stress was induced by the potential lag in the feedback response, the stress induced could be considerable. Fortunately, the stress that could have been induced by the response time lag in feedback is in compression, under which the material is much stronger than in tension. This is the second potential cause of the failure observed consistently from one side.

Above all, the method of flame introduction could have been problematic and needs to be looked at for improvement. However, this method is also the way the heating takes place for such applications as vanes which are, similarly to the specimen responding to the MTS feedback system, dimensionally confined by the inner and outer shrouds. Although the shrouds are made with the same materials, the differential in the rate of reaching the final temperature is expected between the vane and the shrouds due to their different volumes.

Appendix E: Estimating Boria Vaporization Time

This appendix is provided to supplement the discussion of chemical kinetics of the reactions that result in oxidative degradation. When a crack open to the environment reaches the interphase, the O_2 and H_2O in the oxidizing environment react readily with *BN* to form liquid phase B_2O_3 by Equations (11-12) of Chapter II. As the liquid boria gets leached out of borosilicate, the remaining silica solidifies to the adjacent fibers and matrix, causing degradation in the ability of the CMC to perform the bridging mechanism that provides the material the toughness. In this appendix, the reaction time for such volatilizing reactions is estimated based on the assumption that the interphase becomes hardened as the reactions complete. The method of estimation is as prescribed by Parthasarathy et al [146], and all the data and equations used are also from the same reference.

For a first order estimation that assumes that water vapor plays no factor in the evaporation in liquid boria, which is described by Equation 15 of Chapter II;

$$B_2O_3(l) \rightarrow B_2O_3(g) \tag{15}$$

,where *l* and *g* stand for liquid and gaseous phases of B_2O_3, respectively. Assuming that the activity of liquid boria is 1, the partial pressure of the gaseous boria is determined as follows;

$$P_{B_2O_{3\,(g)}}(T) = k \cdot \exp\left(-\frac{Q}{RT}\right) \tag{E1}$$

,where $P_{B_2O_{3(g)}}$ is the partial pressure of gaseous boria in Pascal *(Pa)*; *T* is the local temperature at the interphase in Kelvin; *k* is a constant, and *Q* is the activation energy in *J/mol* for the reaction (15); *R* is the gas constant, i.e. 8.314 *J/K·mol*. The *k* and *Q* are extrapolated from the data [146] to be approximately $3.0\text{X}10^{13}$.and 380000 *J/mol*. For the local temperature of 1300 K, the partial

pressure of gaseous boria is then 1.64×10^2 *Pa.* The flux of gaseous boria, $J_{B_2O_3(g)}$ is in the unit of

mol/m²·sec.

$$J_{B_2O_3(g)} = -D \cdot \left(-\frac{\partial C}{\partial x} \right) = -D \cdot \left(-\frac{P_{B_2O_3(g)}}{R \cdot T \cdot L} \right) \tag{E2}$$

,where *D* is the diffusivity of B_2O_3 in air, i.e. 0.0001 *m²/sec*; *C* is the molar concentration of

gaseous boria in *mol/m³*, *x* the direction of the flux in meter *(m)*; $P_{B_2O_3(g)}$ is the partial pressure of

gaseous boria in *Pa* determined from Equation (D1); R is the gas constant in *J/K·mol*, and *T* is

temperature in *K*; *L* is the length of a crack in meter *(m)*. The crack considered for this illustration

is one that emanates from a side edge of a specimen, and the flux is determined for the crack

length of 1 *mm*. The crack considered here is schematically illustrated in Figure 133.
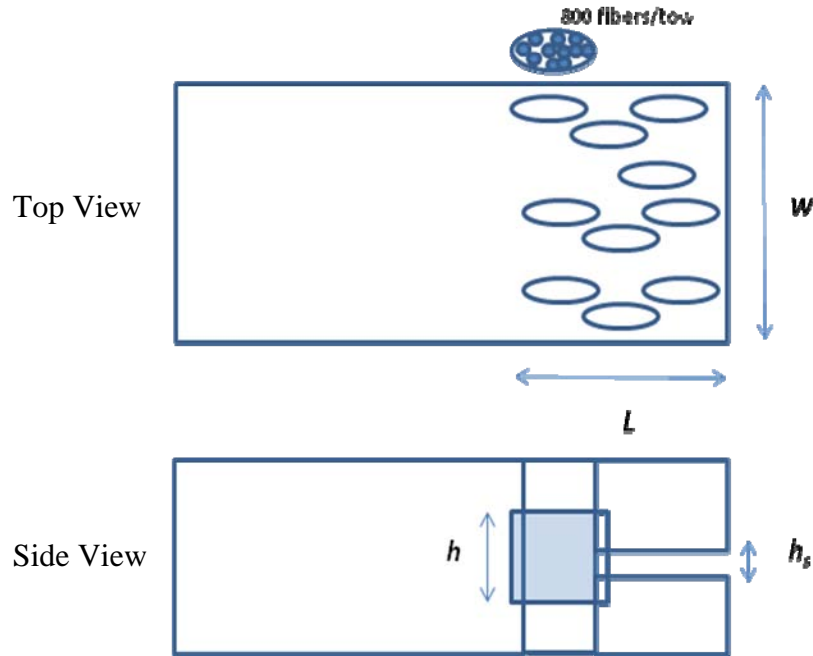
Figure 133: Schematic of crack illustrated [93]

The flux determined as above is 2.03×10^{-7} $mol/m^2 \cdot sec$ for the local temperature of 1300 K. To use the flux information to extract the reaction time, the interphase exposed by the crack needs to be estimated in terms of mole. Modeling the exposed interphase as a thin-walled cylinder, the volume, V is;

$$V = t \cdot \left(2\pi \cdot r \cdot h\right) \qquad \text{(E3)}$$

, where t is the interphase thickness, i.e. 5.0×10^{-7} m; r is the radius of the fiber and interphase as one, i.e. 5.05×10^{-6} m; h is the crack opening displacement (*COD*), i.e. 5.0×10^{-6} m. In addition, the width and height of the crack, w and h_s are 5 mm and 1.67×10^{-6} m, respectively. h_s is estimated to be one third of the *COD*.

The molar weight and the density of B_2O_3 (*l*) is 0.06962 (*kg*), and 2460 kg/m^3, respectively. The number of mole of B_2O_3 (*l*) produced by oxidation is, for each fiber, determined by dividing V (m^3) by the molar weight, $MW_{B_2O_3}$ (*kg*) and density, $\rho_{B_2O_3}$ (kg/m^3) to be 3.7×10^{-15} *moles*. This is multiplied by the number of fibers open to the crack, $n_{B_2O_3}$; 8000 fibers are estimated based on the crack dimension such that, i.e. 10 tows, each containing approximately 800 fibers. The rate of formation of the gaseous boria determined by multiplying the flux (i.e. 2.03×10^{-7} $mol/m^2 \cdot sec$) by the surface area exposed by the crack (i.e. $\pi \cdot r \cdot h_s$)·is 5.18×10^{-18} *moles/sec*. The reaction time is determined by the following;

$$time = \frac{n_{B_2O_3(l)} \cdot V}{MW_{B_2O_3} \cdot \rho_{B_2O_3} \cdot J_{B_2O_3}} \cdot \frac{1}{(\pi \cdot r \cdot h_s)} \qquad \text{(E4)}$$

Substituting the values determined above in this equation results in the reaction time of 692 seconds (sec). As this is a rough estimation of highly complicated chemical reactions, the exact value of 692 seconds should not be taken as a definitive value. Instead, the hundreds of

seconds as a rough timeframe provides a basis to consider how long the liquid phase remains in relation to the fatigue life.

The actual partial pressure would have been higher if the reactions involving moisture such as Equations (16-18) were to be factored into the analysis. If the actual partial pressure was greater than that estimated in this illustration by a factor of 10, then the corresponding reaction time for the same conditions and crack geometry is 69 sec, which is still a finite period of time during which 69 fatigue cycles would have occurred.

If, unlike in the illustrated example, the fibers were exposed directly to the burner rig environment with the temperature nearing 2000 K, the reaction time would be, for the same conditions and crack geometry, less than 0.01 sec. The completion of this reaction in such environment, however, does not translate to the solidified interphase through which neighboring fibers are welded and fracture together as a group, because the SiO_2 would be less viscous and flow in such high temperature environment containing moisture. Diffusion of oxidants is facilitated through the less viscous SiO_2, making the underlying SiC and BN susceptible to oxidation

Therefore, the reaction time for boria volatilization could be on the order of tens to hundreds of seconds for the illustrated case involving a crack propagating from the side edge. If, however, the local temperature was higher, for instance through the direct exposure to the burner rig environment, the reaction time becomes significantly shortened.

Bibliography

1   D. Anson and D.W. Richerson, "The Benefits and Challenges of the Use of Ceramics in Gas Turbines," In <u>Ceramic Gas Turbine Component Development and Characterization</u>, eds M. van. Roode, M.K. Ferber, and D.W. Richerson, ASME press, New York, 2002.

2   E. Lara-Curzio, "Properties of Continuous Fiber-Reinforced Ceramic Composites for Gas Turbine Applications," In <u>Ceramic Gas Turbine Component Development and Characterization</u>, eds M. van Roode, M.K. Ferber, and D.W. Richerson, ASME press, New York, 2003.

3   Mikio Hiromatsu, Shigeto Nishide, Kozi Nishio, Ken-ichiroh Igashira, Go Matsubara, and Takeshi Suemitsu, "Development of Hot Section Components Composed of Ceramic Matrix Composite (CMC) at the Research Institute of Advanced Material Gas-Generator (AMG)," In <u>Ceramic Gas Turbine Component Development and Characterization</u>, eds M. van Roode, M.K. Ferber, and D.W. Richerson, ASME press, New York, 2003.

4   M. van Roode., W.D. Brentnall, P.F. Norton, and G.L. Boyd, "Ceramic stationary Gas Turbine Development Program - First Annual Summary." ASME Paper 94-GT-313, Presented at the International Gas Turbine and Aeroengine Congress and Exposition, The Hague, The Netherlands, June 13-16, 1994.

5   M. van Roode, D.A. Rohy, S. Waslo, and W.P. Parks, Jr, "Ceramic Stationary Gas Turbine Development," Presented at 1995 Yokohama International Gas Turbine Congress, Yokohama, Japan, October 22-27, 1995.

6   D. Anson, W.J. Sheppard, and W.P. Parks, Jr., "Impact of Ceramic Components in Gas Turbines for Industrial Cogeneration," ASME Paper 92-GT-393, Presented at the International Gas Turbine and Aeroengine Congress and Exposition, Cologne, Germany, June 1-4, 1992.

7   J.A. DiCarlo and M. van Roode, "Ceramic Matrix Composite Development for Gas Turbine Engine Hot Section Components," *Proceedings of GT2005 Turbo Expo 2005: Power for Land, Sea and Air* May 8-11, 2006, Barcelona, Spain.

8   M. Verrilli and A. Calomino, *Proceedings of ASME Turbo Expo 2004, Power for Land, Sea and Air*, GT2004-53974, June 14-17, 2004, Vienna, Austria.

9   D.N. Brewer, M. Verrilli, and A. Calomino, "Ceramic Matrix Composite Vane Subelement Burst Testing," *Proceedings of GT2005 ASME Turbo Expo 2005: Power for Land, Sea and Air*, May 8-11, 2006, Barcelona, Spain.

10   A.M. Calomino and M.J. Verrilli, "Ceramic Matrix Composite Vane Sub-element Fabrication," *Proceedings of ASME Turbo Expo 2004, Power for Land, Sea and Air*, GT2004-53974, June 14-17, 2004, Vienna, Austria.

11   T. Sourmail, "Coatings for Turbine Blades,"
     http://www.msm.cam.ac.uk/phase-trans/2003/Superalloys/coatings/index.html) (2003).

12   "IHPTET Air Dominance Through Propulsion Superiority,"
     (http://www.pr.afrl.af.mil/divisions/prt/ihptet/brochure/Turbines.htm).

13   K.J. LaRochelle, "Tensile Stress Rupture Behavior of a Woven Ceramic Matrix Composite   in
     Humid Environments at Intermediate Temperature," Ph.D. Dissertation, Air Force Institute of
     Technology (March 2005): Advisor: S. Mall.

14   W.D. Carruthers, P.F. Becher, M.K. Ferber, and J. Pollinger, "Advanced in Development of
     Silicon Nitride and Other Ceramics," *Proceedings of ASME Turbo Expo 2002*, June 3-6, 2002,
     Amsterdam, The Netherlands.

15   G.S. Corman, A.J. Dean, S. Brabetz, M.K. Brun, K.L. Luthra; L. Tognarelli and M. Pecchioli,
     "Rig and Engine Testing of Melt Infiltrated Ceramic Composites for Combustor and Shroud
     Applications," *Journal of Engineering for Gas Turbines and Power*, 124 459-464 (2002).

16   G.S. Corman, J.T. Heinen, and R.H. Goetze, "Ceramic Composites for Industrial Gas Turbine
     Engine Applications: DOE CFCC Phase 1 Evaluations," *Journal of Engineering for Gas
     Turbines and Power*, 123 513-519 (2001).

17   J.A. DiCarlo and H.M. Yun, "Modeling the Thermostructural Capability of Continuous Fiber
     -Reinforced Ceramic Composites," *Journal of Engineering for Gas Turbines and Power*, 124,
     465-470 (2002).

18   D. Brewer, "HSR/EPM combustor materials development program," *Materials Science and
     Engineering: A* 261 284-291 (1999).

19   D.B. Marshall and A.G. Evans, "Failure Mechanisms in Ceramic-Fiber/Ceramic-Matrix
     Composites," *Journal of the American Ceramics Society*, 68 [5] 225-231 (1985).

20   J.W. Holmes and X. Wu, "Elevated Temperature Creep Behavior of Continuous Fiber-
     Reinforced Ceramics," In High Temperature Mechanical Behavior of Ceramic Composites, eds
     S.V. Nair and K. Jakus, Butterworth-Heinermann, Boston, 1995.

21   K.M. Prewo and J.J. Brennan, "High Strength Silicon Carbide Fiber Reinforced Glass Matrix
     Composites," Journal of Materials Science, 15 [2] 463-8 (1980).

22   J.A. DiCarlo, H.-M. Yun, G.N. Morscher, and R.T. Bhatt, "SiC/SiC Composites for 1200°C and
     Above," NASA/TM 2004-213048 (2004).

23   J.A. DiCarlo, H.M. Yun, J.B. Hurst, "Fracture mechanisms for SiC fibers and SiC/SiC

Composites under stress-rupture conditions at high temperatures," *Applied Mathematics and Computation*, 152 473-481 (2004).

24   D. Brewer, "Overview of CMC Development Activities in NASA's Ultra-Efficient Engine Technology (UEET) Program," Presented at NASA Seal/Secondary Air System Workshop, Cleveland, *OH*, 26 October, 2000. (http://www.grc.nasa.gov/WWW/TurbineSeal/papers/2000/V1-23Brewer.pdf).

25   L.U.J.T. Ogbuji, "Recent Developments in the Environmental Durability of SiC/SiC Composites," NASA/CR 2002-211687 (2002).

26   H.M. Yun, J.Z. Gyekenyesi, D.R. Wheeler, and J.A. DiCarlo, "Tensile Behavior of SiC/SiC Composites Reinforced by Treated Sylramic SiC Fibers," *Ceramics Engineering and Science Proceedings*, 22 [3] 521-531 (2001).

27   J.A. DiCarlo and H.M. Yun, "Microstructural Factors Affecting Creep-Rupture Failure of Ceramic Fibers and Composites," In Ceramic Material Systems with Composite Structures, eds N. Takeda, L.M. Sheppard and J. Kon, *American Ceramic Society*, Westerville *OH*, 1998.

28   J.L Ryba, "Creep-Rupture Behavior of a Woven Ceramic Matrix Composite at Elevated Temperatures in a Humid Environment," Master Thesis, Air Force Institute of Technology (March 2006): Advisor: S. Mall.

29   R.J. Kerans, "Viability of Oxide Fiber Coatings in Ceramic Composites for Accommodation of Misfit Stresses," *Journal of the American Ceramics Society*, 79 [1] 1664-68 (1996).

30   R.J. Kerans and T.A. Parthasarathy, "Interface Properties in High-Strength Nicalon/C/SiC Composites, As Determined by Rough Surface Analysis of Fiber Push-Out Tests," *Journal of The American Ceramics Society*, 81 [7] 1881-87 (1998).

31   T.A. Parthasarathy, R.J. Kerans and N.J. Pagano, "Effective Fiber Properties to Incorporate Coating Thermoelastic Effects in Fiber/Matrix Composite Models," *Journal of the American Ceramics Society*, 82 [3] 579-84 (1999).

32   R.J. Kerans, R.S. Hay, T.A. Parthasarathy and M.K. Cinibulk, "Interface Design for Oxidation-Resistant Ceramic Composites," *Journal of the American Ceramics Society*, 85 [11] 2599-632 (2002).

33   T.A. Parthasarathy, D.B. Marshall and R.J. Kerans, "Analysis of the Effect of Interfacial Roughness on Fiber Debonding and Sliding in Brittle Matrix Composites," *Acta Metall. Mater*. 42 [11] 3773-3784 (1994)

34 R.J. Kerans and T.A. Parthasarathy, "Fiber Coating Design Parameters for Ceramic Composites as Implied by Considerations of Debond Crack Roughness," In <u>Ceramic Microstructures: Control at the Atomic Level</u>, eds. A.P. Tomsia and A. Glaeser, Plenum Press, New York, 1998.

35 R.J Kerans, "The Role of Coating Compliance and Fiber/Matrix Interphase Topography on Debonding in Ceramic Composites," *Scripta Metall. Meter*, 32[4] 505-509 (1995).

36 R.J Kerans and T.A. Parthasarathy, "Debond Crack Roughness, Interface Properties and Fiber Coating Design in Ceramic Composites," *Key Engineering Materials,* 127-131 51-62 (1997).

37 R.J. Kerans, "Issues in the Control of Fiber-Matrix Interface Properties in Ceramic Composites," *Scripta. Metall. Mater,*. 31[8], 1079-1084 (1994).

38 L.P. Zawada, Senior Materials Research Engineer, AFRL/MLLN, WPAFB, *OH*. Personal Communication, 05 January 2006.

39 L.U.J.T. Ogbuji, H.M. Yun, and J. DiCarlo, "Effect of Adventitious Carbon on the Environmental Degradation of SiC/BN/SiC Composites," NASA/TM 2002-211494 (2002).

40 L.P Zawada, Senior Materials Research Engineer, AFRL/MLLN, WPAFB, *OH*. Personal Conversation, 14 April 06.

41 S. Mall and K.J. LaRouchelle, "Fatigue and stress-rupture behaviors of SiC/SiC composite under humid environment at elevated temperature," Composite Science and Technology, 66 2925-34 (2006).

42 G.N. Morscher, "Tensile Stress Rupture of SiCf/SiCm Minicomposites with Carbon and Boron Nitride Interphases at Elevated Temperatures in Air," *Journal of the American Ceramics Society*, 80 [8], 2029-2071 (1997).

43 S. Mall, "Effects of Moisture on Fatigue Behavior of SiC/SiC Composite at Elevated Temperature," *Materials Science and Engineering: A*, 412, 165-170 (2005).

44 K.J. LaRochelle and S. Mall, "Temperature and Moisture Effects upon Stress Rupture Life of Syl-*iBN*/BN/SiC Composites," *Ceramics Engineering and Science Proceedings*, 24 [4] 459-64 (2003).

45 K.L. More, P.L. Tortorelli, L.R. Walker, N. Miriyala, J.R. Price and M. van Roode, "High-Temperature Stability of SiC-Based Composites in High-Water-Vapor-Pressure Environments," *Journal of the American Ceramics Society*, 86 [8] 1272-81 (2003).

46 L.U.J.T. Ogbuji, "Degradation of a SiC/SiC composite in the burner rig: investigation by fractography, *Materials at High Temperatures*, 17 [2] 369-72 (2000).

47 E.J. Opila and R.E. Hann Jr., "Paralinear Oxidation of CVD SiC in Water Vapor," *Journal of the American Ceramics Society*, 80 [1] 197-205 (1997).

48 G. N. Morscher, "Intermediate Temperature Stress Rupture of Woven SiC Fiber, BN Interphase, SiC Matrix Composites in Air," Ph.D. Dissertation, Case Western Reserve University (January 2000).

49 J.J. Brennan, "Interfacial Characterization of a Slurry-Cast Melt-Infiltrated SiC/SiC Ceramic-Matrix Composite," *Acta Materialia*, 48 4619-28 (2000).

50 G.N. Morscher, G. Ojard, R. Miller, Yasser Gowayed, Unni Santhosh, Jalees Ahmed, and Reji John, "Tensile Creep and Fatigue of Sylramic-*iBN* Melt-Infiltrated SiC Matrix Composites: Retained Properties, Damage Development, and Failure Mechanisms," in press, *Composites Science and Technology*, 2008.

51 S.S. Lee, L.P. Zawada, J.M. Staehler and C.A. Folsom, "Mechanical behavior and high-temperature performance of a woven Nicalon^{TM}/Si-N-C ceramic-matrix-composite," *Journal of the American Ceramics Society*, 81 [7], 1797-811 (1998).

52 A.G. Evans, F.W. Zok, and T.J. Mackin, "The Structural Performance of Ceramic Matrix Composites," In High Temperature Mechanical Behavior of Ceramic Composites, eds S.V. Nair and K.Jakus, Butterworth-Heinermann, Boston, 1995.

53 R.J. Kerans, R.S. Hay, N.J. Pagano, and T.A. Parthasarathy, "The Role of the Fiber-Matrix Interface in Ceramic Composites," *Ceramics Bulletin*, 68 [2] 429-42 (1989).

54 J.W. Hutchinson and H.M. Jensen, "Models of Fiber Debonding and Pullout in Brittle Composites with Friction," *Mechanics of Materials*, 9 [2] 139-63 (1990).

55 A.G. Evans, F.W. Zok and J. Davis, "The Role of Interfaces in Fiber-Reinforced Brittle Matrix Composites," *Composite Science and Technology*, 42 3-24 (1991).

56 R.C. Robinson and J.L. Smialek, "SiC Recession Due to SiO2 Scale Volatility under Combustion Conditions. Part I: Experimental Results and Empirical Model," *Journal of the American Ceramics Society* 82 [7] 1817-25 (1999).

57 K.L. Luthra, "Simulation of Gas Turbine Environments in Small Burner Rigs," *High Temperature Technology*, 7 [4] 187-192 (1989).

58 R.C. Robinson, "NASA GRC's High Pressure Burner Rig Facility and Materials Test Capabilities," NASA/CR 1999-209411 (1999).

59 G. Richardson, C.S. Lei, and R.N. Singh, "Mechanical Properties of Ceramic Matrix Composites Exposed to Rig Tests," *Ceramics Engineering and Science Proceedings*, 25 [4] 153-159 (2004).

60 M.J. Verrilli and L.C. Martin; D.N. Brewer, "RQL Sector Rig Testing of SiC/SiC Combustor Liners," NASA/TM 2002-211509 (2002).

61 L.S. Langston, Editor of Journal of Engineering for Gas Turbines and Power, Personal Correspondence, 21 May 06.

62 L. Jacobson, C. Persson, S. Melin, "Experimental Methods for Thermomechanical Fatigue in Gas Turbine Materials," *Proceedings of the 15th European Conference of Fracture*, August 11 -13, 2004, Stockholm, Sweden.

63 D. Carruthers, "Coatings for Si3N4 and SiC Ceramics: an Historical Perspective," Presented at the ORNL EBC Workshop, Nashville, TN, November 6-7, 2002. (http://www.ornl.gov/sci/de_materials/documents/CarruthersRevised.pdf)

64 I. Glassman, Combustion, Academic Press, New York, 1996.

65 M. Cuy, Research Engineer, NASA Lewis Research Center, Cleveland, *OH*, Personal Correspondence, 19 May 06.

66 T. Ertürk and G.M. St.Hilaire, "Burner Rig Thermal Fatigue of Hot Pressed SiC Continuous Fiber Silicon Nitride Ceramic Composites under Constant Applied Stress," In Mechanisms and Mechanics of Composites Fracture 209-19, eds R.B. Bhagat, S.G. Fishman, and R.J. Arsenault, ASM International: Materials Park, *OH*, 1993.

67 T. Ertürk and J. McKelliget, "Heat Transfer During Burner Rig Thermal Fatigue of Ceramic Matrix Composites," *Ceramics Engineering and Science Proceedings*, 16[4] 95-104 (1995) (http://jmckelliget.caeds.eng.uml.edu/burnpap.pdf).

68 Picture Courtesy of the National Aerospace Laboratory – The Netherlands (2006) (http://www.nlr.nl/eCache/DEF/267.html).

69 K.L. More, P.F. Tortorelli, and L.R. Walker, "Verification of an EBC's Protective Capability by First-Stage Evaluation in a High Temperature, High-Pressure Furnace, *Proceedings of 2003 ASME Turbo Expo, Power for Land, Sea and Air*, GT2003-38923, June 16-19, 2003, Atlanta, Georgia, USA.

70 M. van Roode, K. More, D. Brewer, G. Linsey, "Durability Testing and Characterization of SiC/SiC Ceramic Matrix Composites for Gas Turbine Combustor Applications," *Proceedings of the ISOABE Conference*, Bangalore India, September 2-7, 2001.

71 L. Cheng, L. Zhang, Y. Xu, X. Luan, and D. Wang, "Experimental Testing System Simulating Environments of Aero-Engines," *Proceedings of the 5th International Conference on High Temperature Ceramic Matrix Composite (HTCMC-5)*, Seattle, WA, September 12-16, 2004.

72 H. Mei, L. Cheung, X. Luan, L. Zhang, Y. Xu and D. Wang, "Simulated Environments Testing System for Advanced Ceramic Matrix Composites, *International Journal of Applied Ceramic Technology*, 3 [3] 252-257 (2006).

73 L.P Zawada, Senior Materials Research Engineer, AFRL/RXLN, WPAFB, *OH*, Personal Conversation, 14 April 06.

74 K.L. Luthra and G.S. Corman, "Status and Challenges for the use of Melt Infiltrated CMCs (HiPerComp^{TM}) in Industrial Gas Turbine Applications," Presented at the 5th International Conference on High-Temperature Ceramic Matrix Composites (HTCMC-5), Seattle, WA, 13 September 2004.

75 M. J. Verrilli, Senior Materials Research Engineer, GE Aviations, Evansdale, *OH*. Personal Conversation, 22 July 08.

76 G.S. Corman and K.L. Luthra, "Silicon Melt Infiltrated Ceramic Composite (HiPerComp^{TM})," In Handbook of Ceramic Composites, ed Narottam P. Bansal, Kluwer Academic Publishers, Boston, 2005

77 L.U.J.T. Ogbuji, "A Pervasive Mode of Oxidation Degradation in a SiC-SiC Composite," *Journal of the American Ceramics Society*, 81 [11] 2777-84 (1998).

78 R.E. Jones, D. Petrak, J. Rabe, A. Szweda, "*SYLRAMIC*^{TM} SiC fibers for CMC reinforcement," *Journal of Nuclear Materials*, 283-287 556-9 (2000).

79 J.A. DiCarlo and H-M. Yun, "Non-oxide (Silicon Carbide) Fibers," In Handbook of Ceramic Composites, ed Narottam P. Bansal, Kluwer Academic Publishers, Boston, 2005

80 M J. Verrilli, Unpublished Test Results, GE Aviations, Evansdale, *OH*. Personal Correspondence, 6 September 07.

81 L.P. Zawada, Unpublished Test Results, Senior Materials Research Engineer, AFRL/RXLN, WPAFB, *OH*. Personal Conversation, 15 May 08.

82 L.U.J.T. Ogbuji, D.R. Wheeler, T.R. McCue, "Process-Induced Carbon and Sub-Layer in SiC/BN/SiC Composites: Characterization and Consequences," NASA/TM 2001-211069 (2001).

83 N.S. Jacobson, J.L. Smialek, and D.S. Fox; E.J. Opila, "Durability of Silica-Protected Ceramics in Combustion Atmospheres," *Proceedings of the 1995 2nd International Conference on High-Temperature Ceramic Matrix Composites*. Part 1, Santa Barbara, CA, August 21-24, 1995.

84 J. L. Smialek, R.C. Robinson, E.J. Opila, D.S. Fox, and N.S. Jacobson, "SiC and Si$_3$N$_4$ recession

due to SiO2 scale volatility under combustion conditions," *Advanced Composite Materials* 8 [1] 33-45 (1999).

85   D.S. Fox, E.J. Opila, and R.E. Hann, "Paralinear Oxidation of CVD SiC in Simulated Fuel-Rich Combustion," *Journal of the American Ceramics Society*, 83 [7] 1761-67 (2000).

86   E. J. Opila and R.C. Robinson, "The Oxidation Rate of SiC in High Pressure Water Vapor Environments," *Electrochemical Society Proceedings*, 99-38 398-406 (1999).

87   G. Hetherington, K.H. Jack ,and J.C. Kennedy, "The Viscosity of Vitreous Silica," *Physics and Chemistry of Glasses*, 5 [5], 130-36 (1964).

88   C.J. Brinker and G.W. Scherer, Sol-Gel Science: The Physics and Chemistry of Sol-Gel Processing, Academic Press, Inc., New York, 1990.

89   G. Urbain, Y. Bottinga and P. Richet, "Viscosity of liquid silica, silicates and alumino-silicates," *Geochimica Cosmochimica Acta* 46 1061-72 (1982).

90   R.H. Doremus, "Viscosity of silica," *Journal of Applied Physics*, 92 [12] 7619-28 (2002).

91   E.J. Opila, "Variation of the Oxidation Rate of Silicon Carbide with Water-Vapor Pressure," *Journal of the American Ceramics Society*, 82 [3] 625-36 (1999).

92   E.J. Opila, D.S. Fox, and N.S. Jacobson, "Mass Spectrometric Identification of Si-O-H (g) Species from the Reaction of Silica with Water Vapor at Atmospheric Pressure," *Journal of the American Ceramics Society*, 80 [4] 1009-12 (1997).

93   T.A. Parthasarathy, Director of Materials and Processes, UES, Inc., Personal Conversation, 17 October, 2008.

94   N.S. Jacobson, G.N. Morscher, D.R. Bryant, and R.E. Tressler, "High Temperature Oxidation of Boron Nitride: II, Boron Nitride Layers in Composites," *Journal of the American Ceramics Society*, 82 [6] 1473-82 (1999).

95   J.W. Holmes and B.F. Sorensen, "Fatigue Behavior of Continuous Fiber-Reinforced Ceramic Matrix Composites, In High Temperature Mechanical Behavior of Ceramic Composites, eds S.V. Nair and K. Jakus, Butterworth-Heinemann, Boston, 1995.

96   A.G. Evans, F.W. Zok and R.M. McMeeking, "Fatigue of Ceramic Matrix Composites," *Acta Metallurgica Materialia* 43 [3] 859-75 (1995).

97   J.M. Staehler, S. Mall, L.P. Zawada, "Frequency Dependence of High-cycle Fatigue Behavior of CVI C/SiC at Room Temperature," *Composites Science and Technology*, 63 2121-31 (2003).

98   J.W. Holmes, X. Wu, and B.F. Sorensen, "Frequency Dependence of Fatigue Life and Internal Heating of a Fiber-Reinforced Ceramic Matrix Composite," *Journal of the American Ceramics Society*, 77 [12] 3238-86 (1994).

99   S.F. Shuler, J.W. Holmes, X. Wu, and D. Roach, "Influence of Frequency on the Rate of Damage Accumulation in a C-Fiber SiC-Matrix Composite," *Journal of the American Ceramics Society*, 76 2327-2336 (1993).

100 R.F. Allen and P. Bowen, "Fatigue and Fracture of a SiC/CAS Continuous Fiber Reinforced Glass Ceramic Matrix Composite at Ambient and Elevated Temperatures," *Ceramics Engineering and Science Proceedings*, 14, 265-72 (1993).

101 B.F. Sorensen and J.W. Holmes, "Influence of Stress Ratio on the Fatigue Life of a Continuous Fiber-Reinforced Ceramic Matrix Composites," *Journal of the American Ceramic Society*, 85 [2] 359-65 (2004).

102 S.R. Turns, <u>An Introduction to Combustion: Concepts and Applications</u>, 2nd ed. McGraw-Hill, U.S., 2006

103 Modified from Figure 2.9 on p. 33 of the HVOF manual Diamond Jet® DJ HVOF Spray Gun (2003).

104 A.M. Kanury, <u>Introduction to Combustion Phenomena</u>, Gordon and Breach, U.S., 1995.

105 C.J. Montgomery, S.M. Cannon, M.A. Mawid, and B. Sekar, "Reduced Chemical Kinetic Mechanisms for JP-8 Combustion," AIAA Paper 2002-0336, 40th AIAA Aerospace Science Meeting, Reno, NV, January 14-17, 2002.

106 M.A. Mawid, T.W. Park, B. Sekar, and C. Arana, "Application of Pulse Detonation Combustion to Turbofan Engines," *Journal of Engineering for Gas Turbine and Power*, 125 270-283 (2003).

107 C.J. Jachimowski, "Chemical Kinetic Reaction Mechanism for the Combustion of Propane," *Combustion and Flame*, 55 213-224 (1984).

108 S-C. Kong, Assistant Professor, Iowa State University, Personal Correspondence, 19 May 2006.

109 "Greener by design – the technology challenge," *Aircraft Engineering and Aerospace Technology* 73 [6] Emerald Group Publishing Limited, December, 2001.

110 R.D. Hudson, Jr., <u>Infrared System Engineering</u>, John Wiley & Sons, New York, 1969.

111 B.J. McBride and S. Gordon, Computer Program for Calculation of Complex Chemical Equilibrium Compositions and Application, NASA RP-1311, June 1996.

112 R.D. Branam, Assistant Professor, Department of Aeronautics and Astronautics, Air Force Institute of Technology, WPAFB, OH Personal Conversation, 12 March 08.

113 Y. Katoh, L.L. Snead, T. Nozawa, T. Hinoki, A. Kohyama, N. Igawa and T. Taguchi, "Effect of Interphase Thickness on Tensile Properties of Hi-Nicalon[TM] Type-S FCVI Composites," 2004 (www.ms.ornl.gov/programs/fusionmatls/pdf/dec2004/2_CERAMIC/KAT*OH*.PDF)

114 D.M. Mieskowski, T.E. Mitchell and A.H. Heuer, "Bubble Formation in Oxide Scales on SiC," *Journal of the American Ceramic Society*, 67 [1] C-17-18 (1984).

115 D. Broek, Elementary Engineering Fracture Mechanics, 4th ed. Kluwer Academic Publishers, Boston, 1986.

116 G. Fantozzi, P. Reynaud and D. Rouby, "Fatigue Behaviour of Structural Ceramic Composites," *Advances in Science and Technology*, 45 1664-73 (2006).

117 T.T. Kim, S. Mall and LP. Zawada, "Fatigue Characterization of Melt-Infiltrated (MI) Woven Hi-Nic-S/BN/SiC CMC Using a Unique Combustion Heating Test Facility," 33rd International Conference on Advanced Ceramics and Composites (ICACC) -Manuscript ID 529430 (2009).

118 R.J. Kerans, Division Technical Advisor, Metals, Ceramics and Non-destructive Evaluation Division, Air Force Research Laboratory, WPAFB, Personal Communication, 12 May 2009.

119 R.S. Hay, G. Fair, E. Urban, J. Morrow, J. Somerson and M. Wilson, "Oxidation Kinetics and Strength Versus Scale Thickness for Hi-Nicalon[TM]-S Fiber," Submitted to 8th Pacific Rim Conference on Ceramic & Glass Technology, Vancouver, British Columbia, Canada, 31 May – June 5, 2009.

120 J.A. DiCarlo, Senior Materials Research Engineer, NASA Glenn Research Center, Cleveland, *OH*, Personal Conversation, 5 May 2009.

121 R.T. Bhatt, Senior Materials Research Engineer, NASA Glenn Research Center, Cleveland, *OH*, Personal Conversation, 5 May 2009.

122 J.A. DiCarlo and H.M. Yun, "Non-oxide (Silicon Carbide) Fibers" In Handbook of Ceramic Composites, ed Narottam P. Bansal, Kluwer Academic Publishers, Boston, 2005

123 A.E. Evans, F.W. Zock, R. M. McMeeking and Z.Z. Du, "Models of High-Temperature, Environmentally Assisted Embrittlement in Ceramic-Matrix Composites," *Journal of the American Ceramic Society*, 79 [9] 2345-52 (1996).

124 G.N. Morscher, J. Hurst and D. Brewer, "Intermediate-Temperature Stress Rupture of a Woven Hi-Nicalon, BN-interphase, SiC-Matrix Composite in Air," *Journal of the American Ceramic Society*, 83 [6] 1441-9 (2000).

125 J.N. Ding, Y.G. Meng and S.N. Wen, "Specimen size effect on mechanical properties of polysilicon microcantilever beams measured by deflection using a nanoindentor." *Materials Science and Engineering B* 83, 42-7 (2001).

126 K.L. Luthra, "Oxidation-Resistant Fiber Coatings for Non-oxide Ceramic Composites," *Journal of the American Ceramic Society*, 80 [12] 3253-57 (1997).

127 L.P. Zawada, Senior Materials Research Engineer, AFRL/RXLN, WPAFB, *OH*. Personal Conversation, 18 June 08.

128 A. Bejan and A.D. Kraus, Heat Transfer Handbook, John Wiley & Sons, New Jersey, 2003.

129 ABAQUS/CAE version 6.7 EF-1 and the user manual by Simulia, RI (2007).

130 R. John, L.P. Zawada and J.L. Kroupa, "Stress Due to Temperature Gradients in Ceramic-Matrix-Composite Aerospace Components," *Journal of the American Ceramic Society*, 82 [1] 161-68 (1999).

131 F.A. Opalski, "Fatigue Behavior of a Cross-Ply Ceramic Matrix Composite under Tension-Tension and Tension-Compression Loading," Master Thesis, Air Force Institute of Technology (December 1992): Adviser: S. Mall.

132 L.P. Zawada, L.M. Butkus and G. Hartman, "Tensile and Fatigue Behavior of Silicon Carbide Fiber-Reinforced Aluminosilicate Glass," *Journal of the American Ceramic Society*, 74 [11] 2851-8 (1991).

133 K.K. Chawla, Composite Materials: Science and Engineering, 2nd ed, Springer, New York, 1998.

134 L.P. Zawada and J.J. Pernot, "Effects of Load Ratio on the Fatigue Behavior of Ceramic Matrix Composites," presented at American Ceramic Society 94th Annual Meeting 14 April 1992, Minneapolis, Minnesota.

135 S. Mall and W.A. Weidenaar, "Tension-compression fatigue behavior of fabre-reinforced ceramic matrix composite with circular hole," *Composites*, 26 [9] 631-6 (1995).

136 K.L. More, K.L. More, P. F. Tortorelli, and L.R. Walker, "Effects of High Water Vapor Pressures on the Oxidation of SiC-Based Fiber-Reinforced Composites," http://www.ornl.gov/sci/de_materials/documents/characterization/More_Effect_High_H2O_CFCC_MatSciForum-01.pdf

137 P.G. Karandikar and T.-W. Chou, "Damage Development and Moduli Reductions in Nicalon-CAS Composites under Static Fatigue and Cyclic Fatigue, *Journal of the American Ceramic Society*, 76 [7] 1720-8 (1993).

138 K.M. Prewo, B. Johnson and S. Starrett, "Silicon Carbide Fiber-Reinforced Glass-Ceramics Tensile Behavior at Elevated Temperature," *Journal of Materials Science* 24 1373-9 (1989).

139 C.Q. Rousseau, "Monotonic and Cyclic Behavior of a Silicon Carbide/Calcium-Aluminosilicate Ceramic Composite," in <u>Thermal and Mechanical Behavior of Metal Matrix and Ceramic Matrix Composites,</u> ASTM STP 1080, eds. J.M. Kennedy, H.H. Moeller, and W.S. Johnson, American Society for Testing and Materials, Philadelphia, 1990.

140 L.P. Zawada, L.M. Butkus and G.A. Hartman, "Room Temperature Tensile and Fatigue Properties of Silicon-Carbide Fiber-Reinforced Aluminosilicate Glass," *Ceramics Engineering and Science Proceedings*, 11 [9-10] 1592-606 (1990).

141 R. John and B. Rigling, "Effect of Height to Width Ratio on K and CMOD Solutions for a Single Edge Cracked Geometry with Clamped Ends," *Engineering Fracture Mechanics*, 60 [2] 147-56 (1998).

142 H. Tada, P.C. Paris and G.R. Irwin, <u>The Stress Analysis of Cracks Handbook</u>. Del Research Corp. St Louis, 1985.

143 C. Droillard and J. Lamon, "Fracture Toughness of 2-D Woven SiC/SiC CVI-Composites with Multilayered Interphases," *Journal of the American Ceramic Society*, 79 [4] 849-58 (1996).

144 B.E. Deal and A.S. Grove, "General Relationship for the Thermal Oxidation of Silicon," *Journal of Applied Physics* 46 3770-3778 (1965).

145 T.B. Hankins and R.D. Branam, "Laser Diagnostic System and Ultra-Compact Combustor Characterization," Presented at the 33rd Annual Dayton-Cincinnati Aerospace Science Symposium, Dayton, *OH*, March 4 2008.

146 T.A. Parthasaranthy, R.A. Rapp, M. Opeka and R.J. Kerans, "A model for the oxidation of ZrB2, HfB2 and TiB2," *Acta Materialia* 55 5999-6010 (2007).

REPORT DOCUMENTATION PAGE

Form Approved
OMB No. 0704–0188

The public reporting burden for this collection of information is estimated to average 1 hour per response, including the time for reviewing instructions, searching existing data sources, gathering and maintaining the data needed, and completing and reviewing the collection of information. Send comments regarding this burden estimate or any other aspect of this collection of information, including suggestions for reducing this burden to Department of Defense, Washington Headquarters Services, Directorate for Information Operations and Reports (0704–0188), 1215 Jefferson Davis Highway, Suite 1204, Arlington, VA 22202–4302. Respondents should be aware that notwithstanding any other provision of law, no person shall be subject to any penalty for failing to comply with a collection of information if it does not display a currently valid OMB control number. PLEASE DO NOT RETURN YOUR FORM TO THE ABOVE ADDRESS.

1. REPORT DATE (DD–MM–YYYY) 10-09-2009	2. REPORT TYPE Doctoral Dissertation	3. DATES COVERED *(From — To)* September 2004 – June 2009

4. TITLE AND SUBTITLE Thermo-mechanical Characterization of Silicon Carbide-Silicon Carbide Composites at Elevated Temperatures Using a Unique Combustion Facility	5a. CONTRACT NUMBER
	5b. GRANT NUMBER
	5c. PROGRAM ELEMENT NUMBER
6. AUTHOR(S) Kim, Ted T., Capt., USAF	5d. PROJECT NUMBER #
	5e. TASK NUMBER
	5f. WORK UNIT NUMBER

7. PERFORMING ORGANIZATION NAME(S) AND ADDRESS(ES) Air Force Institute of Technology Graduate School of Engineering and Management (AFIT/ENY) 2950 Hobson Way WPAFB OH 45433-7765	8. PERFORMING ORGANIZATION REPORT NUMBER AFIT/DS/ENY/09-S01

9. SPONSORING / MONITORING AGENCY NAME(S) AND ADDRESS(ES) Air Force Research Laboratory Materials and Manufacturing Directorate 2230 10th St. WPAFB, OH 45433 The Dayton Area Graduate Studies Institute 3155 Research Blvd. Ste. 205 Kettering, OH 45420	10. SPONSOR/MONITOR'S ACRONYM(S) AFRL/RX and DAGSI
	11. SPONSOR/MONITOR'S REPORT NUMBER(S)

12. DISTRIBUTION / AVAILABILITY STATEMENT
APPROVED FOR PUBLIC RELEASE; DISTRIBUTION UNLIMITED.

13. SUPPLEMENTARY NOTES
This material is declared a work of the U.S. Government and is not subject to copyright protection in the United States.

14. ABSTRACT

This research investigated four different types of CMCs in a simulated gas turbine engine hot section condition that involved the simultaneous application of a combustion environment and mechanical fatigue loading using a unique burner rig facility developed for this study at AFIT. Three of the materials were woven Melt-Infiltrated (MI) BN/SiC reinforced by Hi-Nicalon Type S (Hi-Nic-S), Sylramic (Syl) and Sylramic with insitu BN coating (Syl-*iBN*) fibers, respectively. They were made by the slurry cast method. The other CMC was MI Hi-Nic-S/BN/SiC made using the prepreg MI processing. Prepreg MI CMC and Sylramic-iBN fiber reinforced CMC showed better resistance to the fatigue loading in the combustion environment. Thermally induced stress was determined using finite element analysis to be significant in elevating the stress level locally, causing reduction in the overall stress at which sufficient cracking occurs and leads to failure by means of oxidative degradation. Machined edge was susceptible to cracking and subsequently to oxidation that occurred behind the crack tip.

15. SUBJECT TERMS
Silicon Carbide Composites, BN Interphase, Fatigue, Combustion, Burner Rig, Oxidation, Thermal Stress, Gas Turbine Engine, Hot-Section, Finite element analysis

16. SECURITY CLASSIFICATION OF:			17. LIMITATION OF ABSTRACT	18. NUMBER OF PAGES	19a. NAME OF RESPONSIBLE PERSON Shankar Mall, Professor, ENY
a. REPORT U	b. ABSTRACT U	c. THIS PAGE U	UU	322	19b. TELEPHONE NUMBER (Include Area Code) 937-255-3636, x4587 Shankar.Mall@afit.edu

Standard Form 298 (Rev. 8–98)
Prescribed by ANSI Std. Z39.18